ACOUSTIC EMISSION MONITORING OF PIPES; COMBINING FINITE ELEMENT SIMULATION AND EXPERIMENT FOR ADVANCED SOURCE LOCATION AND IDENTIFICATION

Chika Judith Abolle-Okoyeagu

Submitted for the degree of Doctor of Philosophy

Heriot-Watt University

Institute of Mechanical, Process and Energy Engineering, School of Engineering and Physical Sciences

May 2019

ABSTRACT

Impact is a common source of damage in pipes and pipeline systems, detecting the location and nature of damage is vital for reliability and safety of these systems. This work sets out to assess the capacity of Acoustic Emission (AE) to monitor pipes and pipelines for externally applied mechanical damage. AE is a non-destructive testing and monitoring technique that relies on the propagation of elastic (stress) waves generated by impulsive events such as particle impingement, cracking or fluid flow. These waves are recorded at one or more sensors mounted on the surface of the object to be monitored. The key scientific question was to determine the extent to which the structure of a non-impulsive event could be reconstructed using sensors located on the external surface of a pipe.

The aim was to combine Finite Element simulations with a series of experiments in order that the relationship between the generating event (source) and the resulting stress-time history at a given point on the surface could be elucidated. Experiments and simulations were carried out with impulsive sources (pencil-lead breaks) and dropped objects, the latter being used to represent a non-impulsive event with a reproducible structure lasting around one second. The AE resulting from these sources was recorded over a period of around 2 seconds for both experiments and simulations. Two test objects, a solid cylindrical steel block of diameter 307mm and length 166mm and various lengths of pipe of diameter 100mm and wall thickness 10mm were used, the former to provide a relatively simple and well-studied platform to examine a number of essential principles.

The work on the solid cylinder first validated the simulation of the stress wave from an impulsive source and identified the main modes present, by comparing with analytical solutions. Then it was possible to identify the part of the experimental time series record at a given sensor which is uncontaminated by reflections from the edges and surfaces of the cylinder. The dropped object measurements on the solid cylinder provided clear records of the first and subsequent impacts as the dropped steel balls recoiled and returned back to the surface. There was a clear relationship between the measured AE energy and the estimated incident energy of the dropped objects at a range of timescales irrespective of contamination by reflections.

The work on the pipe sections formed the main series of systematic experiments. First it was established that an unloading time in the simulations of around 10^{-8} seconds gave a

reasonable representation of the frequency structure of experimentally observed stress waves. It was also observed from both experiments and simulations that a low amplitude wave travelling at around 5500ms^{-1} was the first to arrive at any surface sensor. The structure thereafter was complex, probably involving reflections from the inner wall of the cylinder and geometric interference as the wave spreads around the circumference of the pipe. The key finding of this aspect of the work is that the AE line structure of an impulsive source can be reproduced by simulation for short times, for longer times, the damping associated with reflections would require to be measured and introduced into the simulations in order to fully represent the real practical simulation. The degree of damping is important in making a cumulative assessment of multiple impulsive sources.

The dropped objects on the pipe confirmed that a mechanical disturbance which is extended in time can be identified from its energy-time imprint carried on the stress wave. The analysis was carried out at three different timescales; short (initial interactions free of reflections), medium (first contact including recoil) and long (involving several bounces). Generally, for medium and short timescales, the AE energy varied with drop height and mass consistently with existing models for balls on plate. For multiple bounces, the behaviour was more erratic probably due to the imprecise control of ball contact point. The simulations of AE worked well at medium and long timescales, providing an idealised framework unto which could be added effects of restitution and damping. At the short timescale, the twin challenges of time and spatial resolution meant that a solution could not be obtained within the limitations of the computing power available.

It is generally concluded that AE monitoring can be used to identify the nature of a mechanical disturbance on the surface of a pipe. Suggestions for future work include improvements to the simulations to include attenuation and to better simulate the dynamics of mechanical interactions at the surface, and extensions to the experiments to cover the effect of internal and external pipe environment and the use of mechanical sources which involve actual pipe damage.

DEDICATION

This thesis is dedicated to Ikebudu, Chidalu, Esimnachi, Kamsi and Chimamanda Abolle

ACKNOWLEDGEMENTS

I thank Almighty God for giving me the strength and guiding me successfully throughout my work. I am also indeed grateful to a lot of people who helped me in one way or the other and others who touched my life positively throughout my study.

Firstly, I would like to offer my profound gratitude to Prof. Robert Reuben, whose encouragement, guidance and zest for perfection brought the best out of me. I truly couldn't have asked for a better supervisor.

I also owe deep appreciation to Dr.Yuhang Chen for being a source of inspiration all through my thesis.

I would not forget to say a big thank you to the amazing staff and students of HWU particularly Okpu Ambrose Onne, Tina Donnely, Javier Palacio, Aftab Aziz and Noel Ehigiamusoe for making my stay worthwhile.

Finally and most importantly, I am grateful to my lovely parents and the house of bread prayer group Aberdeen for their constant prayers and support.

ACADEMIC REGISTRY

Research Thesis Submission

Name:	Chika Judith Abolle-Okoyeagu		
School/PGI:	School of Engineering and Physical Sciences		
Version: *(i.e. First, Resubmission, Final)*	Final	Degree Sought (Award **and** Subject area)	PhD Mechanical Engineering

Declaration

In accordance with the appropriate regulations I hereby submit my thesis and I declare that:

1) the thesis embodies the results of my own work and has been composed by myself
2) where appropriate, I have made acknowledgement of the work of others and have made reference to work carried out in collaboration with other persons
3) the thesis is the correct version of the thesis for submission and is the same version as any electronic versions submitted*.
4) my thesis for the award referred to, deposited in the Heriot-Watt University Library, should be made available for loan or photocopying and be available via the Institutional Repository, subject to such conditions as the Librarian may require.
5) I understand that as a student of the University I am required to abide by the Regulations of the University and to conform to its discipline.

* *Please note that it is the responsibility of the candidate to ensure that the correct version of the thesis is submitted.*

Signature of Candidate*:*		Date:	

Submission

Submitted By *(name in capitals):*	CHIKA JUDITH ABOLLE-OKOYEAGU
Signature of Individual Submitting:	
Date Submitted:	

For Completion in the Student Service Centre (SSC)

Received in the SSC by *(name in capitals):*			
Method of Submission *(Handed in to SSC; posted through internal/external mail):*			
E-thesis Submitted (***mandatory for final theses***)			
Signature:		Date:	

TABLE OF CONTENTS

LIST OF TABLES

LIST OF FIGURES

NOMENCLATURE

D	Distance between Sensor 1 and Sensor 2 (m)
f	Frequency (kHz)
S_1	Trigger sensor position
E	Young's modulus
ρ	Density (kg/m^3)
Δt	Time difference between hits (s)
υ	Poisson's ratio
$Z_1 Z_2$	Acoustic impedance (kg/m^{2}s)
x	Source sensor distance (m)
λ	Wave length (m)
α	Attenuation coefficient (dB/m)
θ, β, γ	Angles (deg)
y, y_1, y_2	AE signals
S_0	Extensional mode

ABBREVIATIONS

AE	Acoustic emission
ADC	Analogue to Digital Converter
CFL	The Courant–Friedrichs–Lewy
DAQ	Data acquisition
FFT	Fast Fourier Transform
FEA	Finite Element Analysis
K	Kinetic Energy (J)
NDT	Non-Destructive Testing
PLB	Pencil Lead Break
PSD	Power Spectral Density
PZT	Lead Zirconate Titanate
WT	Wavelet Transform
WD	Wavelet Decomposition
RMS	Root mean square
STFT	Short Time Fourier Transform
TOA	Time of arrival

LIST OF PUBLICATIONS BY THE CANDIDATE

- **J. Abolle Okoyeagu**, J. Palacio-Torralba, Y. Chen and R. L. Reuben, (2017). 'The Role of Unload Rate on Acoustic Emission Source Identification in Pipes'. - (Under Review).
- M F Shehadeh, **J Abolle Okoyeagu**, J A Steel and R. L. Reuben. 'The Role of AE Generated by Impact and Crack Spreading in Steel Pipes'. - (In preparation).
- **J.Abolle Okoyeagu**, J. Palacio-Torralba, Y. Chen, R L .Reuben, (2014). 'Acoustic Emission Source Identification in Pipes Using FEA'. 31st Conference of the European Working Group on Acoustic Emission, September.

Chapter 1– Introduction

1.1 Background

Pipelines play a significant role in the transport of both gases and liquids, particularly in the oil and gas industry. There is a constant interest in improved levels of monitoring of these structures, as pipeline accidents are quite often disastrous both to people and the environment [1]. The codes and standards for transmission pipelines, nationally and internationally and within the oil and gas industry, demand rigorous safety measures and one of the main concerns is to provide reliable systems for efficient, real-time monitoring [2]. A good number of studies have recommended Acoustic Emission Monitoring (AEM) for the continuous surveillance of structures, machines and processes [3-8] and this thesis examines how a quantitative approach can be applied to pipeline integrity assessment.

1.2 Overview

AE is a term used to describe high-frequency (0.1 to 1MHz) elastic stress waves generated by the rapid release of mechanical energy often associated with structural degradation [9, 10]. In pipelines, the main known sources are leaks, fatigue, and impact from external forces, although, in some applications, flow noise and abrasion may generate significant AE. Acoustic Emission Testing (AET) is a non-destructive testing method that relies on these propagating elastic waves to detect irregularities in structures, processes, and machines. Over the years, AET has become an accepted Non-Destructive Testing (NDT) technique with potential applications in pipelines [11] and this is due to its ability to provide information on the structural health of a pipeline by using relatively few monitoring points and relying on propagation characteristics to locate faults such as leaks [12]. AET differs from most other NDT methods like ultrasonics or radiography in the sense that information is derived from effects produced on (or in) the material, i.e. it relies on energy that is created within the test material rather than on a means of imaging the flaw [13]. In other words, AE flaw detection monitors degradative processes rather than the presence of a flaw.

Just as in any other NDT testing technique, AET has limitations, the most significant being its inability to effectively determine as many characteristics of an AE source as one might expect for its very high temporal resolution. Much of this is because a number of processes produce AE, and not all of these give rise to signal that is of interest. There are, therefore, still research challenges in determining the nature, severity and location of multiple and/or prolonged sources, using signals acquired at one or more sensors mounted on the pipe surface [11].

1.3 FEA Background

The Finite element analysis (FEA) is a computational technique used to predict and analyse the response of a structure to various external loads, this is done by obtaining approximate solutions to a mathematical problem whose dependent variables satisfies a differential equation within a known independent variable domain.

FEA uses a system of nodes and the object or model that is required to be analysed is split up into elements whose corners are the nodes. The number of nodes depends on the shape of element which forms a grid (mesh). The mesh is given relevant material properties and is then subjected to the loading conditions [14]. In mechanics analysis, nodes are assigned at a variable density throughout the material depending on the anticipated stress levels of a particular area. Regions which will have high stress (or, more importantly, high gradients of stress) require a higher node density than those which experience little or no stress. The solution process involves setting up an algebraic system of equations for the undefined nodal values which then approximates the solution [15]. Thus, instead of trying to calculate the results for the model as a whole, FEA calculates the equations of motion for each individual element and then puts all the individual solutions together to formulate the solution for the whole model.

In FEA, the calculation of stress-strain relationships is based on the constitutive equation, when an external stimulation is applied on a structure, the FEA software solves the partial differential equations for its equilibrium conditions and this is expressed in local or global stress and strain components.

For a linear elastic media with elastic coefficients $\overleftrightarrow{D}$ Hooks law is chosen as the constitutive equation

$$\vec{\sigma} = \overleftrightarrow{D} . \vec{\varepsilon}$$

Where

$\vec{\sigma}$ is the stress tensor with six independent components made of shear τ and normal stresses σ.

Also, $\overrightarrow{\varepsilon}$ is the strain tensor comprising of six independent components which consists of shear γ and normal strain ε component.

The elasticity tensor is described by the Young modulus E and the poisons ratio, γ.

If the variation of work W is induced by Forces F_i and displacement du_i in an equilibrium state, then

$$\delta W = \sum_I F_i \, \delta u_i = 0$$

In general, the external virtual load is equal to the internal virtual work, for a deformable body with a surface S and volume V, the resultant deformation is given as

$$\int_S \delta\vec{u}^t \, . \vec{F}_s \, dS + \int_V \delta\vec{u}^t \, . \vec{F}_v \, dV - \int_V \delta\vec{\varepsilon}^t \, . \vec{\sigma} \, dV = 0 \qquad 1.1$$

Where F_S and F_V are the respective forces acting on the surface and volume of the body and $\vec{\sigma}$ and $\vec{\varepsilon}$ the consistent internal stress and strain components respectively. If mass accelerations are introduced into the system, then D'Alembert principle is formulated, therefore, introducing the material density, equation 1.1 becomes

$$\int_S \delta\vec{u}^t \, . \vec{F}_s \, dS + \int_V \delta\vec{u}^t \, . \vec{F}_v \, dV - \int_V \delta\vec{\varepsilon}^t \, . \vec{\sigma} \, dV - \int_V \rho \frac{\delta^2\vec{u}}{\delta t^2} \, . \delta\vec{u} \, \delta V = 0 \qquad 1.2$$

Equation 1.2 defines the fundamental differential equation solved for every FEA.

When dealing with stress wave propagation, there are additional computational challenges associated with the fact that the stress distribution is not static and this is particularly acute when it is considered that the frequency range of AE propagation is typically in the MHz range. In this work, all the simulation history output for the stress wave was set at every 1 x 10^{-6}s to overcome this challenge.

1.4 Research Methodology and Objectives

The overall aim of this thesis is to examine the extent to which the time series of a mechanical disturbance introduced on the outer surface of a pipe can be reconstructed from signals recorded using surface-mounted AE sensors. The overall objective is to measure the sensor response to sources with prescribed temporal structures on simple cylindrical test objects and to match the measurements with simulations in order to determine the practical transfer function between source and sensor. The specific objectives can be broadly grouped into two parts, the first associated with the modelling approach:

I. To identify, demonstrate and validate the use of the FEA approach for modelling AE due to pencil-lead tests and impacts on various cylindrical objects.

II. To study the effect of different surface unloading rates on the resulting AE wave and develop recognition approaches.

III. To simulate various loading conditions resulting from dropped objects

and the second associated with application to the measurements:

IV. Calibrate AE sensors on a standard solid steel cylinder.

V. Study AE propagation characteristics on a standard solid steel cylinder.

VI. Calibrate AE sensors on a steel pipe.

VII. Study AE propagation characteristics on a steel pipe.

VIII. Understand and explain AE produced by ball bearing impacts on pipes.

IX. To develop tools for the identification of real source temporal structure using a linear array of sensors.

1.5 Contribution to Knowledge

The overall contribution to knowledge claimed here is in improved AE monitoring using a combination of practical measurement backed up by simulation whose purpose is to determine simple propagation parameters. These propagation parameters can then be used to reconstruct a surface disturbance provided that measurements are available for the same event at a specified sensor array. Although some research has been carried out on the use of FEA for acoustic emission wave propagation, none, to the knowledge of the author, examines systematically its use to develop practical surveillance models.

This contribution to knowledge is developed in the following three key areas:

I. It demonstrates an FEA approach to the simulation of AE wave propagation in a pipe using virtual sensors as an adjunct to current AE research techniques which tend to rely mainly on experiments that can be costly and difficult to carry out and in which it is difficult to control the nature of the source.

II. It assesses the real level of distortion of an AE signal as it propagates along the surface of a pipe and suggests the key factors influencing the changes in wave behaviour as a

means to providing a more structured way of reconstituting the temporal and spatial features of AE sources.

III. It evaluates the energy transmitted to a pipe during impact drop in practical situations and suggests the key factors influencing the relationship between mechanical surface damage and the resulting AE source on the surface of the pipe.

1.6 Thesis Outline

This thesis is structured in 8 chapters (six main chapters, with this introduction, plus a chapter on conclusions and recommendations), a brief summary of each of which is given below.

Chapter 1 presents a general background on the theoretical and experimental understanding of AE on pipes and gives a brief summary of the current status of AE monitoring of pipelines. It also gives a framework of the research objectives, the contribution to knowledge and a summary of the thesis.

Chapter 2 presents a critical review of the key research areas related to the thesis by an analysis of current efforts to use FEA to assist in extracting meaningful features. This starts with the current state of understanding of the underlying engineering science and technology of AE (as distinct from ultrasonic NDT). The ways in which the vast amount of data acquired during monitoring are then reviewed.

Chapter 3 presents the FEA simulation framework used in the current work and incudes an overview of the simulation software used (Abaqus) covering both the implementation and methodology. The rationale for selection of the structural elements of the FE model is described including geometry, material properties, mesh and boundary conditions.

Chapter 4 describes the experimental apparatus, procedures, and arrangements including all the calibration tests used to underpin the work. The AE measurement system is described and the experimental approach and procedures are explained.

Chapter 5 presents the simulation and experimental results for work carried out on a reference object, a solid steel cylinder. This object was chosen for its relative geometrical simplicity, which allows a comparison with published analytical solutions to improve the level of validation for both impulsive sources and those with extended temporal structure

Chapter 6 presents the simulation and experimental results for impulsive sources on a length of pipe. The simulations are matched to the results in order to assess the practical changes that need to be made to the simulations to account for practical factors.

Chapter 7 presents the simulation and experimental results for a ball bearing impacts on a steel pipe. The analysis is developed to account for the actual energy dissipated during impact on a pipe and the way in which the time series recorded at a remote sensor can be used to reconstruct the time series at a source.

Chapter 8 summarizes the main findings emerging from the preceding chapters and provides recommendations for practical application and future studies that could complement and extend the findings of this thesis.

Chapter 2 – Literature Review

This chapter reviews four essential elements of the literature relevant to the thesis; 1. AE technology, 2. The engineering science of AE, 3. AE signal processing, interpretation, and 4. Numerical modelling of AE. These are covered in turn below, highlighting those areas where a contribution to knowledge is required. The chapter culminates with an identification of the thesis topic set against the background of existing knowledge.

2.1 AE Technology

AE is the term used to describe the elastic strain energy propagating within a material as one or more of a number of possible wave modes with frequencies in the order of MHz The term "AE technology" is generally used for the measurement and interpretation of these propagating waves, and is distinct from vibration monitoring and the analysis of airborne sound emitted from vibrating surfaces. The key to interpreting AE is the identification of the source and this distinguishes AE technology from ultrasonic NDT, in which the source is known and is carefully structured. A wide range of phenomena, from surface impacts through incremental crack extension to martensitic phase changes have all been identified as generating AE. However, the generation of AE requires a rapid energy release rate, so there is a variable relationship between the energy of the generating event and the energy of the AE that actually ends up propagating through the material. Currently, there is no reliable way of relating the temporal structure of the generating event to the temporal structure of the AE "source", and this thesis attempts to address this by a combination of carefully-controlled experiments backed up by simulations. The other key practical issue tackled in this thesis is the distortion that the AE source temporal structure suffers in travelling from where it is generated to the surface-mounted sensor(s) where it is measured. Again, this is approached by a combination of experiment and simulation on a relatively simple cylindrical geometry, thus allowing some key parameters governing propagation and energy loss to be quantified.

The AE Technique (AET) is a passive non-destructive testing (NDT) technique that has been used widely since the 1970s. Early studies of AE focused on its use for materials characterization where AE events during materials testing were attributed to nano-scale processes such as dislocation movement [16]. More recently, interest has moved to the higher energy AE events associated with machines, structures and industrial processes, caused, for example, by impact,

cracking and fatigue [10, 17, 18]. In all cases, the AE is the result of a local rapid release in strain energy, which is the cause of the propagating wave.

The industrial application of AET has progressed significantly over the past two decades, leading to the production of several codes and standards [19]. Its current application include structural health monitoring of aircraft and bridges, railway rail-wheel interaction, pipeline monitoring [3, 20, 21] and erosion-corrosion processes [22, 23].

An advantage of AET over other NDT methods is its ability to allow continuous monitoring; this implies that damage growth can, in principle, be monitored at all times, (for example, right from the onset of propagation of a fatigue crack). Also, due to the very high temporal resolution of the AE signal, it is often found to contain additional information on the nature of the damage [16]. Other advantages of AE technology over other NDT techniques is its ability to localize the source of an AE event provided that arrival times of individual event waves can be identified at more than one sensor.

Just as in any other NDT technique, AET has limitations, the most prominent being its inherent lack of amplitude calibration, meaning that, although the energy of the propagating wave can be measured in terms of the surface elevation (in the nm range) and the frequency (in the MHz range), this energy cannot generally be directly traced to the energy of the event that caused the disturbance in the first place. This means that it is not generally possible to determine as many characteristics of an AE source as one might expect for its very high temporal resolution. Even for the relatively simple case of pipeline monitoring, there are, therefore, still research challenges in determining the nature, severity and location of multiple and/or prolonged sources, using signals acquired at one or more sensors mounted on the pipe surface [24].

2.1.1 *Acoustic Emission Measurements*

A typical AET monitoring system consists of an array of AE sensors (e.g. piezoelectric contact sensors) and preamplifiers, a signal processing unit, a data acquisition system, and a computer with software for controlling the acquisition, interpretation and storage of data. Figure 2.1 shows a simplified example for a pipeline monitoring system [11, 25] where the array involves two sensors only, although the principle can be applied to longer arrays and with sensors which are located at different circumferential positions. When a structure is under load, any initiating event, such as an impact, a crack extension increment or a leak will generate propagating elastic waves

whose temporal structure should contain information about the initiating event. Because an AE source radiates energy in all directions, any suitable sensor located sufficiently near to the source will be able to record a signal and knowing the locations of the sensors will allow the propagating wave to be sampled simultaneously at a number of places.

AE energy propagating in long structures through different media in long structures are known to be partially transmitted and partially reflected at surface, however, this might not be fully the case in this work as all the cylindrical objects considered are only a few metres long.

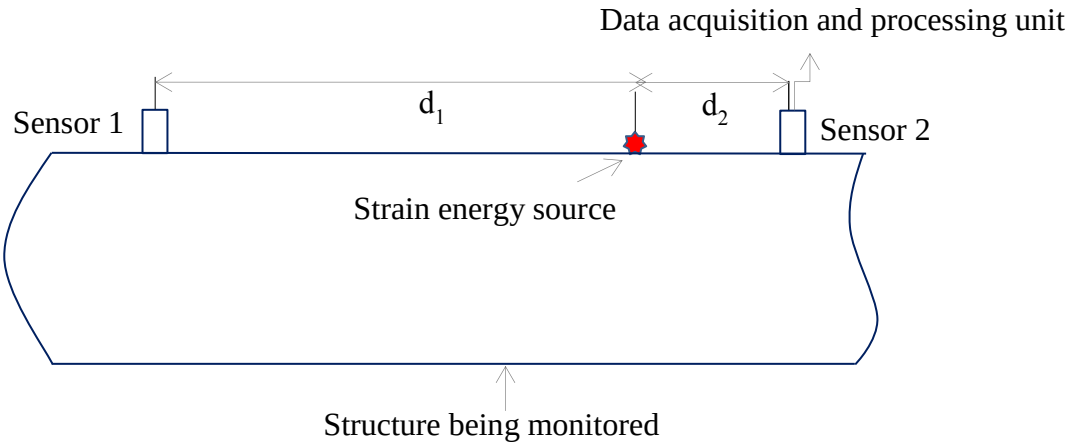

Figure 2-1: *Schematic diagram of AE generation and recording at two sensors at distances d_1 and d_2 from a source*

AE sensors are transducers, which convert a mechanical disturbance to an electrical signal, normally designed to detect waves within the 0.1 to 1MHz frequency range and are usually placed on the surface of the test structure. The typical physical amplitude of an AE wave is in the nm range, so sensors are configured to give good sensitivity in a particular band, rejecting other information which may be present and which may constitute noise. Analogue filters are normally used prior to pre-amplification of the signal in order to optimise sensitivity and reduce noise.

Although a number of specialist AE sensors have been developed e.g.[26] [27] almost all commercial AE sensors employ piezoelectric sensing elements. The most commonly used materials are lead zirconate titanate (PZT) and quartz and, aside from the specific piezoelectric properties, sensitivity is engineered into the sensor construction including the shape, size, and configuration of the piezoelectric element and the housing, backing and surface protection [28]. Although not specifically part of the sensor, the nature of the coupling between the sensor and

the test surface can significantly affect the recorded signal, figure 2.2 shows a schematic diagram of a typical AE sensor.

Generally, there are two types of commercial piezoelectric AE sensor, “resonant” and “wide-band”, although the latter are essentially resonant in a number of overlapping bands. Resonant sensors have high sensitivity in a relatively narrow frequency range but this is at the potential cost of loss of information in the recorded signal. Wideband sensors have a damping or backing added to the piezoelectric element(s) so as to reduce the preferential response of the sensor to particular frequencies and, as a result, analysis of a wider bandwidth of the raw AE is required. In either case, the frequency response of the sensor needs to be taken into account in the interpretation of the signal and in comparing measured with simulated waveforms [29].

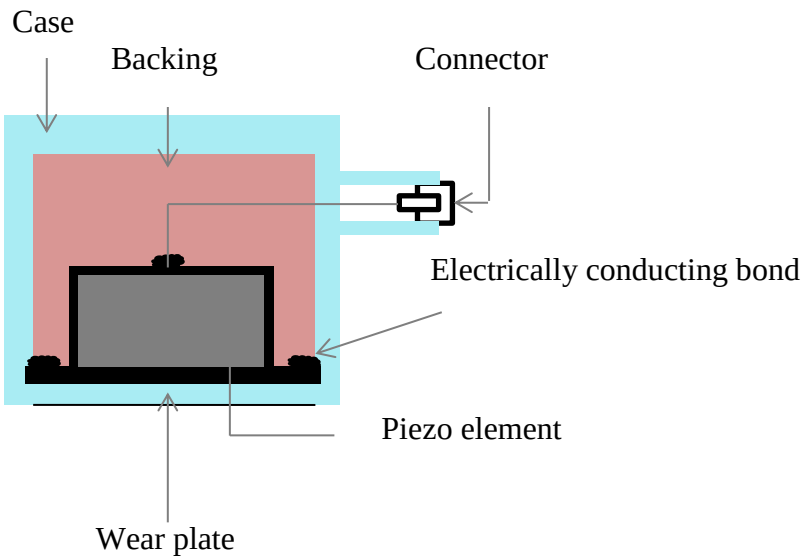

Figure 2-2: *Schematic of a typical commercially available AE sensor [30]*

For AE sensors, there is therefore a concession between sensitivity and bandwidth, i.e. for a narrow application bandwidth, a higher sensitivity can be obtained by simply adjusting the piezoelectric element’s geometry.

Resonant or wideband sensors with sensitive frequencies in the hundreds of kHz are commonly used in AE measurements and, because of this, most AE analysis centres on frequencies between 100 kHz and 1 MHz. With all such measurements, analogue band-pass filters are required to ensure that any noise outside the frequency range of interest is kept as low as possible, especially given the very high gain (typically 40dB or 60dB) used in AE preamplifiers. These high gains

are needed in order to minimise the amplitude of any noise (usually EMI) picked up during transmission of the signal from the sensor to the data acquisition unit.

Unlike capacitive or laser-based measurements, Piezoelectric AE sensors do not provide an absolute measurement of the wave amplitude but this is generally not regarded as a problem because these sensors can be calibrated against standardized sources and, if necessary, against standard sensors. Because of its central importance in this thesis, sensor calibration will be discussed fully in chapter 4.

2.1.2 *Sources of AE*

Classically, there are two types of AE source, artificial sources which are used for various aspects of calibration and for research, and natural sources which are, of course, the objects of monitoring. Some natural sources such as helium jets and pencil lead breaks, are sufficiently reproducible to be used as artificial sources.

Generally speaking, artificial sources aim to be as “white" as possible and as close to impulsive as possible, although there are some artificial sources which are continuous. In some specialist cases, piezoelectric sources with very specific structures, similar to those used in ultrasonic NDT can be used. There are two widely used impulsive artificial AE sources; the transducer pulser and the Hsu Nielsen source or Pencil Lead Break (PLB), the simplest, most common, and of interest in this work being the PLB.

The PLB is widely accepted as a valuable reproducible source for testing AE equipment [37-39]. Generating the event involves the breaking a 0.3mm diameter pencil lead by pressing it on the surface of the test structure and applying a bending moment as illustrated in Figure 2.3. The applied force produces a local deformation on the target surface which is released when the lead breaks. The fracture is therefore normally assumed to be a step-unload which generates an AE disturbance which then propagates over the surface and through the material where it can be detected by sensors placed on the surface of the test structure. The PLB is often used as a quick way to determine the apparent AE wave speed in the test structure, check permissible sensor spacing and check the accuracy of source location. Although the fracture of the lead is effectively a natural source, the generated AE is highly reproducible [40].

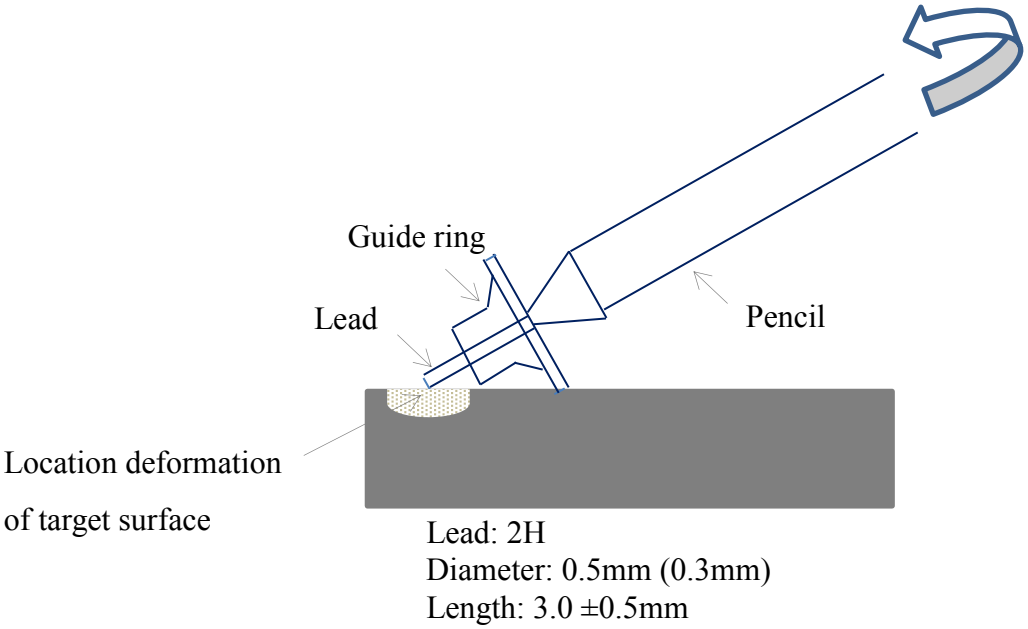

Figure 2-3: *The Hsu Nielson Source [31]*

As far as "natural" sources are concerned, almost anything which causes an impulsive load on (or in) a material can generate AE, and reviewing all of those that have been published would be very lengthy. Therefore, a selection has been taken in this review with an emphasis on the (likely) temporal structure of the source and the relevance to the particular application of this research.

Impacts are important sources of AE in pipelines [32] and many researchers have attempted to study the characteristics of AE signals generated as a result of impact on structures. For example Prosser *et al* [18] studied the AE signals created by impact sources in thin aluminium and graphite/epoxy composite plates and concluded that AE signals produced by high velocity impacts have much higher frequencies. Droubi et al [33] drew similar conclusions while working with particle impacts and found a distinct threshold in mass where whole-body deformation of the target affected the AE signal produced for a given incident kinetic energy.

Burstein et al [34] in their study of the acoustic emission effect of impact angle on slurry erosion–corrosion of stainless steel used a two-electrode electrochemical cell in a slurry rig. They observed that sharp rises in the electrochemical current transient under particle impact were followed by an AE event and these transients were as a result of individual erosion events. They also observed that the rise times at normal incidence were much lower than impacts at oblique angles.

Crack extension during fatigue is one of the most technologically important sources of natural AE [35] given that the principle has significant structural health monitoring implications. In fracture and fatigue of brittle materials, the source of AE is reasonably obvious as the strain energy released above and below the fracture plane. For metals, AE is generated in crack propagation during the intense crack-tip plastic deformation, and this is also seen in other intense plastic deformation processes, such as metal cutting [36]. In composites and even in such structures as suspension bridge cables the events leading up to failure in so-called "damage-tolerant" structures can be followed using AE [37, 38]. This is used commercially in, for example, the testing of composite pressure vessels [39].

Whereas early studies showed that AE can arise from dislocation movement and phase transformations [40, 41], the most common technological use is to monitor impact, crack growth and fatigue. In pipelines, the main known sources are leaks, fatigue and impact from external forces, although, in some applications, flow noise and abrasion may generate significant AE [42].

The energetic conditions for crack propagation were first described by Griffith [54] as the strain energy rate

$$G = -\frac{d'\Omega}{dA}$$

Where the differential describes the incremental amount of energy needed to extend a crack by a given incremental area. Griffith, in his initial approach, assumed that the strain energy release rate equals twice the free surface energy [43], which is only valid for very brittle materials. However, in practice, a plastic deformation zone develops around the crack tip, whose size increases with the applied load until the crack propagates. Nonetheless, the formation and propagation of this plastic zone also results in energy dissipation and Irwin [44] modified the Griffith approach. He separated the strain energy release into a contribution for the formation of new surfaces and an additional contribution for energy dissipation from plastic deformation. Irrespective of whether the crack extension is by brittle or plastic processes, one would expect the strain energy release rate to be proportional to the volume within which the strain is relaxed multiplied by the integral of stress and strain in that volume, i.e.

$$G = \int \sigma \times \varepsilon \cdot dV$$

For brittle crack extension (ie. Close to Griffith conditions), the energy is released rapidly and effectively by elastic recoil. For the case of plastic crack extension, the literature is rather more sparse, although it is known that plastic deformation needs to occur at very high strain rate to generate significant AE [36]. Whereas crack extension sources are micro-scale or even nano-scale in their localisation and event duration, sources due to impact on a surface result within an area about the size of the impactor and over the duration of the impact, both of which tend to be in the millimetre and millisecond range [58-60].

Momber et al [45] have investigated another aspect of pipeline AE monitoring. They used pre-cracked multiphase alloy targets to investigate the effect of abrasive mass flow rate and abrasive particle velocity on the AE signals. Their studies showed that higher impact velocities were characterised by higher AE signal amplitudes. Also, they concluded that material removal dominated by trans granular fracture is associated with burst emission due to the sudden energy release during inclusion fracture whilst material removal dominated by intergranular fracture gives rise to continuous AE signals.

2.1.3 *Condition Monitoring of Pipelines*

AE is a useful tool for monitoring pipeline systems allowing earlier diagnosis, planned maintenance and avoidance of unscheduled shutdown. Condition monitoring of pipelines is generally carried out either for structural integrity monitoring or for process monitoring, and so a good monitoring system should have the ability to detect both structural and process defects e.g. leakage and erosion. Miller et al [46] developed a reference standard for evaluating pipes for leakage with 1-foot location accuracy using two different location techniques and a 25-foot sensor spacing. Changes in pipeline operating parameters can also be monitored directly or indirectly using a model, which relates the AE to the relevant parameter [47]. For example, Sun [48] developed a linear model to estimate the variations of the pressure and flow rate at the ends of a pipeline following the occurrence of a leak and verified his model on a real oil pipeline with a leak.

Jian et al [49] have also presented a novel approach to pipeline leak detection based on a fuzzy clustering neural network, applied to experimental measurements. Shabaik et al [50] have used a numerical scheme to formulate the leak detection problem in state-space form and applied a modified extended Kalman filter (MEKF) in combination with feed forward computations to

predict the leak magnitude. These simulation results showed that the developed state estimation scheme effectively detected small leaks in pipelines within a short period.

Mansour et al [51] have carried out steady and unsteady computational fluid dynamics simulations of leaks in a 0.1m diameter pipe using a 3D turbulent flow model. The simulations revealed a clear influence of the leak on the pressure gradient along the different paths of the flow inside the pipe, although little effect was observed for very small leaks.

There is little, if any, published work in characterising the effects of external mechanical damage or impact on pipelines. Shehadeh [11] has carried out laboratory scale work with dropped weights and has used a solid model to establish the propagation characteristics of the same pipeline but has stopped short of relating the two to identify sources. There is therefore an opportunity to develop this area.

2.2 The Engineering Science of AE

Once generated, AE is essentially a structure-borne sound and its analysis is classically tackled by solving the wave equation. The essential analytical solutions are covered in a monograph by Kolsky [52] and much of the associated relevant technology (albeit applied to buildings and lower frequency sound) by Cremers et al. [70]. This section summarises the underlying engineering science as a background to more recent developments in AE analysis and signal interpretation.

An understanding of AE wave propagation in an elastic medium is obtained by the solution of the general wave equation:

$$\frac{\partial^2 \emptyset}{\partial t^2} = C^2 \nabla^2 \emptyset$$

where $\emptyset$ is a potential function representing the plane waves traveling in the positive and negative directions.

∇^2 is the Laplacian operator in Cartesian coordinates;

t = time (s);

and C = wave velocity (m/s)

For deformation in one dimension (say, x-), the form of the solution for the potential function is

$$\emptyset = f(x - ct) + g(x + ct)$$

where *f* and *g* represent the wave traveling in the positive and negative directions, respectively

2.2.1 *Modes of Elastic Wave Propagation*

Of course, AE waves are rarely, if ever, one dimensional, and can propagate in various ways depending on the nature of the original disturbance and structure geometry; different sources produce different frequency, amplitude, and dispersion characteristics, and multiple reflections from boundaries interfere with the primary wave propagation leading to a complex field which may eventually become regular at long distances from the source [53]. When the medium is of infinite extent and of elastically isotropic material, there exists only two types of waves, both of which propagate at a constant phase velocity through the solid; these are dilatational waves (also called the longitudinal L- or P-waves) and distortional (also called shear or S-waves) [52]. These two types of wave correspond to the two types of stress that can be induced in a material (direct stress in compression and tension and shear stress). The deformation in a longitudinal wave (Figure 2.4) is parallel to the direction of wave propagation, and may be expansion, compression or both, so that the direction of the wave velocity (the speed that the disturbance propagates in the medium) and the particle velocity (the speed of particle motion in the medium) are identical and opposite [54].

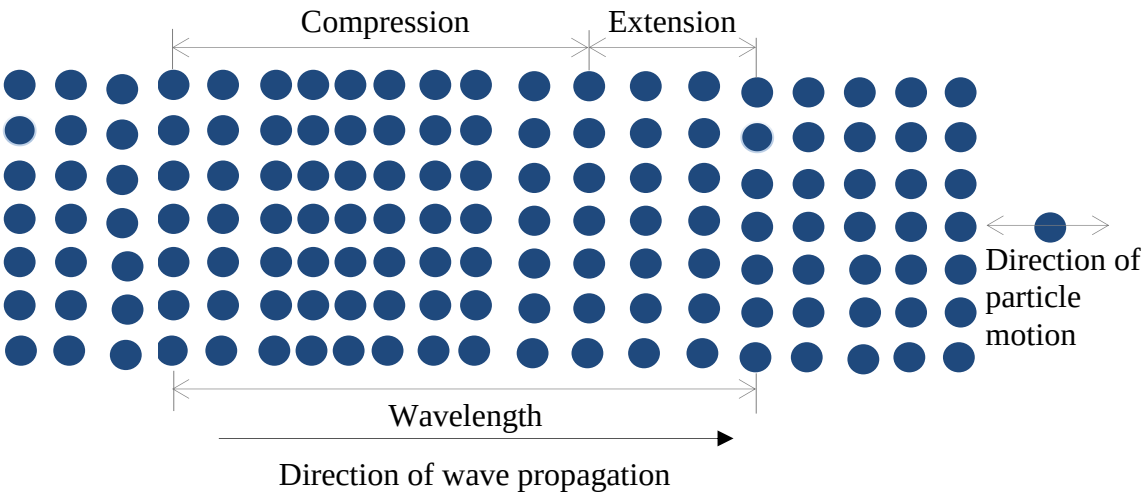

Figure 2-4: *Schematic representation of instantaneous deformation of atoms in a P-wave*

The velocity of longitudinal waves (c_1) is given by:

$$c_1 = \sqrt{\frac{E(1-v)}{\rho(1+v)(1-2v)}}$$

where *E* is Young's modulus of elasticity for the material;

ν is Poisson's Ratio for the material;

and

ρ is the density of the material.

For shear waves, the oscillation is perpendicular to the direction of wave propagation (Figure 2.5). The velocity of shear waves c_2 is given by the following expression:

$$c_2 = \sqrt{\frac{E}{2\rho(1+v)}}$$

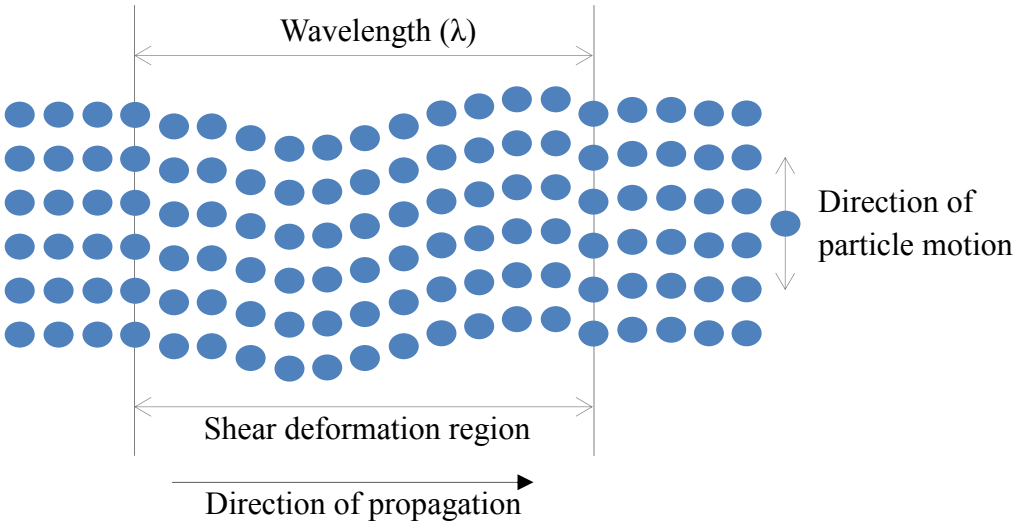

Figure 2-5: *Schematic representation of instantaneous deformation of atoms in an S-wave*

As is evident from Figures 2.4 and 2.5, both P-waves and S-waves require the excitation of a plane of the material, which is rarely the only component of a natural source. However, these two types of waves are routinely used in ultrasonic NDT where the original planar excitation (generated by a specially-designed piezoelectric transducer) propagates as a column within the material which is often treated as a ray for diagnostic purposes.

Rayleigh waves are surface waves, which can be generated by a point disturbance and, as such, are of importance in AE analysis. They have appreciable amplitude only near the surface of a body and the amplitude of the disturbance decays exponentially with depth from the surface, rather like waves on the surface of water. They ideally only exist in a semi-infinite medium, although, in practice, small disturbances on any free surface can generate waves close to this ideal. Rayleigh waves propagate parallel to a free surface at a unique speed, usually slower than the shear wave speed, and the surface wavefront can be planar, if excited along a line as shown in Figure 2.6 or, more likely, cylindrical if excited at a point [55]. As with water waves, each particle within the wave moves in an elliptical orbit.

The velocity of the Rayleigh waves c is given by the following expression:

$$= \sqrt{\frac{2\mu(1-v)}{\rho(1-2v)}}$$

where μ is the shear modulus

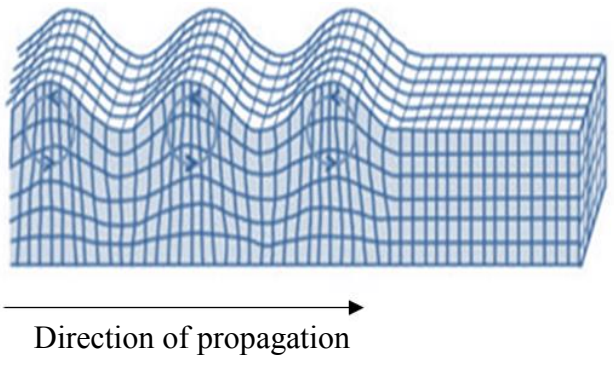

Figure 2-6: *Schematic representation of a 2D section of a Rayleigh wave [56]*

The remaining technologically significant modes of stress wave propagation are collectively known as Lamb waves (or plate waves). These modes can be generated in thin plate-like structures, i.e. those with two free surfaces, so do not require the assumption of a semi-infinite

solid as is the case for Rayleigh waves. In principle, an infinite number of modes is possible in two classes, known as symmetric (extensional) and antisymmetric (flexural) according to the nature of the displacements within the plate, (Figure 2.7). Because these waves propagate between the two parallel free surfaces, they can be used to detect surface damage and a specialised version of ultrasonic NDT using Lamb waves is now well-established [57]. The two basic wave mode classes are shown in Figure 2-8

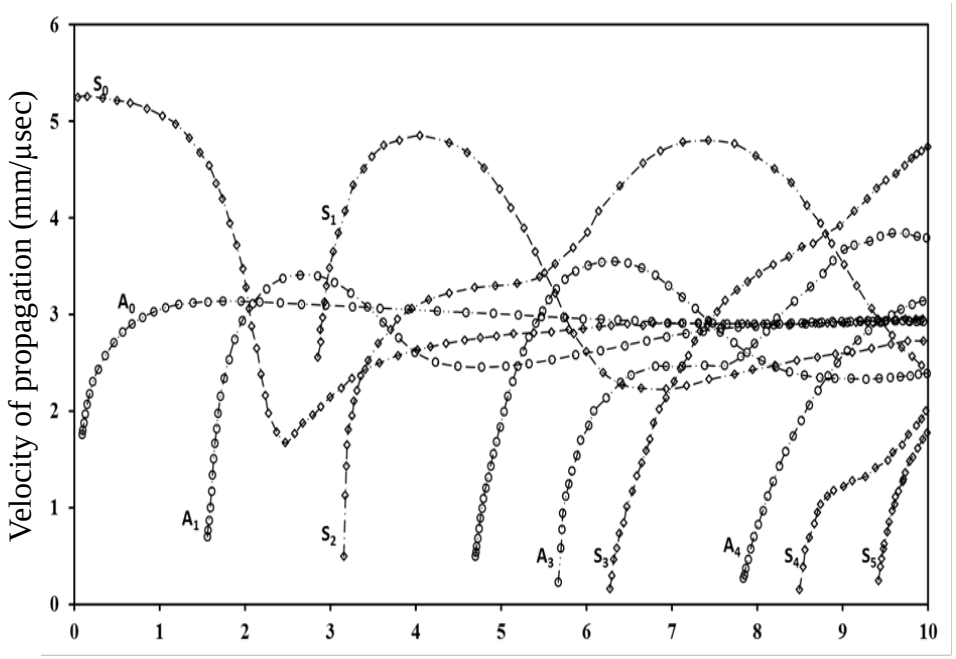

Figure 2-7: *Dispersion curves (amplitude and speed) for Lamb waves in steel ;(Sn) symmetric Lamb wave ;(An) asymmetric Lamb waves. [101]*

In practice, only the 0-modes are of significant amplitude (Figure 2.7). The extensional S_0 mode has a lower amplitude and higher speed than the flexural A_0 component and, when both are generated by a single event, the extensional mode can be detected as a small amplitude component arriving at a sensor before the larger flexural wave [59]. Also, for Lamb waves, the propagation velocity is governed by the type of source, material density and the wavelength. The wavelength is related to the frequency and velocity by $\lambda = \frac{V}{f}$.

where

λ = wavelength

V = Velocity

and

f = frequency

However, for isotropic materials, if x and y are the coordinate axes in the plane of a plate, and u and v are the corresponding displacement along these axes, then the extensional mode in- plane displacement is given by the equations [60].

$$\frac{\partial^2 u}{\partial x^2} + \frac{(1-v)}{2}\frac{\partial^2 u}{\partial y^2} + (1+v)\frac{\partial^2 v}{\partial x \partial y} = \frac{\rho}{A}\frac{\partial^2 u}{\partial t^2}$$

and

$$\frac{\partial^2 v}{\partial y^2} + \frac{(1-v)}{2}\frac{\partial^2 v}{\partial x^2} + (1+v)\frac{\partial^2 u}{\partial x \partial y} = \frac{\rho}{A}\frac{\partial^2 v}{\partial t^2}$$

where v is Poisson's ratio, ρ is the density, A is given by

$$A = \frac{Eh}{(1 - v^2)}$$

and E is the Young's modulus and h is the plate thickness.

Also, if the displacement along the x axis is w

the flexural motion is given by

$$D\nabla^4 w + \rho\frac{\partial^2 w}{\partial t^2} = 0$$

Where the bending stiffness per unit breadth,

$$D = \frac{Eh^3}{12(1 - v^2)}$$

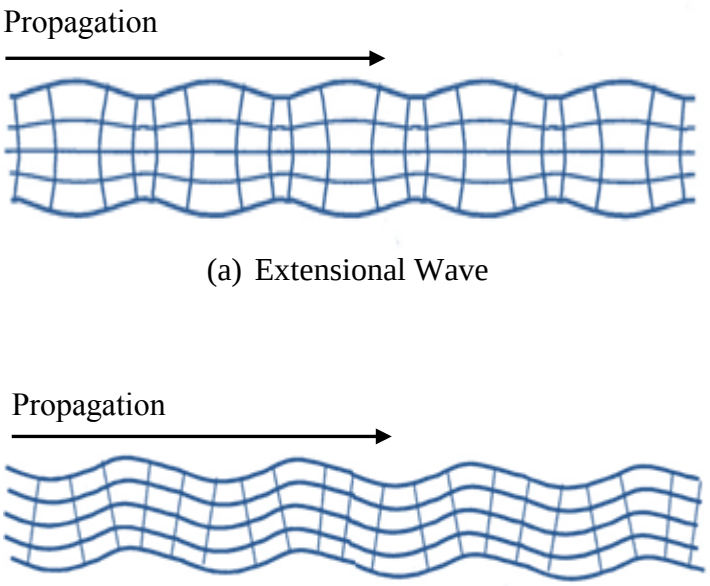

Figure 2-8: *Schematic diagrams of the two classes of Lamb waves (a) extensional and (b) flexural*

The initial disturbance in a real AE source is likely to be of mixed mode and will not be located at a point in space or time, making an analytical (or even numerical) solution to the wave equation highly impracticable. Even for simple sources, wave mode conversions at boundaries [55], interference of different modes, dispersive and non-dispersive components, different propagation velocities and paths, and different types and rates of attenuation combine to make an extremely complex problem requiring a number of experimental observations to obtain relevant parameters [61, 62].

Wave propagation in pipelines depends largely on the geometry of the structure through which it is transmitted, the internal and external environments (e.g. internal pressure and temperature) and the nature of the fluid inside the pipe [11]. The following section covers the essential parameters, which needs to be measured in order that attenuation and boundaries between the pipe and its external and internal environment can be taken into account.

2.2.2 *Medium Boundary Effects and Attenuation*

When mixed mode AE is propagating in any structure, energy will be lost with distance from the source and this energy may be lost in different ways from the different modes. Adding the fact that the different modes propagate at different speeds, it can be seen that the original source time-frequency structure will suffer some distortion and it is important to understand the ways in which

energy can be lost during propagation in pipelines. When a wave meets a boundary between media, it is partly reflected and partly transmitted [55], the partitioning between the transmitted and reflected waves depends on the angle of incidence and the relative acoustic impedances of the two media on either side of the boundary; if both materials are closely matched in acoustic impedance, a large proportion of the energy will be transmitted and this is the basis of choice of couplant and the need to avoid air bubbles. Furthermore, both the reflected and transmitted wave modes could be different from the incident wave (mode conversion), Figure 2.9.

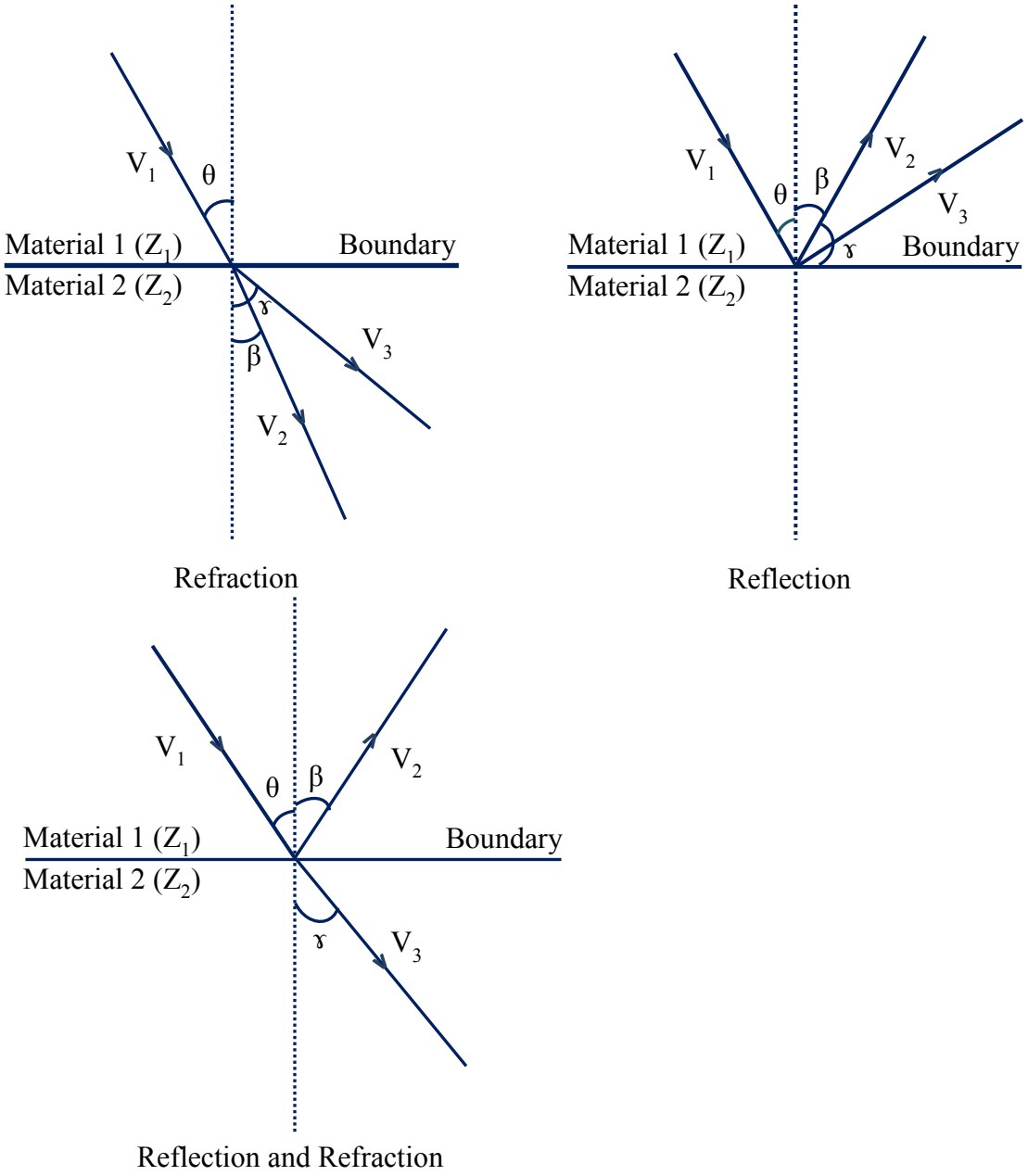

Figure 2-9: *Reflection, refraction and mode conversion of waves at boundaries*

For pipelines, this means that the effective attenuation due to "leakage" in energy at boundaries will vary according to the type of fluid being carried (mostly, whether it is liquid or gas) and surrounding medium (mostly if the pipe is buried and/or coated and if the surroundings are wet or dry) [63].

For two materials with acoustic impedances Z_1 and Z_2, the percentage of energy transmitted at the boundary E_t is given by:

$$E_t = \frac{4Z_1Z_2}{(Z_1 + Z_2)^2} \times 100$$

And, consequently, the percentage of energy reflected E_r is given by:

$$E_r = \left[\frac{Z_1 - Z_2}{Z_1 + Z_2}\right]^2 \times 100$$

The acoustic impedance is defined by $Z = \rho.V$, where ρ is density of the material (kg/m^3) and V is the wave speed (m/s).

The acoustic impedances of some common materials can be seen in Table 2.1.

Material	Acoustic Impedance (kg/m^2)
Steel	46×10^6
Water	1.48×10^6
Air	4.3×10^6
Oil	1.86×10^6
Methane	13.1×10^6
Clay	1.8×10^6
Gravel	2.91×10^6 - 4.0×10^6
Sand	2.6×10^5

Table 2-1: *Acoustic impedance of some materials of relevance to pipeline transmission [64]*

Longitudinal and shear waves are reflected or refracted when they impinge on a boundary, and, generally, four different waves are generated i.e. a wave of each type is reflected and refracted. One reflected wave is of the same type and the same angle as the incident and the second is of different type with an angle given by Snell's law:

$$\frac{\sin\theta}{V_1} = \frac{sin\,\beta}{V_2} = \frac{sin\,\gamma}{V_3}$$

where θ, β and γ are the wave propagation angles shown in figure 2.9,V_1, V_2, and V_3 are the wave speeds (m/s).

For the practical situation of detecting AE generated on the outer surface of a pipeline using sensors mounted on the outer surface, it is unlikely that much information about the source will be transmitted in P- or S-waves as much of the energy in these waves would be lost within the first few reflections. It is, however, possible that some of any energy generated in these modes could be converted to surface waves (Lamb or Rayleigh waves on the inner or outer circumference) and hence propagate to a distant sensor [65].

Although surface waves on a pipeline do not propagate towards a boundary as such, it is possible that some energy will be lost at the inner or outer surface as a Rayleigh wave propagates and also that the amount of energy lost will depend on the relative acoustic impedances of the pipeline and its surroundings. For Rayleigh waves, this could in principle, be accounted for as a component of attenuation, which could be measured for a given pipeline diameter and medium [60]. For Lamb waves, the reflection coefficients cannot easily be estimated due to the complex range of mode conversions [55, 66].

AE waves are attenuated by several mechanisms, including material absorption, scattering and diffraction, dispersion [60, 65] and when encountering interfaces, as described above.

In geometric attenuation, the wave amplitude (A) decreases as source-sensor distance increases (r) and this occurs when the wave spreads with a constant energy. Geometric attenuation is a consequence of energy conservation in which the wavefront energy remains constant throughout the propagation path. Wave propagation in plates is normally considered to be two-dimensional, expanding as a cylindrical wavefront, and this concept can be extended to thin-walled cylinders, although it needs to be accepted that, once the wave front diameter reaches

the circumference of the pipe, its edges will impinge on each other. In geometric attenuation, wave amplitude (A) decreases inversely as the square root of propagation distance(r), $A = \frac{k}{\sqrt{r}}$. Geometric attenuation is quite small in pipelines because the wave front becomes plane after a short distance.

The effect of internal friction on an AE signal can be described by an exponential amplitude drop with distance which gives a steep attenuation close to source. Internal friction is due to the damping capacity of the material and occurs as a result of the conversion of the mechanical energy to thermal energy in a strained material [67]. Internal friction is normally measured using cyclic loading (e.g. using a torsion pendulum). In fluids, internal friction can be treated analytically but, with solids, this is quite complex and depends on the nature of individual solids [68]. In plates and shells, the transition distance at which internal friction starts to dominate over geometric spreading is given by $4.34 \,/\, \alpha$, where α is the attenuation factor in dB/m [69].

Scattering and diffraction are another major cause of attenuation and they are manifest as an amplitude drop when waves travel through media with complex boundaries such as holes, inclusions, bubbles, slots, cracks, and cavities. Scattering occurs when the AE waves propagate through the void or inclusion, while diffraction occurs when AE waves propagate around edges e.g. cracks. Generally, these effects cause a drop in amplitude in the wave while it propagates a distance depending on the kind of distribution centre involved [70].

Dispersion is an attenuation mechanism which only affects dispersive waves (such as Lamb waves) whereby the shape of an AE pulse changes as it propagates through the material due to switching of energy between modes [71]. In elastic solids, Rayleigh waves show no dispersion at the surface, but they become dispersive when the wave velocity changes with depth.

In practical AE monitoring applications, it is not normal to separate the different attenuation mechanisms. This has led a number of authors simply to use an absorption law to describe all mechanisms, where the AE signal energy decreases exponentially with distance,x, from the source $E = E_0 e^{-kx}$. For dispersive waves, the attenuation coefficient could also depend on frequency thereby leading to some form of structural filtering [72, 73]. Shehadeh et al [63] have taken this approach in measuring attenuation in a relatively long (around 3 metres) steel pipe with various internal and external environments (air, water and wet and dry sand). They found the effective attenuation coefficient to increase with the degree of supposed “leakage” to the

environment caused by better impedance matching (essentially due to the amount of water in the environment). Because the simulations in the current work have no attenuation mechanism built into them, matching the simulations with actual measurements is a potential way of introducing the likely effect of attenuation over very long distances.

2.3 AE Signal Classification

For general monitoring purposes, it is useful to classify AE signals into continuous and burst signals. Burst signals result from distinct events in a material, typical examples being crack growth increments and impact. Continuous signals result from sources which are themselves continuous, the most obvious examples in pipelines being leaks and flow noise. Between these two extremes lie a range of (more realistic) source types which have some kind of temporal structure which may or may not be discernible once the AE has propagated from the source to a remotely-placed sensor. Figure 2-10 shows a schematic representation of these different AE signal types.

Normally, the shape of a burst waveform is characterised by a sinusoid which decays exponentially, whereas continuous signals are characterized by a random oscillatory appearance, and they are usually a collection of emission events from one or more sources that yields sustained signals [65].

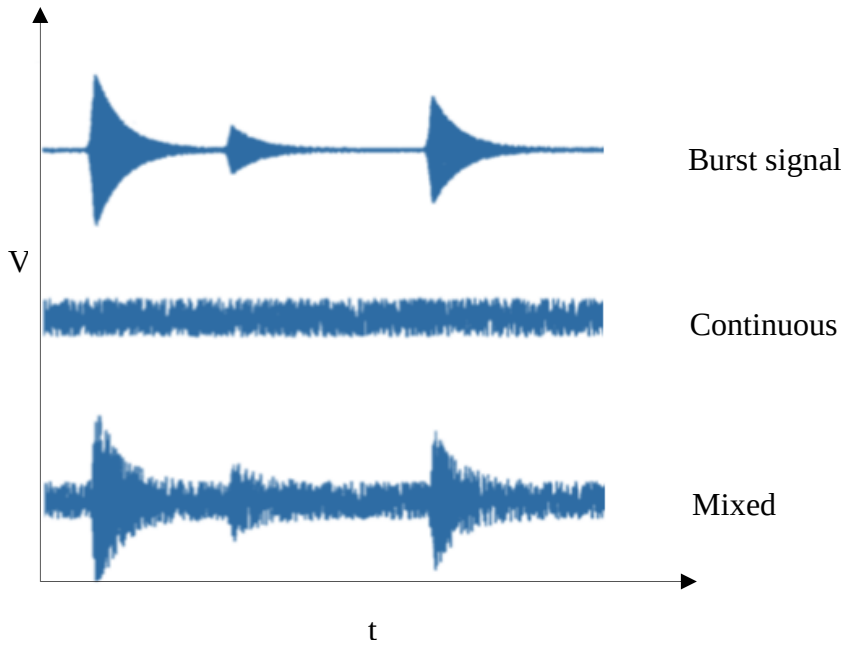

Figure 2-10: *Schematic representation of different AE signal types [65]*

More often, practical AE generating events are extended in time but are not continuous, and there is little in the way of conventional wisdom for treating such "pulsatile" signals. A common method employed in the processing of this pulsatile signal first includes producing a mechanically-based model of the signal taking into account the events generated and how these events are organized in time and space [77].

AE signal features can be represented either in the time or frequency domain. For many applications, time domain analysis is adequate as it allows the location of events which are captured by two or more sensors [74]. Frequency analysis is often used to identify source type and spectral decomposition can help to differentiate between various propagation modes [75, 76]. The Fast Fourier Transform (FFT) is a commonly used tool for converting the discrete time domain (data) into the frequency domain.

Generally, the FFT technique reduces computational round-off errors and computational time involved in converting time domain data . For instance, Mao et al [77] have used an FFT analysis for the monitoring of laser welding processes, showing that there were significant differences in the acoustic emission frequency content in the conduction and keyhole processing regimes. Harčarik et al [78] have also studied the possibilities of using FFT for the analysis of mechanical vibration combined with sound data, highlighting how frequency domain processing can be used to harmonize data resulting from different physical processes often with different frequency characteristics. Similarly, Mostafapour et al [32] have applied the FFT technique to investigate leak detection in pipes; they specifically studied the vibration behaviour of pipes through resonance frequencies using signals generated by the pipe wall vibration, results showing a good agreement between the experimental and modelled spectra. The FFT is essentially an energy spectrum and is sometimes complemented or replaced by the power spectral density (PSD), depending on the significance of the measure required for monitoring purposes [79]. Both the FFT and PSD require the frequency spectrum to be constant in time (stationary) [80].

For non-stationary signals, the Short-Time Fourier Transform (STFT) and Wavelet Transform (WT) are normally used [81]. The WT is quite effective in AE signal analysis because it does not decompose the signal into sinusoids, but rather into functions which are more like burst signals in their nature. Suzuk et al [81], in their study on AE signals emitted during tensile loading of a model unidirectional GFRP concluded that the features of waveforms are best revealed by the

WT contour maps and by an overview of wavelet coefficients, despite the long computation time required to extract these.

The STFT technique defines the energy distribution of the signal as a time-varying spectrum and using a constant sliding window size for the analysis provides a constant resolution for all frequencies. As shown in figure 2.11 there is a trade-off between time resolution and frequency resolution.

On the other hand, the WT basically works by analyzing the signal using multi-scaling where the resolution of time and frequency varies in the time-frequency plane [82, 83]. The technique uses multi–scaling to analyze the signal as shown in figure 2.11 where the resolution of time and frequency varies in the time-frequency plane with longer time intervals giving more precise low-frequency information and shorter time intervals giving high-frequency information. Unlike the FFT, the time domain included in the raw signal is conserved in the WT [24].

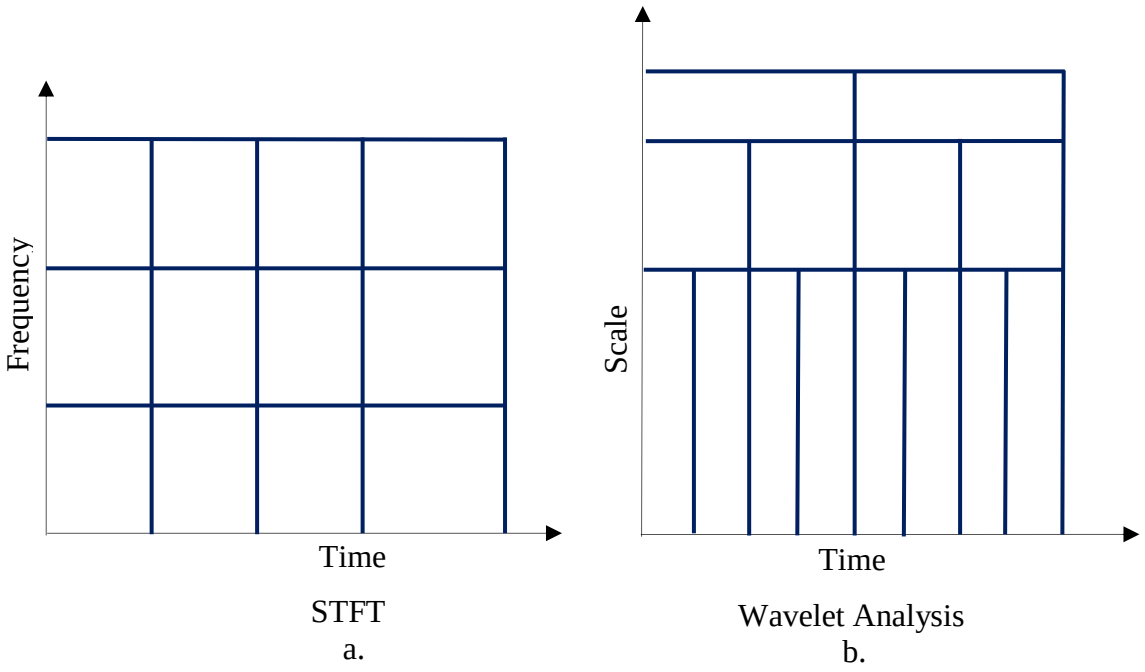

Figure 2-11: *The resolution in (a) STFT and (b) WT (longer time intervals giving more precise low frequency information and shorter time intervals giving high frequency information)*

The WT is a function $f(t)$ of time t [118]:

$$WT_f(a,b) = \frac{1}{\sqrt{a}} \int_{-\infty}^{\infty} f(t)\psi^* \left(\begin{matrix} t-b \\ a \end{matrix} \right) dt$$

where $a > 0$, the superscript * denotes a complex conjugate and t is time.

No matter how the raw data are processed, it is usually necessary to represent an AE record in terms of a small number of features. In the simplest type of AE signal analysis, individual time features are extracted from raw AE waveforms for burst signals as described below [65] and shown in figure 2.12.

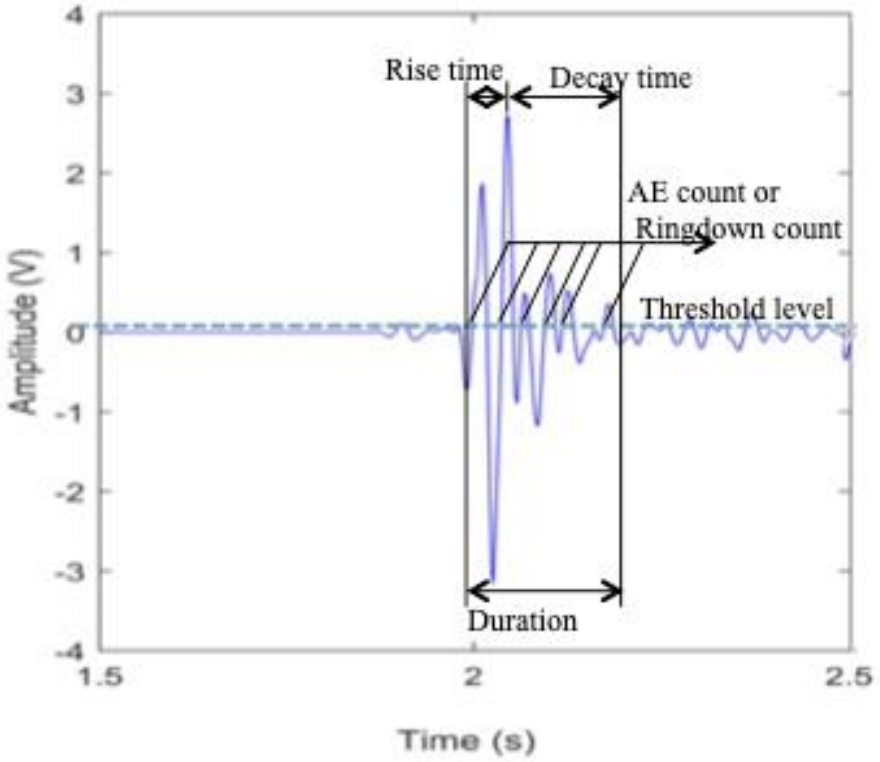

Figure 2-12: *Typical measured AE signals from sensors, as extracted from experiments carried out in this work*

I. The AE rise time is the time interval between the first threshold crossing and the maximum amplitude of the burst signal.

II. The AE decay time is the time interval between the maximum amplitude and the last time that the burst signal exceeds a pre-set threshold.

III. AE count or ring down count is the number of times the burst signal amplitude exceeds the preset threshold and count rate is AE count per unit time.

IV. Signal duration is the time interval between the first and the last threshold crossing of the burst signal.

V. AE event count is the number of times where a burst signal crosses a preset threshold and AE event rate is the time rate at which AE event counts occur.

The AE energy (or power) of a signal can be an important indicators of the intensity of the source, but, since this changes as the wave travels from source to sensor, some kind of calibration is necessary. Energy analysis is also important for continuous signals where it is difficult to locate AE sources. In well-calibrated systems where the attenuation is known in terms of the dimensions of the structure, energy or power can be used to give an indication of the severity of the fault [84]. The energy in a recorded AE signal can be obtained by integrating the square of the amplitude over a time, t, as follows:

$$E_0 = \int_0^t v^2(t)dt$$

where

E is acoustic emission energy in V^2. s;

$v(t)$ is the AE waveform level in volts (V);

and t is time in seconds (s)

AE waves are non-stationary, nonlinear transients and thus travel in more than one mode and speed when propagating in large structures so it is very important to determine the time of arrival (TOA) for the different wave components [85]. Also AE event source location is based on the TOA of transient signals measured at different sensors [3]. Normally, the TOA is estimated as the time when the raw signal amplitude first crosses a pre–set threshold as shown in figure 2.12. This threshold technique has been used to determine AE source location [86] and in order to improve the accuracy of the threshold technique, it has been suggested [87] that sufficient gain should be used to amplify the lower frequency non-dispersive components and the large amplitude, high frequency, dispersive components of the wave be filtered out of the raw signal. A number of investigators have also used arrival time of particular elements of an AE signal for

monitoring applications. For example, Mba et al [88] used the threshold technique to monitor bearing defects on a radially loaded bearing to allow them to segment the time series to focus on the fault signal, which affects only part of one revolution.

Cross-correlation is another conventional time-based technique widely used in AE signal analysis. It gives the TOA difference between two signals and is generally used in systems where the wave propagates without reflections [86].

The cross-correlation function is given by:

$$R_{y_1 y_2}(\tau) = \sum_{t=1}^{T} y_1(t) y_2\,(t+\tau)$$

where $y_1(t)$ and $y_2(t)$are the two time series signals and τ is the time difference between $y_1(t)$ and $y_2(t)$.

The most likely time delay between two complex time series is usually taken as the value of τ corresponding to the highest peak in the cross-correlation function. Daniel et al [89], in looking for methods in determining the onset of AE signals associated with fatigue crack growth, suggested that a time-varying correlation method, and a continuous wavelet transform (CWT)-based binary map were more effective when combined into and a CWT-based correlation method.

As pointed out earlier, the wavelet transform uses multi-scaling, where the resolution of time and frequency vary in the time- frequency plane. Hamstad et al [90, 91], working on source location of a real source (buried dipole) in a 4.7 mm thick aluminum plate have used a wavelet transform (WT) for their analysis and their results indicated good straight-line correlations of propagation distance versus the WT-based arrival times of the fundamental modes at fixed frequencies. Also Ni and Iwamoto [92], working on failure of model composites, used the WT technique in their investigation of the relationship between AE signal attenuation and frequency during fracturing of single fiber composites. They showed that the WT is a powerful tool not only for identifying the micro failure modes but also for elucidating the microfracture mechanisms in composite materials.

2.3.1 *Source Location*

Source identification and source location are key areas affecting the reliability of AET for monitoring [93]. Being able to determine the location of an AE event can contribute to source identification because many source mechanisms are only linked with specific features or conditions and, if the location of a source is known, the number of possible source mechanisms can be reduced, especially for pipes and other long linear structures [94]. The source location is usually determined from the wave times of arrival at an array of sensors in known positions, and, in some cases, it is important that the dispersive nature of the AE and attenuation are taken into consideration [95].

Linear source location is the simplest approach, considering only one-dimensional propagation at a single speed so that, if the wave propagation direction and velocity are known, then two sensors are sufficient [96]. This technique can be applied to long cylindrical test objects, for example pipes whose diameter is significantly less than the spacing between each sensor. The 1D source location technique is illustrated in Figure 2.13.

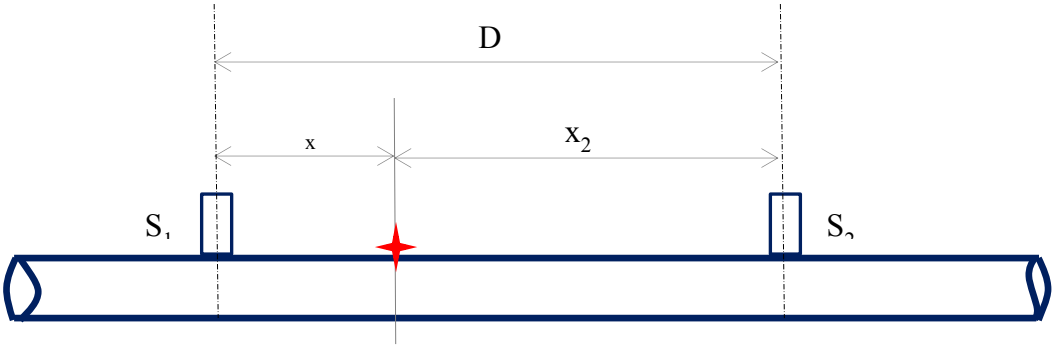

Figure 2-13: 1D source location [11]

From figure 2.13, the stress wave travelling at a velocity,c, generated at the source (✦) arrives at times t_1 and t_2 at sensors S_1 and S_2, respectively. If the two sensors (S_1 and S_2) are placed at a distance (D) apart, then the source location x measured from the first hit sensor is given by:

$$x = \frac{1}{2}\,(D - \Delta t c)$$

where D is the distance between the two sensors and Δt is the difference between arrival times.

As commented above, linear source location is applicable to pipes where the diameter of the pipe is small compared to the distance between the two sensors. However, an AE source may contain different wave modes traveling at different velocities and since these waves are produced at the same location, they will have different TOAs at the sensor [3].

Two-dimensional source location can be applied most simply to a plane or curved surface if it is assumed that the stress waves travel in all directions and at a constant velocity, i.e. circular symmetry. If the AE wave is generated from a source P_1, at co-ordinates (x_s,y_s) as in Figure 2.14 and the wave arrival times t_1 and t_2 are recorded at positions S_1 and S_2, respectively, then the source location is given by the equation of a hyperbola [97].

$$r_1 - R = (t_2 - t_1).c = \Delta t.c$$

and

$$R = \frac{1}{2}\left[\frac{D^2 - \Delta t^2.c^2}{\Delta t.c + D\cos\Theta}\right]$$

where

R and r_1 are the distances between the two sensors S_1 and S_2 respectively.

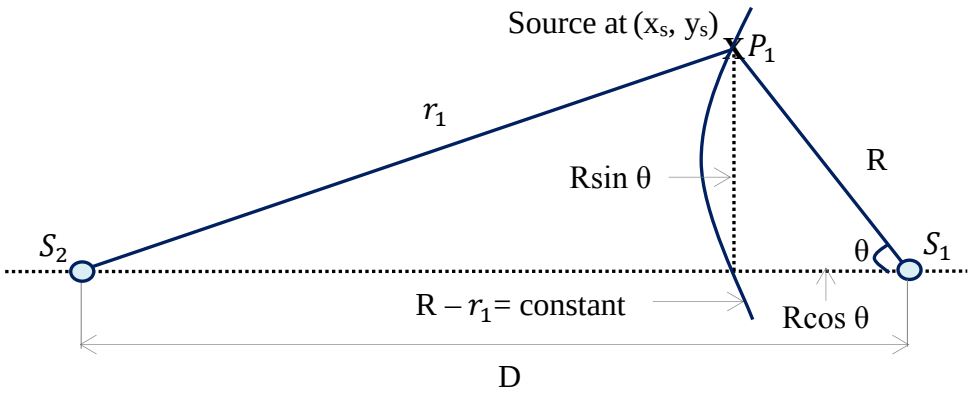

***Figure 2-14** : Schematic diagram of source location in 2 dimensions*

Barat et al [98] have derived a method for AE source location on a cylindrical surface, using three sensors (S_0, S_1 and S_2) located at points with cylindrical polar coordinates $(R, 0, 0)$, (R, Θ_1, Z_1) and (R, Θ_2, Z_2). They showed that the shortest source to sensor distance on the cylindrical surface is given by:

$$\delta_1 = \sqrt{R^2(\Theta_1 - \Theta)^2 + (z_1 - z)^2} - \sqrt{R^2\Theta^2 + z^2} \quad 2.1$$

$$\delta_2 = \sqrt{R^2(\Theta_2 - \Theta)^2 + (z_2 - z)^2} - \sqrt{R^2\Theta^2 + z^2} \quad 2.2$$

If the TOA differences (Δt_1 and Δt_2) between the two sensors S_1 and S_2, respectively, and the reference sensor S_0 are determined experimentally and, assuming a constant wave speed (c), the distances between S_1, S_0 and S_2 will be given by

$$\delta_1 = \Delta t_1 c \quad 2.3$$

$$\delta_2 = \Delta t_2 c \quad 2.4$$

and solving Equations 2.1 to 2.4 allows the values of Θ and z to be determined.

If the waves are known to be dispersive, as for Lamb waves, only one sensor is required due to the fact that the disturbance caused by the source is propagating at different wave speeds. Whereas Lamb waves have a wave velocity determined by the wavelength and plate thickness [99]. Most AE waves are non dispersive at higher frequencies and this makes source location easier [100]. Jeong et al [101] have achieved source location using the wavelet transform of the dispersive AE modes, provided it is known which modes are involved. Holford and Carter [60], showed that, in instances where both extensional and flexural waves are propagating at the same time, source location can be achieved by using high pass and low pass filters with appropriate cut-off frequency to identify two components with wave speeds C_{HF} and $C_{LF.}$ The difference in arrival times can then be used to determine distance, d from the source to the sensor:

$$d = \Delta t \left[\frac{c_{HF}.c_{LF}}{c_{HF} - c_{LF}}\right]$$

It should, however, be noted that the above technique is not effective for small structures or short distances because flexural and extensional waves are not well separated from each other [5]. Shehadah et al [3] used a similar technique to locate AE sources on a long pipe generated by a standard Hsu–Nielsen source, they used a filter to identify two wave components and a sliding window energy technique to provide improved location over existing methods. This work is referred to in some detail later in this thesis.

2.4 Acoustic Emission Modelling

The quantitative use of AE for NDT and monitoring is relatively new and the earliest studies were on the analysis of propagation models to determine analytical solutions for the spatial/temporal wave field [102, 103]. However, for all but the simplest structures and sources, analytical solutions quickly become unwieldy and many investigators have turned to computer simulation to solve the relevant wave propagation problems associated with AE NDT. The application of computer simulation is now established for many NDT methods, including, for instance, to model air-coupled ultrasonic NDT [104, 105] and to study the ultrasonic wave propagation behaviour in an aluminium block [106]. The two sub-sections below examines respectively the state of knowledge of analytical solutions and the application of numerical methods through computer simulation to AE problems.

2.4.1 *Analytical Approaches to AE*

The basic physics of stress wave propagation in solids is outlined by Kolsky [52] and the solutions of the wave equation for the commonly-observed AE modes are described in Sections 2.2 above. However, most practical problems do not warrant a full-field description of the AE wave and the most useful analytical solutions are focused onto the response to a source at designated points on a surface, one effective technique is the ray tracing technique which considers the wave energy arriving at the point under study and so reduces the amount of computation needed [107].

A series of papers by Ceranolgu and Pao have set out the basis of a ray-tracing approach to AE analysis [66, 108]. They have used both the Cagniard's method and generalized ray theory to obtain the transient wave response to stimulation at the epicentre of an elastic plate. These solutions are discussed in more detail in comparison with measurements and simulations in chapter 5.

The method has also been developed by Wilcox et al [109] who used a ray-tracing technique to predict the received time domain waveform at a sensor due to an AE event. The technique considers the generated signal to be conditioned by a series of transfer functions, whose product $H(\omega)$ is the Fourier Transform of the received time-domain signal so that the time series of the recorded signal can be calculated by performing an inverse Fourier Transform on $H(\omega)$.

Horn [110] has used the wave propagation direction and surface displacements as model input to develop a reverse ray tracing method, in which he retraced the propagation of the signal from various small arrays until a crossing point was found for two or more rays and used this as the source location.

Some researchers have concentrated on the use of the ray tracing technique for attenuation measurements, for example, Lim et al [111], developed a geometrical acoustic ray tracing method within a 3D solid models, demonstrating it on a number of simple geometries. A variant of the method was used by Nivesrangsan et al [72] to estimate attenuation in various parts of an array mounted on a small diesel engine cylinder block.

El-Shaib [112] developed the method further by simulating AE propagation in objects of different shapes and sizes and comparing the results with parallel experiments. He compared his simulated attenuation results to attenuation from measurements. He concluded that parameters such as reflection coefficient, and the relative proportions of bulk and surface wave energy could be determined using suitably calibrated experiments. Using a simple division of wave modes and a point source, the reflection coefficients, the degree of internal friction and the proportion of energy carried in surface and bulk waves [38].

Most relevant to this work, Shehadeh et al. [63] applied the same technique to study the effects of external and internal environments on the propagation of AE signals in pipelines; there was good agreement between the simulated results and his experimental measurements.

2.4.2 *Numerical Approaches to AE*

The challenge with most computer simulations is in balancing computational time with a realistic simulation of the physical phenomenon. In some applications, it is more effective to combine two simulation techniques such as was the case for Delrue et al [113] who modelled the response images from non-contact air-coupled ultrasonic inspection sensors applied to aluminium samples. Their simulation combined a ray tracing technique with a spectral solution implemented within Comsol. Their studies showed that the simulation results were in good agreement with the experimental results, implying that combining both simulation methods can be beneficial for the interpretation of air-coupled experiments.

The governing equation for explicit FEA is

$$u^{(i+1)} = u^{(i)} + \Delta t^{(i+1)} \dot{u}^{\left(i+\frac{1}{2}\right)}$$

$$\dot{u}^{(i+\frac{1}{2})} = \dot{u}^{(i-\frac{1}{2})} + \frac{\Delta t^{(i+1)} + \Delta t^{(i)}}{2} \ddot{u}^{i}$$

where u is the displacement, u̇ is the velocity, ü is the acceleration, and t is the time from the start of the simulation, the superscripts referring to the time increment.

At the start of the increment, the accelerations are computed by using

$$\ddot{u}^{(i)} = M^{-1}.\ (F^{(i)} - I^{(i)})$$

where F is the vector of externally applied forces, I is the vector of internal element forces, M is the mass matrix, $\ddot{u}$ is the acceleration and again the superscripts refer to the time increments.

However, most progress has been made using Finite Element Analysis, a computational technique used to analyse many complex engineering problems, most commonly those involving mechanics of solids. The main purpose of mechanics FEA simulation is to predict the response of a model to some form of external loading or to some non-equilibrium initial conditions, e.g. initial displacement, velocity or acceleration. In this respect, it is suited to simulating AE generated by a source which can be described in this way.

The form of FEA used in this work is explicit FEA, mostly used to solve static and dynamic problems involving deformable bodies. Accelerations and velocities at a given point in time are regarded as being constant during a time increment and then are used in the solution for the succeeding point in time [104].

Finite element analysis of stress waves in solids has been a subject of much research in the past years, notably applied to the Hopkinson bar [114, 115] and, more recently, in the stress wave analysis of polymer bars [116].

The FEA technique has also been proposed as a numerical technique for modelling AE wave propagation [117]. Unlike ultrasonic NDT waves, AE wave propagation is quite complex, even in simple homogeneous materials e.g flat plates. This is due to the fact that AE waves are usually

generated by rather uncontrolled events, in contrast with ultrasonic NDT, where the wave generation is controlled with ultrasonic transducers [99].

Perhaps the first set of researchers to attempt a numerical solution to wave propagation relevant to AE were Ceranoglu and Pao [66, 108] in 1981. They developed a numerical technique for evaluating the transient displacement response at any point on the surface for five different types of point source at the surface of a plate using the ray tracing technique. However, they only considered a small number of rays and reflections due to the inadequate limited hardware capacity at the time. Nevertheless, these authors managed to draw a number of useful conclusions relevant to the analytical approach in chapter 5 of this thesis.

Prosser et al, in 1999 [118] used a dynamic finite element method to model the Mindlin plate theory which considers shear deformation through the plate thickness. They used equations of motion based on exact linear elasticity and made calculations using properties for both isotropic and anisotropic materials. There was a good agreement between the FE method and the theoretical approach and the inconsistencies in the waveforms at longer times were attributed to differences in reflections from the lateral plate boundaries.

Hamstad et al [119], studying the effects of varying waveguide shape on measured AE signal characteristics, numerically analysed different aluminium waveguides. They used FEA simulations to model Lamb waves generated by a pencil-lead break in thin and thick plates. Although their simulations were mainly on AE wave propagation on simple structures, a comparison of their FEA results to experimental studies on effects of source rise time, monopole vs. dipole sources, plate thickness and plate width were in good agreement. Zelenyak et al [120] used FE to model AE wave propagation in an aluminium plate with an attached waveguide, again to investigate the effect of waveguide geometry. Their results showed that the waveguide diameter had a significant effect on signal amplitude as established by experiment.

Sause [121] has used FE to simulate composite failure. He modelled both the source event and the propagation. His fracture analysis showed that the detected acoustic emission signal is not only dependent on the source mechanism, but also on medium of propagation. He also concluded that the excitation of distinct Lamb modes is influenced by microscopic conditions near the source and suggested that source influences should be considered when carrying out source identification studies.

Sause et al [122] have also modelled the sensor response to a PLB on an aluminium plate. They specifically investigated signals acquired from conical elements using a multi-scale finite element model for the simulation, and suggested that it is possible to predict the absolute sensor response for arbitrary wave propagation in plates.

Relative to the AE energy dissipation from impacts, Droubi etal [33] have attempted to measure the energy dissipated in a carbon steel target during airborne particle impact; they studied the relationship between the particle impact speed, diameter and AE energy. His studies showed that although AE energy increased with particle diameter, this was only possible for particle diameters of about 1.5mm, he cited the different energy dissipation mechanisms as the reason for this.

Ukpai et al [22] have likewise studied the different mechanisms of transfer of energy from erosive wear events using acoustic waves. They carried out an experiment with a submerged impingement jet (SIJ) rig, then analysed the acoustic energy and used this to characterise the erosive wear damage of steel samples. Their correlation of the acoustic energy and sand loading showed an increase in both RMS and AE energy with increase in the size of the impacting glass bead for the single impact experiments. Similarly, for the multiple impact experiments, the AE energy increased as the sand concentration and sand concentration was increased.

Also, Crivelli [13] in a study to investigate the suitability of AE energy for determining the severity of an impact have used AE sensors to monitor impact samples under different impact energy levels, he correlated the AE impact energy and impact damage. He carried out this studies by subjecting nine panels fixed on a pneumatic circular frame to three different impact from a drop weight and measuring the AE energy. He concluded that AE was not only suitable for measuring impact severity and their results showed a good correlation of AE energy and the area of impact but also that post-impact damage are associated to pre-failure and up-to-failure release in AE energy.

As can be seen from the foregoing work on the implementation of the FEA technique to AE wave propagation has generally stopped short of predicting the transfer function between source and sensor.

This work therefore aims to measure the sensor response to sources with prescribed temporal structures on simple cylindrical test objects and to match the measurements with simulations in

order to determine the practical transfer function between source and sensor and to give higher accuracy representations of experimental measurements.

2.5 Identification of Thesis Topic

The literature reviewed has revealed that a complete generic description of AE propagation from source to sensors in pipes has yet to be elucidated in a way that it can be applied to the identification of temporally extended sources in long linear structures, such as pipelines.

Much of the work applying FEA has been focussed on a description of propagation [122, 123], but relatively little has been done on the relationship between what goes in at the source and what is recorded at a sensor [121]. Even for the propagation work, few researchers have addressed the issue of attenuation in a way that it is of any practical significance [92, 124].

Therefore, the focus of this study is on what information can be deduced about the identity of an AE source from an array of sensors distributed along a pipe. In order to do this, it is essential that the simulations are complemented with a series of parallel experiments where as much control as possible is exerted over the source and the test object boundaries.

The initial challenge is to model an AE source as close as possible to that used in the experiment, starting with the relatively simple pencil-lead break on a very well-calibrated test object (solid cylinder), and moving on to a short length of test pipe as the object and more complex loading systems involving a dropped object onto the pipe.

Finally, for source recognition, it is expected that it will be necessary to take into account how signals are distorted as they travel from source to sensor. Here again, a coupled approach with simulations and measurements at various places along the pipe allows the signal distortion (attenuation vs frequency) to be introduced into the simulations in a way that can be measured practically on a real system.

The approach taken here, in which the FEA technique has been combined with matching experiments, has the potential to be very useful for AE monitoring of structures.

Chapter 3 - Finite Element Modelling and Simulation

This chapter presents the FEA simulation aspect of this work and explains the approach taken for the simulation model design using the Abaqus FEA package. It also provides a background to the numerical simulation of the elastic stress wave propagation as a result from a PLB or a ball bearing drop on a test object of cylindrical geometry.

The constraints on time step, element size and the stability criteria of the time-stepping integration technique are covered. The chapter further discusses the physical approach used in developing the FE model.

3.1 Overview of the Abaqus Software

There are more than 30 different FEA packages available [125], many designed to solve specific engineering problems although often the inbuilt models can be easily modified to suit most applications. The basis of any FEA programme is to divide the whole structure being analyzed into finite elements and calculate the structure's mechanical behaviour by integrating the corresponding variables. The use of FEA has improved dramatically in the last two decades due to the advances in modeling software and improved constitutive models. Systems that had been hitherto almost impossible to solve can now be easily analyzed using FEA. For example material failure under very high strain rates would normally be predicted from expensive and dangerous experiments, and empirical predictions which could sometimes be erroneous [126].

The proprietary commercial software Abaqus was specifically chosen for this work because it is a powerful finite element commercial code which contains an extensive library of elements and material models, thus making it possible to analyse complex geometric structures and non-linear material responses, and provides a wide range of flexible options to accommodate advanced applications by providing a user subroutine interface to increase its functionality. It also offers a number of procedures to solve a variety of engineering problems, e.g. static stress analysis, dynamic stress analysis and transient heat transfer analysis [127]. Abaqus offers accurate analysis techniques to determine the local element failure and can then adjust the element stiffness to precede damage analysis e.g. it has the capability to predict element failure by the most common failure criteria such as those from the theories of maximum stress and maximum strain, and thus quite suited for linear and nonlinear explicit dynamics problems such as those involving impact [128, 129].

In this work, Abaqus' explicit dynamic analysis was applied to obtain the transient stresses resulting from pressure and impact. The ultimate objective of the FE simulations carried out here is to be able to predict the time and frequency distortion of a non-instantaneous source as the AE it generates propagates along a pipeline.

3.2 Overview of the Simulation

A number of different sets of simulations were carried out in support of this work. Described below are the preliminary simulations used to establish the key parameters and approaches; which the remaining simulations follow.

ABAQUS was used to simulate steel pipes fixed at both ends and subject to pressure loading one metre from one end, (Figure 3.1). The pipe model was simulated as a three dimensional elastic deformable solid with inner and outer diameters of 0.08 and 0.1m, respectively, and lengths of 2.5m, 5m and 10m. The source was simulated as a 100N force spread over a surface area of $0.003m^2$ with three different time profiles, the key variable being the rate of unloading, which were varied over three orders of magnitude, unloading from 100N in 1×10^{-9}s, 1×10^{-8}s, and 1×10^{-7}s, respectively. Each length of pipe had three sensor positions, chosen to cover the pipe length on the far side of the sensor from the source. Table 3.1 summarises the sensor positions on each pipe simulation.

Pipe length (m)	**Sensor positions (m from source)**		
2.5	0.5	1	1.5
5	1.5	2.5	4
10	4	5	9

Table 3-1: *Summary of simulated pipe lengths and sensor positions for the first PLB simulations*

The force and unloading rates were chosen to be in the region of the estimated time it would take a fracture, propagating at the speed of sound, to cross the diameter of a 0.5mm pencil lead in order that the simulated responses could be compared with observed responses of pencil lead breaks. This time (about 0.3μs) is reasonably close to that simulated by Sause [122] although the forces (chosen to give a reasonably strong response at all sensor positions) are around 50-100 times those measured and calculated by him for pencil lead unloads.

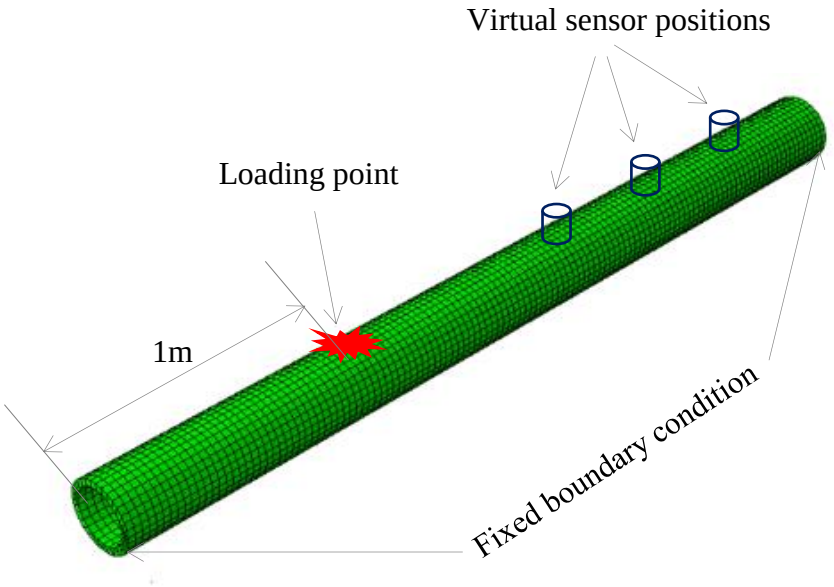

Figure 3-1: *Schematic diagram of the pipe simulation model*

Generally, the numerical method for the solution of time-varying differential equations may be either implicit or explicit. The main objective in each case is to determine the state of a model at time $t + \Delta t$ from time t. If the state at time t is represented by $Y\ (t)$, then an explicit method determines $Y\ (t\ +\ \Delta t)$ from the current state

$$Y(t + \Delta t) = F\big(Y(t)\big)$$

The explicit solution method was initially designed for dynamic problems, although it is sometimes applied when solving quasi-static problems with very small inertial effects [130].

Abaqus uses an explicit central difference integration method to solve for the displacement, $u(x, y, z, t)$ from increment i (time t) to increment $i\ +\ 1\ (time\ t\ +\ \Delta t)$:

$$\dot{u}^{\left(i+\frac{1}{2}\right)} = \dot{u}^{\left(i+\frac{1}{2}\right)} + \frac{\Delta t^{(i+1)} + \Delta t^{(i)}}{2}\ddot{u}^{i}$$

$$u^{(i+1)} = u^{(i)} + \Delta t^{(i+1)}\dot{u}^{\left(i+\frac{1}{2}\right)}$$

where $\dot{u}$ represents the velocity, $\ddot{u}$ is acceleration, the superscript (i) is an increment number and $(i \pm \frac{1}{2})$ is the value of a variable midway between the increments.

For a dynamic problem, the input acceleration at the source is given by:

$$\ddot{u}^{(i)} = M^{-1} . \left(P^{(i)} - I^{(i)}\right) \qquad 3.1$$

where M is the mass matrix, P is the vector of applied loads and I the vector of internal forces. Equation 3.1 can be used to obtain the accelerations at the start of an integration. The Courant–Friedrichs–Lewy (CFL) condition (time step must be sufficiently small that information has time to propagate through the spatial discretization) [131] was used to determine the maximum allowable size of the time increment Δt :

$$\Delta \mathrm{t} \leq \Delta \mathrm{t}_{cr} = min \left(\frac{L_e}{c_d}\right)$$

where L_e is the element length and c_d is the dilatational wave speed and is given by

$$c_d = \sqrt{\frac{(\lambda + 2\mu)}{\rho}}$$

where λ and μ are the first and second Lame constants and ρ represents the density of the material.

In dynamic explicit simulations, where the variables representing the system response are functions of time, the model is a representation of a real system and an analytical (or mathematical) model is a set of equations that approximates the behaviour of the system. Unlike simulation models, experimental models are developed by exciting a system in a controlled manner and measuring the resulting response. All the simulation carried out in this work is explicit and dynamic in 3D. The next section describes the FE model parameters used.

3.3 **Implementation**

In order to implement the model, a number of key issues need to be resolved beyond the time step increment. The most important of these are element type, mesh size, boundary conditions and introduction of external loads, discussed in turn below.

3.3.1 *Choice of Element Type and Time Step*

Abaqus offers a wide range of elements for different geometries and analysis types. In this work, the simulation of the AE wave propagation on the pipe was modeled using the linear hexahedral type C3D8R elements, with reduced integration points.

The C3D8R element is an 8-node trilinear brick element which offers a solution of equivalent precision at less cost [132]. A reduced integration point indicates that the integration used to define the internal forces and stiffness is an order less than the full scheme, the reason for this approximation being that fully integrated first order elements suffer from volumetric locking when used to characterise near- incompressible material behaviour and non- physical stresses can develop leading to the instability in the simulation and inaccurate results [133].

Another advantage of the reduced integration point is that it lessens the amount of constraint imposed on the solution by the element choice. The C3D8R elements were specifically chosen for the simulation of acoustic emission because the integration point are located in the middle of the element and small elements are generally required to capture a stress concentration at the boundary of a structure.

3.3.2 *Mesh Size and Time Step*

The finite element size (mesh density) is a very important aspect of the FE simulations as the accuracy and simulation-computing time are directly related to mesh size and time step. Also, the mesh size affects the stability of the simulation. Several authors have studied the effect of mesh size density in FE analysis [134-136]. Generally, models with fine mesh yield highly accurate results but with a longer computing time, and coarse meshes mostly lead to less accurate results with more economical computing time.

Using a very fine mesh over the whole pipe model would give accurate results, but would severely limit the length of pipe that can be simulated. Therefore, a coarse mesh was used for the majority of the model and a very refined mesh was used in the local zone surrounding the impact area. The advantage of this technique is that there is an exact representation of the interaction of the wave with the pressure loading while considerably decreasing the number of degrees of freedom in the FEA simulation. For accurate measurement of the AE signal, it is also important to use a density that is adequate to resolve the shortest wavelength and this is related to the velocity and frequency by:

$$\lambda = \frac{c}{f}$$

where λ is the wavelength, c and f represent the wave velocity and frequency respectively

Large element sizes are sometimes used in simplified models to provide fast and rough design estimates; however this is not the case in most FEA models. The general approach used in this work was to refine the mesh size until acceptable behaviour (results stay consistent between meshes) was obtained. Therefore, a number of different mesh size densities were investigated and a mesh size of 0.01mm was chosen as, beyond this mesh size, there were no appreciable differences recorded in the resultant stress waves generated. To ascertain this optimum mesh density, a series of FE models were generated for a 2m pipe with mesh size varying from 0.005mm to 0.05 mm using C38DR elements. Figures 3.2a-c shows the stress distribution of a very fine mesh model, the actual mesh model used and a coarse mesh model, respectively. A visual inspection of the stress distribution profiles shows that results stay consistent between the 0.01 mm and 0.005 mm mesh densities. However, it should be noted that, to maintain a good numerical accuracy under large deformations, Abaqus uses an automatic adaptive re-meshing routine where a new mesh is generated each time element distortions or local error estimates exceed a specified threshold.

In wave propagation modelling, the actual time step used for a model is expressed in terms of its ratio to the critical time step (CFL number) and is given by:

$$CFL = \frac{\Delta t}{\Delta t_{cr}}$$

If ΔL is the smallest element size and C_L is the velocity of the wave

Then $\Delta t = CFL\, \Delta t_{cr} = CFL = \frac{\Delta L}{C_L}$

A large increment number is usually required to solve wave propagation models, because the space is normally discretized such that the wavelength in the model is at least 7 nodes per shortest wavelength. However, global mass and stiffness matrices are not created nor inverted and so increments are computationally inexpensive [137]. To capture the dynamics of the model, a time step of 1×10^{-9}s was used for all the FE simulations in this work. Literature [136] simulations for different structures with mesh size variations from 10 mm to 100 mm using quad shell

elements with an automatic mesh technique have concluded that the finest mesh generates the most accurate results and percentage approximate errors, but this is considerably lower than the mesh sizes used here.

Mesh refinement is a key issue in mesh sensitivity studies, the two key types of mesh refinement in FEA are the global adaptive mesh refinement and local adaptive mesh refinement. In this work, the local adaptive mesh refinement (LAMR) was used, the LAMR evaluates the error over the area of interest, while re meshing the entire model and this reduces the error in other regions.

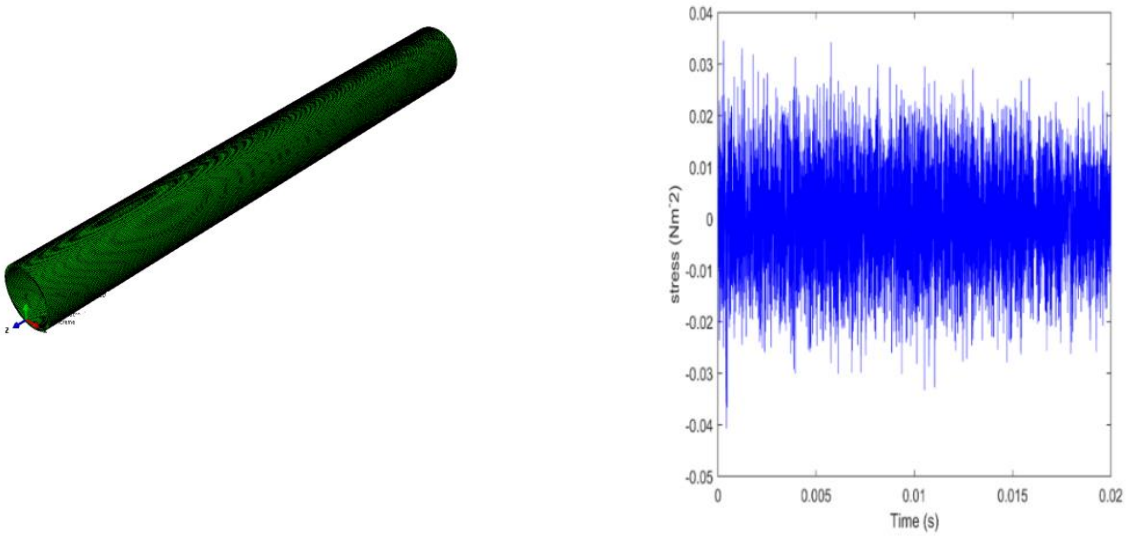

a.

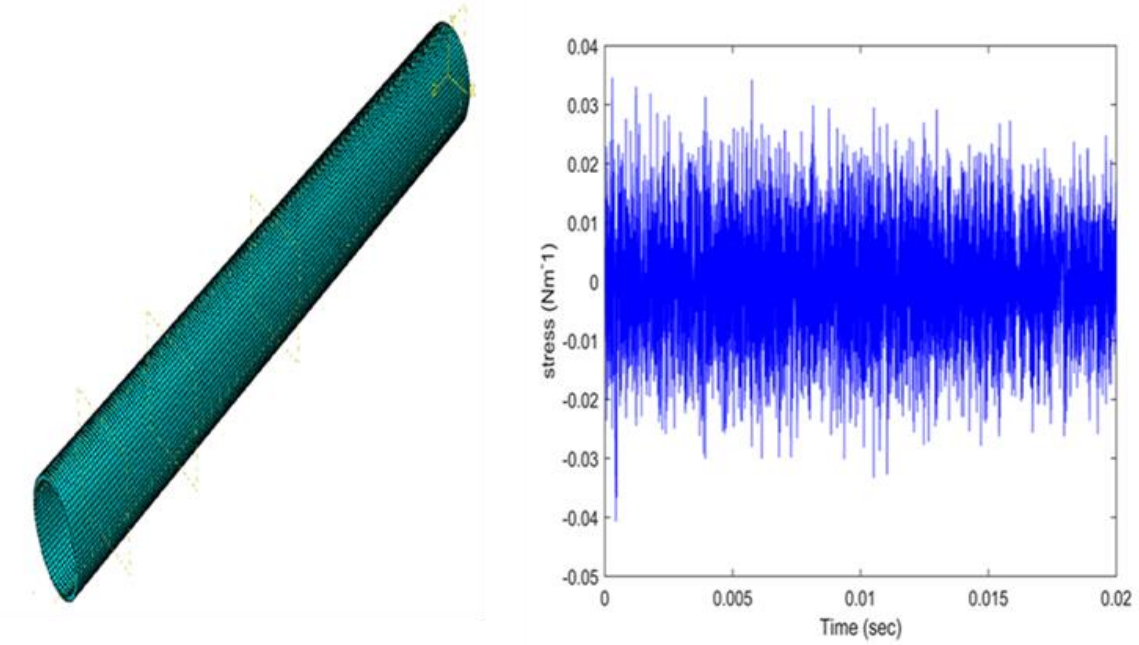

b.

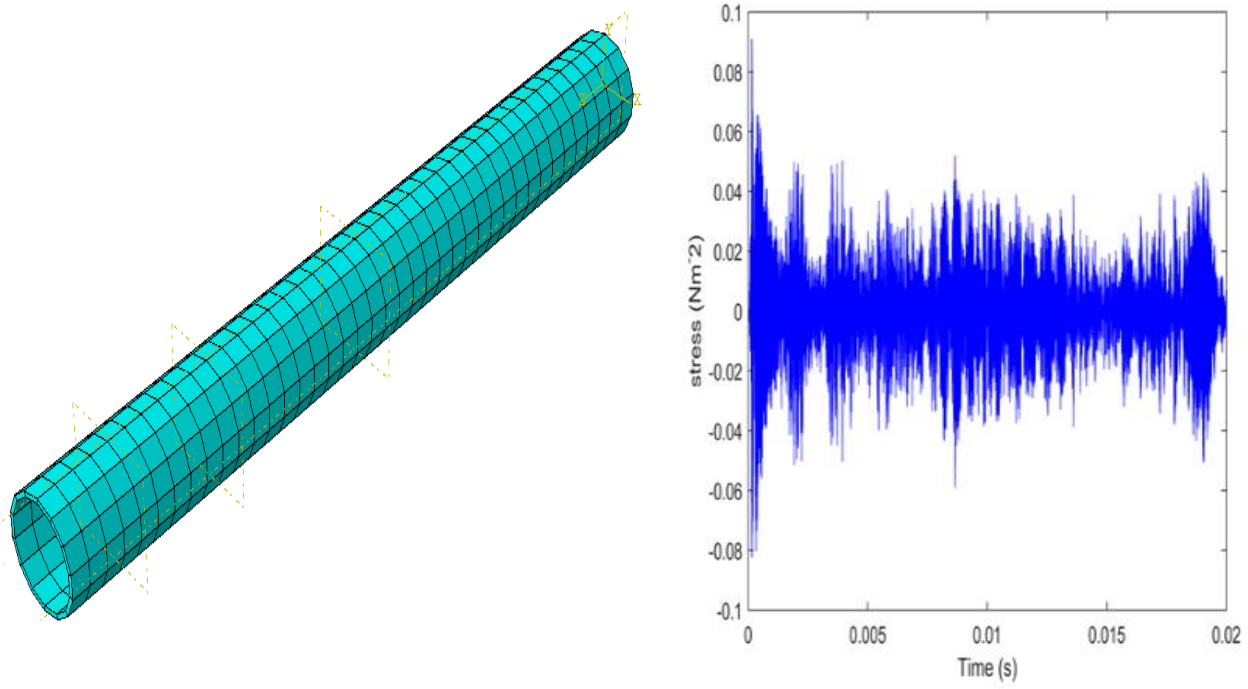

c.

Figure 3-2: *Propagating AE wave simulations for various mesh sizes (a) finest mesh model, (b) mesh model adopted (c) coarse mesh model*

3.3.3 *Loading*

Most of the published work on simulating AE propagation considers the source to be a step-unload and much of the calibration work done on structures uses sources, such as a pencil-lead break, which approximate to a step-unload. The loading conditions are a key element of the current work since they represent the source function and the boundary conditions.

As stated earlier, the unloading rates were chosen to be in the region of the expected time it would take a fracture, propagating at the speed of sound, to cross the diameter of a 0.5mm pencil lead in order that the simulated responses could be compared with observed responses of pencil lead breaks. For all the simulations carried out in this work, the boundary conditions for the displacement components and external loads were kept same as the previous simulations. The results of the different unload rates are discussed in detail in section 6.1.

All the PLB simulations used a 100N force spread over a surface area of $0.003m^2$ with three different time profiles as shown in Figure 3.3, each unloading rate being preceded by a dwell and ramp time of 10^{-8}s. The rise times were chosen to be in the range reported by in the literature while the surface area ($0.003m^2$) and force (100N) are the estimated approximate area and force obtained from the PLB experiment.

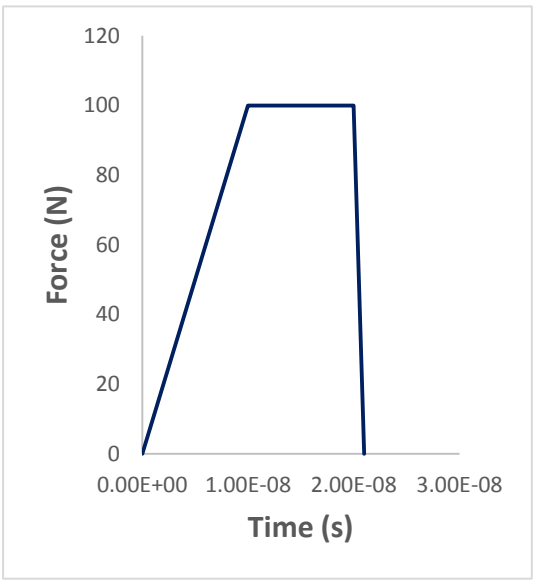

a.

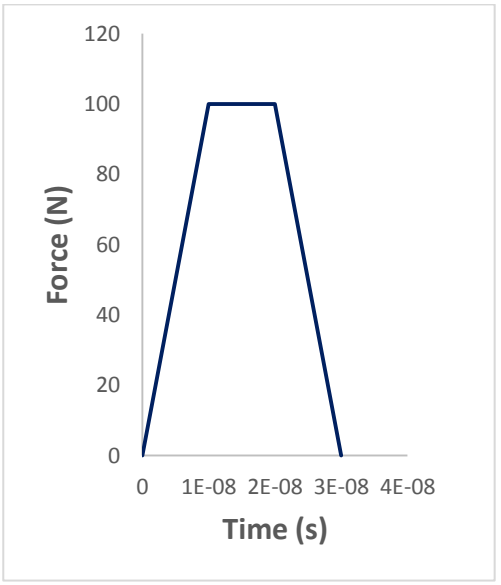

b.

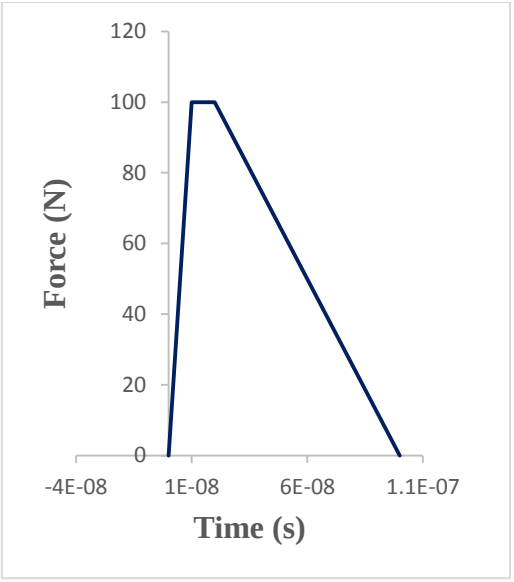

c.

Figure 3-3: *Typical force vs time profiles for the PLB simulations*

Unlike the PLB simulation, the ball bearing involved some contact interaction between the pipe and the ball bearing. Although FE models involving contact interactions are quite complex, some authors have attempted to use it for stress wave propagation [128]. The general contact algorithm offered in Abaqus [138, 139] was used here as it is mostly used for models with multiple components is suitable for both deformable and rigid bodies and is relatively easy to use. Also, it allows for contact definition between many or all regions of a model with a single interaction and has been used in this particular simulation due to its high performance and accuracy. A drawback of the general contact interaction is an increase in analysis time because it defines a large contact area. A surface pair is commonly used to describe multi-focus or coupling imperatives and can outline demand areas used as a component recommended for gathering loads as in the PLB simulation on the pipe. Therefore, to overcome the drawback of the general contact interaction in this work, surface pairs were defined to reduce the computational time.

3.3.4 *Recording of Results*

In order to minimise the amount of data stored and the consequent post-processing, only the surface stress at the positions of the virtual sensors was recorded. This record commenced (at time zero) when the source was applied to the pipe and ended at the end of the simulation (0.02s after application of the source). The simulated results were recorded as time series, each at a given (virtual) sensor position.

Figure 3.4 shows a typical time series of such a record at three levels of detail. The top trace shows the entire record and it can be seen that there is little or no attenuation of the wave which is hardly surprising, given that the elastic model does not have any damping and the wave can reverberate in the relatively short length of pipe. A wave travelling at a typical speed of 2000ms^{-1} can traverse the pipe about 16 times in the space of 0.02s and the model does not have any means of extracting energy from impinging waves at the ends. The middle trace shows a magnified view of the first 7 $\times 10^{-4}$ s and clearly shows the dead time it takes the wave to travel from the source to the virtual sensor, thus allowing an estimate of the wave speed, or at least that of the fastest component. Finally, the bottom trace shows the period of around 4 $\times 10^{-4}$ s around wave arrival, and it can be seen that the arrival waveform is quite complex, clearly involving more than one frequency, indicating multiple modes or, at least, a dispersive mode.

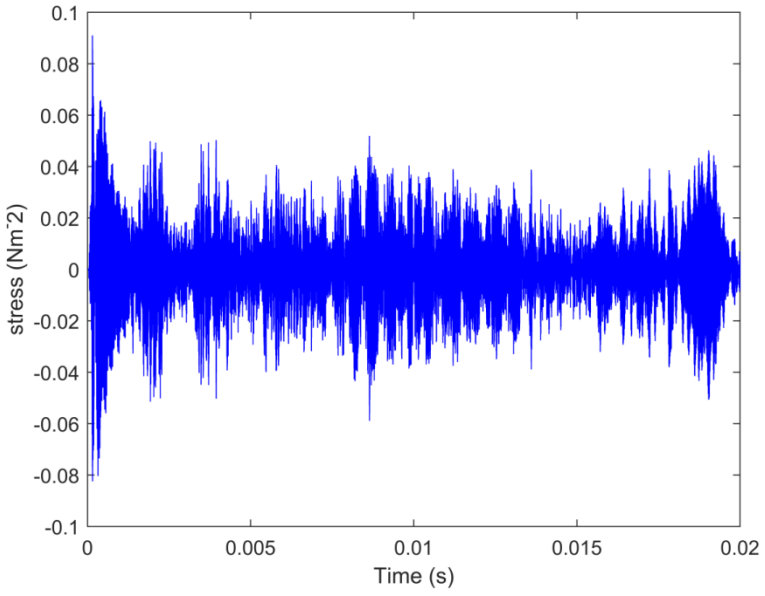

a.

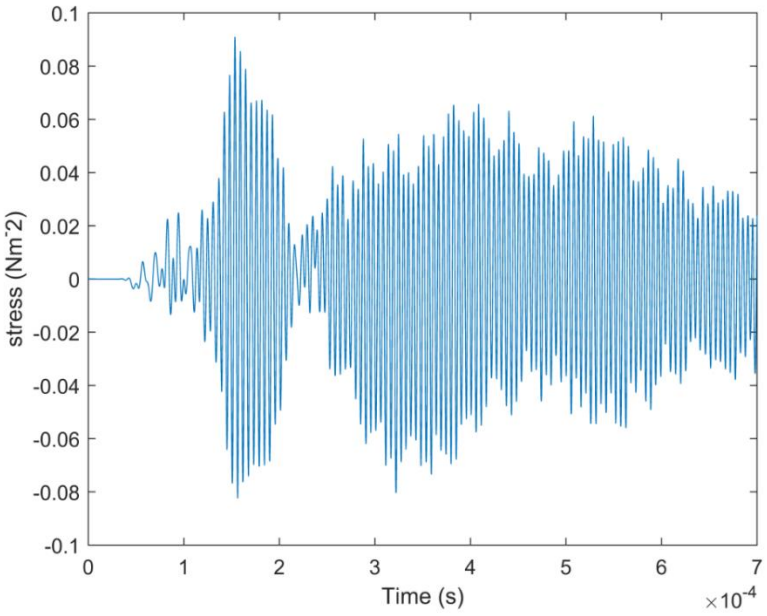

b.

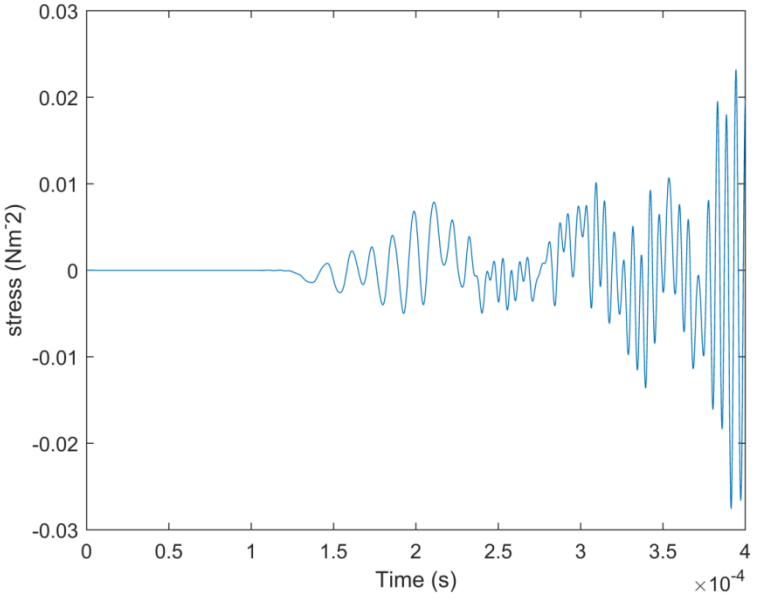

c.

Figure 3-4: *Typical time series of stress at virtual sensor 1m from source unloaded in 10^{-9} s on the 2m pipe (a) At 0.02sec (b) At 7 x 10^{-4} s (c) At 10^{-4} s after arrival*

Chapter 4 - Apparatus and Description of the Experiments

This chapter describes the equipment, experimental apparatus and a procedure used in this work, and is divided into two parts. The first part describes the general set-up of an AE experiment and describes the features and specification of the apparatus used in common throughout this work. The second section covers the experimental procedures, including the reference and calibration experiments carried out on a well-studied solid cylindrical block and the two sets of experiments carried out on a 2m length of steel pipe.

4.1 Experimental Apparatus

Generally speaking, any AE experiment involves a stress wave being generated (AE source) in a test object in which it is transmitted to one or more sensor for detection of the transmitted AE waves, some amplification, filtering and analysis using appropriate software. This is represented schematically in Figure 4.1 and one embodiment is shown in Figure 4.2. Each element is described in turn below.

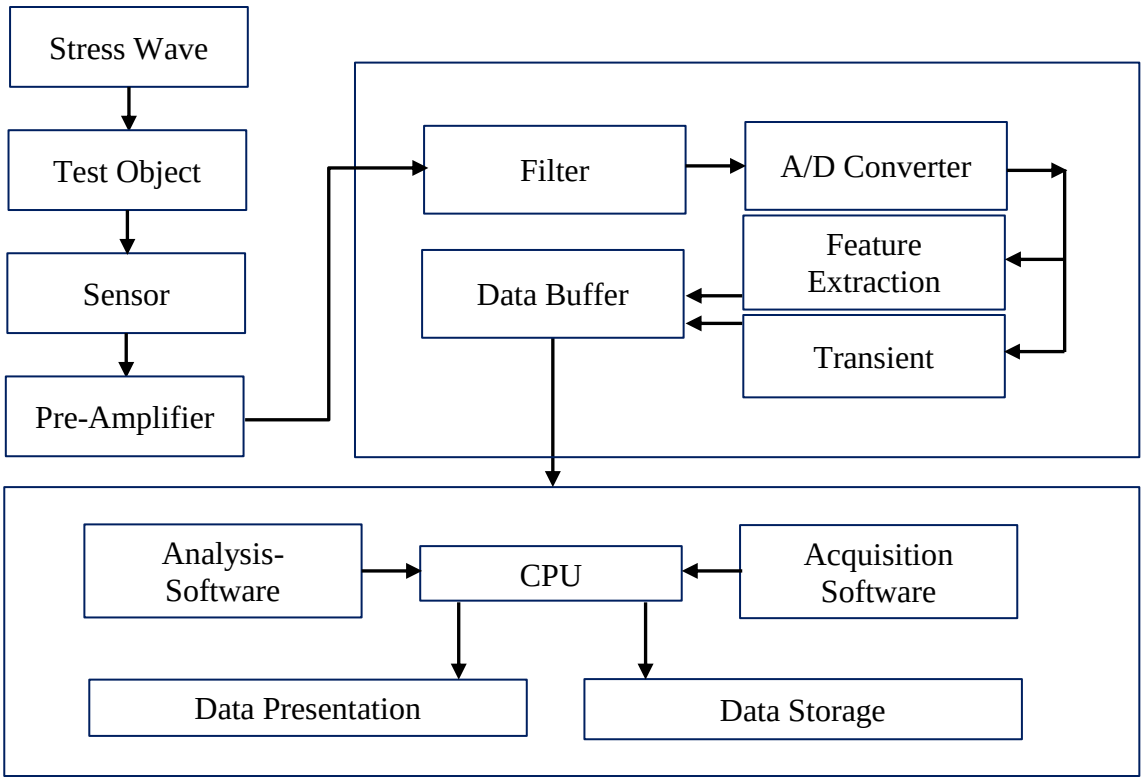

Figure 4-1: *Schematic diagram of an AE measurement chain*

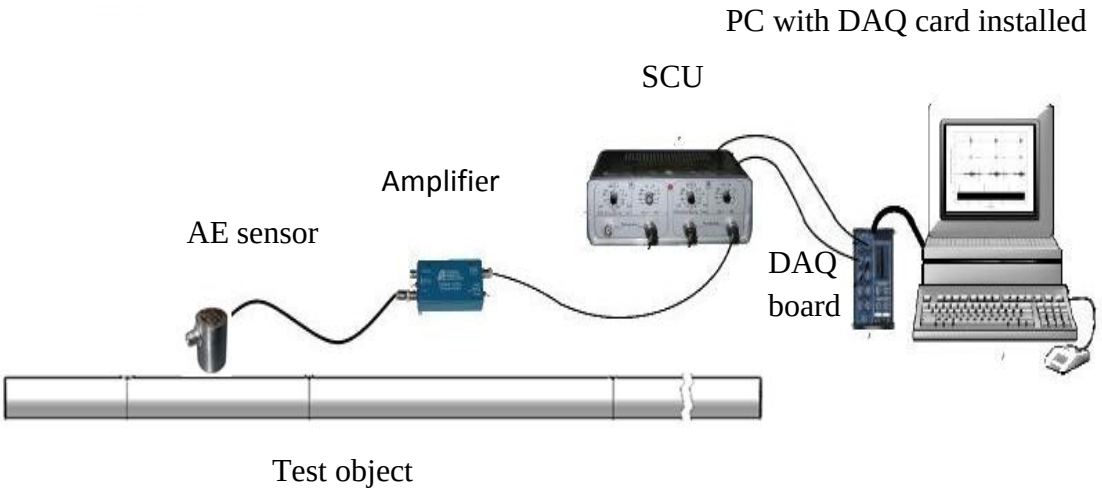

Figure 4-2: *Schematic representation of a typical AE experimental system setup*

4.1.1 ***Sources***

Two different types of source were used in this work, a standard Hsu-Neilson source, consisting of a pencil lead break, widely acknowledged as being close to a step unload and several sizes of dropped objects, which were expected to give sources which were extended in time in a systematic way.

The PLB is a frequently used AE source, due to its simplicity of application and remarkable reproducibility. It is useful for the verification of sensor coupling and also for determining the acoustic attenuation of a structure. A commercial mechanical pencil (figure 4.3) with an in-house machined guide ring was used to generate a simulated AE source (Hsu-Nielsen source) where the guide ring helps to break the pencil consistently, complying with ASTM standard (E976–99) which requires the pencil lead to be of a specific type (HB or 2H pencil lead, 0.3 or 0.5 mm diameter) with a projecting length of 2-3 mm [140].

The dropped objects were steel ball bearings of 4, 8 and 16mm diameter, giving a range of mass of about 0.3 to 17g. The balls were dropped from heights of 100, 200 and 300mm unto the test objects, giving a range of incident kinetic energy varying from 0.03×10^{-2} J to 5×10^{-2}J.

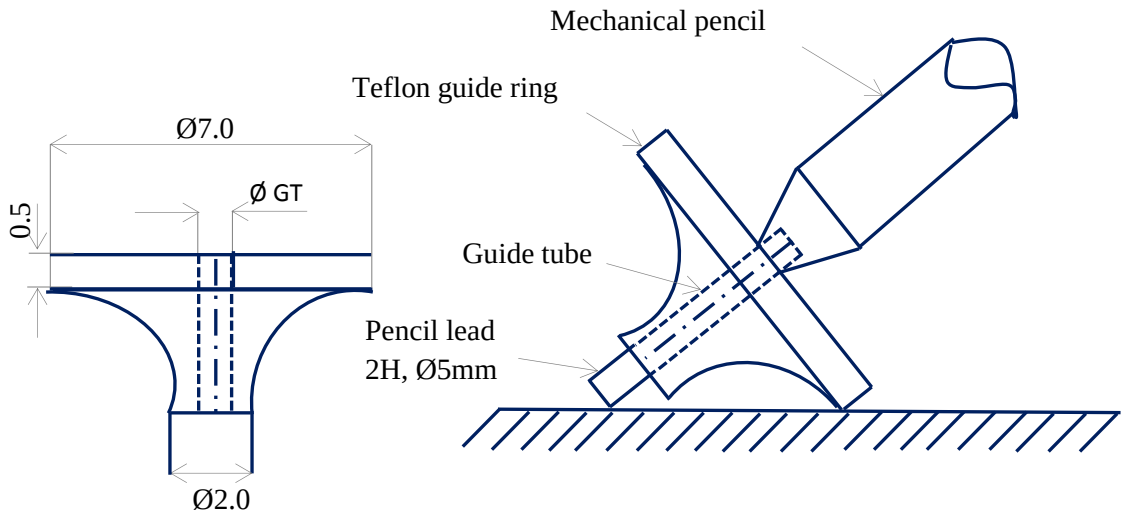

a. Standard guide ring (Nielson hoe)

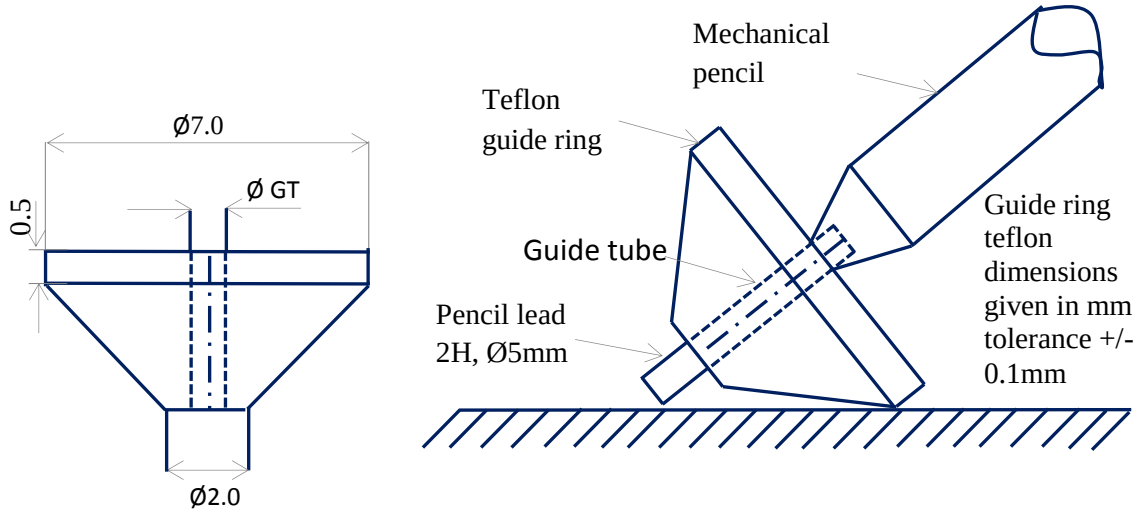

b. Modified guide ring

Figure 4-3: *Dimensions of guide rings and pencil for Hsu-Nielsen source [101]*

4.1.2 *Test Objects*

Two different test objects were used; a solid cylinder and a 2m length of pipe. The solid cylinder was 307mm diameter and 166mm long and was used standing on one of the circular faces, with the opposite circular face being used as the test surface. This configuration was chosen because

it had already been well studied and was known to propagate Rayleigh waves when source and sensor were placed on the same surface.

The pipe was of length 2m, external diameter 0.08 m and internal diameter 0.1m. The external cyindrical surface was used as the test surface with both source and sensor being mounted on it. The configuration was chosen to be close to the actual technological application.

For the solid cylinder experiments, the pencil leads were broken in the same position throughout and was carried out in order to study the behaviour of the AE wave propagation from a simulated source.

Also, for all the PLB experiments on the pipe experiments, the pencil was broken at the same position on the test surface, using the same orientation and the same angle of the pencil. These tests were carried out to check the sensitivity of the sensors and repeatiblity of the individual pencil lead breaks and also to study the propagation of AE waves and source location.

The ball bearing experiments (simulated sources) were used to study impact tests to simulated real sources and therefore assess the potential of AE monitoring to be used in actual pipe networks. As far as possible, the balls were dropped so as to land at the same places on the pipe and cylinder as the corresponding PLBs.

4.1.3 *AE Sensors and Preamplifiers*

An AE sensor converts surface waves propagating along the material under examination into a time-varying voltage signal. The sensors used throughout the experimental aspect of this work were commercial broadband AE sensors of type Physical Acoustics Micro-80D (Figure 4.4). These AE sensors are omnidirectional, sensitive over the frequency range from 175 to 1000 kHz and are based on lead zirconate titanate (PZT) active elements. These sensors were used due to their ubiquity in industrial condition monitoring and relatively broad frequency response with good sensitivity. They are 10 mm in diameter and 12 mm high and have a fairly flat frequency response of over 0.1 to 1MHz, but with two bands of relatively high sensitivity at about 150kHz and 350kHz. The sensors were held onto the test object using magnetic clamps.

The quality and consistency of sensor coupling is important as it provides the means by which the stress waves propagating on the test object are transmitted to the sensor. A well-tried couplant

consisting of a silicone based grease was therefore used on the surface of the test object to fill any gaps due to surface roughness and also eradicate any air gaps which might affect the transmission of AE. To check the quality and consistency of coupling, 20 sets of experiments were carried out by mounting and unmounting each sensor after a pencil lead break and the results are reported in Chapter 5.

Variation of sensor sensitivity, differences in PLBs, sensor removal and installation can all affect the AE recorded. For example, studies carried out by El-Shaib [112] have shown a variation in recorded AE of about 40% between different sensor placements when mounting and remounting the sensors. Also, the energy recorded for a given installation can vary due to the different PLBs by about 20%. For example, the level recorded by S_2 is a little higher than for S_1, for the example shown in Figure 5.12, but this could be due either to differences in sensor sensitivity or variations in coupling, or both.

Figure 4-4: *Micro-80D broadband AE sensor*

The preamplifier was used to amplify the AE signal from the Micro-80D sensor to a level that can be easily transmitted and converted by the Analogue to Digital Converter (ADC). For this, purpose-built commercial preamplifiers, type PAC 1220A, were used (Figure 4.5). These amplifiers have internal band pass filters from 0.1-1.2 MHz and a switchable gain between 40 and 60 dB. The gain was chosen in order to obtain an input voltage of the order of a few volts and this was not normally varied from 40dB.

Figure 4-5: *Preamplifier type PAC 1220A.This preamplifier was powered by a + 28V power supply and used one BNC connector for both power and signal from the sensor.*

At the start of each experiment, the coupling quality for each position was checked using a PLB against expected signal amplitude of around 4-5 volts using the fixed amplifier settings.

4.1.4 *Signal Conditioning Unit and Data Acquisition (DAQ) System*

The signal conditioning unit (SCU) used was an in-house built programmable 4-channel unit capable both of powering of the AE sensors (+ 28V) and pre-processing signals from the sensors prior to ADC acquisition. Although the SCU has the capacity to perform analogue RMS processing with associated amplification or de-amplification, this facility was not used in the current work. This is represented schematically in Figure 4.6 and one embodiment is shown in Figure 4.7.

As the experiments here were aimed at acquiring raw AE signals within the 0.1 to 1MHz frequency range, a high-performance data acquisition system was required. The DAQ system used is a multifunction analogue, digital and timing device without on-board switches or jumpers so that it can be configured and calibrated by the software. It is based on an in-house built desktop PC with a 12 bit, National Instruments PCI-6115 board. This board has the capability of acquiring simultaneously the raw AE signal at 10M samples/s for four channels and uses a full-length PCI slot. The software-programmable ADC gain can be set to 0.2, 0.5, 1, 2, 5, 10 or 50 and can cover an input range from ± 200 mV to ± 42 V. The data can be sampled from 20k samples/s up to 10M samples/s at each channel with a total on board memory of 32Mb. The board supports only differential input configurations and has an over-voltage protection at ± 42V. In all of the work reported here the systems was set up as for source location applications, recording raw AE signals (sampled at 5M samples/s) over two channels.

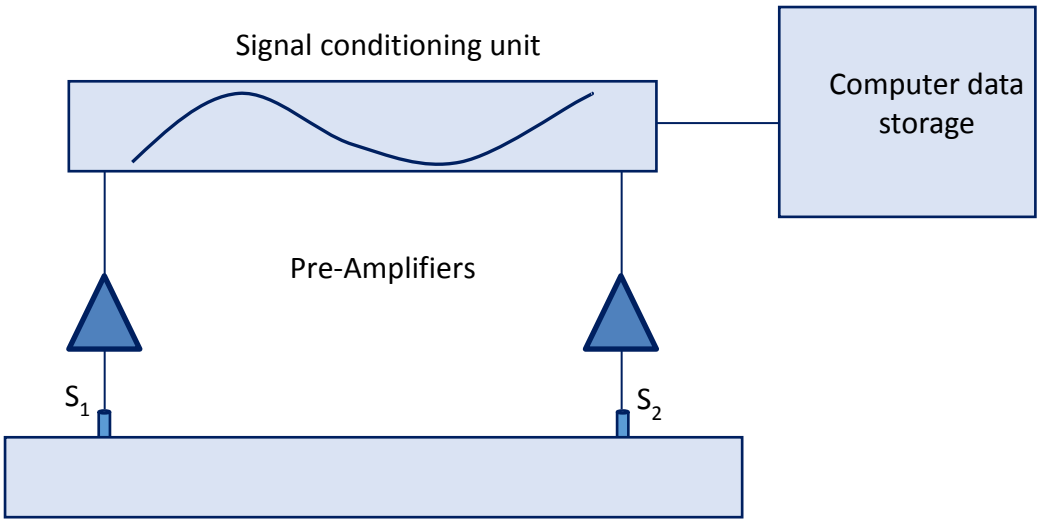

Figure 4-6: Schematic representation of the data acquisition system

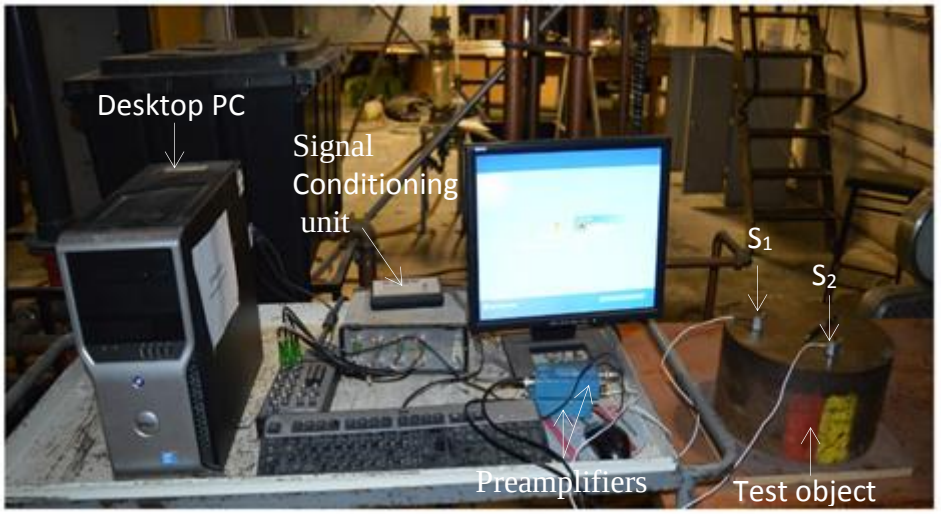

Figure 4-7: *Data acquisition system with accessories*

The DAQ system was controlled using a LabVIEW programme developed by Nivesrangsan [5]. The programme user interface is shown in Figure 4.8 where the settings on the PCI-6115 board can be seen, including input range, pre-trigger data, number of records, sampling frequency, number of channels, trigger channel and trigger level. Because the buffer is a first-in-first-out system, it is possible to capture a short pre-trigger record, which can then be used to establish signal to noise ratio, threshold and signal duration in a way that allows comparison of recorded waveforms with simulated ones, which is an essential part of the current work. The two example traces shown in Figure 4.8 (top trace, trigger sensor nearer the source) have clearly identifiable

arrival time differences and a significant attenuation, given that both sensors are cross-calibrated for amplitude.

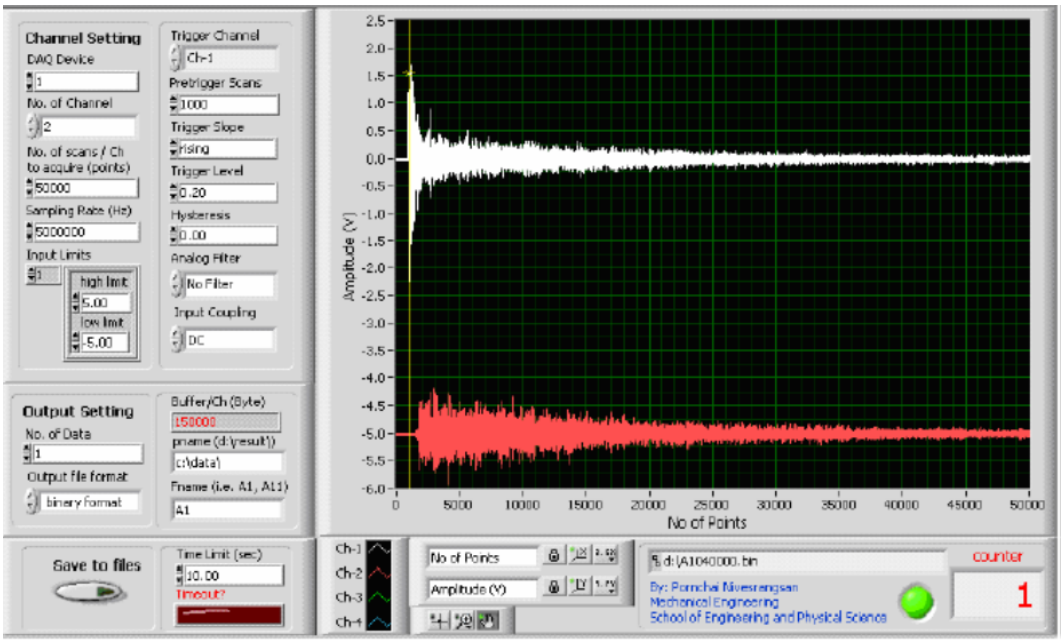

Figure 4-8: *LabView front panel for 2-channel DAQ system*

4.1.5 *Signal Processing*

The proprietary package MatLab was used for signal processing because of its capacity to handle and display very large arrays of data. Each record typically contains 5×10^6 elements, much of which needs to be cut into smaller sections, and the display/zoom facilities within MatLab were very useful in doing this.

Frequency domain analysis can give further insight into AE signals. This technique basically entails the decomposition of time-series data into the frequency domain using a Fast Fourier Transform (FFT) algorithm where signal spectral characteristics are obtained and used to calculate the distribution of the signal energy in the frequency domain [74].

The FFT is also used in demodulated resonance analysis [141]. Here, the AE wave is regarded as a carrier frequency for the lower frequency information. To implement this, the signal is treated using a sliding root mean square RMS to reveal lower frequencies in the envelope of the signal [142].

Some studies use the frequency analysis to filter out noise from an AE signal where AE sources are infiltrated by noise and this improves signal to noise ratio [143]. The recorded AE signals in

this work were discrete bipolar time-series, and were left in that format for much of the comparison with simulated signals described later.

A thresholding technique (figure 4.8) was used to identify the arrival time and duration of the significant part of a record. The trigger sensor was set to have 1000 points of pre-trigger, which allowed the noise amplitude to be determined. A threshold was set at 5 times the maximum noise in the first 1000 points, the wave arrival time being the time at which the signal level first exceeds this threshold.

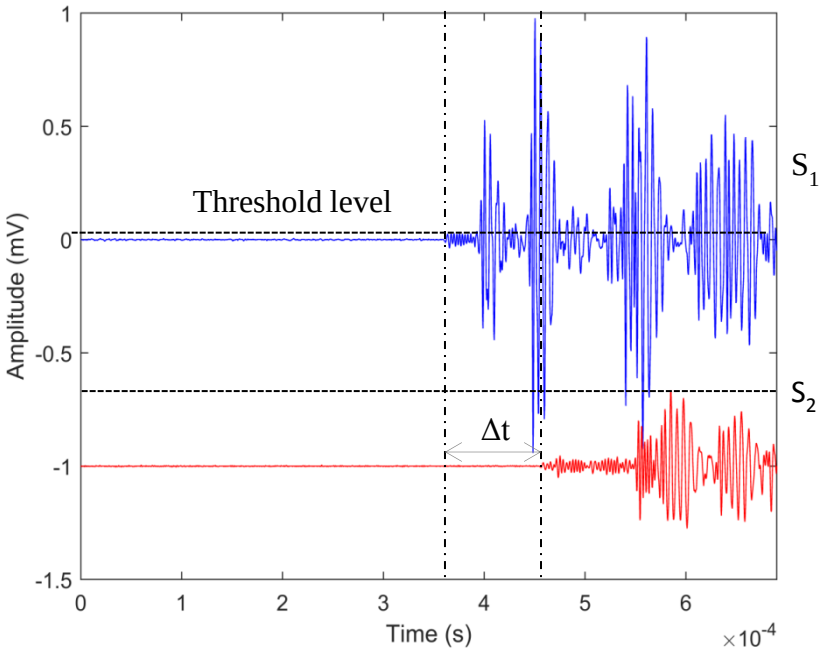

Figure 4-9: *Threshold technique applied to two sensors*

4.2 Experimental Procedures

In all, four different sets of experiments were carried out. The first two sets consisted of PLB and ball bearing tests on the simple solid steel cylinder described in Section 4.1.2, a configuration for which there exist analytical solutions and there is relatively little interference from reflections. The remaining two sets of experiments were carried out on the 2 m length of steel pipe described in Section 4.1.2, one of these using a PLB source and the remaining one using the dropped object sources described in Section 4.1.1. The experiments are described in turn below.

4.2.1 *Reference PLB Tests on Solid Steel Cylinder*

This simple set-up allowed the effect of sensor response to be encoded into the simulations and also allowed for an assessment of the uncontrolled aspects such as sensor placement and coupling, and the consistency of application of the lead break. These experiments also provided

a reproducible means of calibrating the sensors before and after each experiment and to test the robustness and precision of the signal processing, for example for arrival time estimation.

For these tests, two sensors, S_1 and S_2, were mounted on the solid steel cylinder as shown in Figure 4.10. The source was equidistant (0.157m) from both S_1 (the trigger sensor) and S_2 and this was done in order to reduce the number of unnecessary variables, the sensors were always placed equidistant from the source so that first arrival at each sensor should be roughly simultaneous (Figure 5.1). The cylinder was chosen because it is relatively simple in geometry and has been used widely by previous workers [112, 144] for calibration and reference purposes and so has been well studied using the sensors and acquisition system employed here.

The centre of the cylinder was used as a flat, uncomplicated landing surface for the study of the temporal signatures of dropped objects at both the short and long time scales. However, most of the experiments reported in this section used a PLB source, the objective being to assess the extent to which this could be regarded as a step-unload for the purposes of simulation.

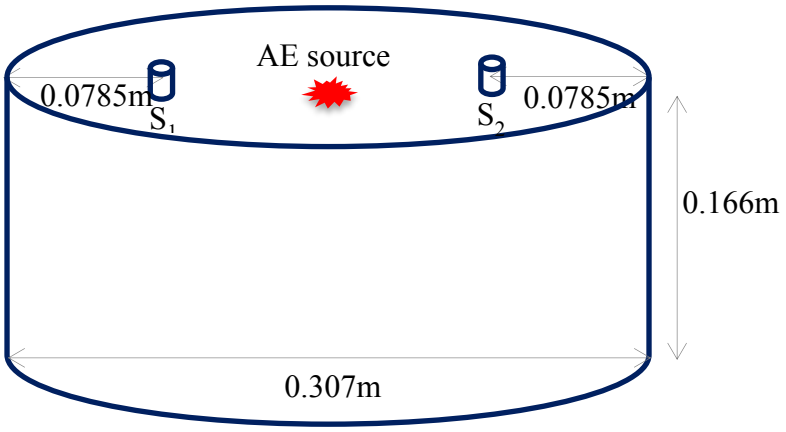

Figure 4-10: *Schematic representation of reference tests on solid cylinder*

The preamplifiers were set at a gain of 40dB and, once the trigger was activated, the system acquired 50,000 points at a sampling rate of 5Msamples/s with a pre-trigger of 1000 points. The system also acquired 50,000 points from the second sensor interlaced with the trigger so that the two sensors were essentially time-correlated.

4.2.2 *Dropped Object on Solid Cylinder*

The second set of experiments on the solid cylinder was the ball bearing drop, carried out to simulate sources with an extended temporal structure. Again, the preamplifiers were set at a gain of 40dB and a sampling rate of 5Msamples/s with a pre-trigger of 1000 points was used. The

system also acquired 50,000 points from the second sensor interlaced with the trigger, and, just as with the first set of experiments, the AE sensors were placed equidistant (0.075m from the source) at the centre of the top surface. A guide tube was used to guide the ball bearing on to the centre of the surface of the cylinder (figure 4.11). A total of 3 drops were made for this condition.

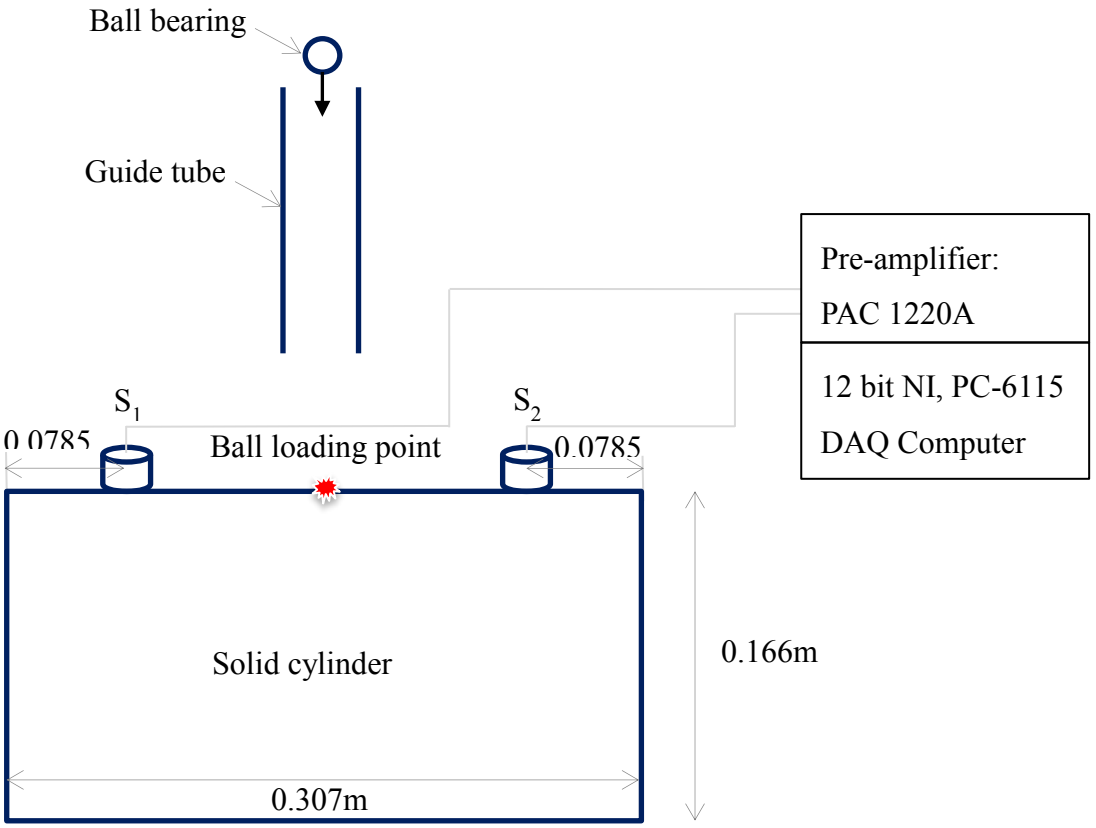

Figure 4-11: *Schematic representation of ball bearing drop on solid cylinder*

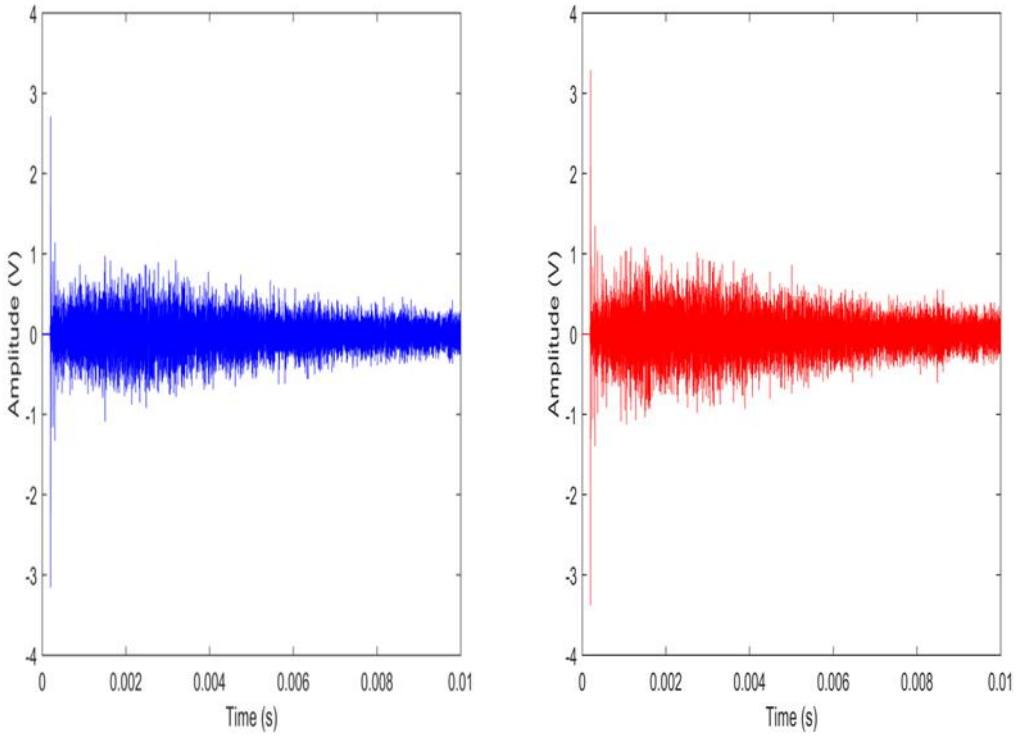

Figure 4-12: *Typical raw AE time series generated by a pencil-lead break, recorded at (a) S_1, (b) S_2 on the solid cylinder (full record)*

Figure 4.12 shows spectra for the records shown in Figure 4.11 for each of the two sensors. These contain broad peaks at around 250 kHz, 600 kHz and 800 kHz, these being the main resonance bands of the sensors, and the range being consistent with the analogue band-pass filter between 0.1 and 1MHz.

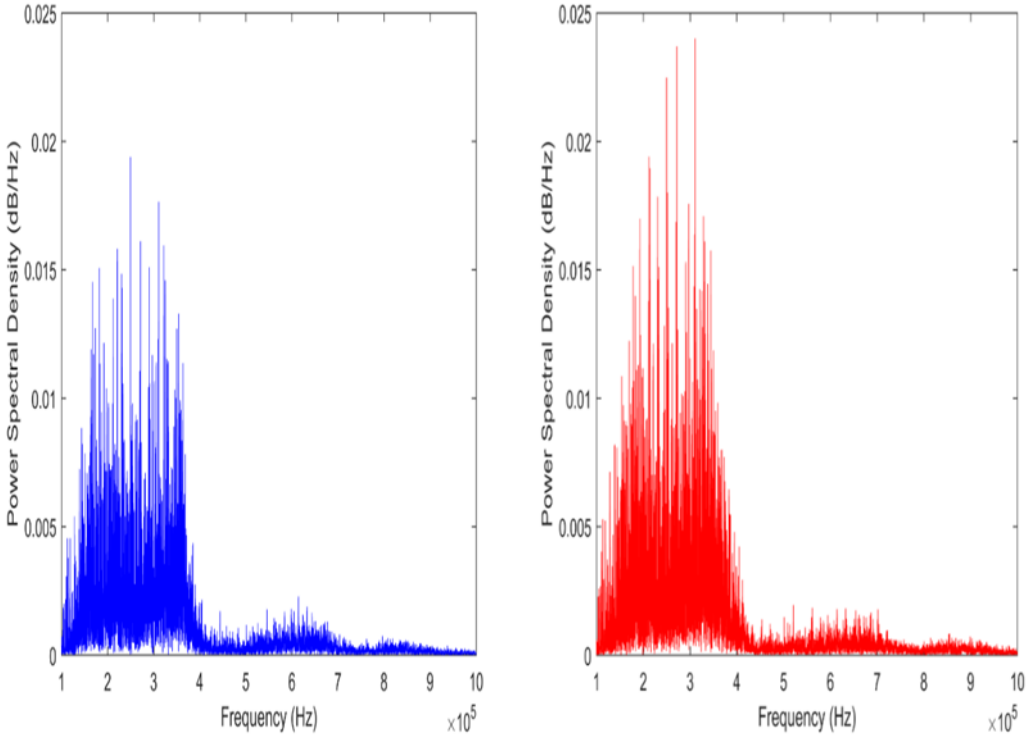

a. Sensor 1 b. Sensor 2

Figure 4-13: *Typical Power spectra of entire time series shown in Figure 4.11 for (a) S_1, (b) S_2 on the solid cylinder*

4.2.3 *PLB experiments on Pipe*

In this set of experiments, two sensors were mounted on the pipe in positions shown in Figure 4.12, one sensor, S_1, acting as the trigger, and 20 pencil lead break records taken. The aim of this experiment was to observe practical AE wave propagation on a hollow cylinder of relatively high aspect ratio (length: diameter) for comparison with the simulations.

The data was sampled at 2.5Msamples/s as this is the lowest that could be used to preserve frequencies up to 1MHz in order to get the longest possible record with the data acquisition system used. The pre-amplifier gain was again set at 40dB.

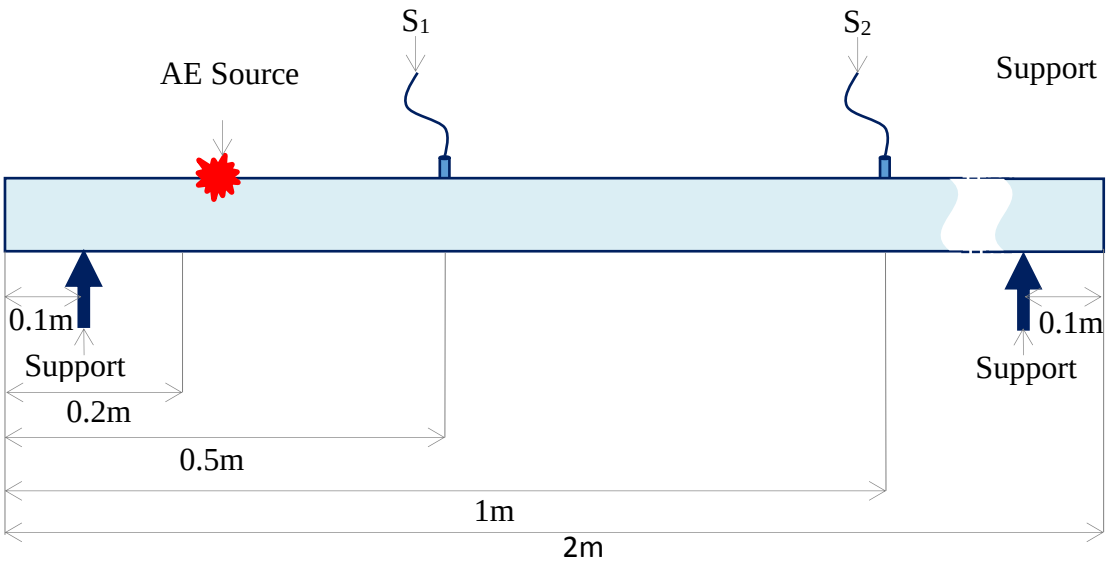

Figure 4-14 : *Schematic representation of PLB experiments on pipe*

The first 20 PLBs were carried out using exactly the same conditions as above but, in this case, each sensor was unmounted and mounted back after each pencil lead break. This was carried out to study the effect of sensor coupling on a surface less smooth than the end face of the solid cylindrical block.

4.2.4 *Dropped Object Tests on Pipe*

The fourth set of experiments used dropped object to simulate sources with an extended temporal structure on a pipe. This was done by varying the amount of incident kinetic energy dissipated as a result of steel ball bearings impacting on the surface of the pipe. Two variables; ball bearing size and drop height, both of which affect the potential energy in a systematic way, were examined as shown in table 4.1.

The same two sensors and positions as described in Section 4.2.3 were used and the ball bearings were released from a clamp via the clamp screw to fall through a Perspex guide tube as shown schematically in figure 4.13 and an embodiment shown in figure 4.14.

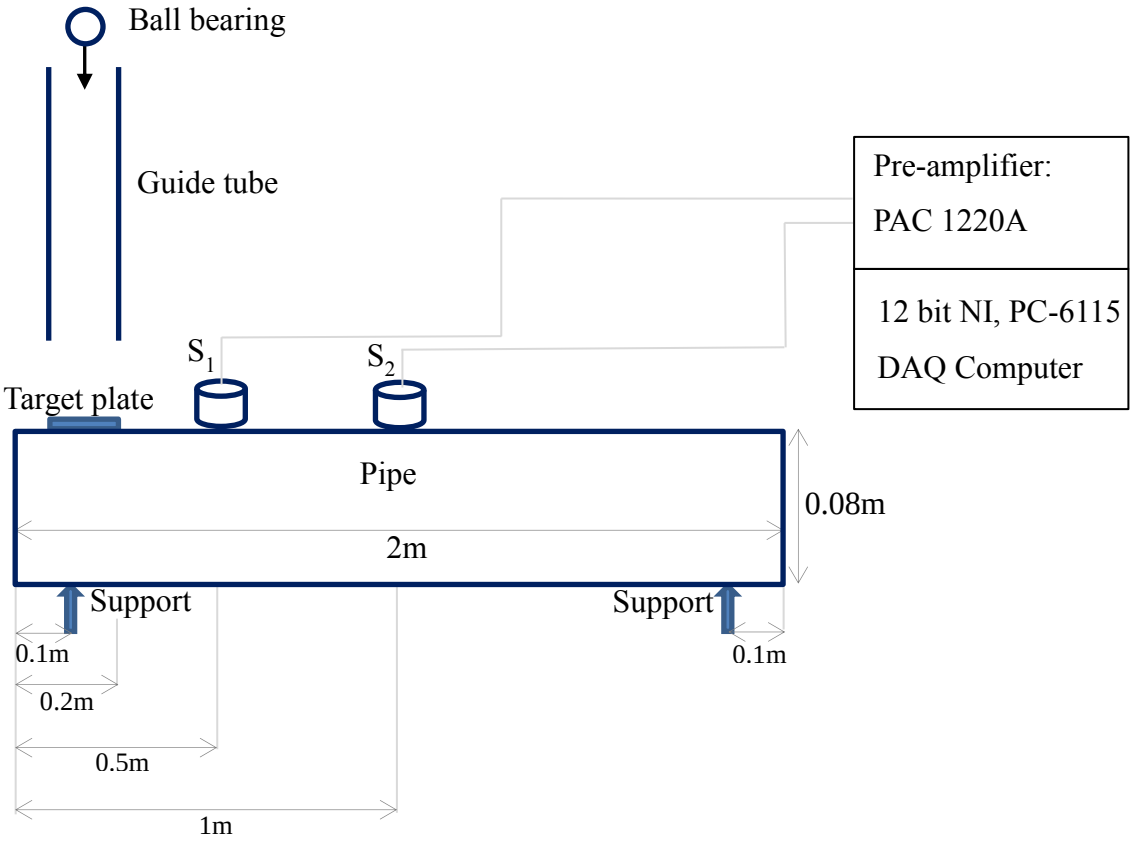

Figure 4-15: *Schematic representation of ball bearing drop on pipe*

Guide tubes of different lengths (0.1, 0.2 and 0.3m) were used to obtain different impact speeds. Because the ball bearing would lose some kinetic energy if it impinged on the sides of the tube, a diameter about ten times larger than the ball bearing size was used. To produce repeatable conditions over a range of experiments, a specially designed clamp held the perspex tube and ball bearing and the clamp screw was used to release the ball bearing into the guide tube. Also, a rectangular flat steel plate (target plate) of thickness 10mm was placed on the pipe surface in order to have a plane area for the ball bearing to drop onto.

Figure 4-16**:** Ball bearing drop on pipe

The ball bearing sizes and heights are shown in table 4.1 along with the estimated potential energy of the impact ($m \times g \times h$). Each object was dropped 20 times each in order to assess the repeatability of each ball bearing release from the clamps. As before, the preamplifiers were set at a gain of 40dB and the sensor nearest the source was used as the trigger and, once activated, the system acquired 50,000 points with a pre-trigger of 1000 points. Again, as before, the system also acquired 50,000 points from the second sensor interlaced with the trigger so that the two sensors were time-correlated within one sample.

Ball Bearing	Diameter (mm)	Weight (g)	PE (x 10^{-2} J) (100mm)	PE (x 10^{-2} J) (200mm)	PE (x 10^{-2} J) (300mm)
Small	4	0.3	0.026	0.052	0.078
Medium	8	3	0.298	0.596	0.894
Large	16	17	1.669	3.338	5.007

Table 4-1: *Dropped object energy*

4.2.5 *Sensor Calibration*

The sensor calibration certificates are shown in Appendix A and these indicate a ratio of sensitivity of 0.94 across the bandwidth of 150 kHz and 350 kHz for the two sensors used. However, it is also necessary to acknowledge that there may be a variation in individual PLBs and also in the coupling when sensors are removed and replaced

Accordingly, both sensors were mounted on the cylinder (as shown in Figure 4.10) and 20 lead breaks acquired without removing and replacing the sensors. Next another 20 lead breaks were acquired with the two sensors being removed and remounted after each individual break. Although S_1 acted as the trigger sensor, there was little or no arrival time difference at the two sensors.

4.3 Summary of Experiments

Table 4.2 summarizes all the experiments carried out on the solid cylinder and on the pipe. The results of these experiments are examined and discussed in Chapters 5, 6 and 7 respectively.

Test Object	**Source**	**Condition**	**No. of Records per condition**	**Chapter**
Solid Cylinder	PLB	2 equidistant sensor positions -Fixed sensor placement -Removal and replacement	20 records of each	5
Solid Cylinder	Dropped object	1. 2 equidistant sensor positions 2. 3 ball sizes, one drop height	1 record of each	5
2m Pipe	PLB	1. 9 sensor positions, 3 pipe lengths 2. 2 sensor positions, fixed pipe length	20 records of each	6
2m Pipe	Dropped object	1. 1 sensor position 2. Ball sizes, 3 drop heights	20 records of each	7

Table 4-2 : *Summary of all experiments carried out*

Chapter 5- Reference Tests on Solid Cylinder

This chapter presents all of the work carried out on the solid steel cylinder, which was chosen as a reference object. The chapter is organized in four main sections, followed by a discussion. This object was chosen for its simplicity compared with pipe and was used because it has already been well – characterized from both the experimental and theoretical points of view. Section 5.1 describes a set of preliminary tests aimed at understanding the long and medium-term time series which are produced by dropping relatively large objects into the flat surface of the cylinder. Section 5.2 summarizes the only analytical solutions that are available for AE propagation in a cylinder following a step – unload in order that the expected types of propagating waves can be identified. Section 5.3 presents the results and analysis of the simulations with various rates of step-unload, whereas section 5.4 presents results for actual pencil-lead breaks. The discussion (section 5.5) seeks to establish the analytical framework for the main series of experiment in pipe sections.

5.1 Dropped Object Experiments

The purpose of these set of experiments was to establish the broad features of a dropped sphere unto a flat surface. The dropped object was chosen as an example of a source which is extended in time and so there was interest in the short, medium and long timescales, but this particular test was focussed on the rebounds so that the coefficient of resilience could be assessed.

Three different sized balls (17g, 3g and 0.3g) were dropped from the same height (0.3m) onto the surface of the solid cylinder giving incident energies of 5×10^{-2}J, 9×10^{-3}J and 8×10^{-4} J (assuming no losses of the potential energy up to impact). The solid nature of the flat end surface of the cylinder ensured that the coefficient of restitution was as close to unity as possible.

Figure 5.1 shows typical raw AE signals for the three potential energies and ball sizes. As can be seen, the ball bounces several times over a period of around 1second, each bounce being characterised by a burst of AE lasting about 0.1second. It is immediately noticeable that there is little visible increase in energy as the ball mass is increased. Discussion of this point is deferred to Chapter 7 to include the wider range of heights and multiple observations in the pipe experiments.

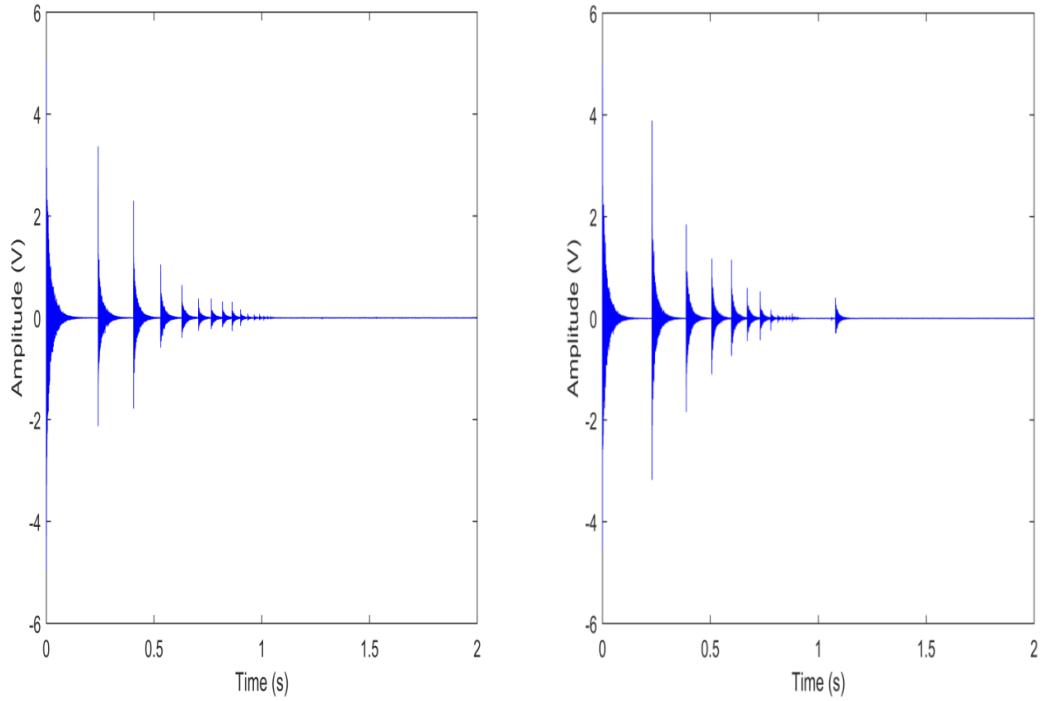

a.

b.

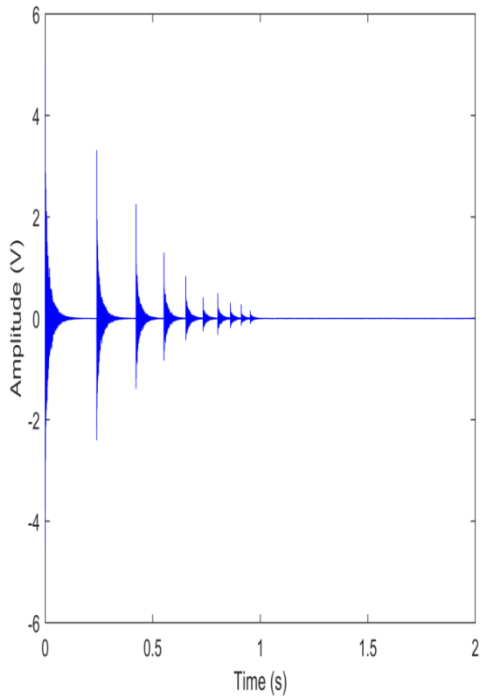

c.

Figure 5-1 *Long-timescale AE signal for three ball sizes. a)17g b) 3g c) 0.3g*

Figure 5.2 shows the 140μs around first wave arrival for the three ball sizes. It can be seen that, irrespective of the ball bearing size, each first arrival is characterized by a low amplitude component of duration about 1μs, followed by a high amplitude component, which contains the peak amplitude.

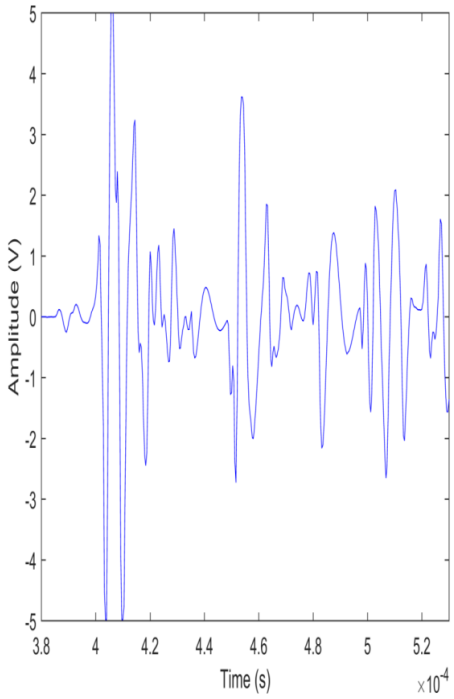

a.

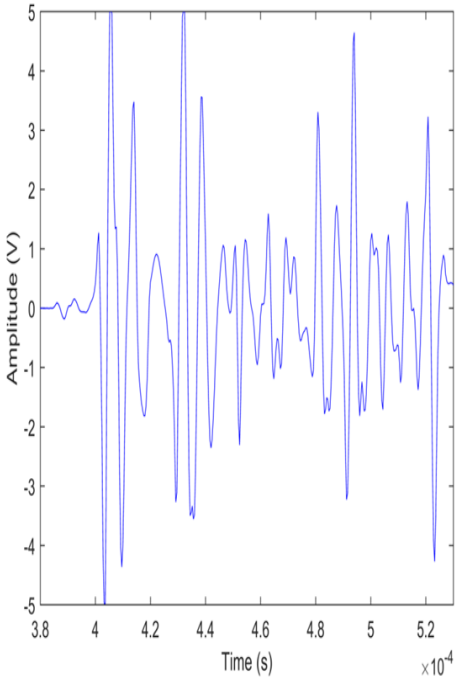

b.

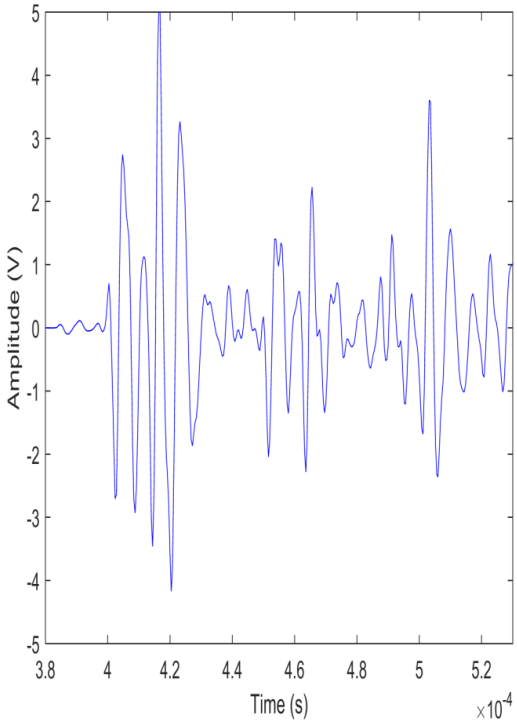

c.

Figure 5-2: Short-timescale AE signal dropped from 0.3m unto the solid cylinder. a)17g b) 3g c) 0.3g

Referring to Figure 5.2, the incident energy can be calculated for each ball bearing bounce as

$$E_{calc} = mgh$$

For the first bounce, h is known (the original drop height) and, for subsequent bounces, it can be approximated as

$$h_n = \frac{1}{2} mg \left(\frac{\Delta t_n}{2}\right)^2$$

where

m is the mass of the ball bearing

h is the height of each ball bearing drop

Δt_n is the time difference between the relevant ball bearing bounce and the previous one

As described in Chapter 2, the measured (AE) energy was calculated for each of the first four impacts for each of the ball bearing masses by integrating over the entire length of the burst.

Figure 5.3 shows a plot of the measured energy against the incident energy in the first four bounces for each of the masses. As can be seen, the relationship between incident energy and measured energy, whilst not linear, is at least continuous for each of the ball sizes. However, there is clearly also an effect of ball radius, since the curves for each of the ball sizes are not continuous.

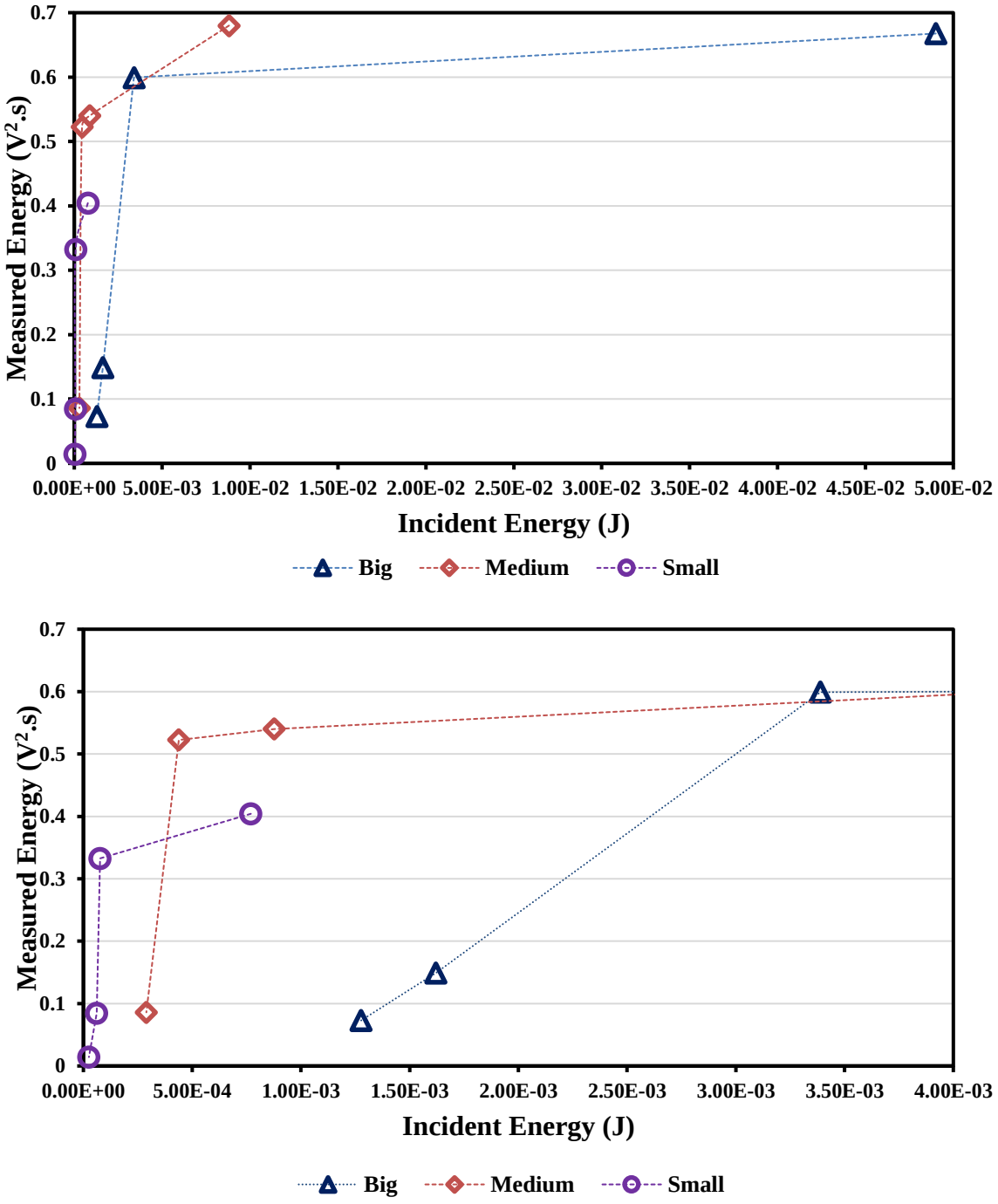

Figure 5-3: *Plot of measured energy vs incident energy in the first four bounces for all ball sizes dropped on the solid cylinder from 30cm*

Figure 5.4 shows a plot of the measured energy against the mass (effectively incident energy) in the first bounce and Figure 5.5 shows the energy, E_0, calculated for the first 50μs, in order to avoid contamination by reflection (see section 5.4).

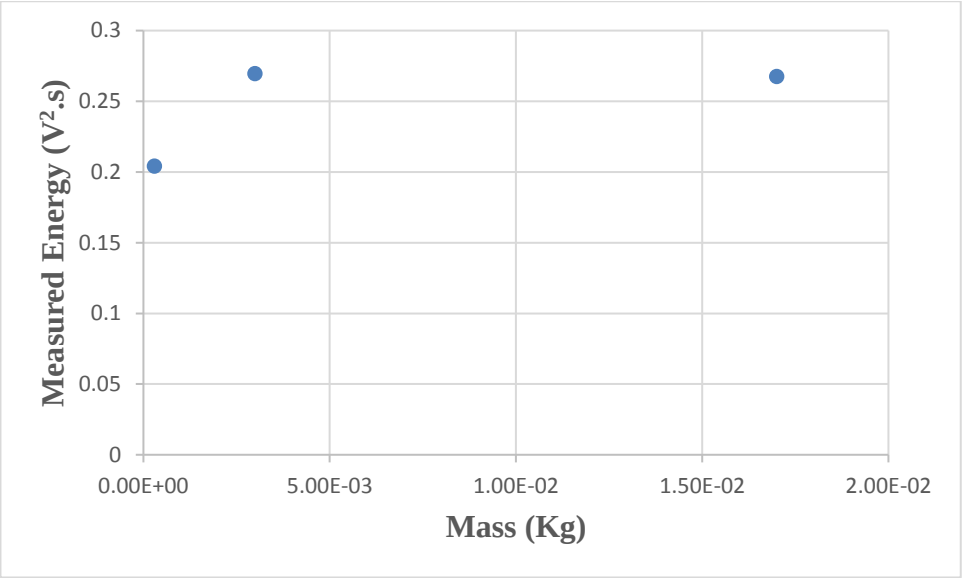

Figure 5-4 *Total measured energy in first bounce vs mass for balls dropped onto solid cylinder*

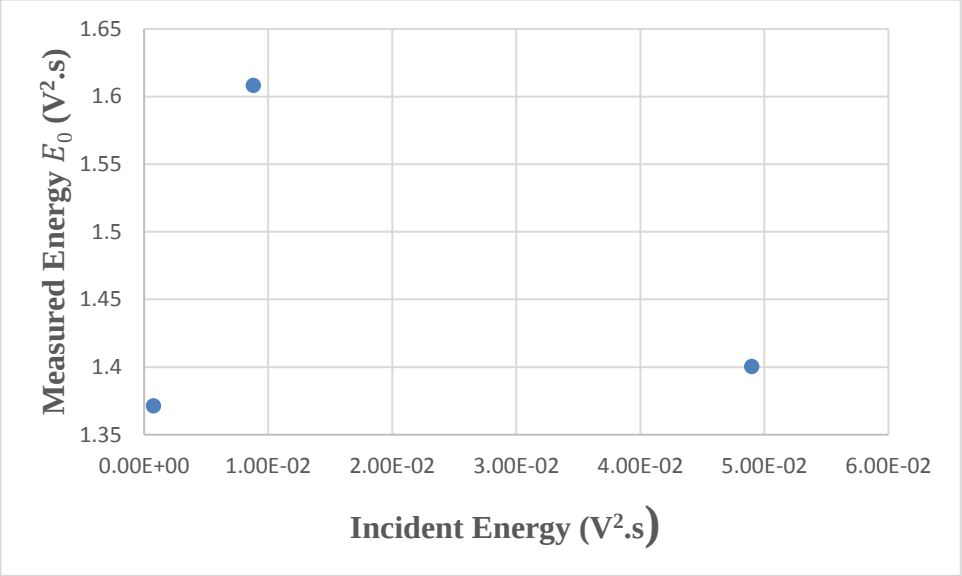

Figure 5-5: *Measured energy in first 50μs for balls drop onto solid cylinder*

Comparing figures 5.3 and 5.5, it is clear that the medium timescale (whole bounce, around 0.1s) shows a relationship between measured energy and incident energy. However, at the short timescale (50μs), the energy within the interaction time does not bear such a simple relation to incident energy, although, with only one observation, there may be a relationship masked by experimental error.

In summary, for the dropped objects, there is clearly useful information in long-timescale processing which gives an indication of the nature of the impact. For the shorter

timescales, more repeat testing is necessary to establish if there is useful information and this discussion is deferred to Chapter 7.

5.2 Analytical Approaches

Having a reasonably exact analytical solution for the surface displacement at a given point on the surface is of value here as it allows a validation of the numerical analysis in a way that is not possible using experiments where the actual input source function cannot be measured easily. There is discussion in the literature about waveforms in AE, much of it seeking to explain experimental results often in quite complex objects. The purpose of this particular section is to assess, as far as possible, the likely wave speeds and frequencies that are likely to be encountered in the reference object as an aid to linking between the simulations and experiment.

Nadal et al. [108] (in the context of developing acoustic microscopes) have modelled analytically the propagation of Rayleigh waves on cylindrical half-spaces in response to an impulsive spherical source, and have published experimental and calculated time series consisting of a short (around 200ns) low amplitude component, followed (around 300ns later) by a short (again around 200ns) component of higher amplitude. Although these authors considered much higher frequencies (5-25MHz) than those to which the current sensors respond, their observations indicate that it is possible that both the low and high amplitude components observed in the experiments are associated with the Rayleigh wave arrival, and that the second-high amplitude event, along with its associated low amplitude precursor are due to the wave returning after having been reflected from the edge of the cylinder.

Ceranoglu and Pao [66], in a series of papers, have suggested a relatively simple analytical approach to a solution for the displacement function time series. Rather than attempting a full-field solution of the wave equation, their approach was based on ray-tracing, identifying paths to reach the sensor for three basic types of wave, which they call pressure waves, and two types of shear waves, one vertically polarised (perpendicular to the surface) and one horizontally polarised (parallel to the surface). Since each type of wave has a distinct velocity, focusing on the early times allows a relatively small number of components to be taken into account, reducing the calculation burden. A similar approach is taken with the experiments and simulations here, following El - Shaib [112],

who carried out a different type of simulation using ray-tracing within a solid model. The method of Ceranoglu and Pao was generalised for layered solids (i.e. orthotropic) and can be simplified in this case because the reference object can be considered isotropic.

Figure 5.6 shows the calculated surface displacement components u_z and u_r resulting from a vertical force applied instantaneously on the same surface of a semi-infinite solid as published by Ceranoglu and Pao. The set-up is analogous to that used in the current work except that here the solid is not infinite and an unload is applied to the surface (i.e. F is negative). The surface displacements are non-dimensionalised according to:

$$u = \frac{\pi \mu h^2 u_\alpha}{F_0}$$

where α is r or x, h is the thickness of the plate, and μ is the first Lamé constant:

$$\mu = \frac{E}{2(1 + \nu)}$$

The remaining non-dimensional variables are:

$$r = {r^*}/{h} \qquad z = {z^*}/{h} \qquad t = {ct^*}/{h}$$

where c is the P-wave speed: $c^2 = {(\lambda + 2\mu)}/{\rho}$, where ρ is the mass density and λ is the second Lamé constant:

$$\lambda = \frac{\nu E}{(1 + \nu)(1 - 2\nu)}$$

As can be seen, the solutions suggest a first arrival at $t = r$, with a main "spike" at a value of t approximately equal to $1.9r$, around the ratio of the P-wave to the S-wave speed. Also, it can be seen that as the receiver moves from $r = 2$ towards $r = 6$ (figure 5.6) the response gets weaker.

The Lamé constants for steel can be calculated to be:

$$\mu = \frac{E}{2(1 + \nu)} = 77.07GPa;$$

$$\lambda = \frac{\nu E}{(1 + \nu)(1 - 2\nu)} = \frac{0.33 \times 205}{1.33 \times 0.34} = 149.6GPa$$

so that the P-wave speed:

$$c = \sqrt{(\lambda + 2\mu)/\rho} = \sqrt{(149.6 + 2 \times 77.07) \times 10^9 / 7800} = 6240ms^{-1}$$

and the S-wave speed:

$$C = \sqrt{\frac{\mu}{\rho}} = 3143ms^{-1}$$

Therefore, with the object in question, we would expect to see a low amplitude arrival of the lower amplitude P-wave at a time corresponding to its traverse from source to sensor across the surface, with a larger spike at a time corresponding to an S-wave traversing from source to sensor. The two arrivals might also be expected to be clearest at source-sensor distances $r \leq 2h$, which is the case for the reference object.

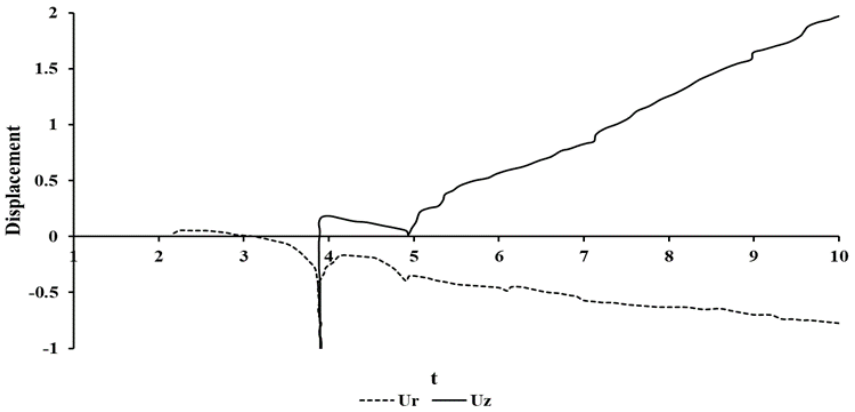

a.

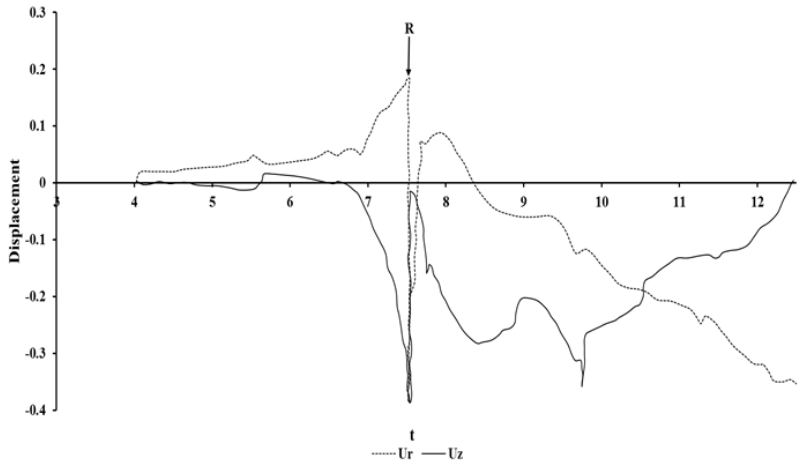

b.

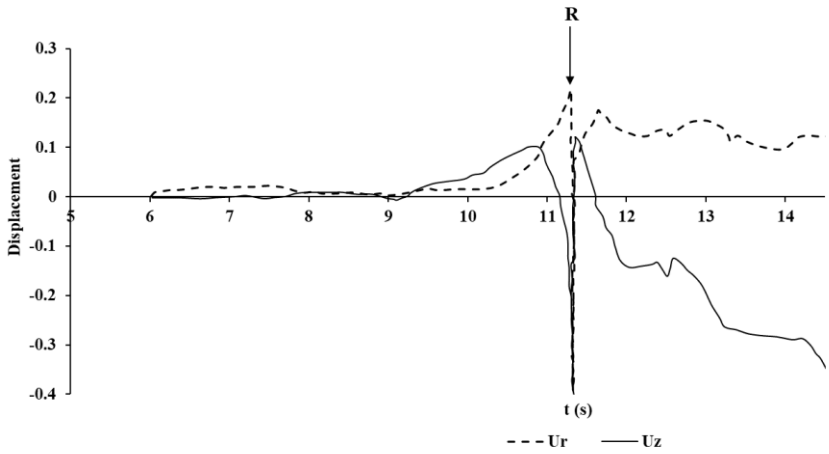

c.

Figure 5-6 *Surface displacement components* $\boldsymbol{u_z}$ *and* $\boldsymbol{u_r}$ *resulting from a vertical force applied instantaneously on the same surface of a semi-infinite solid [161].From top to bottom* $\boldsymbol{at\ r = 2, r = 4\ and\ r = 6}$.

A simpler analytical solution has been offered by Verrujit [145], which takes the exact solutions for an impulsive line load and approximates them with closed-form analytical expressions for the Rayleigh wave. For an instantaneously applied line load (F') (i.e. step load), and relatively large values of time, the (2-Dimensional $x - z$) Rayleigh stress wave in a semi-infinite half-space defined by $-\infty \leq x \leq \infty,\ 0 \leq z \leq \infty$ can be approximated by:

$$\frac{\sigma \pi z^2}{F'} \approx -\frac{1}{1 + {x^2}/{z^2}} + \frac{m}{1 + {(x - c_r^t)^2}/{w_p^2 z^2}}$$

where c_r is the Rayleigh wave speed and m and w_p depend on three key Rayleigh wave parameters, given by Verrujit [145] as functions of Poisson's ratio.

$$\frac{\sigma\pi}{F'} \approx -\frac{1}{x^2} + \frac{mw_p^2}{(x - c_r t)^2}$$

For $\nu = 0.3$, $\eta = 0.534$ and $\beta = 1.078$, and $M = 2.610$, so that

$$C_r = \frac{c_s}{\beta} = \frac{3143}{1.078} = 2916 ms^{-1},$$

$$w_p^2 = 1 - \left(\eta/\beta\right)^2 = 0.755 \text{ and } m = \frac{(1-\eta^2)(2\beta^2-1)}{2M\beta^2 w_p} = \frac{0.715\ X\ 1.324}{2\ X\ 2.61\ X\ 1.162\ X\ \sqrt{0.755}} = 0.180$$

So, non-dimensionalising in terms of the contact area for the applied force, *A*:

$$\frac{\sigma\pi A}{F'} \approx -\frac{A}{x^2} + \frac{Amw_p^2}{(x - c_r t)^2} = A\left[-\frac{1}{x^2} + \frac{0.136}{(x - c_r t)^2}\right]$$

Thus, for a given sensor position, x, the relative stress on the surface will vary with time between $-\frac{0.844A}{x^2}$ at $t = 0$ and $+\frac{0.844A}{x^2}$ at $t = 1$

5.3 Simulation of Reference Object

The simulations described here examine how the AE signal recorded at two virtual sensor positions on the surface of the solid cylinder changes as the unloading rate at the source changes, the objective being to determine the extent to which a PLB can be regarded as a step-unload. The choice of the most appropriate unload rate depends on carrying out a comparison with the experiment, which is shown in section 5.5. In summary, two of the analytical approaches focus on Rayleigh waves and provides values for the wave speed across the surface on which the disturbance initiates. The approach taken by Ceranoglu and Pao is, however, potentially more useful for complex objects as it focuses on ray-tracing, which allows a more flexible approach, useful in long hollow objects such as pipelines where multiple reflections from the inner and outer walls are likely. The reference measurements were simulated as an elastic steel cylinder subjected to a pressure unload similar to that expected from a PLB situated at the centre of the upper surface, with the lower surface fully constrained. Virtual sensors were placed at a distance

0.0785m from each edge of the upper surface so that the source was equidistant (0.157m) from both S_1 and S_2.

As mentioned in chapter 3, the unloading rates were chosen to be in the region of the expected time it would take a fracture, travelling at the speed of sound, to cross the diameter of a 0.5mm pencil lead in order that the simulated responses could be compared with observed responses of pencil lead breaks.

The simulated results were recorded as time series, which, at a given (real or virtual) sensor position, starts when the source is activated. Figure 5.7 shows the simulated displacement time series at the two virtual sensor positions for the first 10ms for the six unload rates used in the simulation. The simulations are recorded as surface displacement-time series, but are directly comparable with the stress time series reported later on the material in linear elastic. As expected, the wave at S_1 (blue) appears to be exactly same as that at S_2 (red), although it might be noted that the screen resolution is not sufficient to show the 4000 points in these records. It is, however, evident that the amplitude of the signal diminishes slowly with time presumably as the waves disperse, reflect and interfere. More importantly, the amplitude of the signal at maximum decreases as the unload time decreases (i.e. unload rate increases).

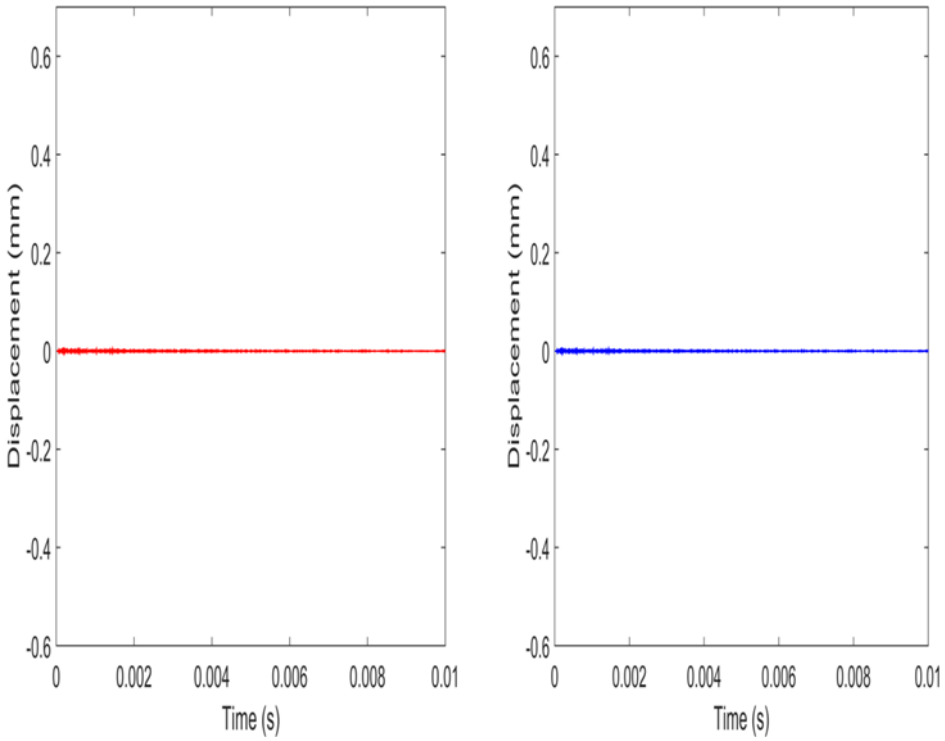

a.

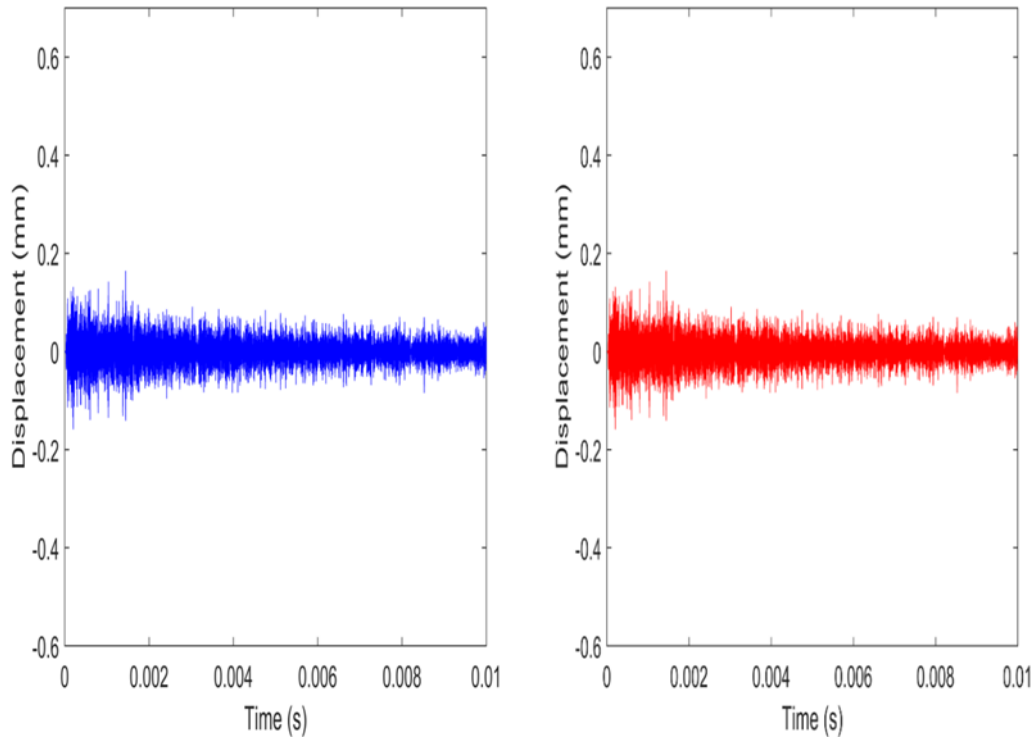
Displacement (mm)
0.6
0.4
0.2
0
-0.2
-0.4
-0.6
0
0.002
0.004
0.006
0.008
0.01
Time (s)

b.

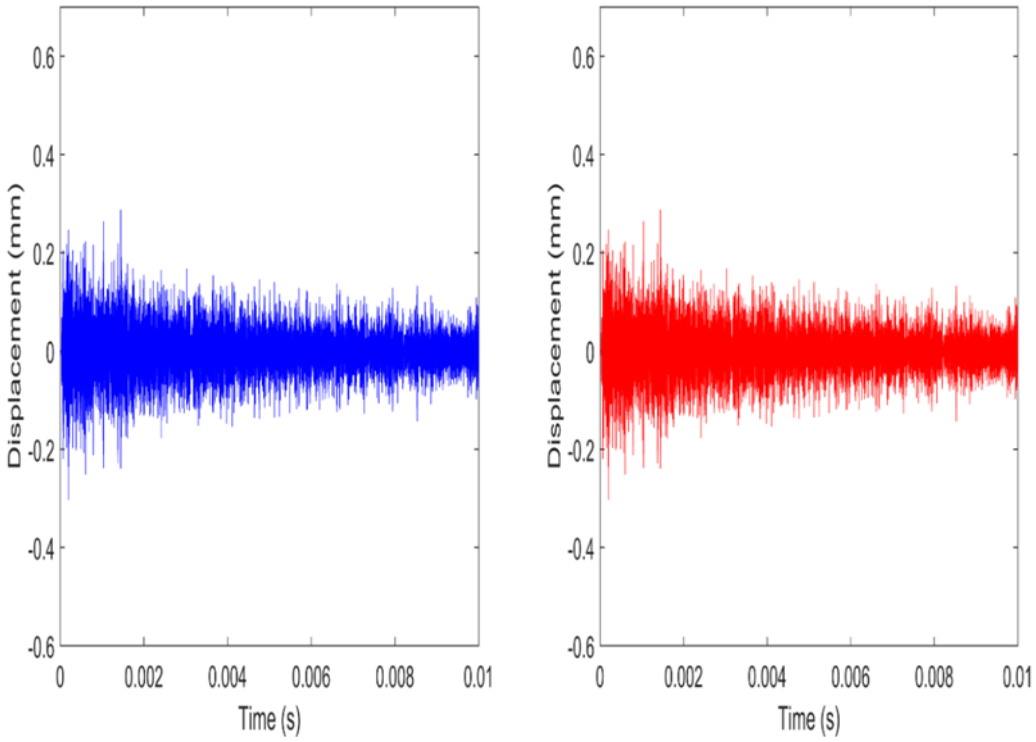
Displacement (mm)
0.6
0.4
0.2
0
-0.2
-0.4
-0.6
0
0.002
0.004
0.006
0.008
0.01
Time (s)

c.

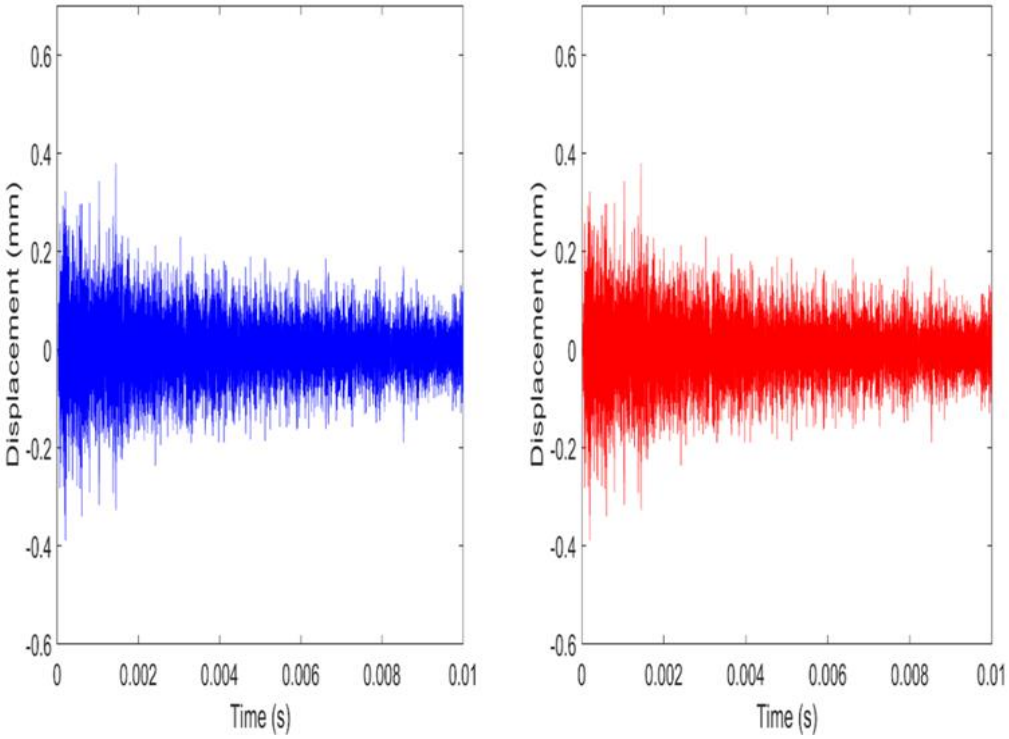
Displacement (mm)
Time (s)
0.6
0.4
0.2
0
-0.2
-0.4
-0.6
0
0.002
0.004
0.006
0.008
0.01

d.

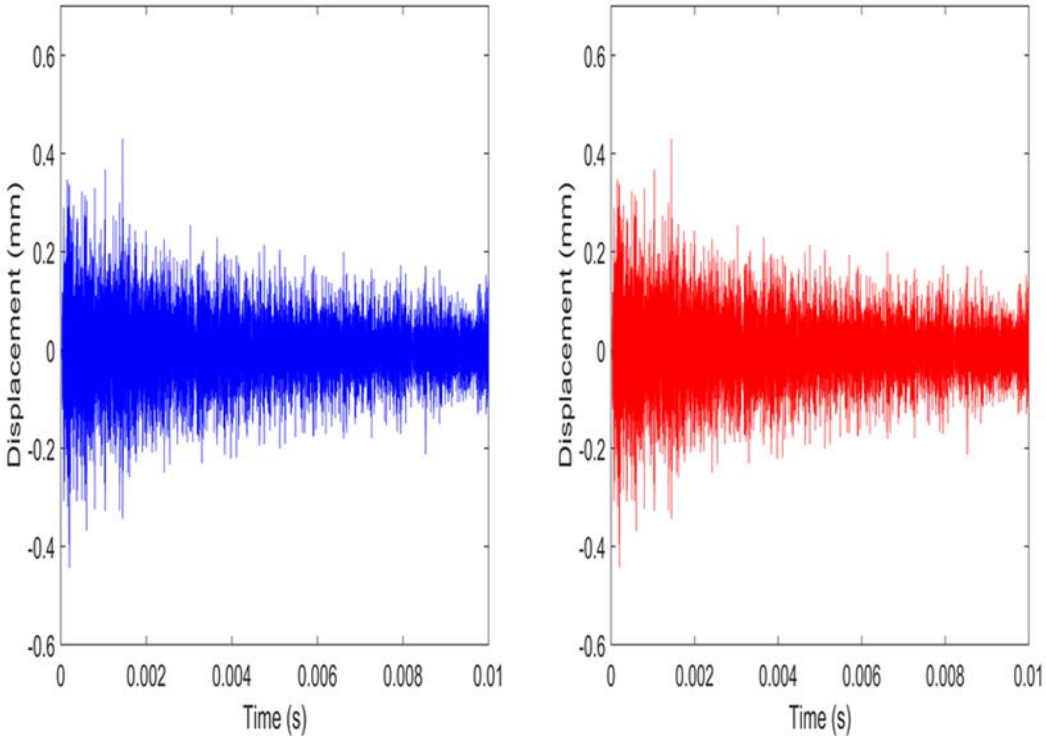
Displacement (mm)
Time (s)
0.6
0.4
0.2
0
-0.2
-0.4
-0.6
0
0.002
0.004
0.006
0.008
0.01

e.

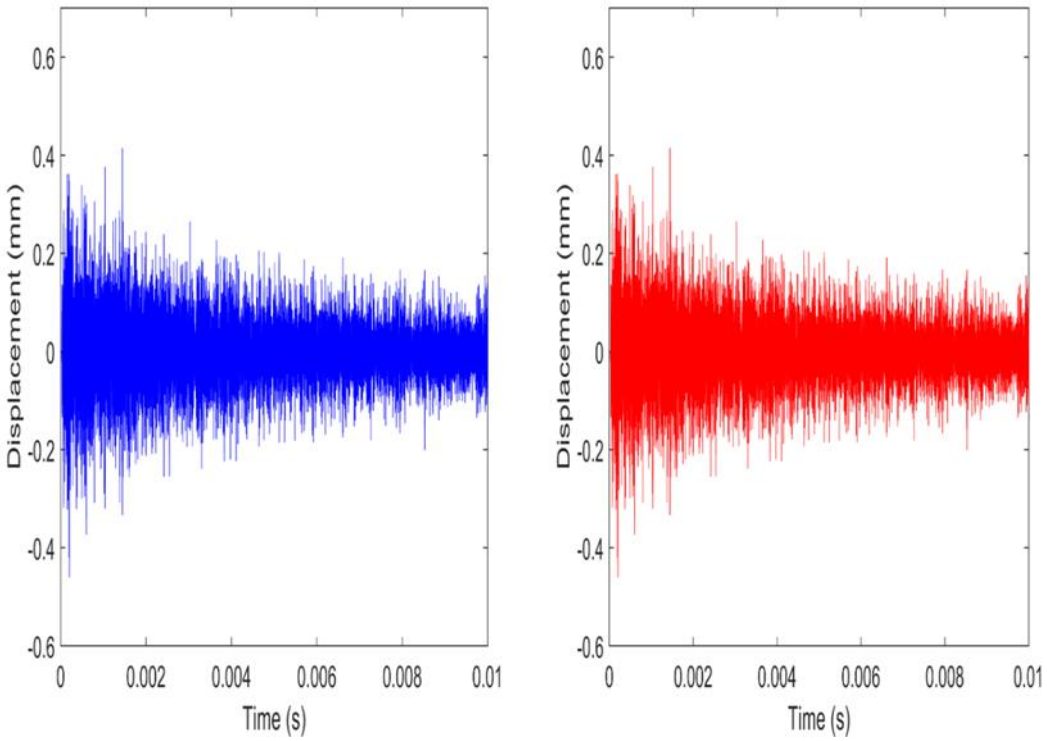

f.

Figure 5-7: *Raw time series of displacement at S_1 and S_2 (0.4M samples per second) for virtual sensors at 0.157m from the simulated source on a solid cylinder unloading in: a) 2×10^{-8} s b) 5.11×10^{-7}s c) 1×10^{-6}s d) 1.5×10^{-6} s e) 1.98×10^{-6}s f) 2.47×10^{-6}s*

Figure 5.8 shows the power spectra of the entire simulated time series shown in Figure 5.7 for all the unload rates for sensor S1. Two key frequencies are present at the position of S1, one at around 200 kHz and the other at around 350 kHz. There is a sharp frequency cut-off at 400 kHz, but this is artificial, and is associated with the effective sampling rate brought about by the time step used in the simulations.

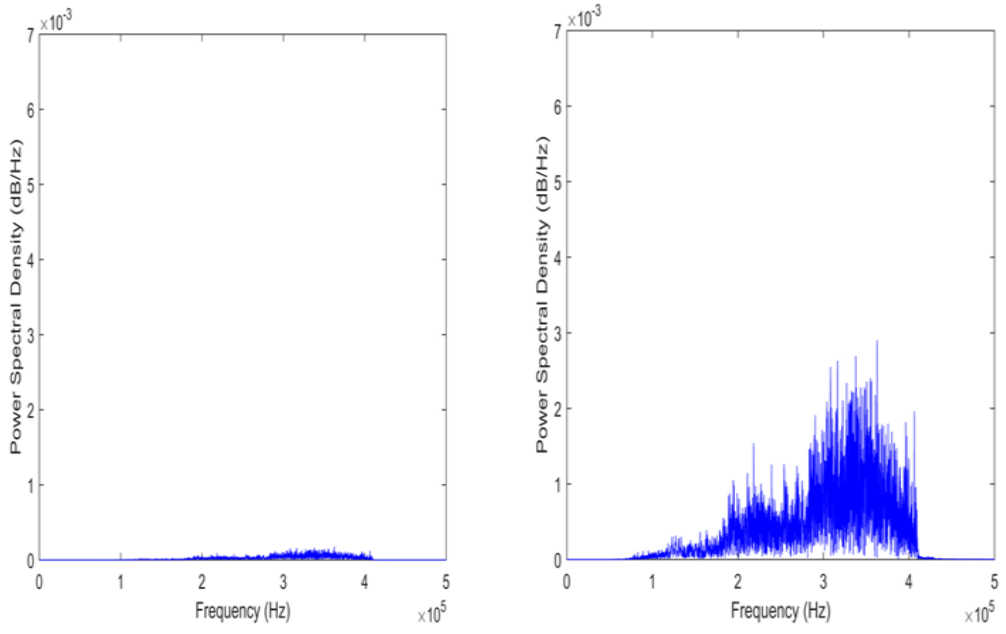

a. b.

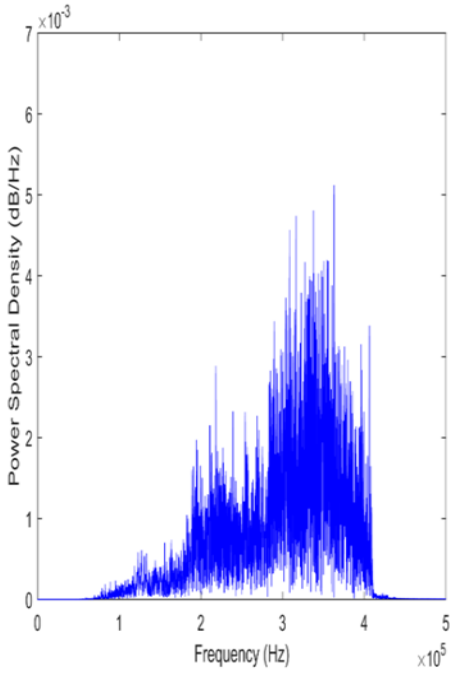

c.

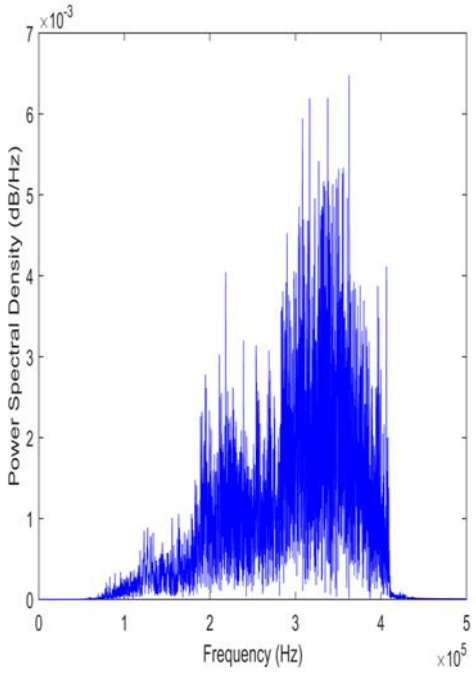

d.

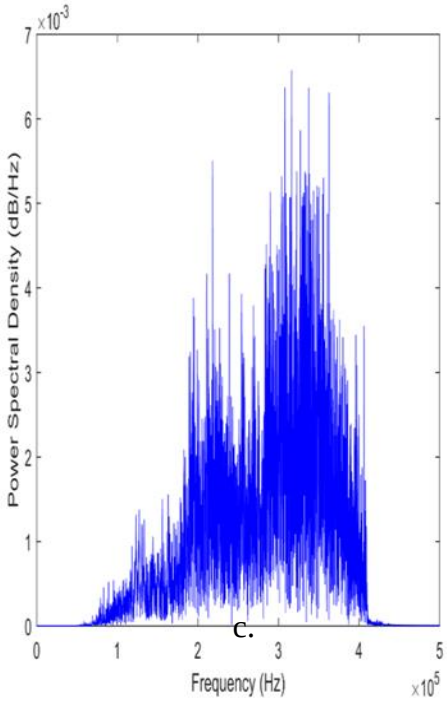

c.

e.

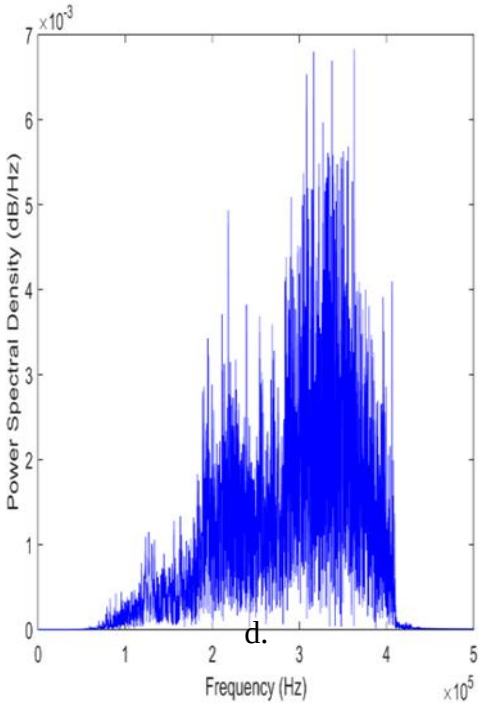

d.

f.

Figure 5-8: *Power spectrum of entire simulated time series shown in Figure 5.8 for a) 2 × 10^{-8} s b) 5.11 × 10^{-7}s c) 1 × 10^{-6}s d) 1.5 × 10^{-6} s e) 1.98 × 10^{-6}s f) 2.47 × 10^{-6}s*

Figure 5.9 shows higher resolution segments of simulated displacement time series for all the unload rates at position S_1 only, as the simulated AE wave for the first 300μs is

the same for both sensors. As can be seen, the different unload rates are rather difficult to distinguish except in terms of the amplitude already noted.

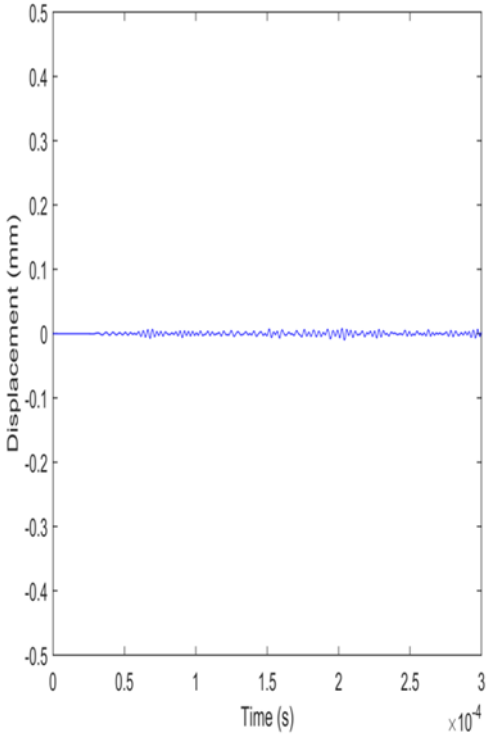

a

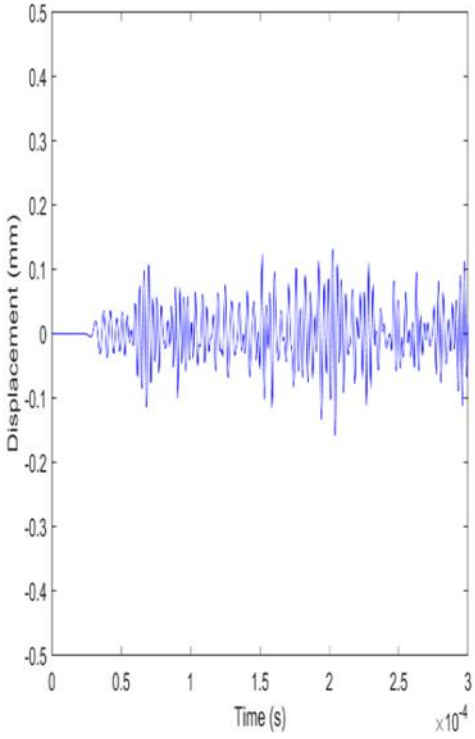

b.

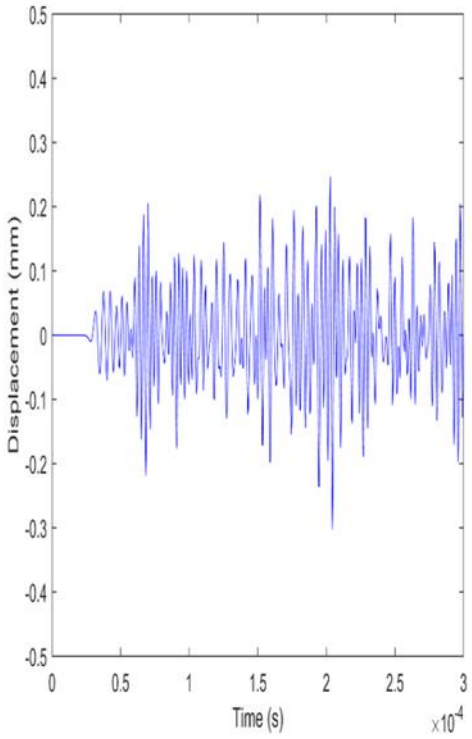

c.

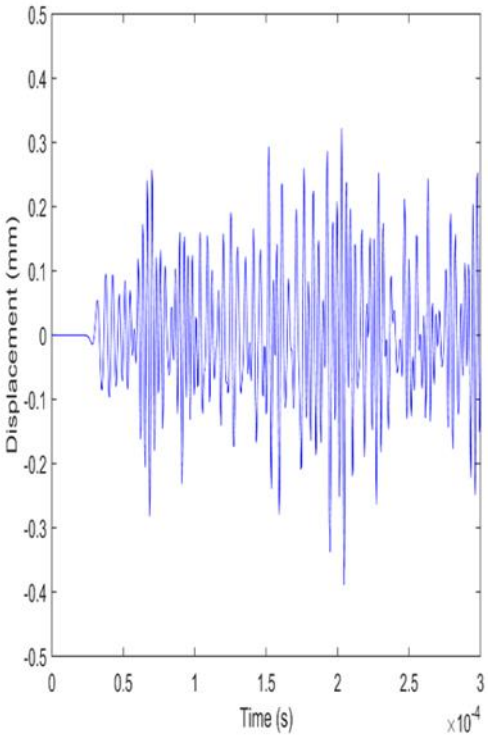

d.

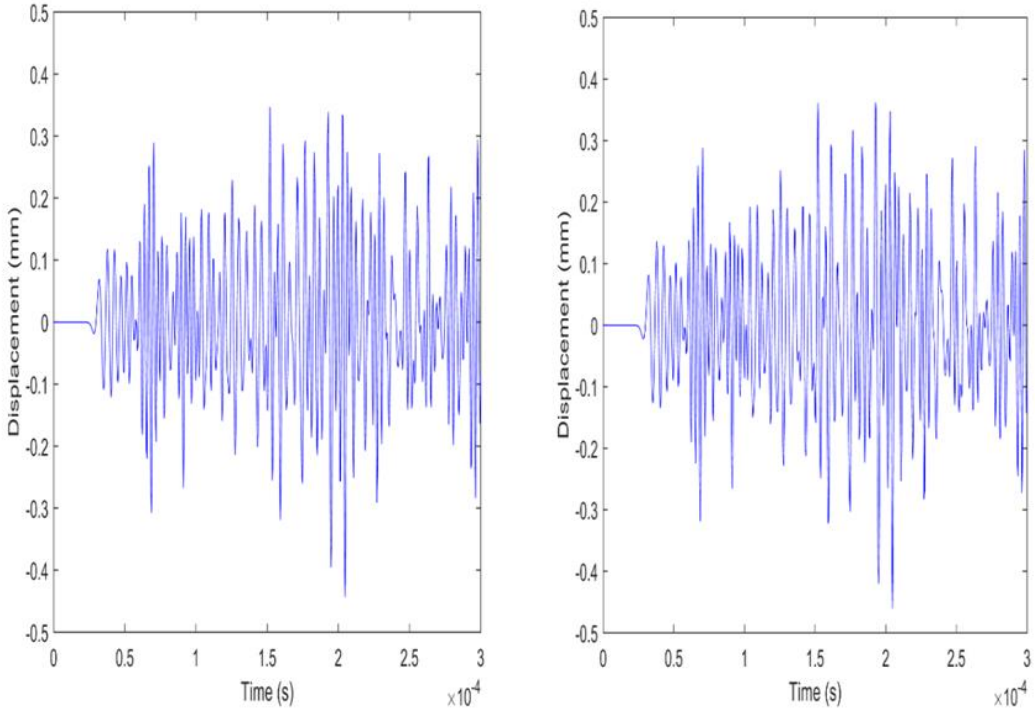

e. f.

Figure 5-9: *Segments of simulated stress time series from first arrival at position S_1 for a)2 × 10^{-8} s b) 5.11 × 10^{-7}s c) 1 × 10^{-6}s d) 1.5 × 10^{-6} s e) 1.98 × 10^{-6}s f) 2.47 × 10^{-6}s*

Figure 5.10 shows the power spectra corresponding to Figure 5.9. These spectra are a lot cleaner than those for the entire record, indicating that the waves are somewhat simpler. Two peaks at around 190 kHz and 310 kHz persist in all of the spectra, the height of the lower frequency one increasing systematically with unload time.

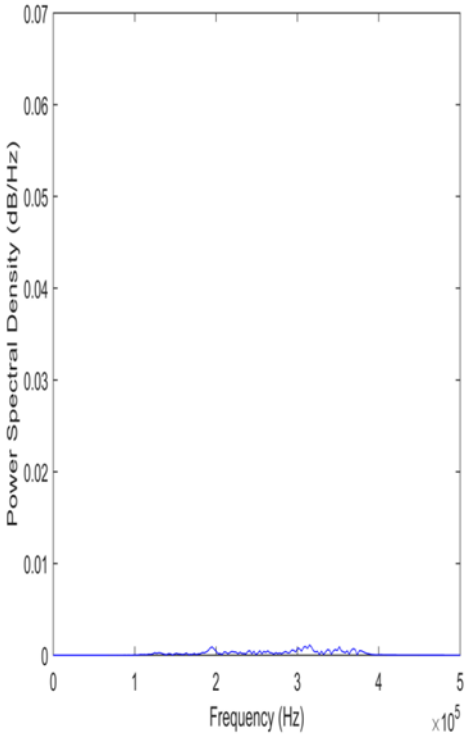
Power Spectral Density (dB/Hz)
Frequency (Hz)
x10^5

a.

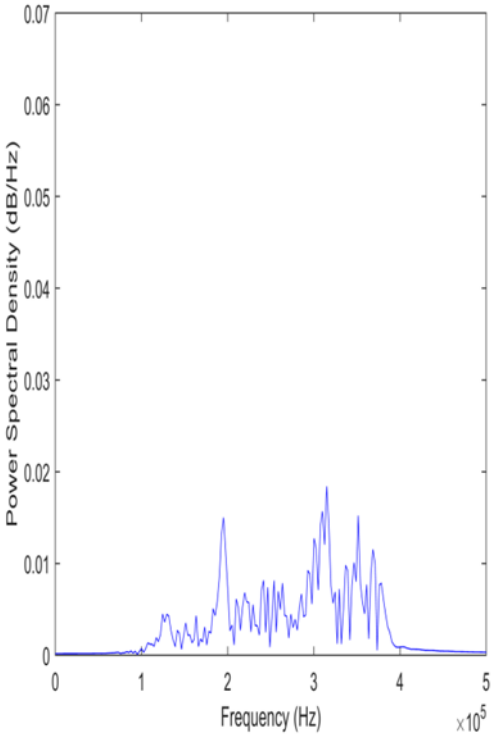
Power Spectral Density (dB/Hz)
Frequency (Hz)
x10^5

b.

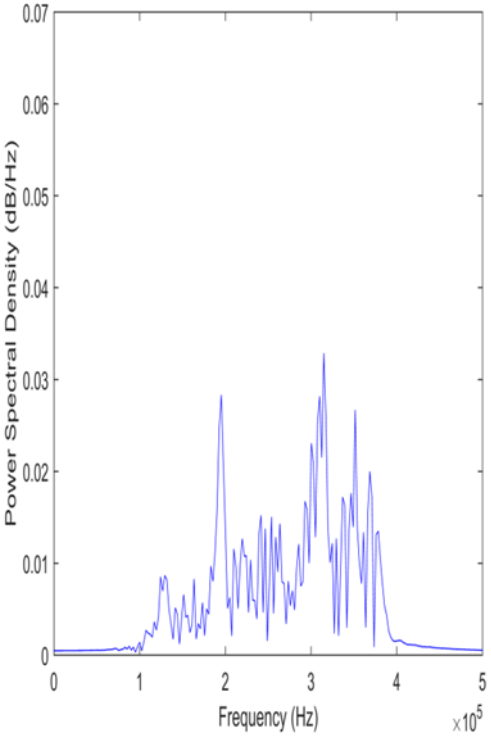
Power Spectral Density (dB/Hz)
Frequency (Hz)
x10^5

c.

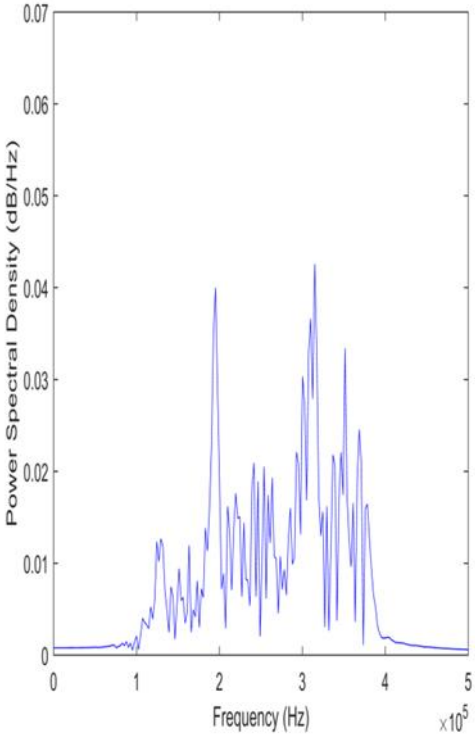
Power Spectral Density (dB/Hz)
Frequency (Hz)
x10^5

d.

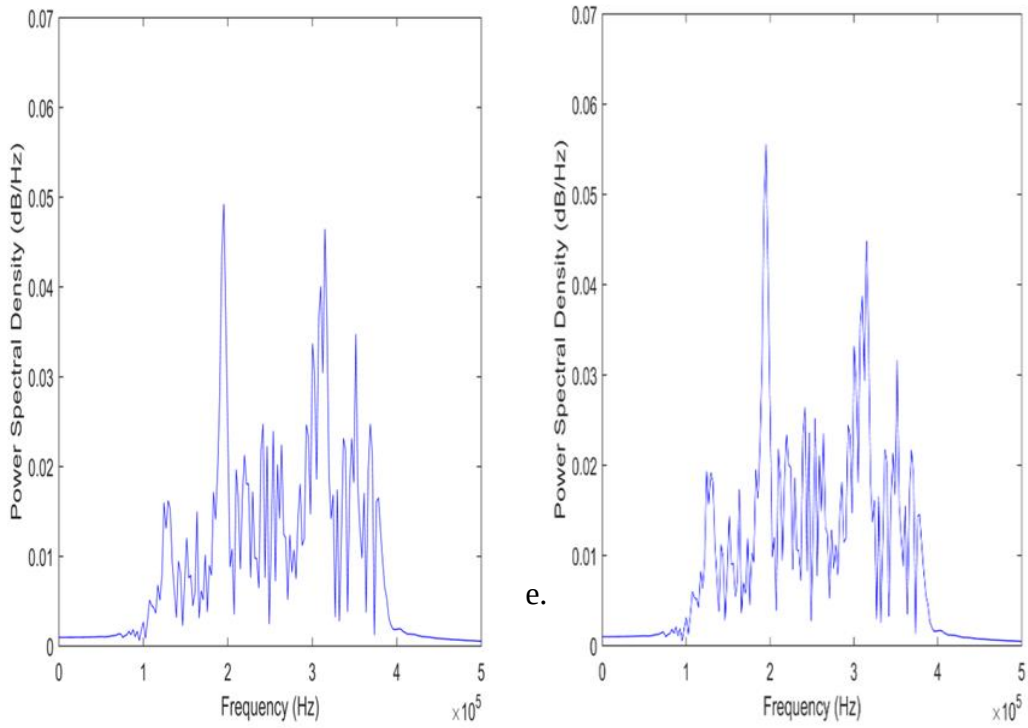

e.

f

Figure 5-10: *Power spectra of time series segments in Figure 5.9 for S_1 for a) 2×10^{-8} s b) 5.11 $\times 10^{-7}$s c) 1×10^{-6}s d) 1.5×10^{-6} s e) 1.98×10^{-6}s f) 2.47×10^{-6}s*

5.4 Impulsive Source Experiments

Section 4.2.5 describes the calibration of the sensors with respect to variations in pencil lead breaks and coupling and in sensor sensitivity. This section examines the practical response of sensors to such an impulsive source.

Calibration was carried out using two measures; the energy of the signal across the entire spectrum, and on the distribution of the energy across the spectrum. This latter measure was determined by dividing the spectrum into two bands, 100-400 kHz and 400 kHz – 1 MHz, and calculating the ratio of the energy into high frequency band to the low frequency band.

The summary data for the 20 pencil-lead breaks are without removing the sensors are:

- **For S_1:** mean energy of 0.1154 with a standard deviation (SD) of 0.0085 and a mean frequency ratio of 0.1782 with an SD of 0.0305.

- **For S_2:** mean energy of 0.1384 with an SD of 0.0096 and mean frequency ratio of 0.1626 with an SD of 0.02805.

The standard deviation of the energy (at about 7% of the mean) shows that the 20 pencil lead breaks are reasonably reproducible, although the difference between the two means indicates that S_2 is reading about 10% higher than S_1, which could either be due to its being inherently more sensitive or to its coupling to the surface being more favourable.

Again, to achieve a systematic analysis of the data, an analysis of variance (Anova) was carried out on the energies of the 20 signals recorded at both S_1 and S_2 on signals obtained from PLB acquired without moving the sensors and with those acquired after removing and replacing sensors. The F-Value was compared to the $F_{critical}$ value using a threshold of 0.05.

For the PLB acquired without moving the sensors, the F-Value was 65.09 while the $F_{critical}$ value was 4.10. For the PLB acquired after removing and remounting the sensor, the F-Value was 76.4 and $F_{critical}$ was 4.10.

Again, the F – Value is much higher than the $F_{critical}$ for the fixed sensor, it can be concluded that the sensor removal creates more variation in the recorded AE signal than does variation of the pencil lead break. However, again as before, neither source of variation is significant at the 5% level.

The experimental results were recorded as time series, which start 1000 points (pre-trigger) before the disturbance caused by the source, arrives at the trigger sensor. Since the analytical focus is to be on the very early parts of the signal, it is important that arrival times can be estimated with reasonable accuracy, so the pre-trigger is helpful in doing this since it provides a background noise reference of known temporal extent in this case corresponding to 2×10^{-5}s.

In practical AE monitoring applications, the source is extended in time and space, and, even if it were not, local and global geometry would dictate that any detected AE is a complex mixture of phases, frequencies, intensities and modes, with some of these modes being dispersive. Some researchers [146, 147] have identified specific modes of (dispersive) AE Lamb waves in plate-like structures, although others [3, 76] have contented themselves with identifying characteristic wave packet speeds and associated frequency ranges.

In order to have a consistent way of identifying arrival, a thresholding technique was adopted using S_1 (the trigger sensor). This consisted of calculating the mean and standard deviation (SD) of the first 1000 points (pre-trigger) and defining arrival as the point at which the amplitude first crosses the mean ± 5SD.

Figure 5.11 shows the first 300μs of the records shown in Figure 5.1 at which resolution the waveforms can be clearly seen. The waveforms display a clear similarity, each consisting of a low amplitude component which is the first to arrive (labelled A in Figure 5.11), followed by a higher amplitude component which contains the highest positive peak (labelled B in Figure 5.11). The higher amplitude component appears to be of higher frequency and attenuates more sharply that the lower amplitude component, which appears to persist over the entire record shown in Figure 5.11. The high amplitude component appears to make a return (labelled C' in Figure 5.11b) which may constitute a reflection. There are some subtle differences in the relative amplitudes of these features between S_1 and S_2, although it is not clear if these are sensor-related or constitute a random variation, hence the need to analyse all 40 records separately.

First, the thresholding algorithm was applied to determine the arrival time of the low-amplitude feature, labelled as t_1 on Figure 5.11. Assuming this feature to correspond to a ray travelling parallel to the surface a distance of 7.5×10^{-2}m, the expected first arrival would be at 1.2×10^{-5}s for a P-wave travelling at a speed of 6240ms^{-1}, or at 2.4×10^{-5}s for an S-wave travelling at a speed of 3143ms^{-1}. Unlike in the simulations, the departure time from the source is not known in the experiments, so this has been calculated by subtracting the transit times from the arrival times at both sensors.

The thresholding technique was used the obtain the first arrival times for the low amplitude and high amplitude waves at S_1 and S_2 for each of the pencil lead breaks then

the time difference was used to calculate the wave speed for each of the breaks and the mean and standard deviation is given below:

- **For S_1:** mean wave speed of 5988ms^{-1} for the fast wave and 3145ms^{-1} for the slow wave with a standard deviation (SD) of 0.2 and 0.09 respectively.
- **For S_2:** mean wave speed of 5071ms^{-1} for the fast wave and 3137ms^{-1} for the slow wave with a standard deviation (SD) of 0.9 and 0.10 respectively.

Because the thresholding is related to sensor calibration, analysis of the data, an analysis of variance (Anova) was carried out on the 20 times of arrival for the signals recorded at both S_1 and S_2 without moving the sensors against those acquired after removing and replacing sensors. The F-Value was compared to the $F_{critical}$ value using a threshold of 0.05 as described in Chapter 4.

For the records acquired without moving the sensors, the F-Value was 33 while the Fcritical value was 4.41.For records acquired after removing and remounting the sensor, the F-Value was 5.63 while the $F_{critical}$ value was 4.41.

As the F –Value is much higher than the $F_{critical}$ for the signals acquired when the sensors where removed and remounted before acquiring the signal, this implies that the sensor removal creates more variation in the arrival time estimation than does the PLB variation. However, since both values are below the $F_{critical}$,the differences in arrival time estimation are not significant in either case at the 5% level.

A number of other investigators (e.g. 101, 141) have noted that practical AE signals often consist of a lower amplitude faster "wave" with low attenuation, followed by a higher amplitude, slower "wave" with high attenuation, which appears to be happening here. In each case, the pulse is presaged by a downward spike (labelled C and C' on Figure 5.11), so a return time (Δt_1 in Figure 5.11a) can be identified. Two methods were developed for locating the times at C and C', using thresholding and time frequency analysis.Taking the second of these as the more likely, the arrival time difference (Δt_2 in Figure 5.11b) can be calculated as the time taken for a P-wave to travel 0.075m, i.e. 1.2×10^{-5}sec, less the time taken for either an S-wave to travel 0.075m, i.e. 2.38×10^{-5}s which seems to be approximately in accord with the observation.

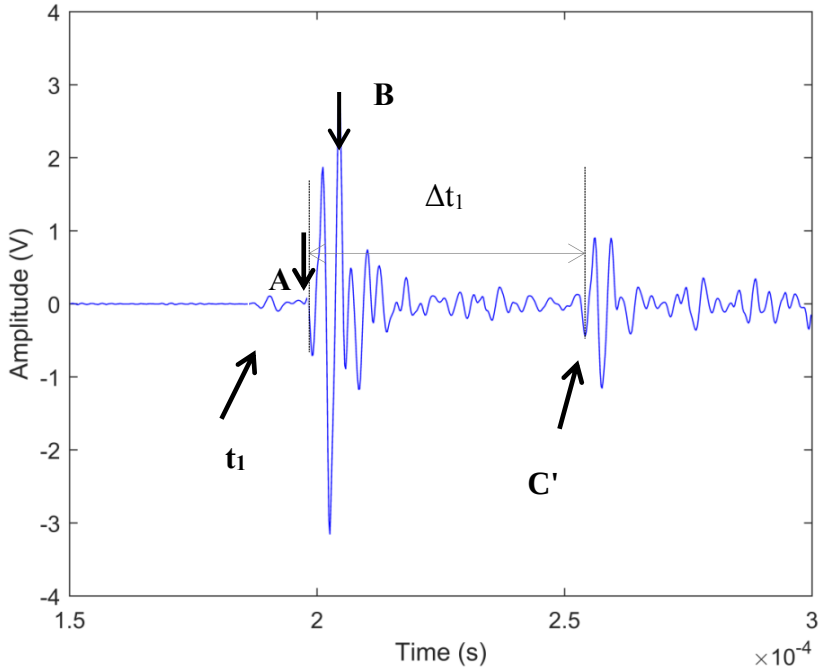

a. Sensor 1

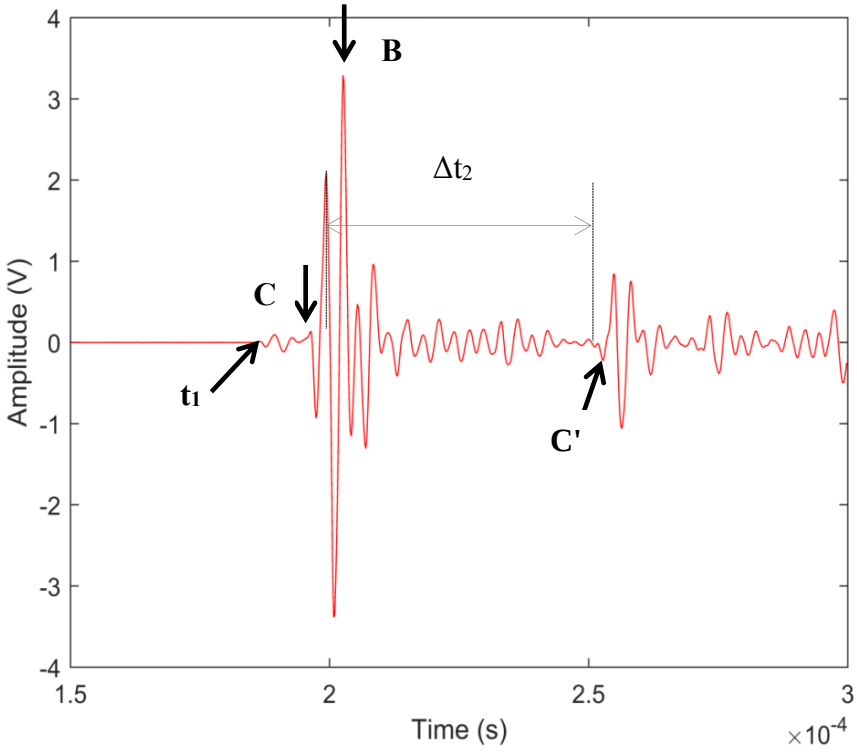

b. Sensor 2

Figure 5-11: *Typical raw AE time series recorded at (a) S_1, (b) S_2 on the solid cylinder (first wave arrival).*

The time difference $\Delta t_1 = 5x10^{-5}$s corresponds to a distance of 0.3m at P-wave speed and 0.16m at S-wave speed. One possible interpretation is that the pulses arriving at C and C'

are P-waves, which have travelled vertically through the cylinder reflecting back from the lower surface. A second possible explanation (which accords with section 5.2) is that the pulses arriving at C and C' are S waves which have travelled across the surface and reflected back from the edge.

Figure 5.12 shows power spectra of the time series segments highlighted in Figure 5.11 for S_1 and S_2 on the solid cylinder. The two examples shown suggest that there are some features within the spectra that are not merely associated with the sensor response, and those analysed further in the next section.

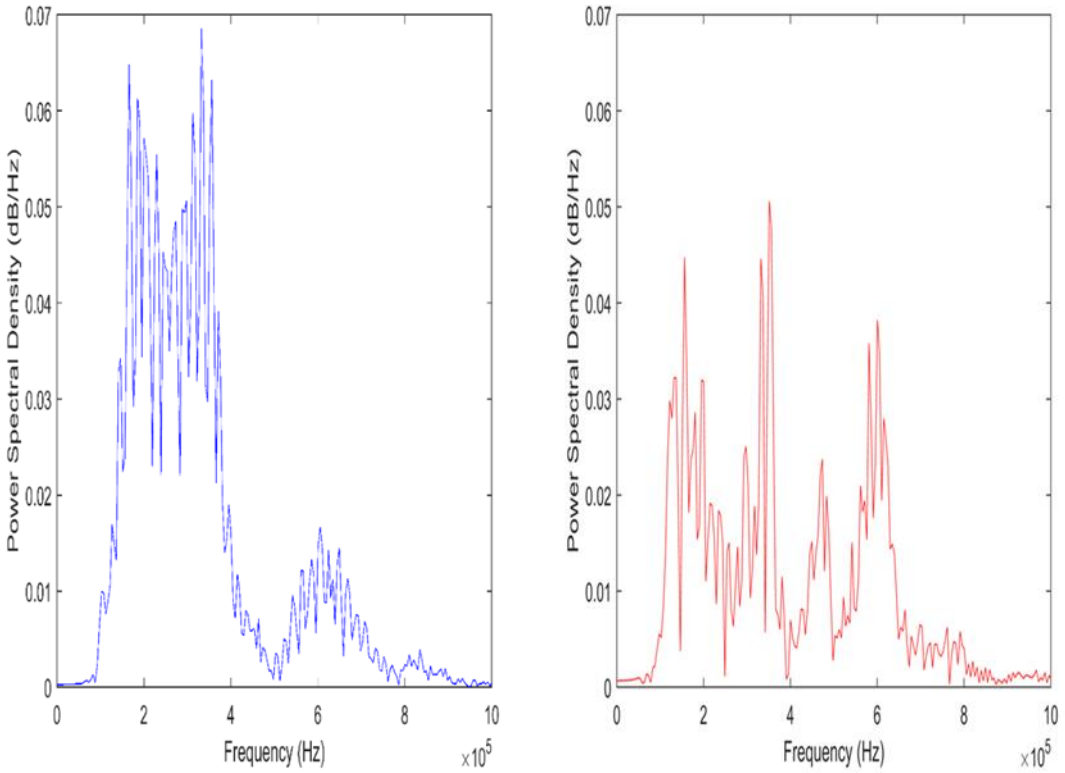

Figure 5-12: *Power spectra of time series segments highlighted in Figure 5.11 for S_1 and S_2 on the solid cylinder*

5.5 Discussion of Reference Tests

The temporal structure of the first 10ms in the simulated (Figure 5.9) and measured (Figure 5.11) responses is rather similar, with a low amplitude, faster moving lower frequency component, followed by a higher amplitude, higher frequency pulse. Beyond this, the simulated signals remain at high amplitude and this is probably because the attenuation associated with reflections is absent from the simulation model.

The speeds of the two waves in the simulation can be easily estimated to be around $3000ms^{-1}$ and $1250ms^{-1}$ if both are travelling across the surface from source to sensor. The first of these speeds corresponds closely to the Rayleigh wave speed, but the second does not correspond to any pure modal wave speed.

However, the time of arrival (around $5 \times 10^{-5}s$) corresponds to a P-wave travelling a distance of around 0.3m, essentially from the top to the bottom of the cylinder and back again. This would also accord with the first of the two explanations given for Figure 5.13. These observations are independent of unload rate in the simulations as the two arrival times are unaffected by unload rate.

The entire records, examples of which are shown in Figure 5.1 and 5.7 will therefore contain a mixture of modes and reflected waves. For the experimental records, since the sensors are similarly positioned, a comparison of energy (as the RMS of the complete record) and the power spectrum can be used to indicate the consistency of the 20 pencil lead breaks and the consistency in response of the two sensors as described in section 5.4.

To further analyse the spectra shown in Figure 5.12, three new bands were chosen (by inspection); below 200 kHz (low frequency, LF), 200-500 kHz (medium frequency, MF) and above 500 kHz (high frequency, HF), giving three power values; P_{LF}, P_{MF} and P_{HF}, and three indicators as proportions of the total power:

$$f_i = \frac{P_i}{P_{LF} + P_{MF} + P_{HF}} \text{ , where } i \text{ is LF, MF or HF}$$

A summary of the total power frequency structure of all of the experimental and simulated data on the solid cylinder for sensor position S_1 is shown in Table 5.1. The experimental values are based on the average power values for the 20 measurements. Similarly, fractions have been calculated for the simulations for S_1 and each of the unload rates. As sensors S_1 and S_2 are nominally equidistant, the total power frequency structure for S_1 and S_2 are exactly the same but slightly different for the experiments. The condition codes are introduced for the simulations for ease of reference.

Condition	Code	f_{LF}	f_{MF}	f_{HF}	P_{tot}
Experiment, sensor 1	ES_1F	0.3881	0.4328	0.1791	3.2289
Experiment, sensor 2	ES_2	0.3785	0.4882	0.1333	4.0682
Simulation, unload rate 1	$Sim1S_1R$	0.3891	0.5681	0.0428	0.0257
Simulation, unload rate 2	$Sim2S_1R$	0.3935	0.565	0.0415	0.4193
Simulation, unload rate 3	$Sim3S_1R$	0.408	0.5548	0.0373	0.754
Simulation, unload rate 4	$Sim4S_1R$	0.4338	0.5336	0.0326	0.9985
Simulation, unload rate 5	$Sim5S_1R$	0.4693	0.5007	0.0299	1.1389
Simulation, unload rate 6	$Sim6S_1R$	0.5121	0.4578	0.0301	1.1835

Table 5-1: *Total signal power and fractions of power in the three frequency bands at S_1 for both experiments and simulations. Unload rate increases from 6 (lowest) to 1 (highest)*

Figure 5.13 shows a comparison of the measured (E) and simulated (Sim) power spectral content at sensor position S_1 for the shorter time series where f_1, f_2 and f_3 are the fractional power in the LF, MF and HF bands. It can be seen that, at longer unload times, the lower frequencies seem to shift and this is consistent with the expected higher frequencies generated as a step unload is approached.

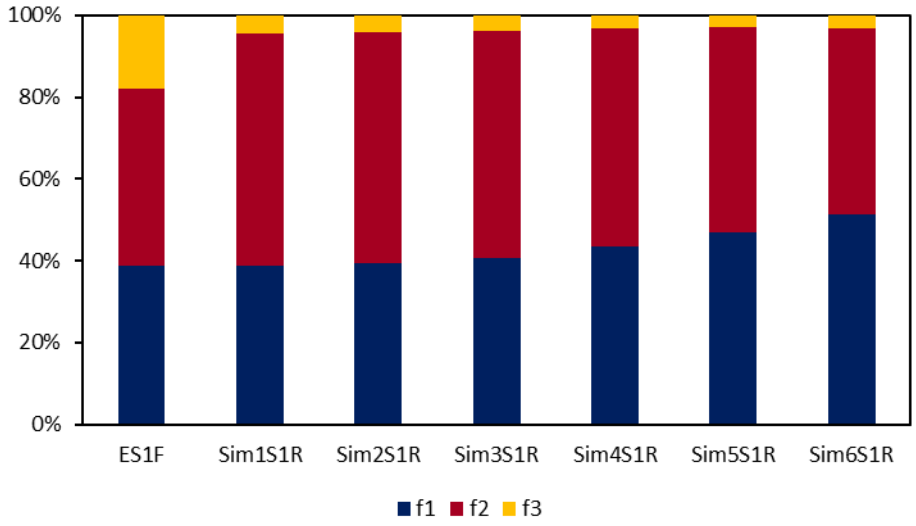

Figure 5-13: *Comparison of measured (E) and simulated (Sim) power spectral content at sensor position S_1 and time series segments (R) and (F). (f_1, f_2 and f_3 fractional power in LF, MF and HF bands)*

Also, given that the experimental spectra have generally less low frequency content than the simulations this would suggest that the fastest unload rate is the most appropriate of those considered in this work, although the lower content in the HF band for the simulations is partly an artefact of the time-step used in the simulations.

The shifts in spectral content between LF and MF bands are shown in Figure 5.14, where it can be seen that the ratio of low to medium frequency decreases consistently with the unload rate. This analysis, which disconts the HF band, suggest that the lower unload rates (between 4 and 5) might be closer to the observed situation.

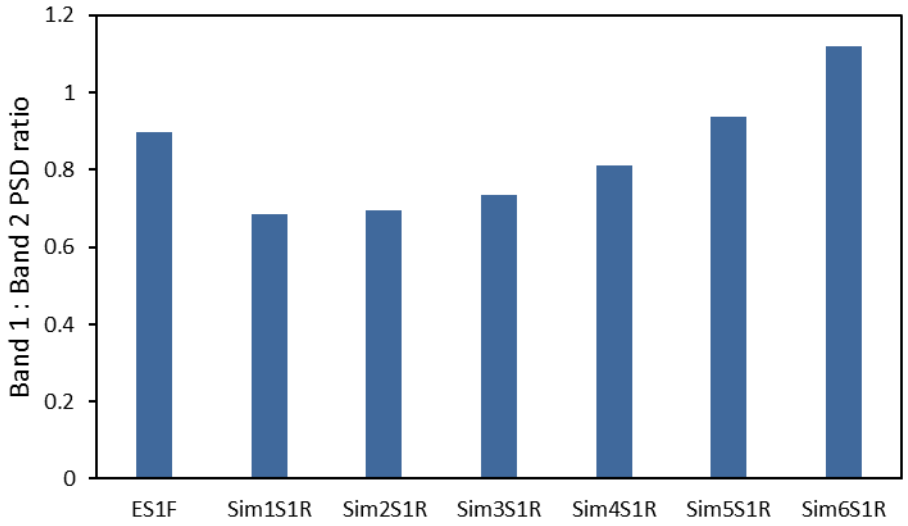

Figure 5-14: *Comparison of measured (E) and simulated (Sim) low frequency power spectral ratio (P_{LF}/P_{MF}) for each of sensor positions S_1 and time series segments R*

Figure 5.15 shows the effect of unload rate on total simulated power content of the signal at S_1. It can be seen that the total power increases significantly from the fastest rate while the slope decreases towards the slowest unload rates. It might also be noted that the total power at the highest unload rate is around 60 times lower than that at the lowest rate.

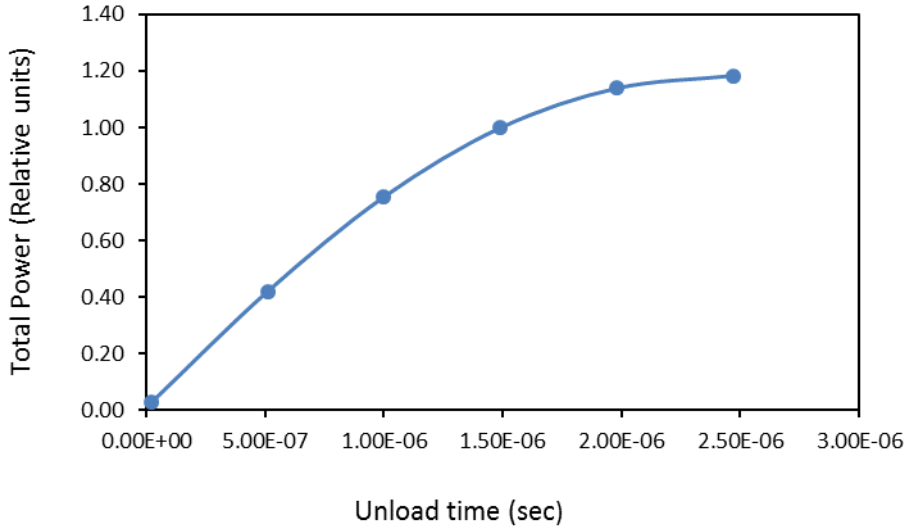

Figure 5-15: *Simulated power vs unload time*

5.6 Summary of Findings on Reference object

This section presents summary of findings on the reference block, which can be carried over into the rest of the thesis. The findings are in four broad areas; sensor calibration, dropped object behaviour, comparison with analytical solutions and comparison between simulation and experiment.

5.6.1 The inter-sensor calibration was carried out against a background of the existing calibration certificates, published work [146] and the sensors and data acquisition system used here. The summary is that S_2 reads slightly higher than S_1 and this agrees with the calibration certificate. There is also significant variability when sensors are removed and replaced in the same position, even on a relatively flat surface. The variability associated with individual pencil lead breaks is small relative to the effect of removal and replacement.

5.6.2 It is clear that detailed analytical solutions are of limited use for any more than general guidance on the interpretation of simulated or measured AE responses to step unloads. It seems that, in the reference object, with sensors equidistant, and on the same face as the source, the first wave to arrive is a lower amplitude, lower frequency Rayleigh wave. Superimposed on this are pulses of higher frequency corresponding to subsequent reflections of a P-wave from the lower surface of the cylinder.

5.6.3 The simulated and measured signals on the reference object exhibit similar behaviour in the first 25-30μs.Thereafter, the measured signals are much cleaner, and this

is most likely associated with the energy losses associated with reflections, for which there is no provision in the simulations.

5.6.4 The frequency domain of the simulations shows an artificial cut-off at around 400 kHz, associated with the time-step chosen, a necessary compromise between simulation precision and computation time. Notwithstanding this, there is a shift towards higher frequencies in the simulations as the unload rate increases, but this is accompanied by a significant drop in total signal power.

5.6.5 Comparison of the ratio of mid to low frequency power between simulated and measured signals would suggest that an appropriate unload rate is around the lower middle of those chosen for study here.

Chapter 6 - Experimental and Simulation Results for Impulsive Sources on Pipe

This chapter presents the simulation and experimental results for impulsive sources on the larger and more complex structure of a pipe. First of all, the results of the preliminary FE simulations are discussed and compared with those from the simpler solid cylinder, with a view to establishing the general structure of the AE.

6.1 Preliminary FE Simulations on Pipe

The aim of the preliminary set of FE simulations described here was to give an initial idea of the expected changes in the acoustic emission signal recorded at two virtual sensor positions along the length as the unloading rate at the source changes

It was important to establish reasonable time steps and model size to give a good trade-off between simulation precision and computational time so that an appropriate experimental object could be chosen. Three lengths of virtual pipe, 2.5, 5 and 10m were used with virtual sensors at various positions from the source (Table 6.1). The source was simulated as a 100N force spread over a surface area of $0.003m^2$ with three different time profiles, the key variable being the rate of unloading, with unloading times 10^{-9}s, 10^{-8}s, and 10^{-7}s, respectively, Figure 6.1.

The FE simulation was then used to calculate the Cauchy stress-time history separately for three sensor positions for each of the three pipe lengths and their respective unloading rates, giving a total of 27 stress time histories. In order to limit the computation time and also avoid excessive complication due to reflections from the ends of the models, the pipe was fixed at the ends (Figure 6.2 – see section 3.3.3), and a time step of 1×10^{-7} with a simulation time of 2×10^{-3}s was used for the FE simulations.

Pipe length (m)	**Sensor position (m from source)**		
2.5	0.5	1	1.5
5	1.5	2.5	4
10	3	5	9

Table 6-1 : Sensor positions for pipe simulation

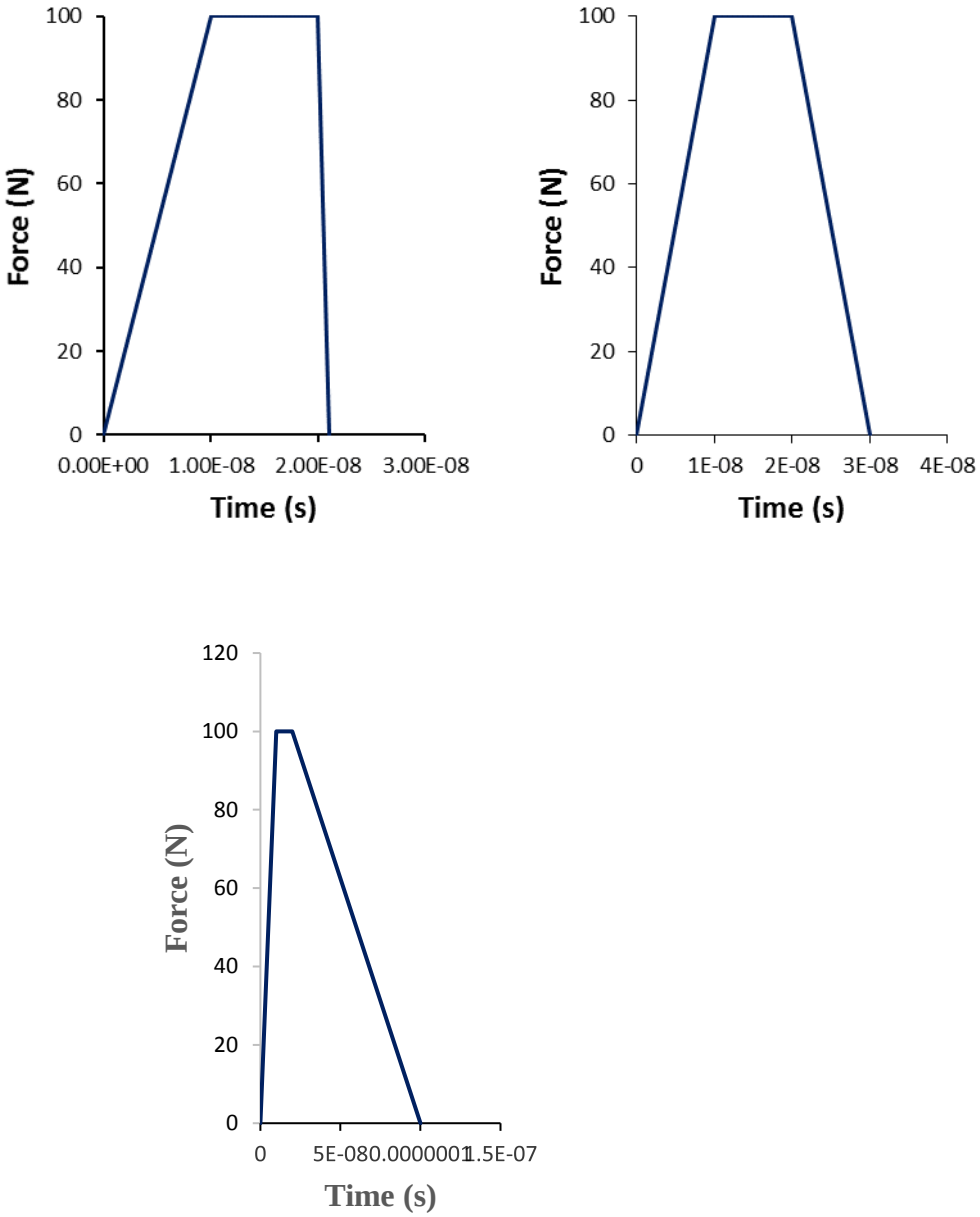

Figure 6-1: *Force vs time profiles for preliminary source simulation*

The fastest unload rate was studied and analysed in this work as preliminary studies showed that there is no appreciable difference between the unload rate studied and the other unload rates.

Figures 6.3 to 6.5 show the time series of the fastest unload rate on the 2.5m, 5m and 10m pipes respectively. As can be seen, the time series consists of a lower frequency, lower amplitude component, which precedes the arrival of a higher frequency, higher amplitude component. The length of the lower frequency component increases as the source-sensor

distance increases, and its arrival time also increase. An estimate for each of the wave speeds was made for the fastest of the unload rates for each of the pipe length and sensor positions and the results are shown in Table 6.2.

The speed of the faster wave appears to be about 5000ms^{-1} if moving over the surface. Similarly, the speed of the slower wave appears to be about 1700ms^{-1}.

Pipe length (m)	**Source – sensor distance** (ms^{-1})	**Fast wave speed** (ms^{-1})	**Slow wave speed** (ms^{-1})
2.5	0.5	5385	1762
	1	5265	1602
	1.5	5160	1568
5	1.5	5896	1888
	2.5	5720	1801
	4	5417	1797
10	3	5647	1896
	5	5492	1613
	9	5280	1582

Table 6-2: *Wave speeds for the fastest unload rates for each of the pipe length and sensor positions*

Figure 6.6 to 6.8 show spectra for short, medium and long source - sensor distances for the fastest unload rate for each of the pipes. Comparing with the respective time series indicates a move from mixed slow plus fast waves to predominantly fast waves. As the source – sensor distance increases, there is a shift in spectral content from the low frequency peak (around 100 kHz) towards the higher frequency peak (around 200 kHz). This would suggest that the fast wave has a higher frequency than the slower wave.

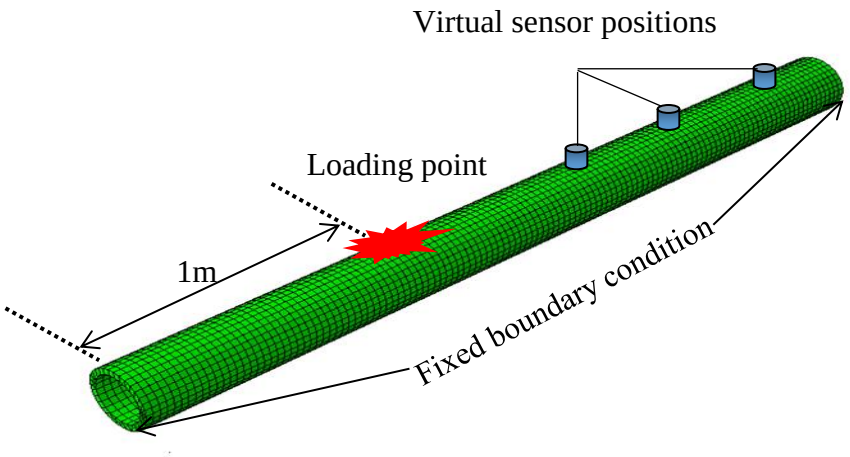

Figure 6-2: Schematic diagram of preliminary pipeline model

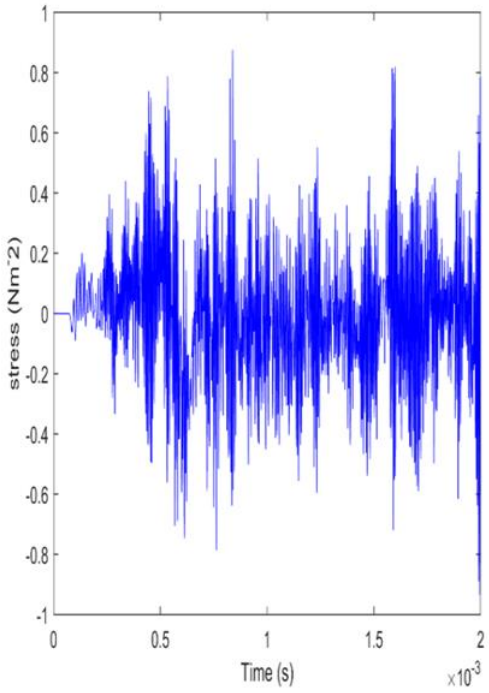

a.

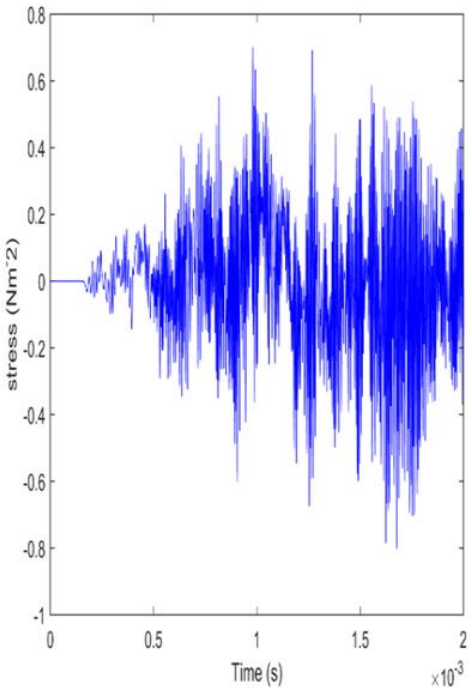

b.

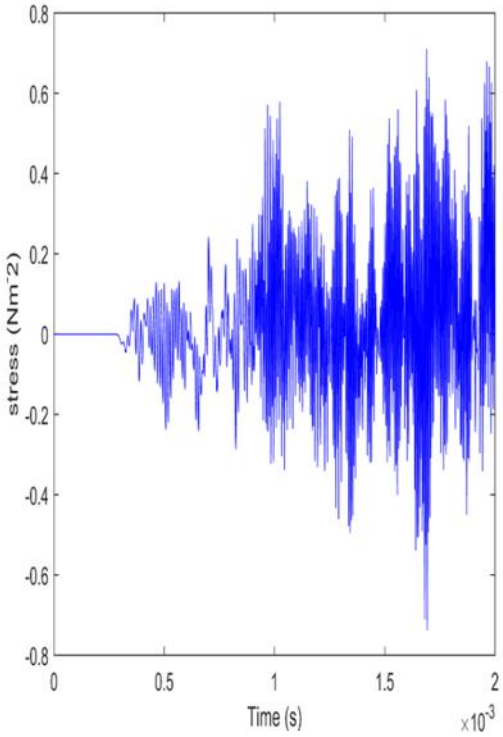

c.

Figure 6-3: *Time series of the fastest unload rate on the 2.5m pipe at virtual sensor distances a) 0.5m b) 1m and c) 1.5m*

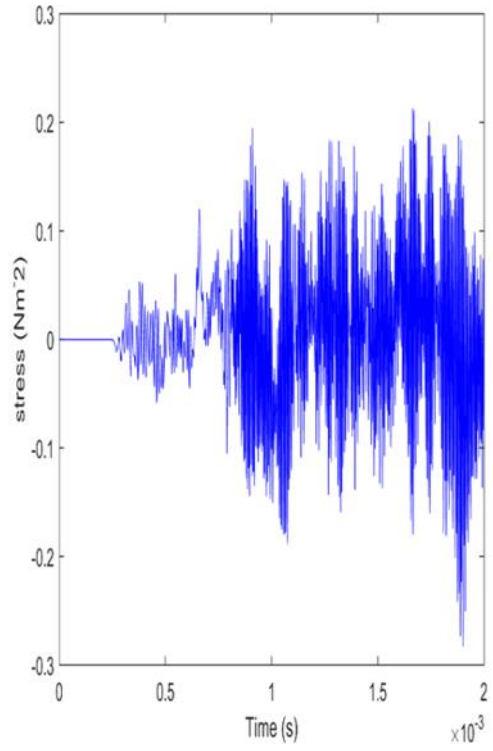

a.

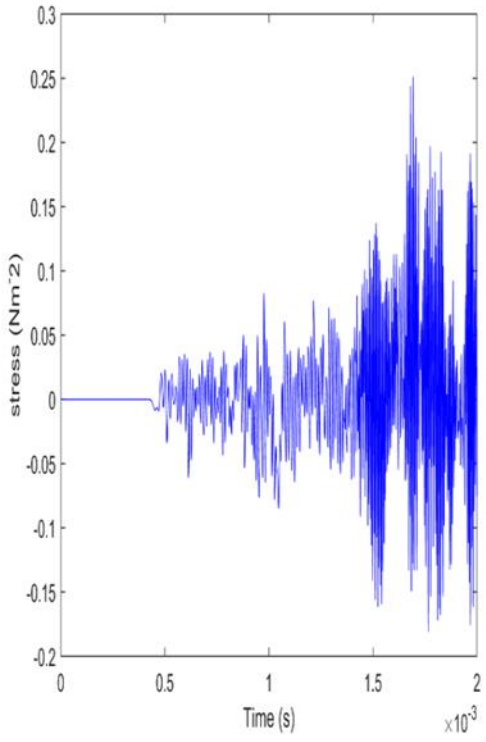

b.

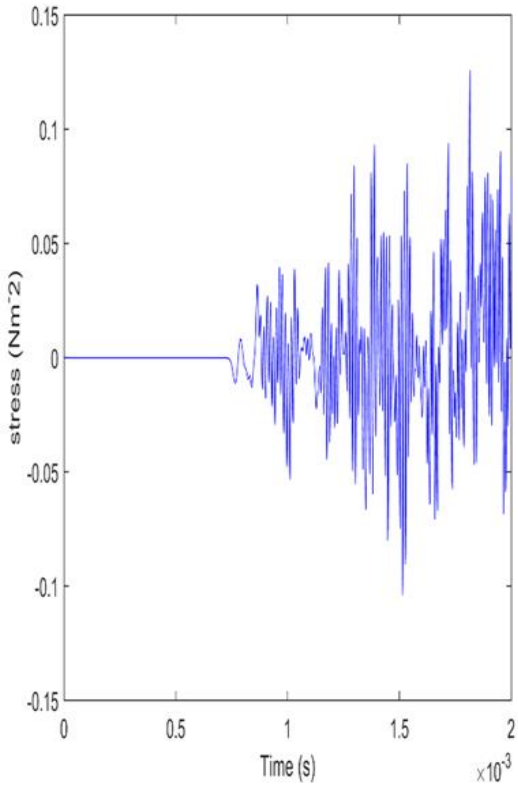

c.

Figure 6-4: *Time series of the fastest unload rate on the 5m pipe at virtual sensor distances a) 1.5m b) 2.5m and c)4m*

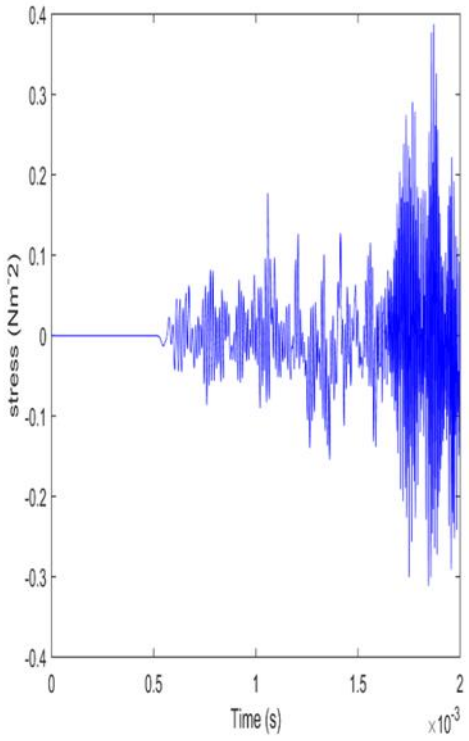

a.

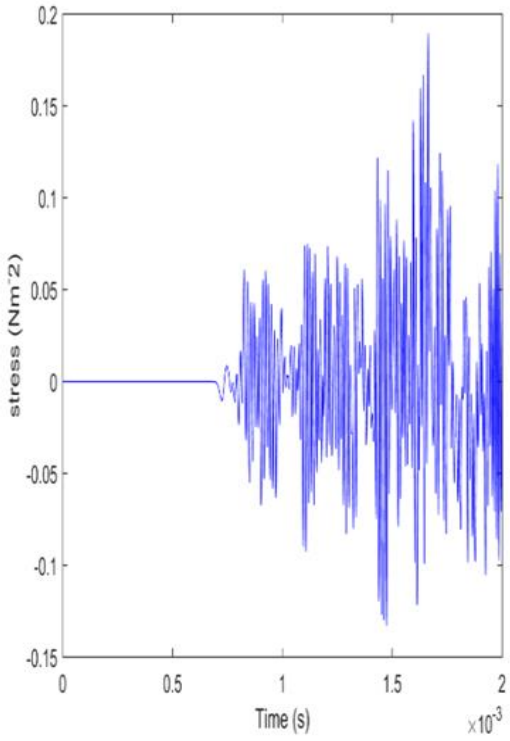

b.

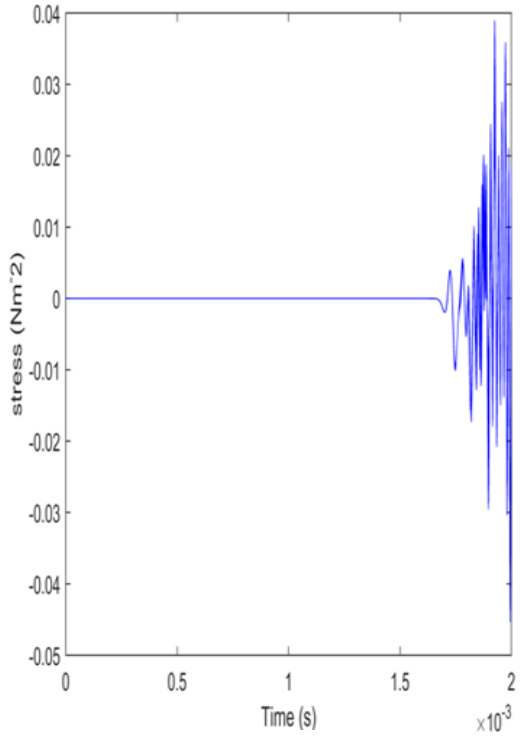

c.

Figure 6-5: *Time series of the fastest unload rate on the 10m pipe at virtual sensor distances a) 3m b) 5m and c)9m*

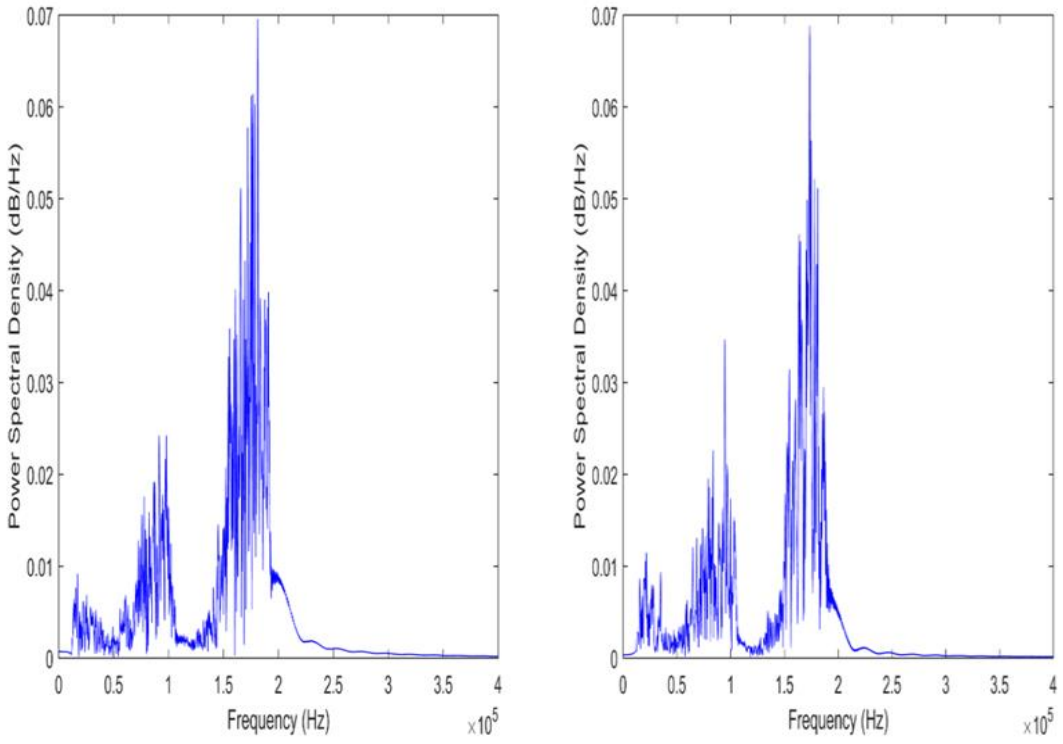

a.

b.

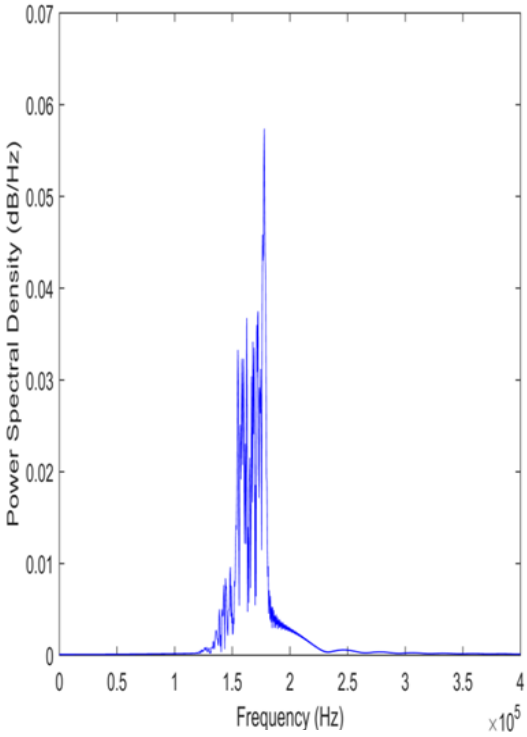

c.

Figure 6-6: *Spectra for short, medium and long source sensor distances for the fastest unload rates on the 2.5m pipe at virtual sensor distances a)0.5m b)1m and c)1.5m*

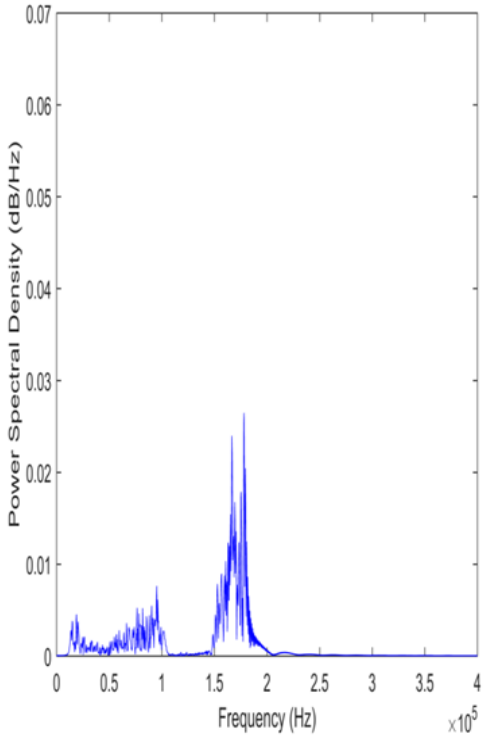

a.

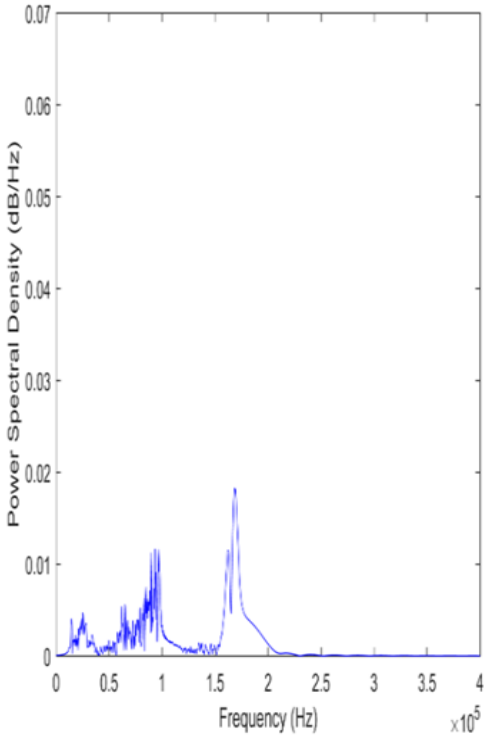

b.

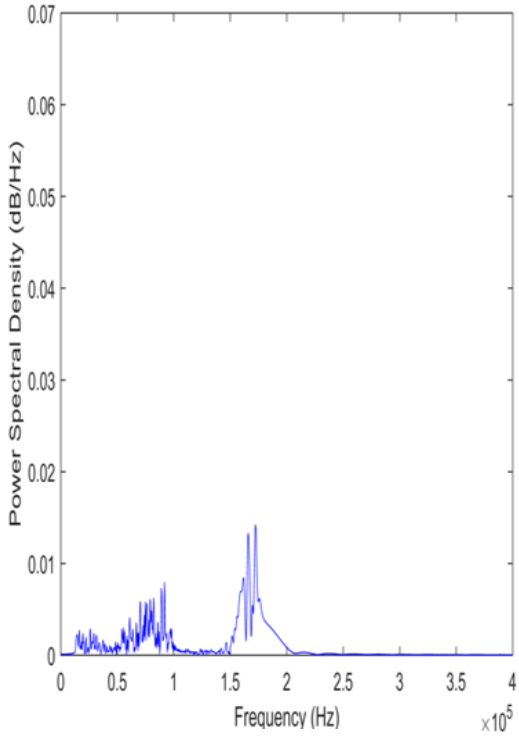

c.

Figure 6-7: *Spectra for short, medium and long source sensor distances for the fastest unload rates on the 5m pipe at virtual sensor distances a) 1.5m b) 2.5m and c)4m*

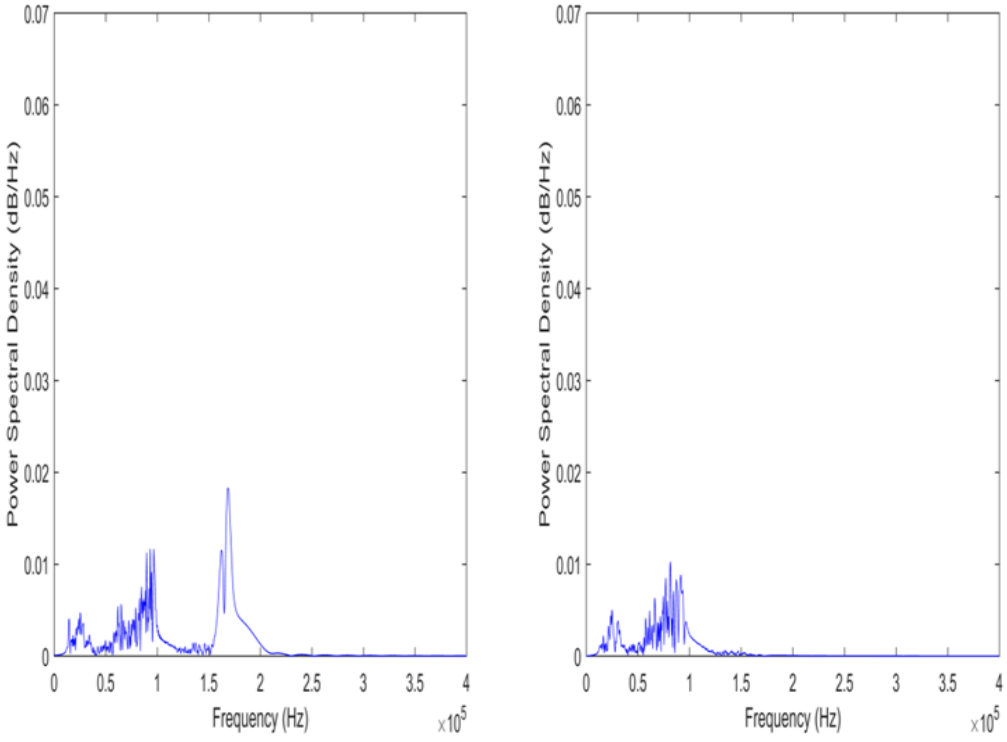

a. b.

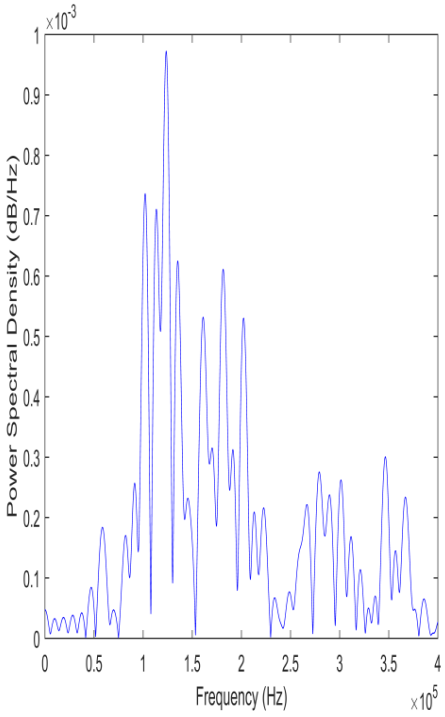

c.

Figure 6-8: *Spectra for short, medium and long source sensor distances for the fastest unload rates on the 10m pipe at virtual sensor distances a) 3m b) 5m and c) 9m*

6.2 Main PLB Simulation on Pipes and Comparison with Experiments

The second set of PLB simulations on pipes was carried out to establish the extent to which a simulation of a near-instantaneous AE source could represent a measurement using virtual sensors placed at two distances from a PLB source on a pipe. To do this, the analytical focus was shifted to the first few μs of simulated and measured AE on a shorter length of pipe (Figure 6.9) with a view to assessing the best simulated unload rate to match the observed signals. Just as with the reference object reported in Chapter 5, parallel measurements and simulations of AE propagation from a PLB (source) to sensors placed at the same positions as the simulations were carried out. As described earlier, the elastic steel pipe on simple supports was subjected to a pressure loading similar to that expected from a PLB at a distance 0.2m from one end. The source was simulated as a 100N force spread over a surface area of $0.003m^2$, applied as a steep ramp over 1×10^{-8}s and unloaded in times of 2×10^{-8}s, 5×10^{-7}s, 1×10^{-6}s, 1.5×10^{-6}s, 2×10^{-6}s and 2.5×10^{-6}s. Two 'virtual AE sensors' were set at positions corresponding to those shown in figure 6.9.

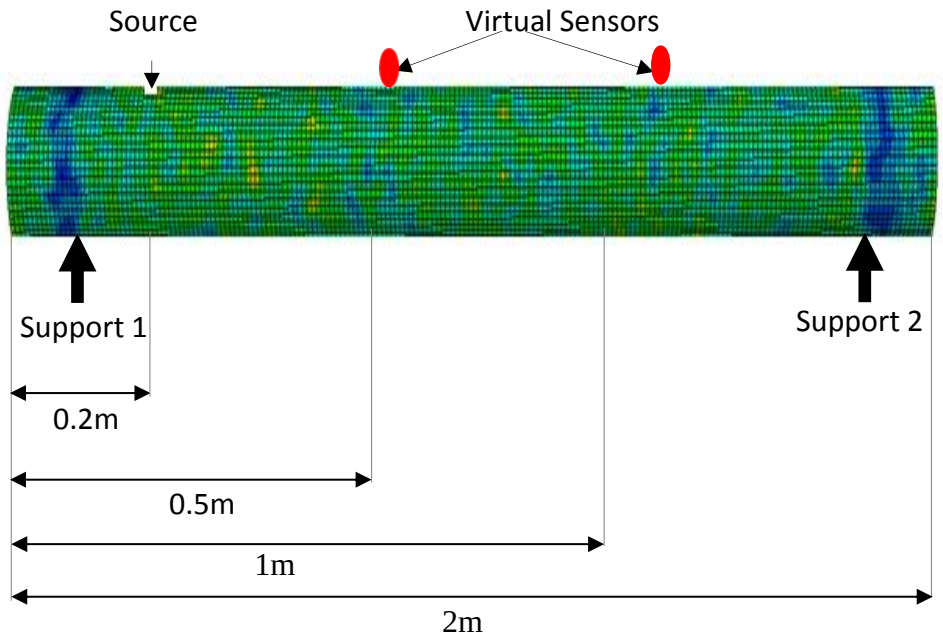

Figure 6-9: *The FEA pipe model showing the Cauchy stress after 0.02s*

In fairly small pipe lengths, it would be expected that the waves would be reflected several times within the record, and so the focus was on the first few tens of microseconds so as to avoid the complexities of (largely unknown) reflection coefficients.

Figures 6.10 and 6.11 show typical raw AE records and the corresponding power spectra at the two sensors. An S-wave will travel the full length of the pipe in around 6×10^{-4}s, so it is clear that the system's ring-down time corresponds to around 20 traverses of the length of the pipe. As with the preliminary measurements, the power spectra for the entire record appear to show a shift from lower frequencies to higher frequencies as source-sensor distance increases with a major peak at just below 200 kHz. There are several other peaks, the most noticeable of which is at just below 400 kHz, although there is also some activity at around 150 kHz. The 200 kHz and 400 kHz peaks are both associated with the sensor frequency response shown in the appendix, although their relative magnitudes may be indicative of changes in the signal frequency content. To obtain a rough measure of this, the spectra were divided into two bands; low frequency between 100 kHz and 400 kHz and high frequency between 400 kHz and 1 MHz and the relative power calculated by integrating the spectra and determining the ratio between the two bands. The ratio of high-frequency to low-frequency power for the two sensor positions over the 20 records was 0.1516 with an SD of 0.0554 for S_1 and 0.1702 with an SD of 0.0507 for S_2. An Anova was carried on these data sets and the F-Value was 1.2 compared with $F_{critical}$ of

4.1 which shows that there is no significant difference in frequency content at the two sensor positions over the 20 records, to the 5% confidence level.

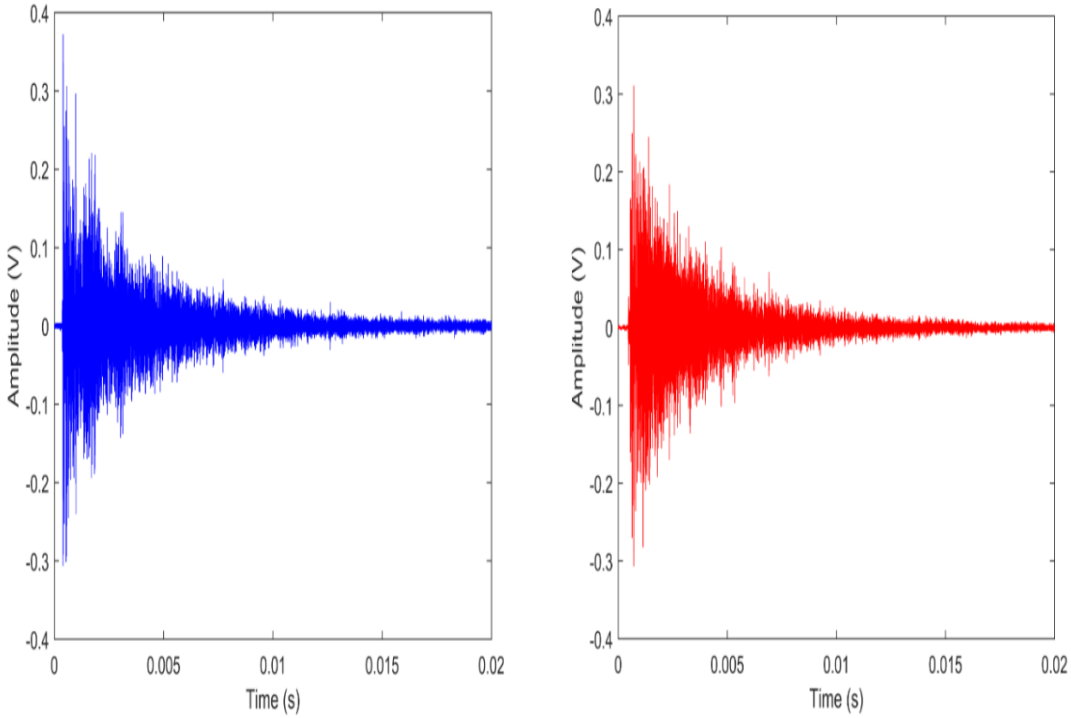

a. Sensor 1 b. Sensor 2

Figure 6-10 : *Typical raw AE time series recorded at (a) S_1, (b) S_2 on the pipe (full record)*

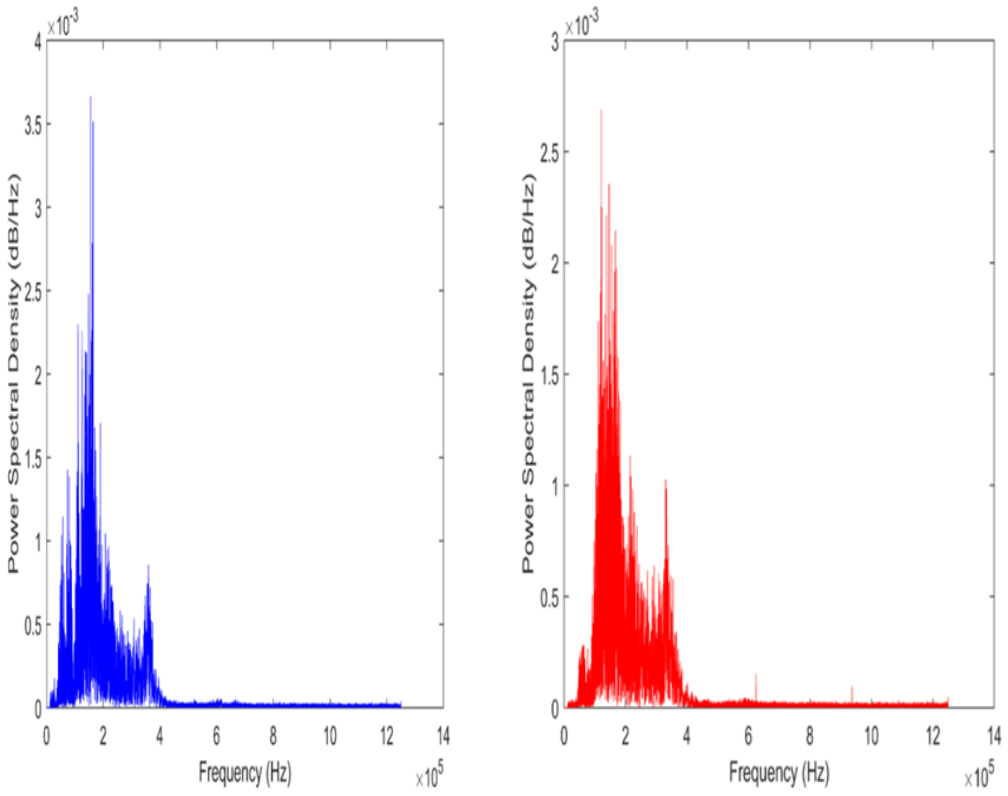

a. Sensor 1 b. Sensor 2

Figure 6-11: *Power spectra of entire time series shown in Figure 6.10 for (a) S_1, (b) S_2 on the pipe*

Figure 6.12 shows the 250 μs around first wave arrival for each of the two sensors for a typical example PLB. It can be seen that the first arrival at S_1 is characterized by a low amplitude component, followed by a high amplitude component, which contains the peak amplitude (t_p), whereas an apparently similar feature at S_2, also labelled, is preceded by a medium amplitude component. The low amplitude component appears to increase in length between S_1 and S_2, showing that it is traveling faster than the medium amplitude, and the medium amplitude component also seems to be moving faster than that carrying the peak.

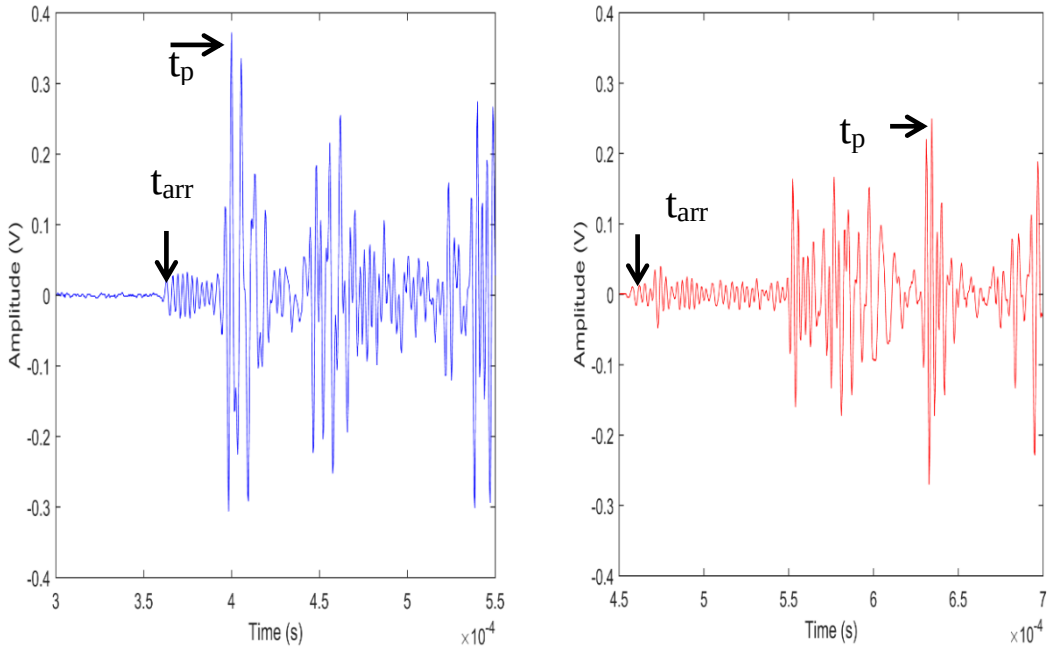

a. Sensor 1 b. Sensor 2

Figure 6-12 : *Raw AE time series recorded at (a) S_1, (b) S_2 on the pipe (first wave arrival)*

In order to have a consistent way of identifying arrival, a thresholding technique [83] was adopted using S_1 (the trigger sensor). This entailed calculating the mean and standard deviation (SD) of the first 1000 points (pre-trigger) and identifying arrival as the point at which the amplitude first crosses the mean ± 5SD, shown as t_{arr} on Figure 6.12a. Applying this same thresholding technique to S_2 gives a point (t_{arr} on Figure 6.12b) which, as expected, is later than the corresponding arrival at S_1. Dividing the distance between the two sensors by the arrival time difference for each of the 20 lead breaks yielded an average apparent wave speed of 5076ms^{-1} with a standard deviation of 189ms^{-1}, somewhat lower than the P-wave speed and somewhat higher than the S-wave speed (ms^{-1}) but consistent with the first arrival speed in Tables 6.2 for the preliminary pipe experiments and with first arrival speed on the cylinder.

To provide a good comparison with the simulations, it was necessary to condition the S_1 and S_2 signals to have the same time-base. As time in Figure 6.12 was measured from the start of the pre-trigger and that for the simulation was measured from when the source was activated, it was essential first to assess the departure time (from the source) for the arrivals at S_1 and S_2, and this was achieved by subtracting the time taken for the wave to travel from the source to the sensor, using the speed determined from the arrival time differences at the two sensors. Figure 6.13 shows the re-based time series (corresponding to Figure 6.12) where time, t′, is now measured from departure from the source.

Since the simulations did not incorporate any mechanism for damping or for loss of energy on reflection, separating the effects of damping from those due to losses on reflection was achieved by ensuring that both time-series were truncated before any reflection arrived at the real or virtual sensor. Assuming circular symmetry of the source, it was expected that the first reflected wave will arrive at a given sensor after travelling the (shorter) distance to the end of the pipe, back again, plus the distance from the source to the sensor, i.e. a total of 0.7m, giving an arrival time since departure from the source for the particular example considered of 1.35×10^{-4} sec for S_1 and a total of 1.2m, giving an arrival time of 2.32×10^{-4} sec for S_2, shown as t'_{refl} in Figures 6.13a and 6.13b, respectively.

However, this analysis has brought up a new issue as it is obvious that the portion of the signal which included the peak for S_2 (t'_p in Figure 6.13b) was not the same feature identified as the peak in Figure 6.12b (t_p). Therefore, in order to attain a compromise between characterising these different components and reducing the effect of reflections, a second wave speed was determined using the time difference between the two t_p values, as identified in Figure 6.12b, giving a mean "slow" wave speed of $2000ms^{-1}$ with a standard deviation of 478, corresponding with the slow wave speed identified in the preliminary simulations in Table 6.2. This allows the time of arrival of the first reflection of the component containing t_p in Figure 6.12 to be determined. For example, this second return time is shown as $t'_{p,refl}$ in Figure 6.13. Accordingly, two segments of the time series were identified for diagnostic purposes; the segment between t'_{arr} and t'_p (which includes mostly the faster-moving component) and the segment between t'_p and t'_{refl} (which includes both the faster-and slower-moving components).

The RMS values for the "fast" and "slow" segments are shown in Table 6.3

	Fast segment (t'_{arr} to $t'_{p,}$)	Slow segment (t'_p to $t'_{p,refl}$)
S_1	0.0705 ± 0.012	0.1325 ± 0.0426
S_2	0.1340 ± 0.039	0.1201 ± 0.039

Table 6-3 : RMS values for the "fast" and "slow" segments in truncated time series

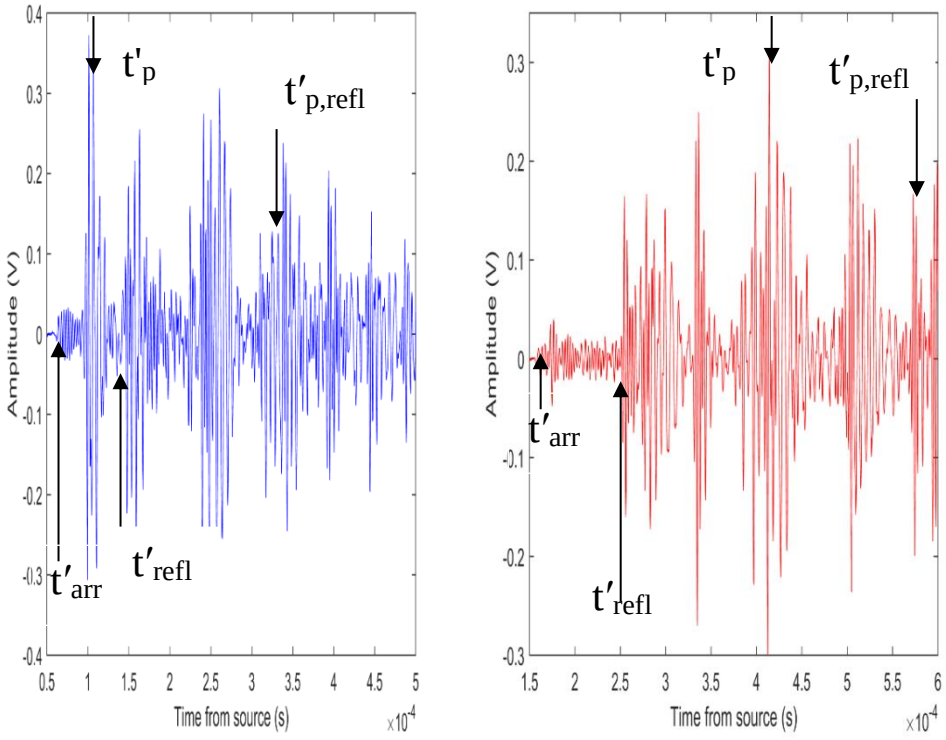

a. Sensor 2 b. Sensor 2

Figure 6-13: *Segments of typical AE time series recorded at S_1 and S_2 on the pipe, identifying reflection arrivals for slow and fast wave packets*

Figure 6.14 shows the corresponding spectra for the segments shown in Figure 6.13. Notwithstanding the low resolution for the fast segment at S_1 (due to its short duration), the spectra are similarly narrow to Figure 6.11, although there is a little more high-frequency content, again with S_2 showing a slightly higher power in the 200-400 kHz range. A division of the spectrum into two bands did not capture some of the differences in the spectra visible in Figure 6.14. Therefore, by inspection, three new bands were chosen; below 200 KHz (low frequency, LF), 200-500 kHz (medium frequency, MF) and above 500 kHz (high frequency, HF), giving three power values, P_{LF}, P_{MF} and P_{HF}, and three indicators as proportions of the total power:

$$f_i = \frac{P_i}{P_{LF} + P_{MF} + P_{HF}}$$

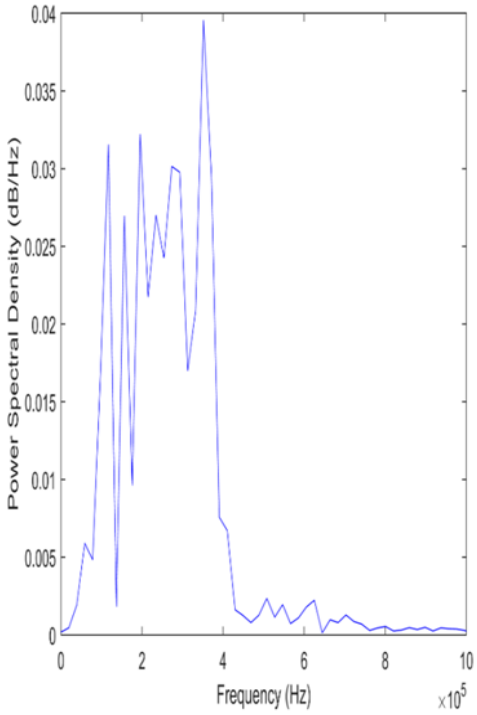

a. Fast segment at S_1

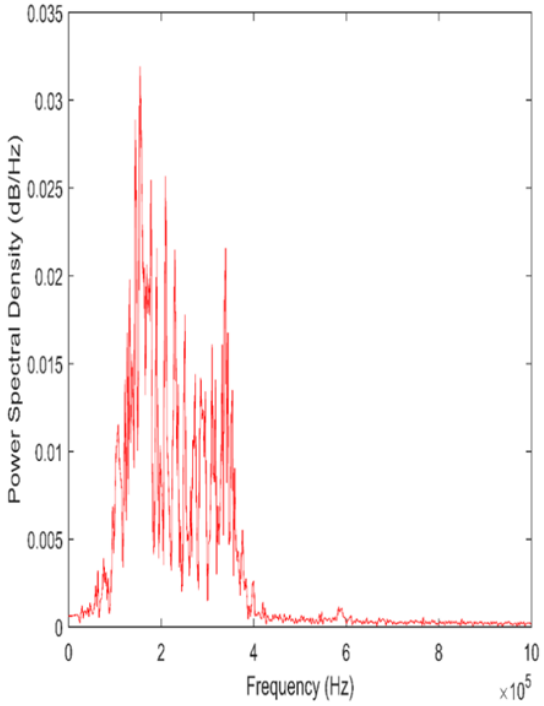

b. Fast segment at S_2

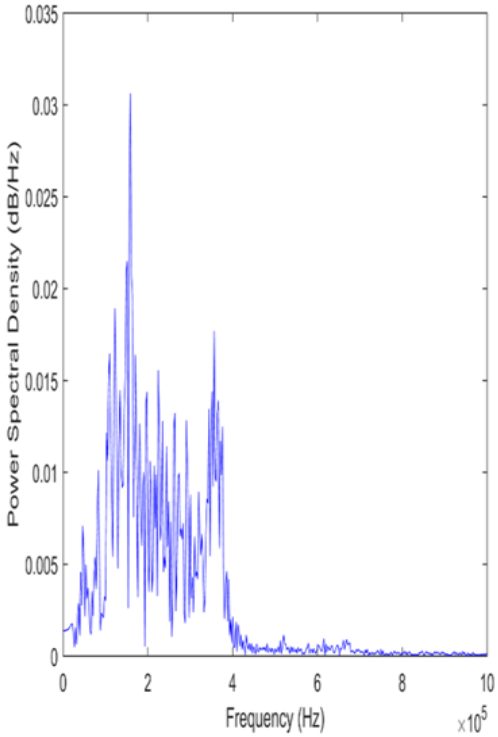

c. Slow segment at S_1

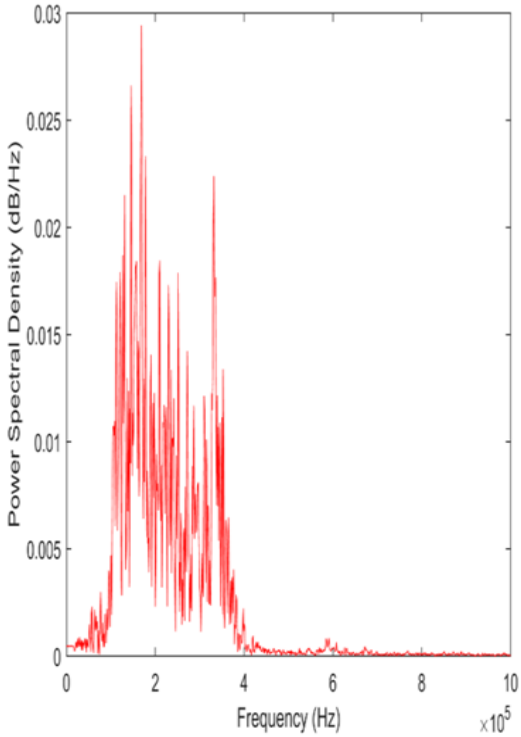

d. Slow segment at S_2

Figure 6-14 : *Power spectra of time series segments highlighted in Figure 6.13 for S_1 and S_2 on the pipe*

Figure 6.15 shows a typical plot of the simulated stress time series at the two virtual sensor positions for the first 20ms. As anticipated, this shows none of the damping seen in the equivalent experiment (Figure 6.10).

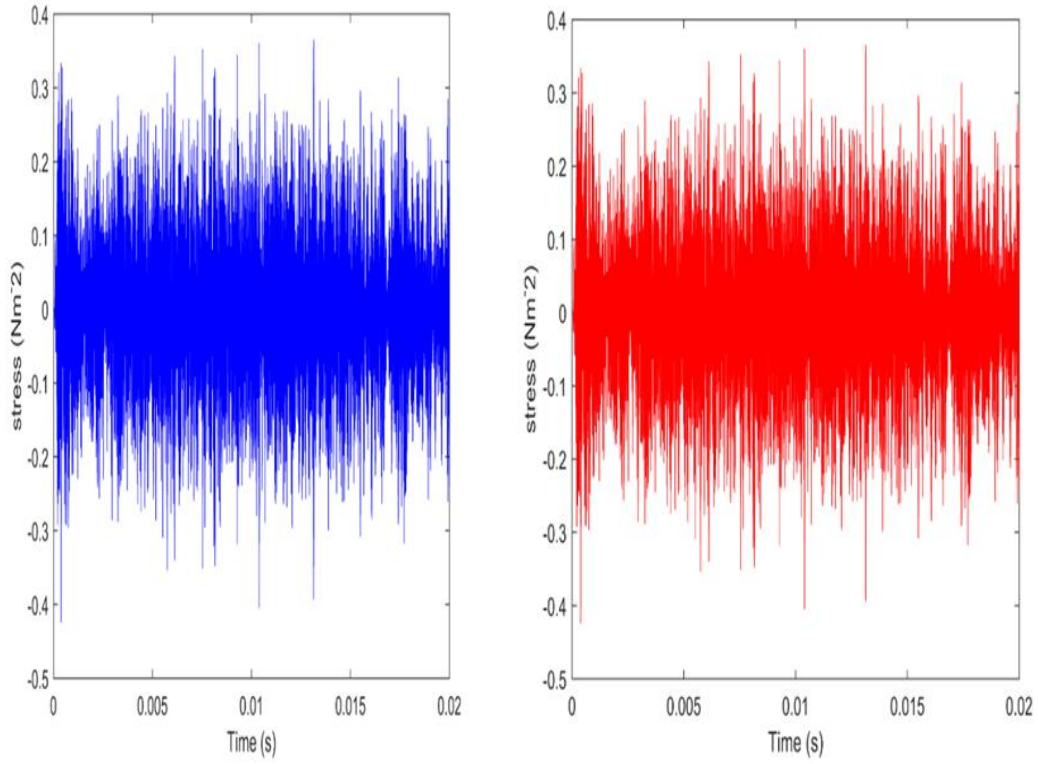

a. Sensor 1 b. Sensor 2

Figure 6-15 : *Raw time series of Cauchy stress (0.4M samples per second) for virtual sensors at 0.5m and 0.7m from the simulated source on a pipe unloading in 2.46 × 10^{-6} s*

As can be seen, by comparing Figures 6.16 and 6.11, the power spectrum of the full record for the simulated series is a narrower band than either of the experimental ones. Two main frequencies are present at the position of S_1, one at around 100 kHz and the other at around 170 kHz, and, apart from the observable difference in total power, the spectra are near-identical over the range of unloading rates with a very sharp cut-off at just above 200 kHz.

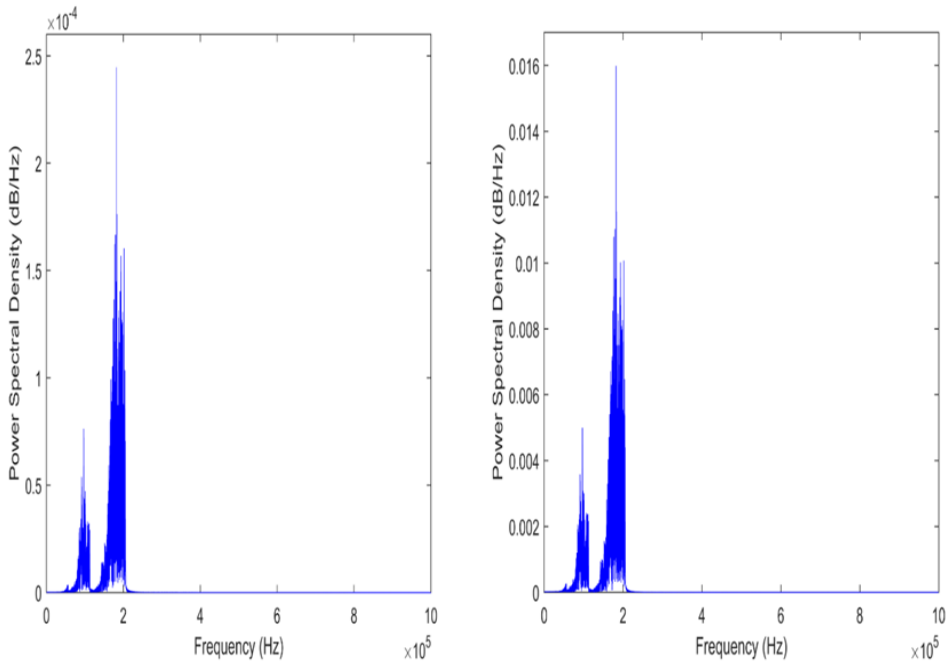

a. Unload time 2.1×10^{-8}s b. Unload time 2.5×10^{-6}s

Figure 6-16 : *Power spectrum of entire simulated time series shown in Figure 6.21 for (a) the fastest unload rate and (b) the slowest unload rate*

Figure 6.17 shows a magnified view of the part of the simulated time series corresponding to the key events identified for the experiment. There is a certain consistency in both time series, although the simulated wave is much "cleaner". The spectra for the simulated segments (Figures 6.18 and 6.13) are similar to those shown in Figure 6.16, but there are major differences between the sensor positions, albeit less so for the unload rate.

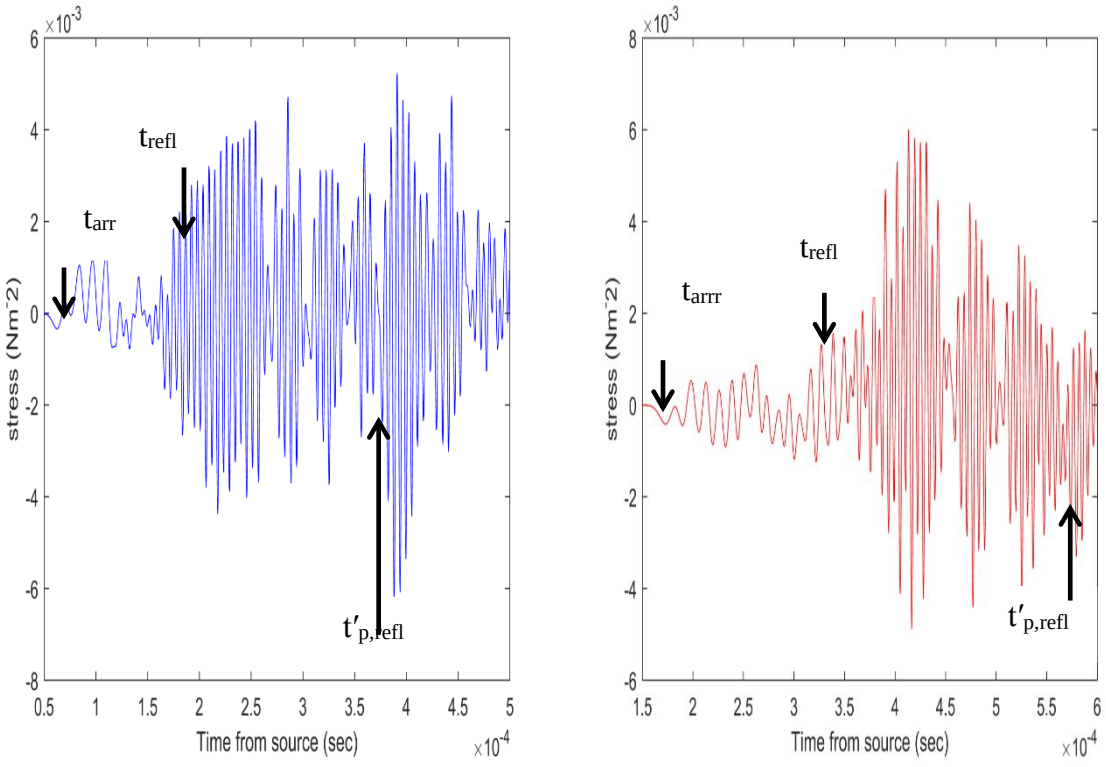

a. Sensor 1 b. Sensor 2

Figure 6-17: *Segments of simulated stress time series for fastest unload rate at positions (a) S_1, (b) S_2*

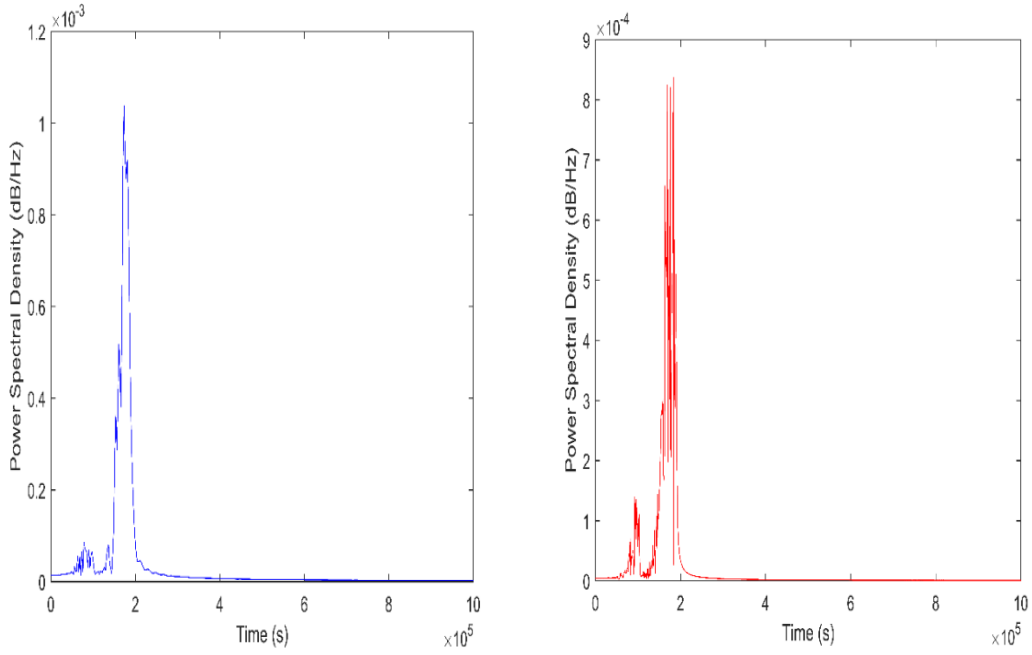

a. Sensor 1 b. Sensor 2

Figure 6-18: *Power spectrum of simulated stress time series between t_{arr} and t'_{pref} for the fastest unload rate at positions (a) S_1, (b) S_2*

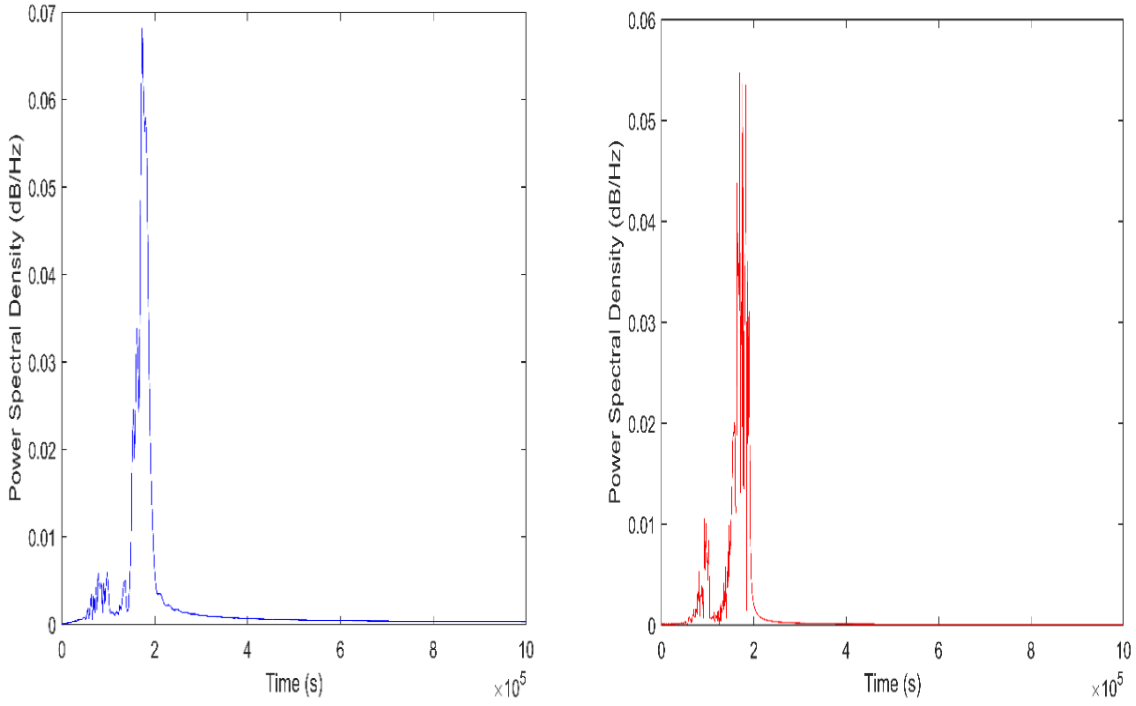

a. Sensor 1 b. Sensor 2

Figure 6-19: *Power spectrum of simulated stress time series between tarr and t'_{prefl} for the slowest unload rate at positions (a) S_1, (b) S_2*

The experimental values for the three fractions are based on the average power values for the 20 measurements and the corresponding fractions have been calculated for each of the sensors and each of the segments. In the same way, fractions have been calculated for the simulations for each of the sensor positions, each of the segments and each of the unload rates. It should be noted that the experimental power values can be compared with each other and the simulations can be compared with each other, but the simulations are not amplitude calibrated relative to the experiments.

Figure 6.20 shows the spectral content for the average of the experimental measurements for each position and each segment, compared with the average of the simulations across all of the unload rates. This comparison confirms the observation made earlier that higher frequency elements are generally less evident in the simulations than in the experiments. Coupled with the different appearance of the first wave arrival in the simulations, this would suggest that the experimental source is more complex than a step direct compressive stress unload, as it is in the simulation. Notwithstanding this, and despite the differences in measured spectral components across the 20 tests, some similarities between experiment and simulation can be seen in Figure 6.20. First of all, the HF band is most prevalent in the "fast" segment as "seen" at S_1, signifying that the lower amplitude, first arriving wave is of higher frequency. Secondly, the HF power in the "fast" segment is considerably reduced by the time it reaches S_2. This could be due to selective attenuation of the higher frequency components, although the attenuation mechanisms in the simulations are confined to the geometric ones. More likely, the "fast wave" has a more complex time-frequency structure which becomes more evident as more of it overtakes the slower components. Also, both simulation and experiment exhibit a lower HF content in the slow segment, despite the possibility that it contains some reflected fast elements. The shifts in spectral content between LF and MF bands are highlighted in Figure 6.21, where it can be seen that, again, the fast components behave consistently between experiment and simulation, with the LF band becoming more prevalent with distance from the source. However, the ratio of low to medium frequency behaves differently between experiment and simulation when the longer segment is considered and this could be due to a greater influence of reflected elements in the simulation.

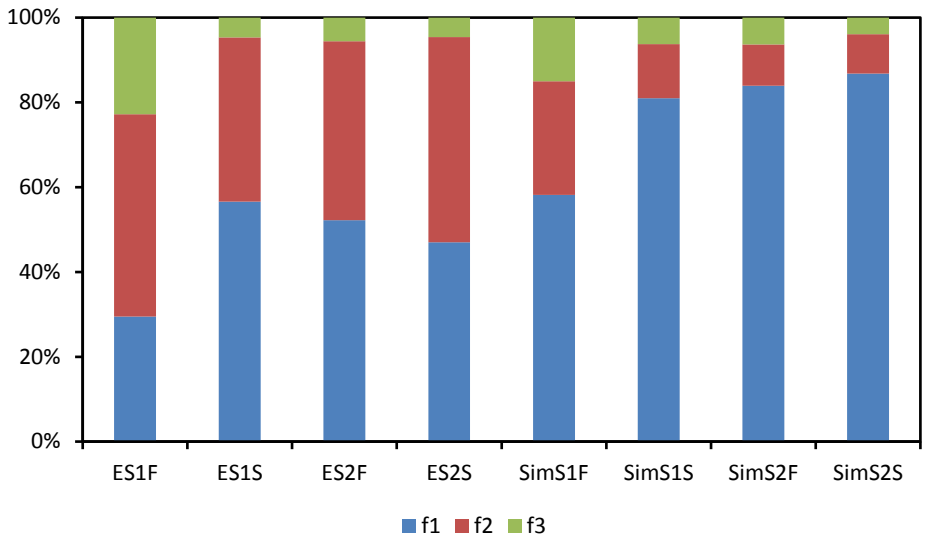

Figure 6-20: *Comparison of measured (E) and simulated (Sim) power spectral content for each of the sensor positions (S_1 and S_2) and each of the time series segments (S) and (F).(f1, f2 and f3 fractional power in LF, MF and HF bands, for configuration code, see Table 6-4)*

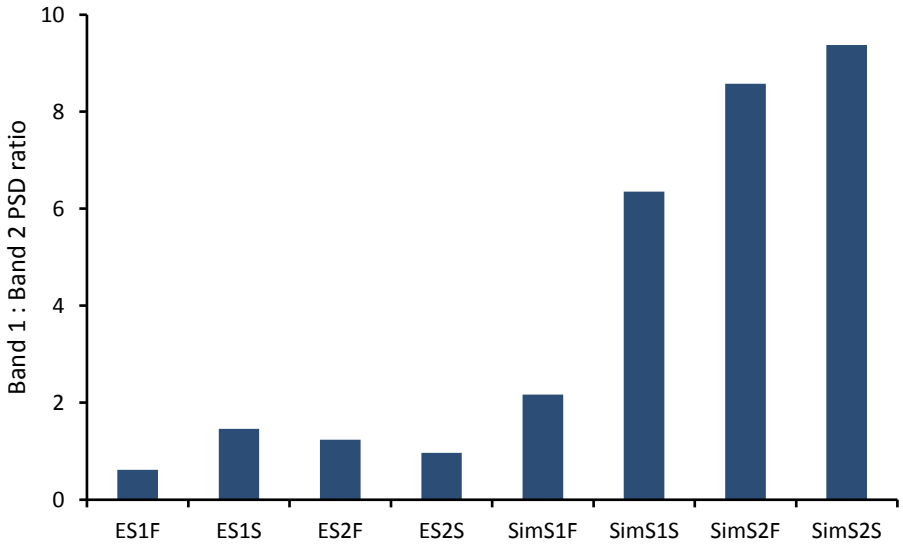

Figure 6-21: *Comparison of measured (E) and simulated (Sim) low-frequency power spectral ratio (PLF/PMF) for each of the sensor positions (S_1 and S_2) and each of the time series segments (S) and (F). (For configuration code, see Table 6-4)*

Figure 6.22 shows how the unload rate affects the spectral content of the simulated fast and slow segments at each of the sensor positions. It might be noted at the outset that the resolution of the fast segment at S_1 is relatively low due to its short time duration, (Figure 6.14a). Considering this, it appears that there is little or no effect of unloading rate on the frequency content at S_1, while there are some clear systematic changes at S_2, there being a shift to lower frequencies as the unload rate decreases (longer unload times). This observation is consistent with the expected higher frequencies generated as a step unload is approached. This general observation is confirmed when considering the "slow"

segments, there being no observable changes with unload rate at S_1 and there being a systematic shift towards higher frequencies at the higher unload rates at S_2. Given that the experimental spectra have generally less low-frequency content than the simulations (Figure 6.20), this would suggest that the fastest unload rate is the most appropriate of those considered here.

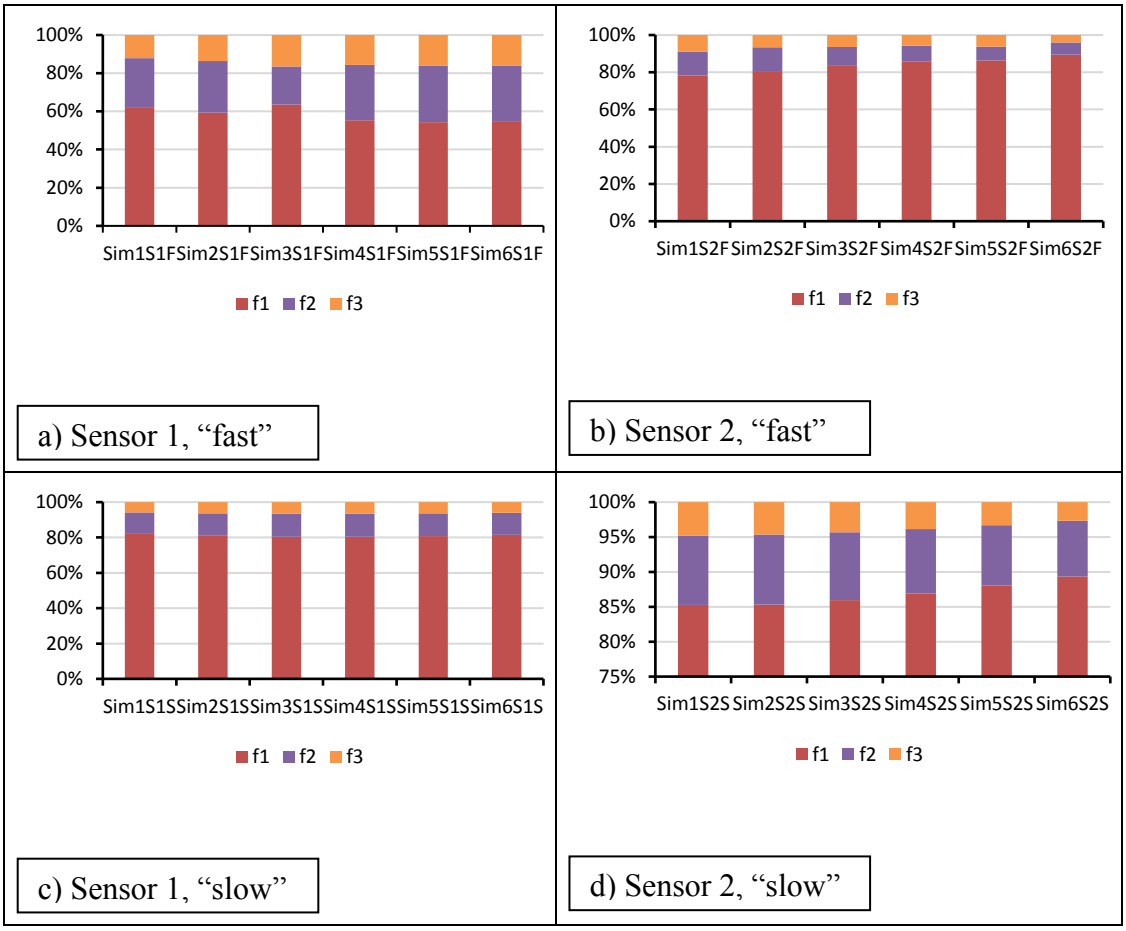

Figure 6-22: *Effect of unloading rate on simulated power spectral content for each of the sensor positions (S_1 and S_2) and each of the time series segments (S) and (F). (f1, f2 and f3 fractional power in LF, MF, and HF bands, for configuration code, see Table 6-4)*

Figure 6.23 shows how the total power of the simulated signal varies with unloading rate for each of the segments at each of the sensors. In general, this increased significantly from the fastest rate with the slope decreasing slightly at the slowest unload rates. The somewhat anomalous shape of the slow segment at sensor position 2 is attributed to it containing more "double-counting due to reflections.

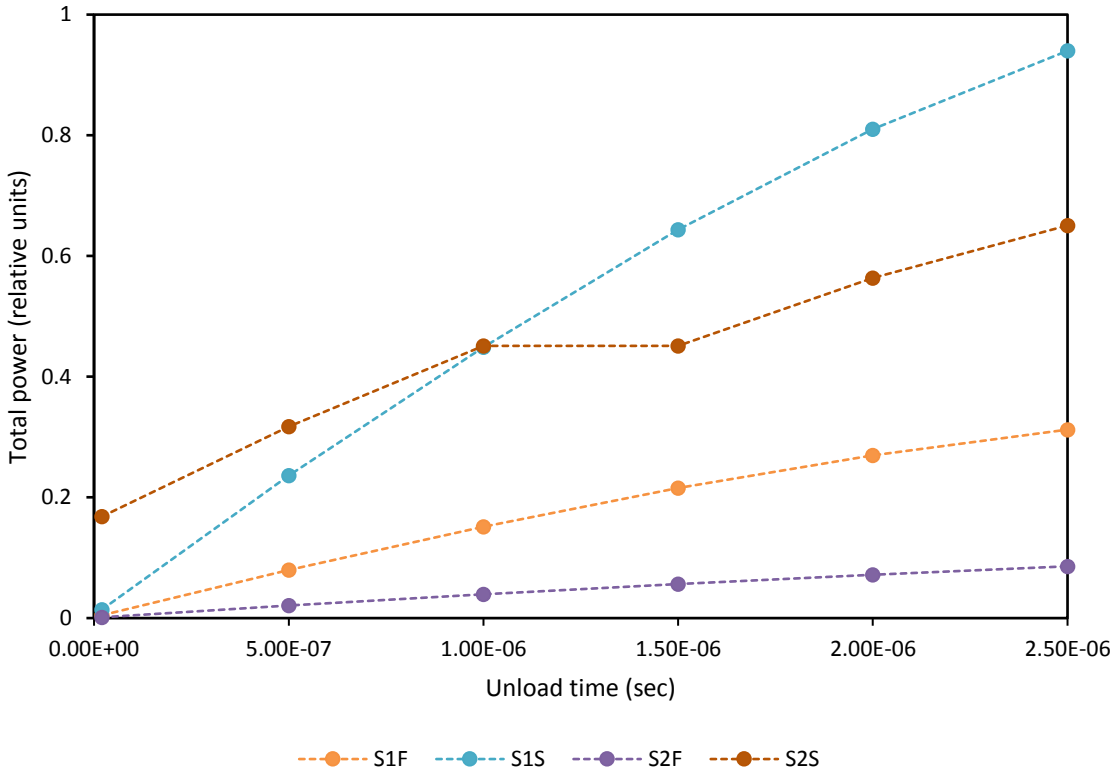

Figure 6-23: *Effect of unloading rate on total simulated power content for each of the sensor positions (S_1 and S_2) and each of the time series segments (S) and (F)*

6.3 Summary of findings

This section summarises the findings of both the PLB experiments and matching FE simulations.

6.3.1 An analysis of the first set of simulations shows that stress time series gave arrival times and speeds consistent with those found on the reference object. The faster component moving at around 5500ms^{-1} appeared to have a peak frequency at around 200 kHz, whereas the slower component, moving at around 1700ms^{-1} appeared to have a peak frequency at around 100 kHz.

6.3.2 In the second set of simulations, a comparison of the simulated and experimental results indicates that the actual unloading rate is at the high end of those investigated, although the frequency content of the resulting wave is not highly sensitive to unloading rate. The amplitude of the simulated signal was however, rather sensitive to unloading rate.

6.3.3 A comparison of the first few tens of microseconds of the simulated an experimental waveforms suggests that, although the first arrival is consistent with a wave speed of

around 5000ms^{-1}, the real wave generated by a pencil-lead break is probably not due to a simple compressive direct stress unload. Also, an analysis of the unload rates studies shows that the faster unload rates in the simulations gave rise to increased high-frequency contents in the first-arriving waves, but resulted in a considerable reduction in signal amplitude and total signal power.

6.3.4 The inter sensor calibration on the pipe against the calibration certificates shown in the appendix confirms that S_2 is slightly more sensitive than S_1. Also, just as in the solid cylinder, there is a significant variability when sensors are removed and remounted even in the same position; this is thought to be due to changes in coupling conditions and magnetic clamp tightening force.

Chapter 7– Experimental and Simulation Results for Ball Bearing Drop on Pipe

This chapter develops a preliminary framework for the characterization of AE resulting from low velocity impact events on a pipe. Unlike the PLB tests described in Chapter 6, the temporal and spatial distribution of the AE source is less controlled here, and is more representative of a real source. Because the ball bearings were not dropped directly onto the pipe surface, the ball drops are also somewhat less well controlled than those reported in Chapter 5 for the solid cylinder so a comparison of the two is carried out first for a subset of the experiments. The chapter is organized into two main sections, dealing primarily with the experiments and the simulations.

7.1 Dropped Object Experiments on Pipe

As pointed out in Chapter 4, unlike the ball bearing drop on the solid cylinder, the ball bearings were dropped onto a flat steel plate placed on the pipe, for practical reasons. Three ball bearing sizes were dropped from three heights, giving a range of potential energies, as shown on Table7-1. The final column of this table (drop height 300mm) corresponds to the conditions under which ball bearings were dropped onto the solid cylinder, so a direct comparison can be made between direct impacts and those made through the flat plate.

Ball Bearing	Diameter (mm)	Weight (g)	PE ($J\times10^{-2}$) (100mm)	PE ($J\times10^{-2}$) (200mm)	PE ($J\times10^{-2}$) (300mm)
Small	4	0.3	0.026	0.052	0.078
Medium	8	3	0.298	0.596	0.894
Large	16	17	1.669	3.338	5.007

Table 7-1: *Potential energies (J) for weights dropped from the three heights*

7.1.1 *Results*

Figures 7.1-7.3 show typical records of the first 2 seconds of raw AE for all potential energies and ball sizes. As can be seen, just as with the solid cylinder, the ball bounces are characterised by a burst signal of duration of about 0.1s, the peak of the burst reducing with successive bounces. A comparison of Figure 7.3 with the cylinder equivalent (Figure 5.2) shows that the amplitude is a little higher for the pipe, although there are fewer

bounces, somewhat further apart. It might be noted that the heaviest ball dropped from the largest height (Figure 7.3c) has saturated the preamplifier and that the actual signal will be somewhat higher than depicted. The saturation seen in figure 7.3c was expected as is usually the case in applications with strong AE-sources. The saturation in this case was a result of the ball weight and height combination in relation to the AE equipment used; with the AE equipment used in the experiment, each measurement channel has a saturation limit (e.g. ±5 V or ±10 V) above which signal information is lost.

Importantly, there are clear changes in energy between the masses and the drop height, an effect that was not observable in the narrower set of tests on the solid cylinder.

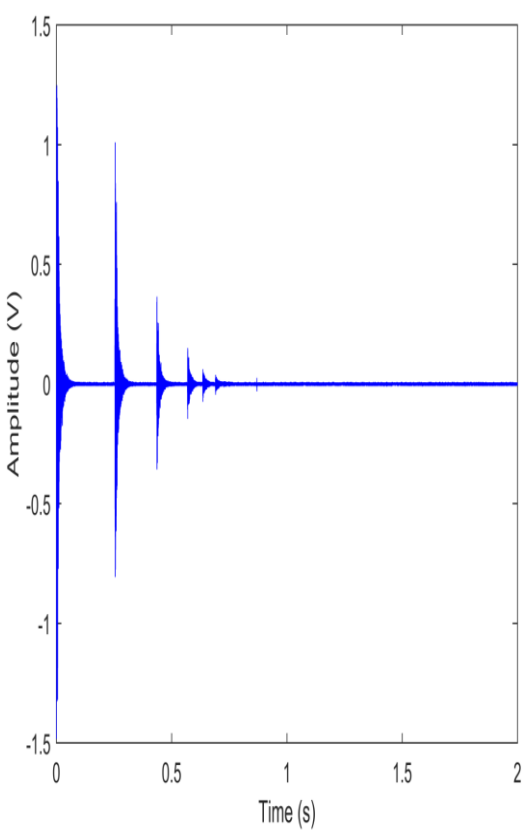

a.

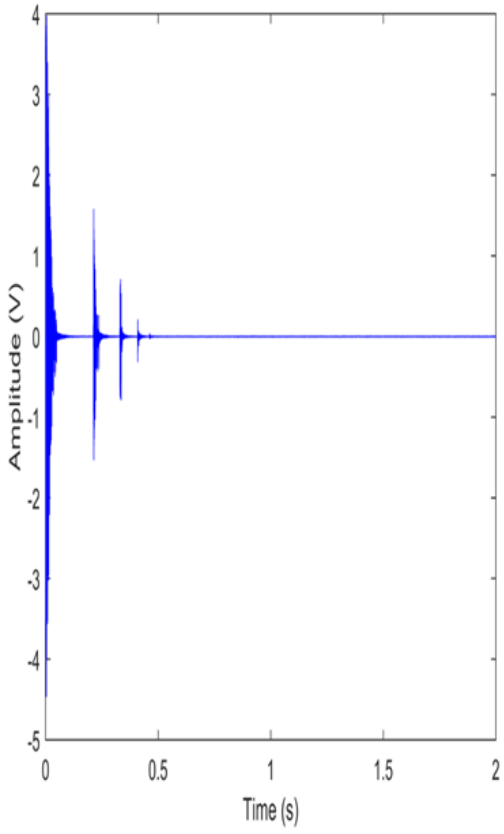

b.

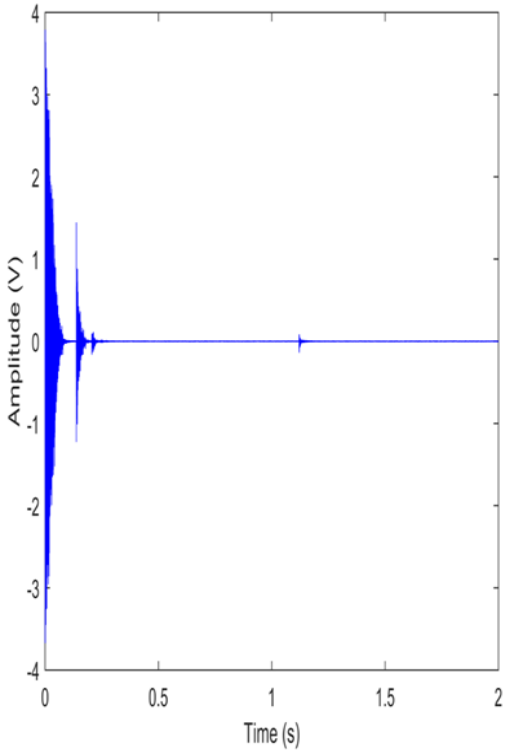

c.

Figure 7-1 : *Typical raw AE signal for balls dropped from 10cm height a) 0.3g b) 3g c) 17g for sensor at 0.5m on the 2m pipe*

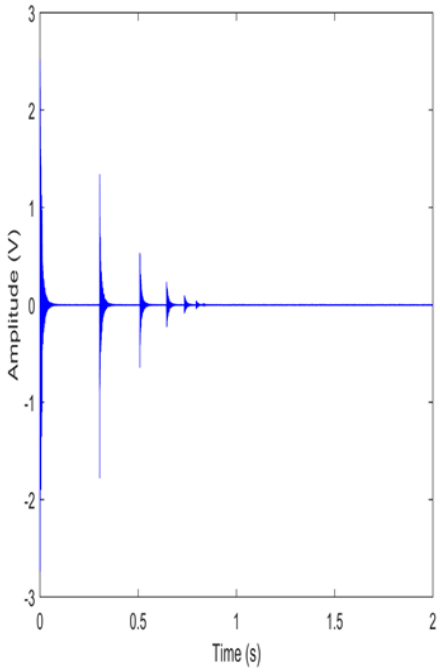

a.

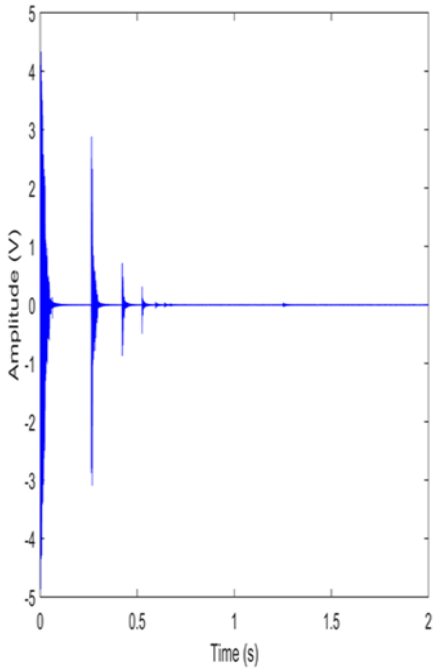

b.

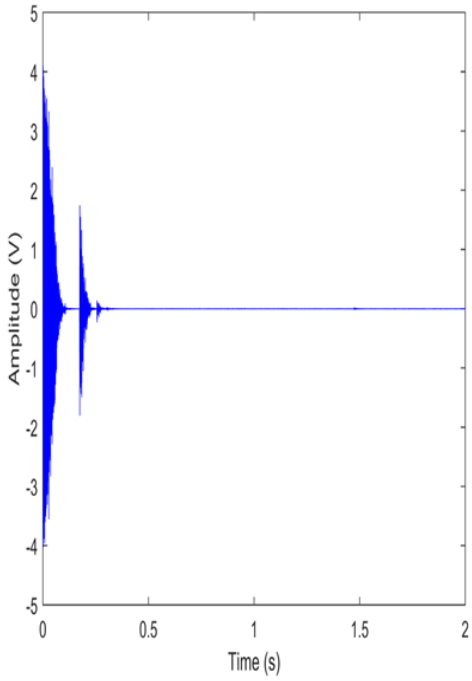

c.

Figure 7-2: *Typical raw AE signal for balls dropped from 20cm height a) 0.3g b) 3g c) 17g for sensor at 0.5m on the 2m pipe*

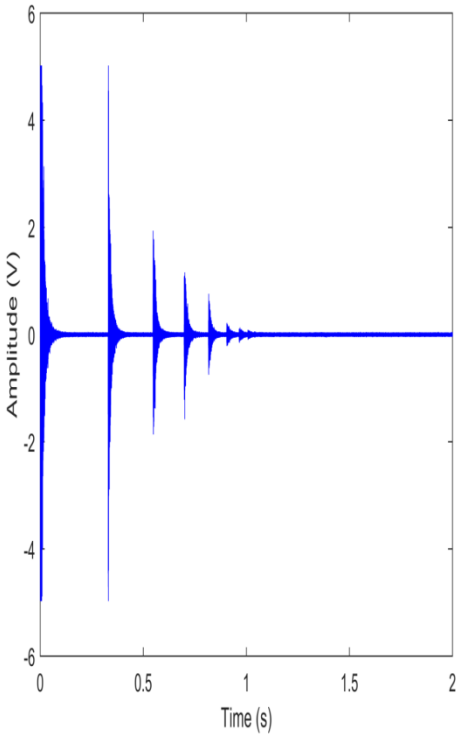

a.

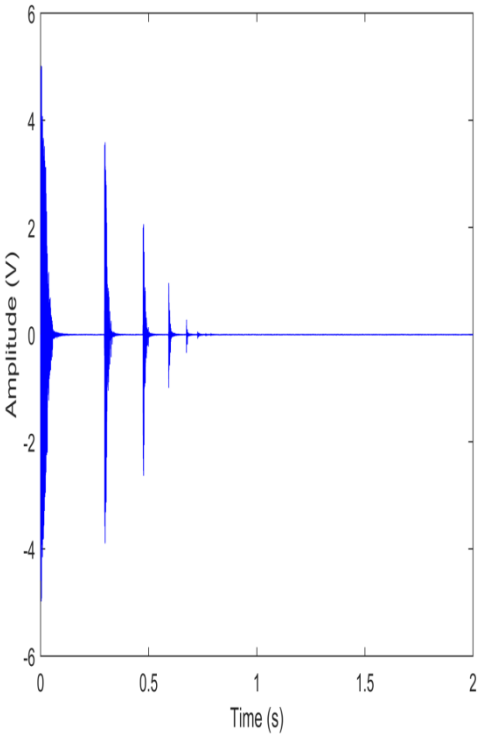

b.

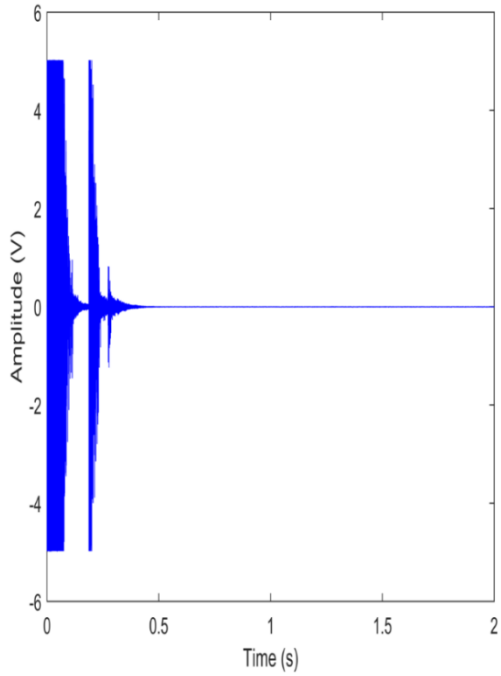

c.

Figure 7-3: *Typical raw AE signal for balls dropped from 30cm height a) 0.3g b) 3g c) 17g for sensor at 0.5m on the 2m pipe*

Figures 7.4 to 7.6 show the first 100 μs around first wave arrival at the first sensor for typical ball bearing drops on the 2 m pipe for each of the nine combinations shown in Table 7.1. Comparison with the equivalent signals for the solid cylinder (Figure 7.6 with Figure 5.3) shows the records for the pipe to be more complex, although it is uncertain if this is due to the nature of the impact or the different propagation route. Also, it can be observed that, regardless of the drop height and ball bearing size, each first arrival is again characterized by a low amplitude component followed by a high amplitude component, which contains the peak amplitude. Comparing the ball drops with the pencil lead breaks for the same sensor position (Figures 7.4 to 7.6 with Figure 6.12) this feature is common to both source types and is therefore most likely to be attributable to the propagation route.

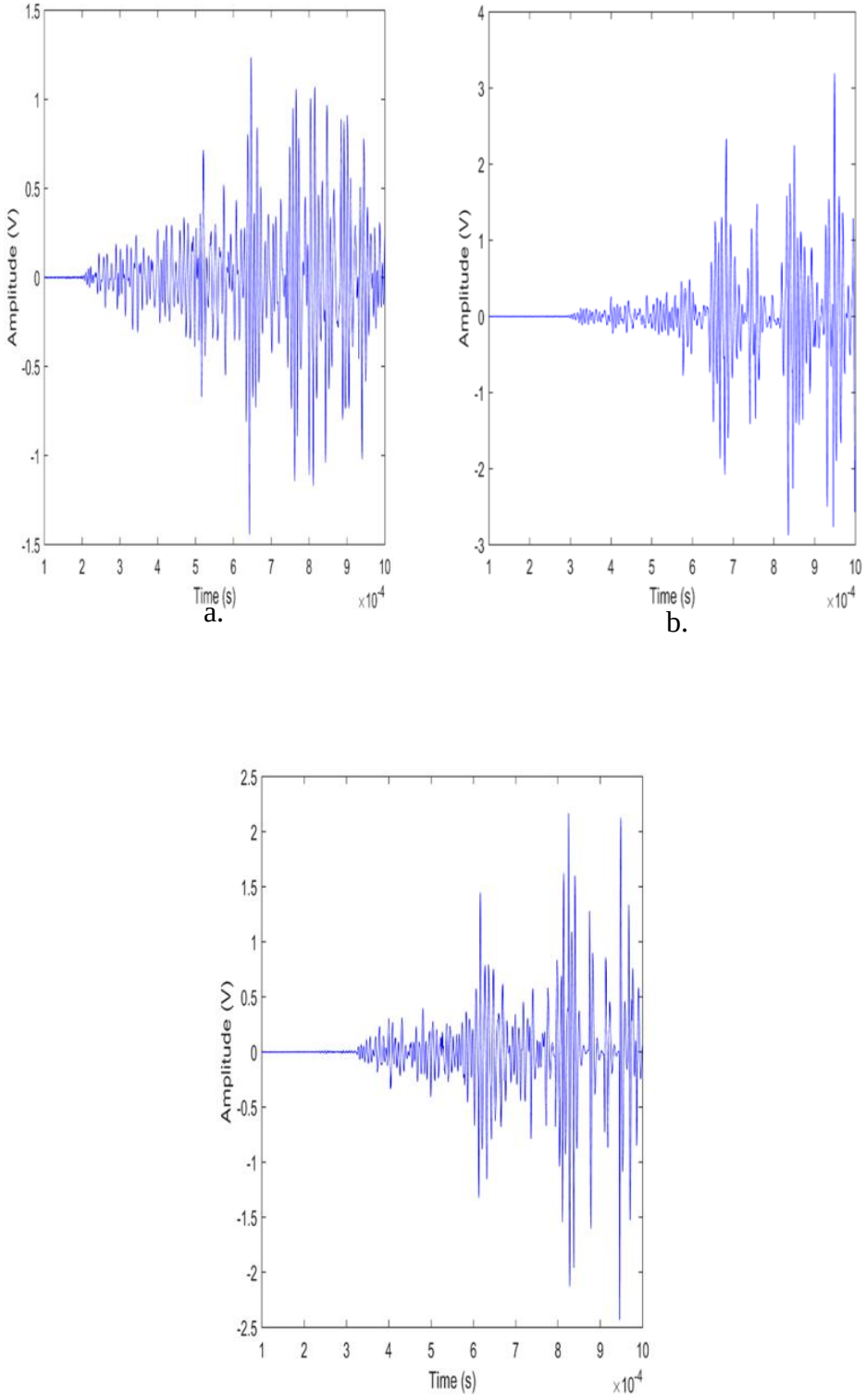

Figure 7-4: *Typical raw AE time series recorded at S_1, on the pipe (first wave arrival) for three ball sizes dropped from 10cm height (a – 0.3g, b – 3g, c –17g)*

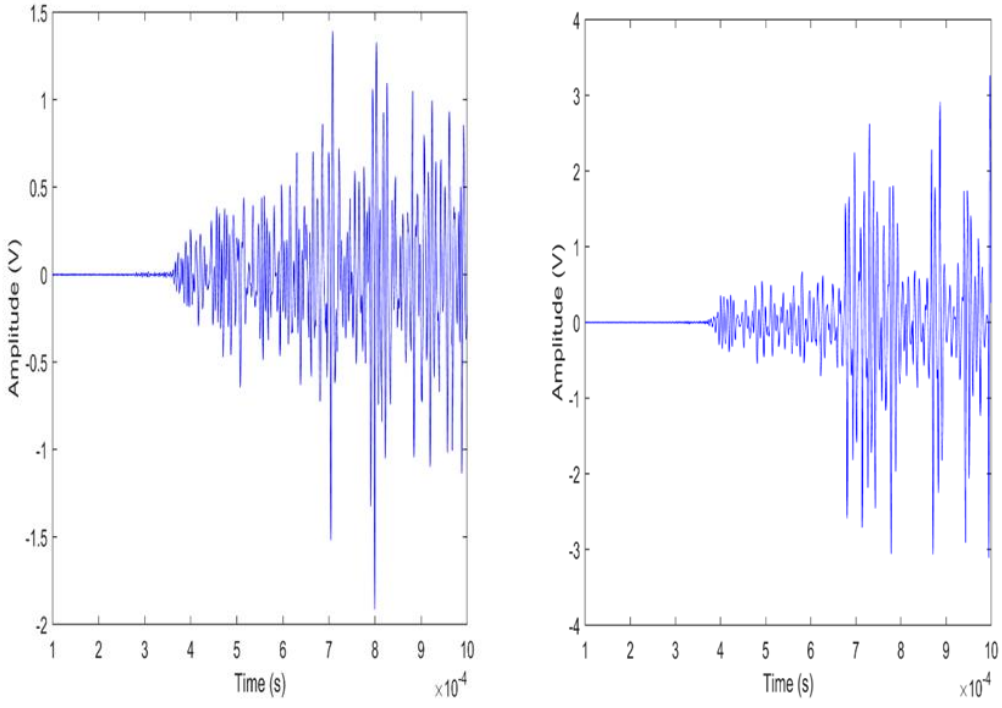

a. b.

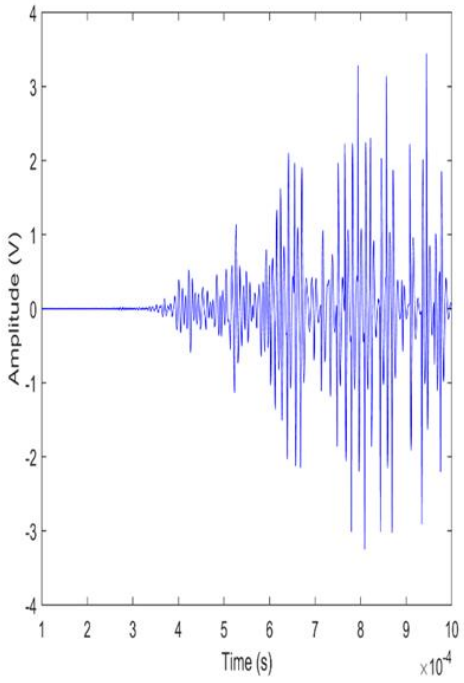

c.

Figure 7-5: *Typical raw AE time series recorded at S_1, on the pipe (first wave arrival) for three ball sizes dropped from 20cm height (a – 0.3g, b – 3g, c –17g)*

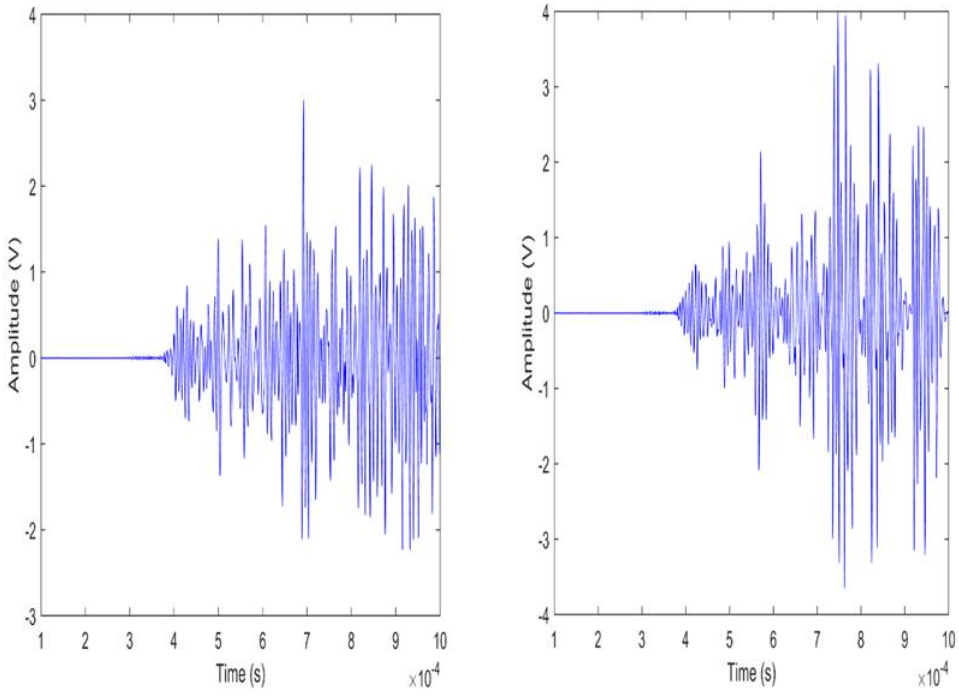

a. b.

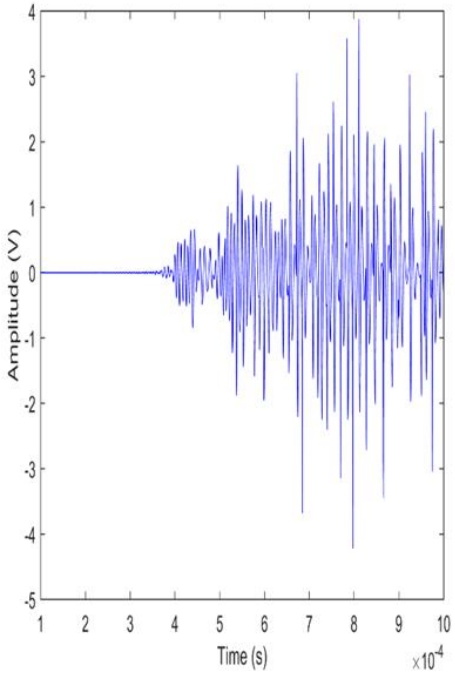

c.

Figure 7-6: *Typical raw AE time series recorded at S_1, on the pipe (first wave arrival) for three ball sizes dropped from 30cm height (a – 0.3g, b – 3g, c –17g)*

7.1.2 *Detailed comparison of pipe and cylinder dropped objects*

This section compares the dropped object results on the pipe with those obtained on the solid cylinder, and is confined to the same range of parameters, i.e. 30cm drop height for

all three ball sizes. Here, an equivalent analysis to that presented in Section 5.3 is carried out at the three timescales: long (several bounces), medium (first bounce) and short (impact free from reflections).

Figures 7.7 and 7.8 show plots of incident energy vs. measured energy for the first four bounces for balls dropped onto the reference object and onto the pipe. The plots for the reference object are the same data as in Figure 5.4, but plotted at a different scale to facilitate comparison. For the same reason, the plots are shown at two scales on the ordinate so that the trends at low incident energy can be more clearly seen. Table 7.2 shows the data in Figure 7.8, including the mean and standard deviation of the 20 observations (bearing in mind that the data for the solid cylinder are based on a single observation).

From figures 7.7 and 7.14, it can be seen that for the medium and short timescales, the AE energy varied with drop height and mass consistently with existing models for balls on plate. However, for multiple bounces, the behaviour was more erratic probably due to the imprecise control of ball contact point. It is clear from these plots that the pipe experiments show similar general behaviour to those on the solid cylinder, i.e. that the measured energy increases with incident energy, but that the rate of increase is lower for the heavier masses (and radii). This is most likely to be due to the fact that the heaviest masses are have enough momentum to displace the plate if they do not land directly above the contact line between plate and pipe. The somewhat anomalous behaviour of the second bounce for the heaviest ball is likely to be an artefact of the saturated amplifier for the first bounce (Figure 7.3c), leading to an underestimate of the incident energy using the algorithm described in Chapter 5.

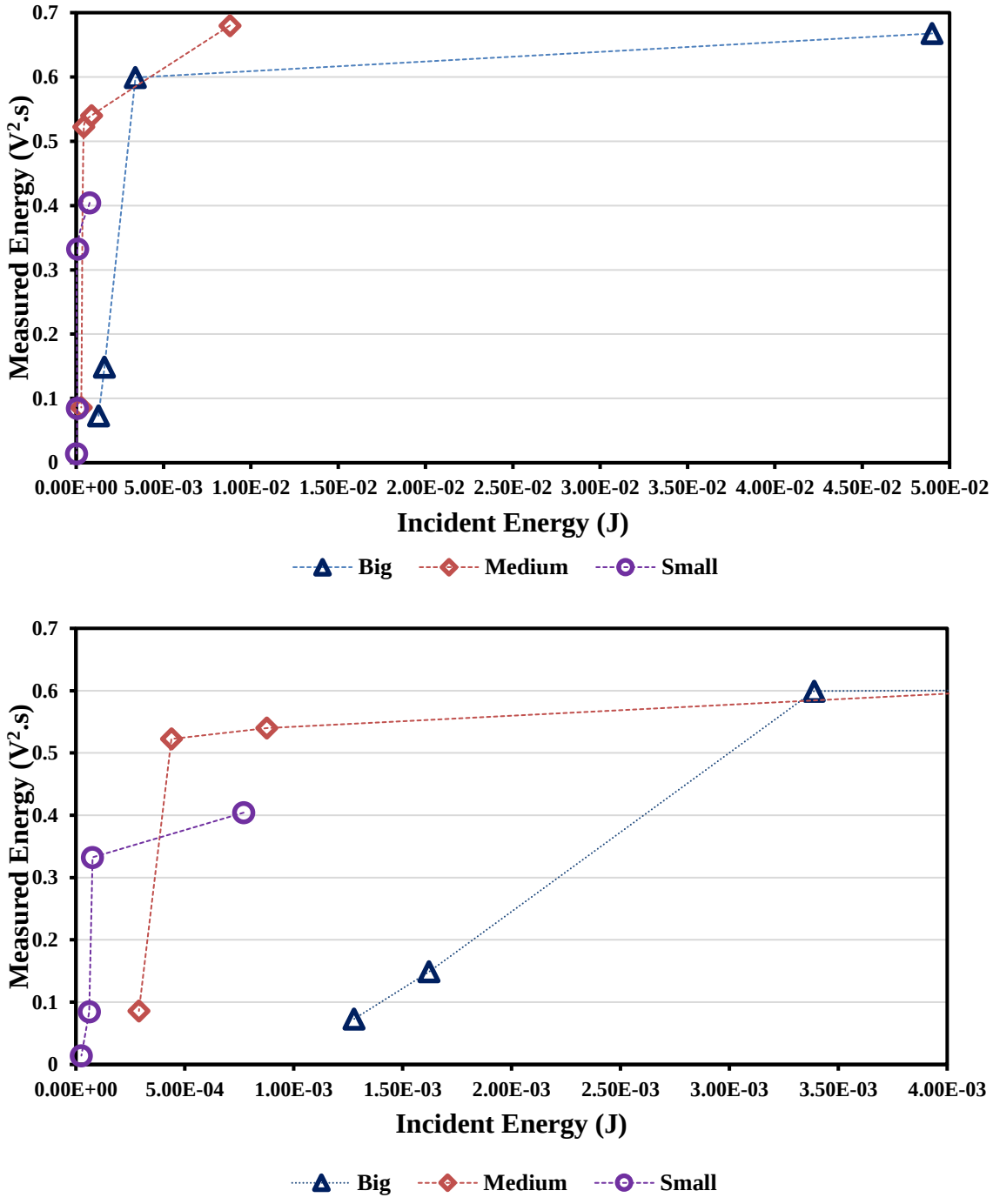

Figure 7-7*: Plot of measured energy vs incident energy in the first four bounces for the three ball sizes dropped from 30cm height onto the cylinder*

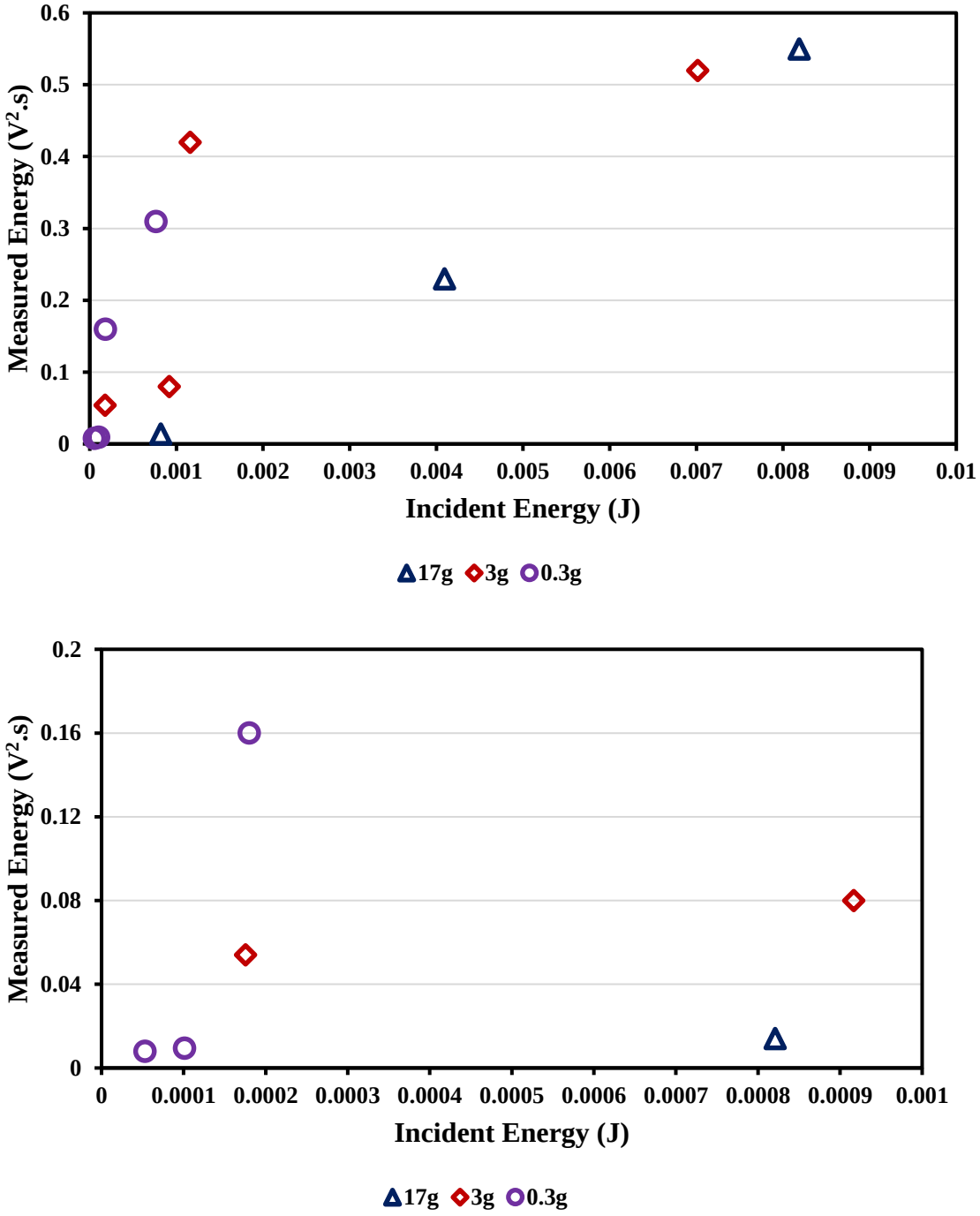

Figure 7-8 *Plot of measured energy vs incident energy in the first four bounces (long timescale) for the three ball sizes dropped from 30cm onto the pipe*

Figures 7.9 and 7.10 show plots of measured energy vs incident energy for the first bounce for each of the ball sizes for both the reference object and the pipe. As already observed, the mass (or perhaps the radius) of the ball does not lead to the expected linear increase in measured AE energy and this effect is even more marked for the pipe than it was for the solid cylinder. As shown in Table 7.2, the standard deviation on the relevant points is

only about 20% of the mean, so this appears to be a real effect in both the cylinder and the pipe, and is elucidated in the following section.

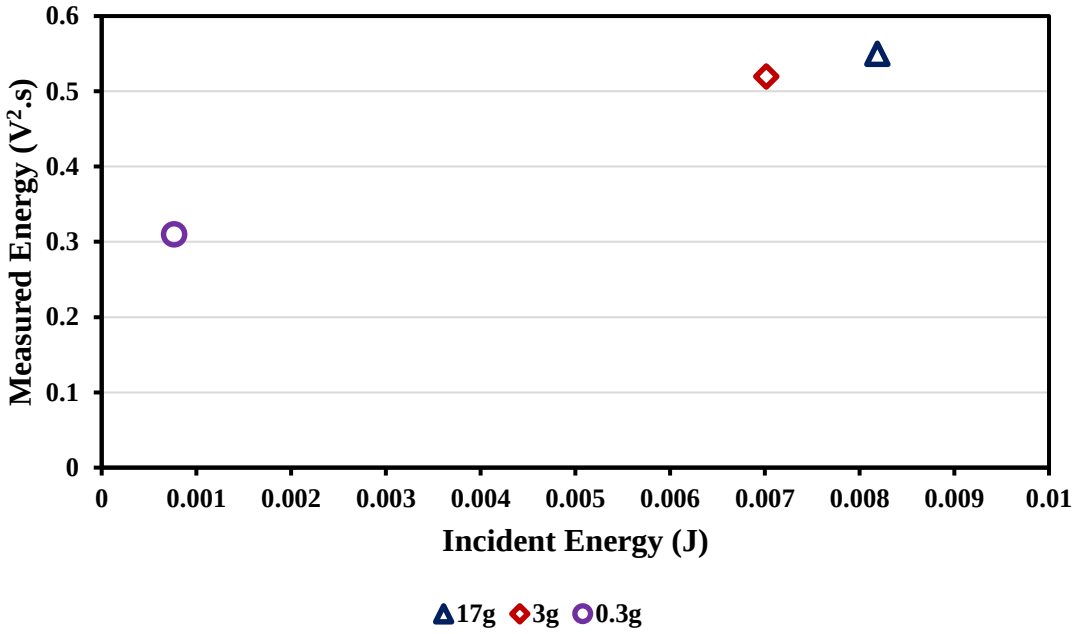

Figure 7-9: *Plot of measured energy vs incident energy in the first bounce (medium time scale) for the three ball sizes dropped from 30cm height onto the cylinder*

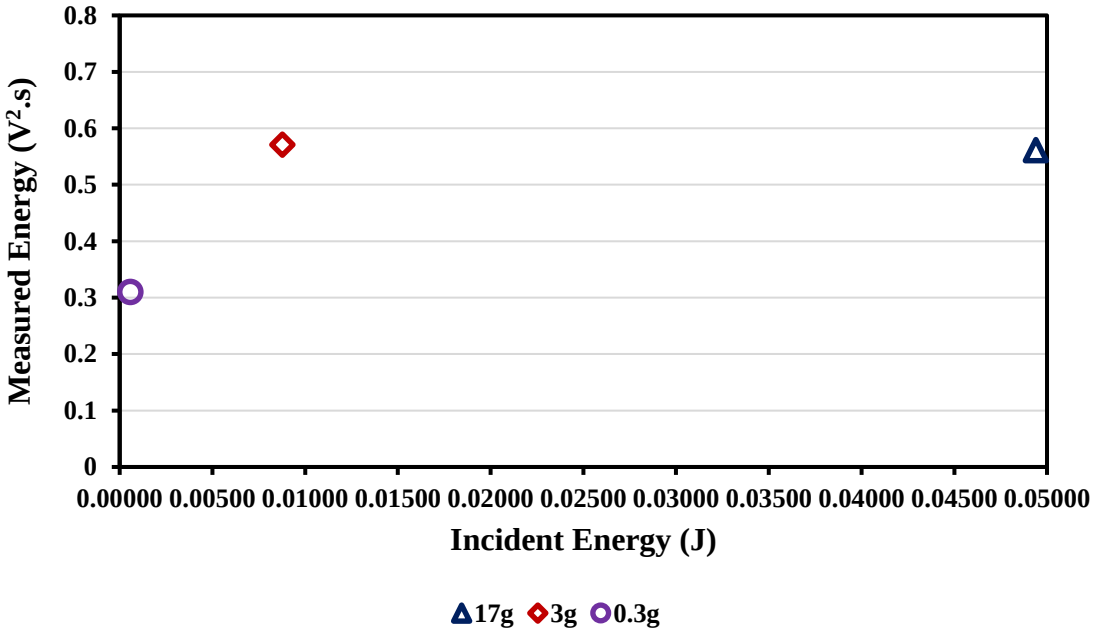

Figure 7-10: *Plot of measured energy vs incident energy in the first bounce (medium time scale) for the three ball sizes dropped from 30cm height onto the pipe*

Finally, Figures 7.11 and 7.12 show the energy associated with the first interaction of the ball with the cylinder and the pipe (i.e. before the wave has been able to reflect from the ends or edges of the test object, as determined in Sections 5.4. and 6.3, respectively). As

with the relatively clean impacts on the cylinder, the evolution for the pipe again shows an increase with the mass of the ball between the small and medium sizes and a decrease for the largest. The relatively large values of the measured energy for the pipe are attributable to the longer integration time because the boundaries of the pipe are further away from the source and sensor than they are in the cylinder.

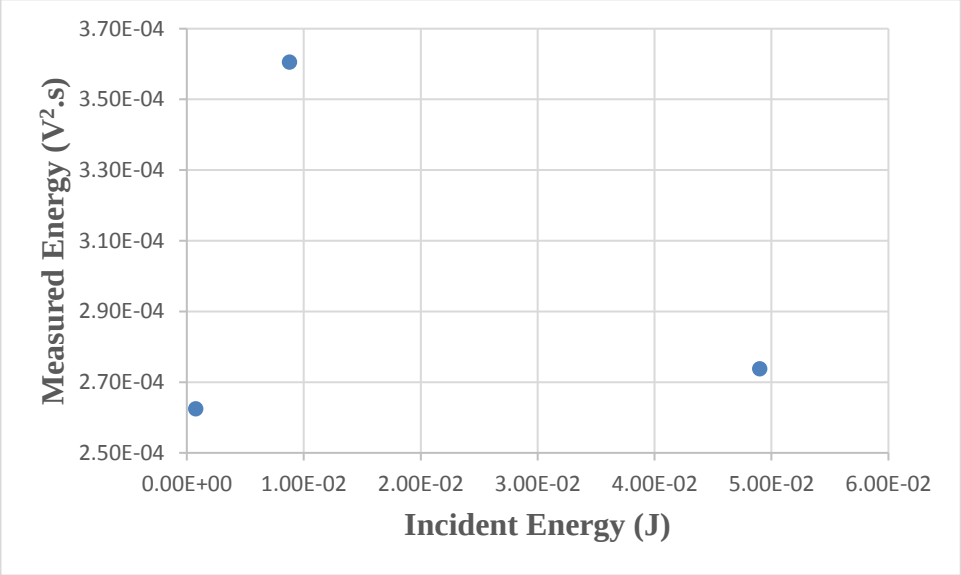

Figure 7-11: *Plot of measured energy vs incident energy in the short time scale (impact free from reflection) for the three ball sizes dropped from 30cm height onto the cylinder*

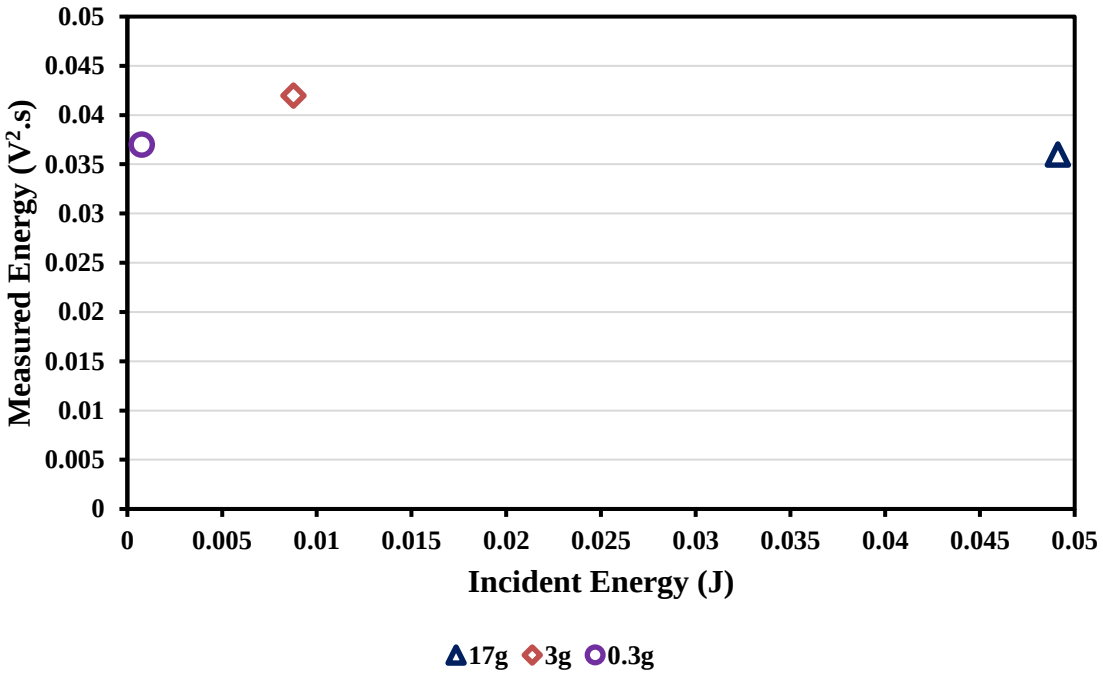

Figure 7-12: *Plot of measured energy vs incident energy in the short time scale (impact free from reflection) for the three ball sizes dropped from 30cm height onto the pipe*

In summary, the impact experiments on the pipe seem to behave consistently with those on the rather idealised shape of the cylinder. Discussion of the causes of the observed changes is deferred to the next section where the full data set on the pipe is analysed.

7.1.3 *Analysis of full range of pipe dropped object experiments*

Figure 7.13 shows a plot of the measured energy *vs* incident energy for the first four bounces for the remaining two ball sizes and all drop heights onto the pipe. These graphs show the same general trends as observed for the 30cm drop but, again, the curves are not smooth with some erratic behaviour compared with the solid cylinder. It seems that the coefficient of restitution for the plate on top of the cylindrical surface is somewhat less reliable than it is for the flat face of the solid cylinder, so the erratic behaviour is probably real, showing that the resolution of relatively closely spaced impacts is good even after the wave has travelled some distance on the pipe.

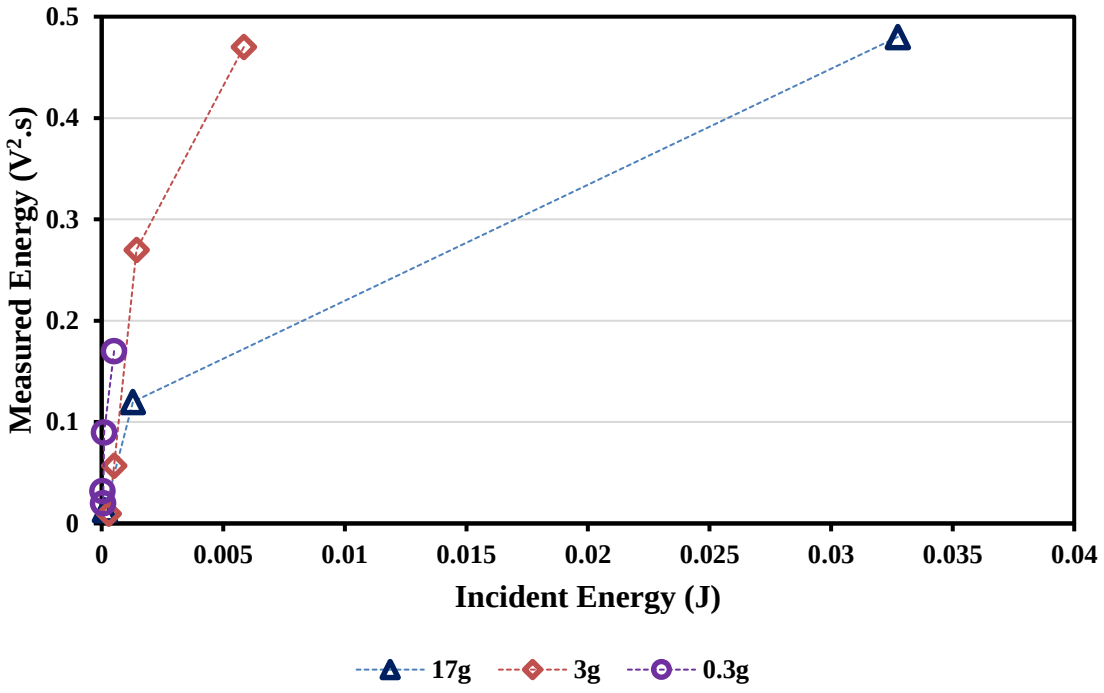

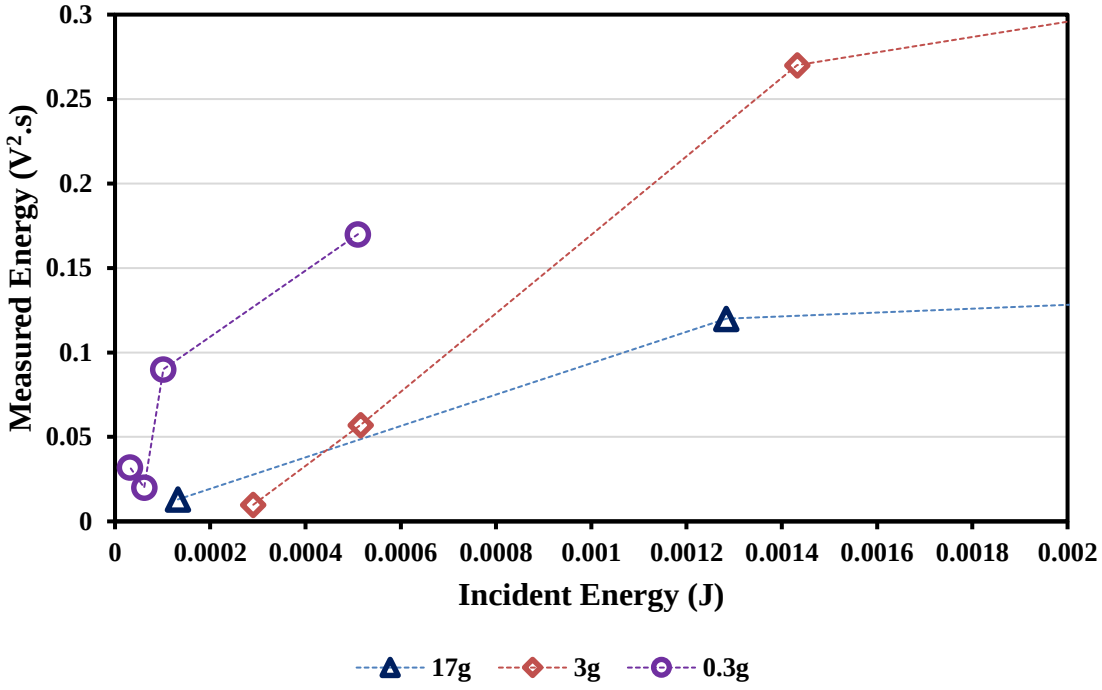
Measured Energy (V².s)
0.3
0.25
0.2
0.15
0.1
0.05
0
0
0.0002
0.0004
0.0006
0.0008
0.001
0.0012
0.0014
0.0016
0.0018
0.002
Incident Energy (J)
17g
3g
0.3g

a.

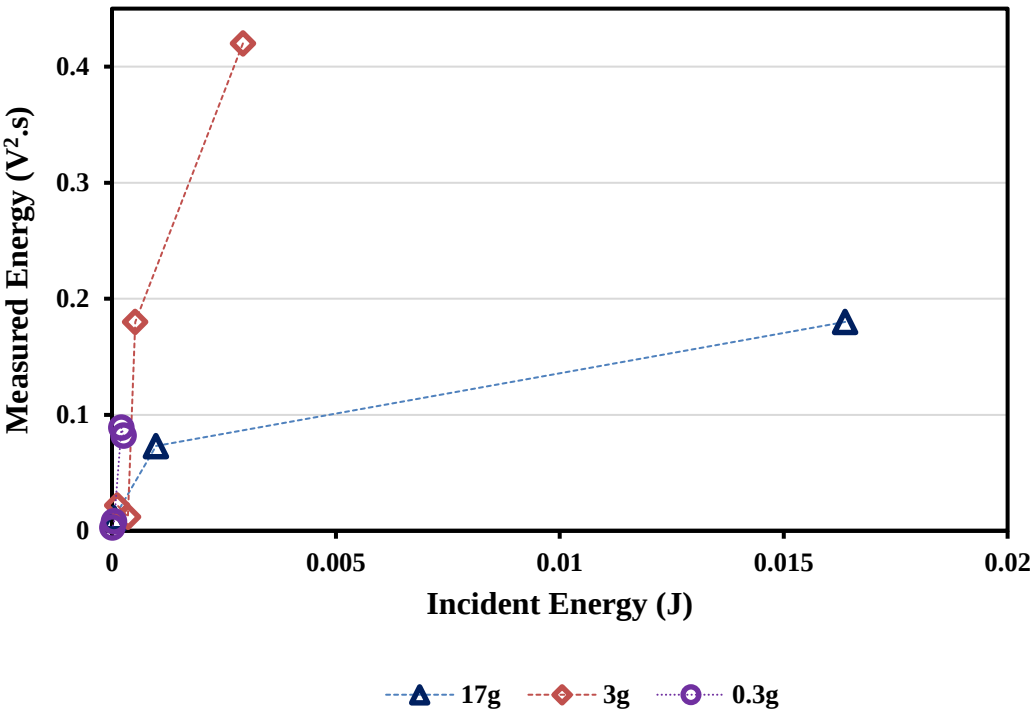
Measured Energy (V².s)
0.4
0.3
0.2
0.1
0
0
0.005
0.01
0.015
0.02
Incident Energy (J)
17g
3g
0.3g

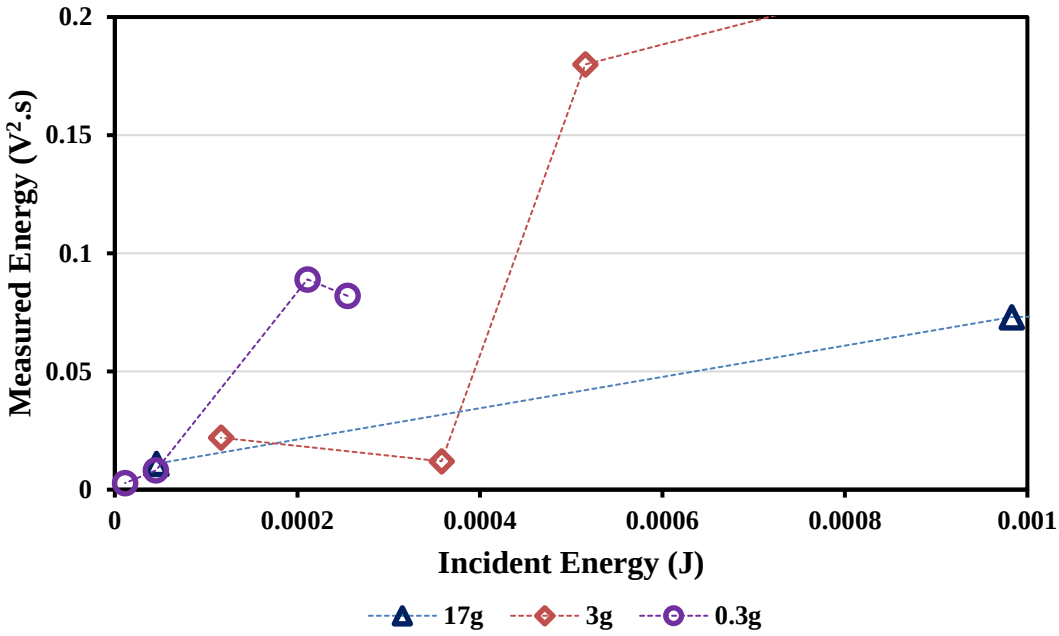

b.

Figure 7-13: *Plot of measured vs incident energy for the first four bounces for all ball sizes dropped onto the pipe from a) 20cm b) 10cm*

Figures 7.14 and 7.15 show the measured energy *vs* incident energy for the first contact at the medium- and short-timescales for all ball sizes and all drop heights onto the pipe In this presentation, where no assumptions are made about the incident energy (except that the ball potential energy is all incident on the surface), the relationship between measured and incident energy is much clearer than in Figure 7.13. The first bounce for all ball sizes dropped onto the pipe from all heights gave nine different energies, with the range of energy values recorded by each ball bearing drop being shown as error bars.

For each ball size (or mass) there is a monotonic increase in measured energy with incident energy, the gradient decreasing with increasing incident energy. This effect is seen in both the short- and medium-timescales, and is consistent with detailed scientific studies on ball on plate impacts. For example, McLaskey and Glaser [151] have observed that the force impulse of a steel ball on a steel plate increases in a linear fashion with change in momentum, while the coefficient of restitution decreases with incoming velocity, which would lead to a decreasing gradient with drop height for a given ball mass. Heavier masses and larger ball height drops are also likely to lead to localised plastic deformation of the target and a consequent drop in coefficient of restitution, which would again reduce the gradient of measured energy against incident energy.

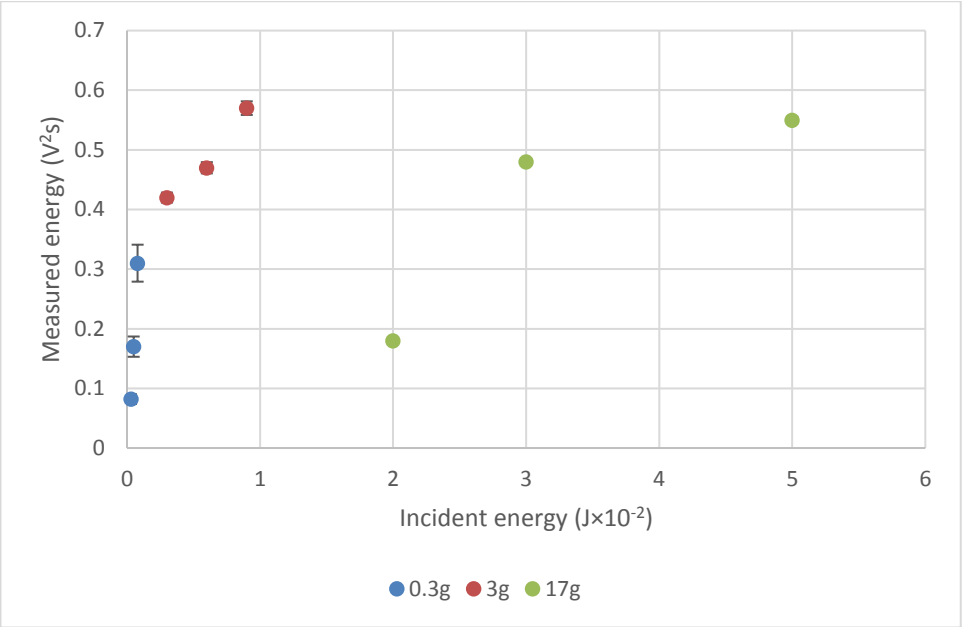

Figure 7-14: *Plot of measured vs incident energy for the first bounce for all ball sizes dropped onto the pipe from all heights*

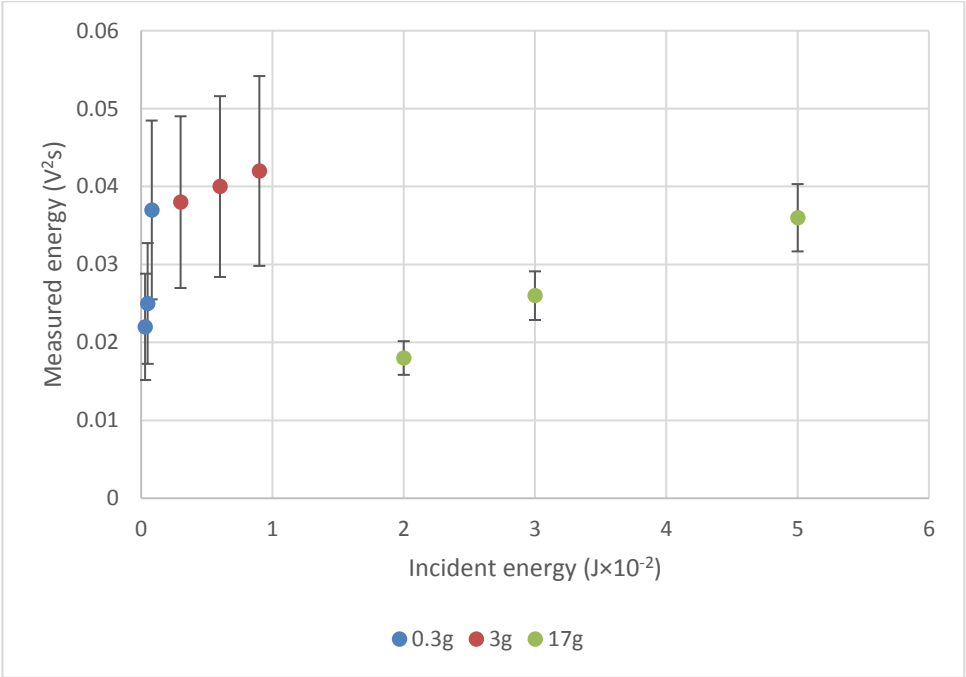

Figure 7-15: *Plot of measured vs incident energy in the short timescale for all ball sizes dropped onto the pipe from all heights*

Mass / height (g / mm)	PE ($J \times 10^{-2}$)	Measured AE Energy ($V^2.s$) (Mean [SD])			
		Bounce 1	Bounce 2	Bounce 3	Bounce 4
0.3 / 100	0.03	8.2×10^{-2} [2×10^{-2}]	8.9×10^{-2} [6×10^{-3}]	8.2×10^{-3} [3×10^{-4}]	2.8×10^{-3} [4×10^{-7}]
0.3 / 200	0.05	1.7×10^{-1} [1×10^{-2}]	0.9×10^{-1} [3×10^{-5}]	2×10^{-2} [1×10^{-6}]	3.2×10^{-2} [3×10^{-7}]
0.3 / 300	0.08	3.1×10^{-1} [1×10^{-3}]	1.6×10^{-1} [1×10^{-3}]	9.5×10^{-3} [1×10^{-4}]	8×10^{-3} [7×10^{-6}]
3 / 100	0.3	4.2×10^{-1} [2×10^{-2}]	1.8×10^{-1} [2×10^{-6}]	1.2×10^{-2} [3×10^{-8}]	2.2×10^{-2} [3×10^{-9}]
3 / 200	0.6	4.7×10^{-1} [3×10^{-3}]	2.7×10^{-1} [1×10^{-5}]	5.7×10^{-2} [6×10^{-6}]	9.8×10^{-3} [2×10^{-5}]
3 / 300	0.9	5.2×10^{-1} [3×10^{-3}]	4.2×10^{-1} [3×10^{-3}]	8×10^{-2} [2×10^{-6}]	5.4×10^{-2} [2×10^{-6}]
17 / 100	2	1.8×10^{-1} [1×10^{-3}]	7.3×10^{-2} [2×10^{-6}]	1.1×10^{-2} [7×10^{-7}]	
17 / 200	3	4.8×10^{-1} [2×10^{-3}]	1.2×10^{-1} [7×10^{-5}]	1.3×10^{-2} [7×10^{-7}]	
17 / 300	5	5.5×10^{-1} [8×10^{-3}]	2.3×10^{-1} [7×10^{-4}]	1.4×10^{-2} [5×10^{-5}]	

Table 7-2: *Medium- and long-timescale measured AE energies vs. incident energies (J) for all weights dropped from the three heights (reduced precision used for clarity)*

Mass / height (g / mm)	PE ($J \times 10^{-2}$)	Measured AE Energy ($V^2.s$) (Mean [SD])
0.3 / 100	0.03	2.2×10^{-2} [4×10^{-3}]
0.3 / 200	0.05	2.5×10^{-2} [5×10^{-3}]
0.3 / 300	0.08	3.7×10^{-2} [2×10^{-2}]
3 / 100	0.3	3.8×10^{-2} [1×10^{-2}]
3 / 200	0.6	4×10^{-2} [5×10^{-3}]
3 / 300	0.9	4.2×10^{-2} [2×10^{-2}]
17 / 100	2	1.8×10^{-2} [5×10^{-5}]
17 / 200	3	2.6×10^{-2} [5×10^{-3}]
17 / 300	5	3.6×10^{-2} [6×10^{-3}]

Table 7-3: *Short-timescale measured AE energies vs. incident energies (J) for all weights dropped from the three heights (reduced precision used for clarity)*

7.2 Preliminary Simulation of Dropped Objects on Pipe

Whilst recognising that an FE model of the dynamic interaction between the pipe and ball bearing, which includes the conversion to AE and its subsequent propagation, is extremely challenging, a preliminary simulation was attempted to try to compare with the measurements. To achieve this, a 3D pipe model was built using the mesh density, material properties and element type discussed in Chapter 3. Next, a 3D ball bearing model was built and a contact interaction algorithm was used to simulate the impact.

The Abaqus FEA software provides two algorithms for modelling contact and interaction problems; the general contact algorithm and the contact pair algorithm. The general contact algorithm in Abaqus was used in this work because it employs an advanced tracking mechanism which allows for efficient contact conditions. For two surfaces ASURF and BSURF, the contact algorithm is shown schematically in figure 7.16.

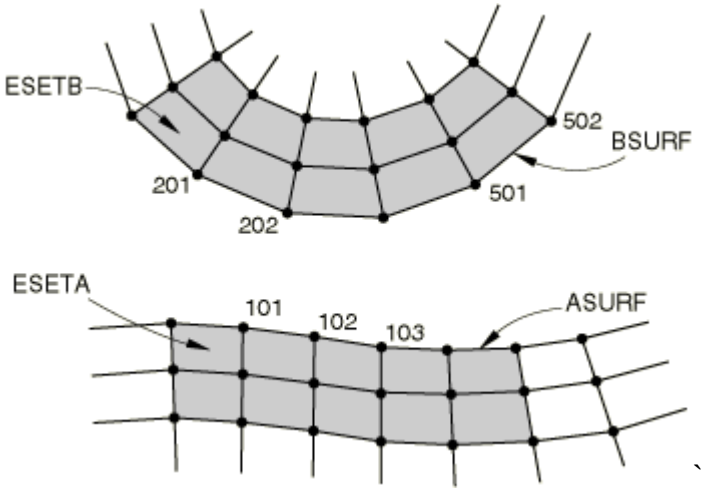

Figure 7-16: *Schematic representation of contact alogorith in Abaqus [127]*

In the contact algorithm shown in figure 7.16, the slave node 101 comes in contact anywhere on the master surface (BSURF). At the point of contact, it is constrained to slide along BSURF, regardless of the surface deformation. Node 101 is in contact with the element face with end nodes 201 and 202 at time t_1. Therefore, the load transfer at this time occurs between node 101 and nodes 201 and 202 only. Subsequently, at time t_2, node 101 is in contact with the element face with end nodes 501 and 502 and the load transfer will occur between node 101 and nodes 501 and 502.

7.2.1 *Finite element model overview*

As before, Abaqus was used to simulate a steel pipe fixed at both ends and subject to loading 0.2m from one end, (Figure 4.12). The pipe and ball models were both simulated as three dimensional, elastically deformable steel solids. Both the steel ball and pipe sections were modelled as 3D homogenous linear elastic continua, and 8-node linear brick elements (C3D8) were used to discretize the model, linear elements being used on the assumption that the stresses/displacements caused by the deformation and the propagating wave were within the elastic range. The stresses/displacements at all intermediate locations were obtained by linear interpolation between the corresponding corner nodes [148]. In addition, a full integration was chosen rather than a reduced integration and this was to avoid the excitation of any zero-energy or spurious modes in the model. As before, elements of size 0.01mm and time step of 1×10^{-9} seconds were used for all the dropped object FE simulations. Stress time-histories were recorded at a distance of 0.5m from the location of impact with each simulation running for a total time of 2s. As the ball bearing was expected to make multiple contacts with the pipe, the general contact algorithm in Abaqus was used as this automatically allows node-to-face and edge-to-edge contact so that all element faces experienced contact on all sides. In addition, this interaction property allowed the number of simultaneous contacts per slave node to be correctly captured.

7.2.2 *Simulation Results*

Just as with the corresponding experiments, the simulated results were recorded as time series, which start when the source is activated. The stress time signals obtained from the simulations at S_1 for 0.3g, 3 and 17g balls dropped from 0.1m, 0.2m and 0.3m heights are shown in Figure 7.17, 7.18 and 7.19, respectively, for the first 2 seconds. Comparing these with the corresponding experiments (Figures 7.1 to 7.3) shows a number of similarities and a number of differences. Most obviously, the duration of the individual bounces is far longer in the simulations, most noticeably for the lightest ball. This can be attributed to the undamped reverberation of the AE wave in the simulations and this is supported by the periodicity observed in the individual bounces (seen most clearly in Figure 7.18a), which correspond roughly to the return times of pencil lead break experiments and simulations observed in Chapter 6. Some of the other differences, such as the lack of attenuation in consecutive bounces and the different bounce rates between

simulations and experiment are less easy to explain at the level of temporal resolution of the simulations.

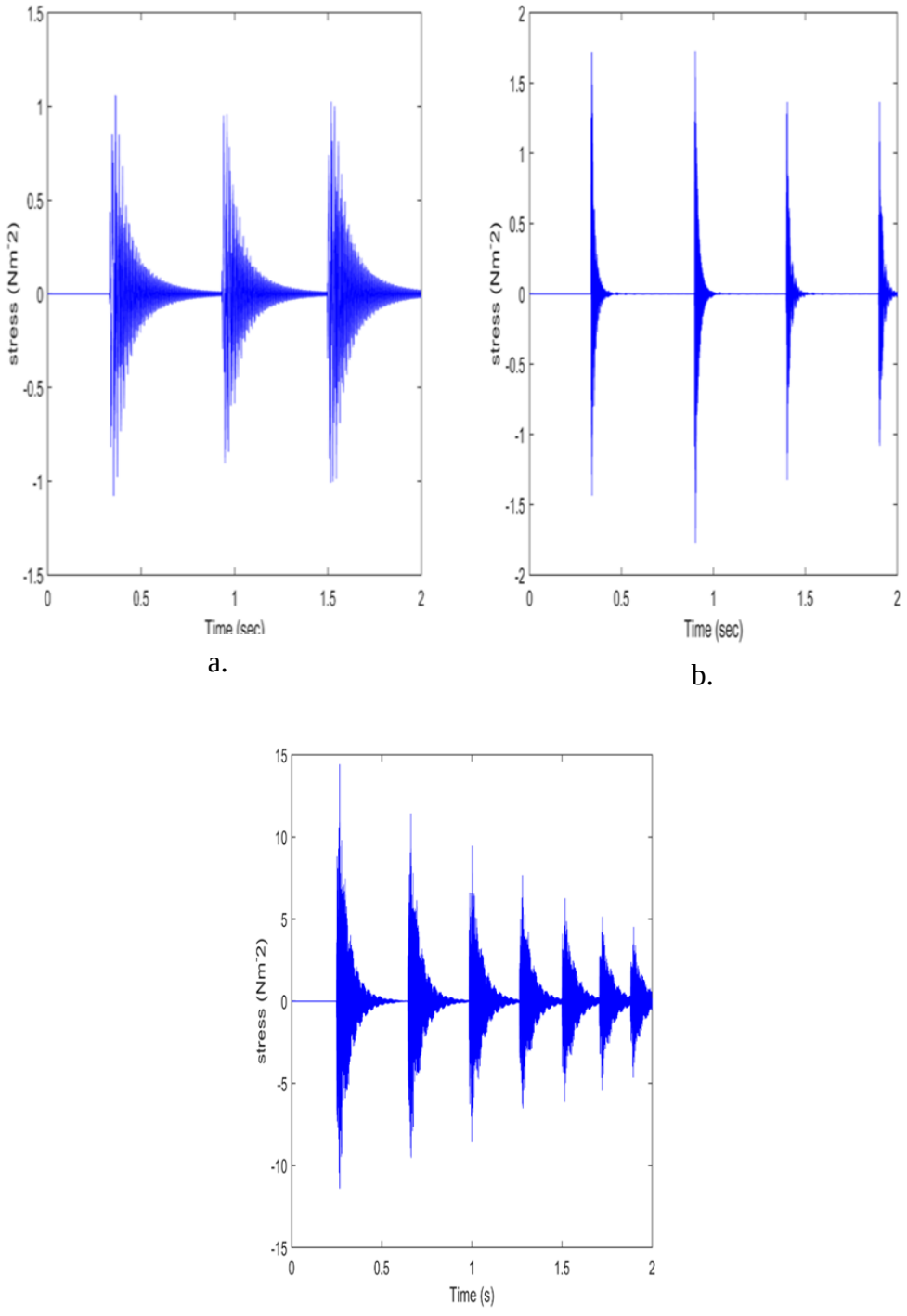

Figure 7-17: Time series of Cauchy stress for virtual sensors at 0.5m from the simulated source on a pipe for balls dropped from 10cm height a) 0.3g b) 3g c) 17g

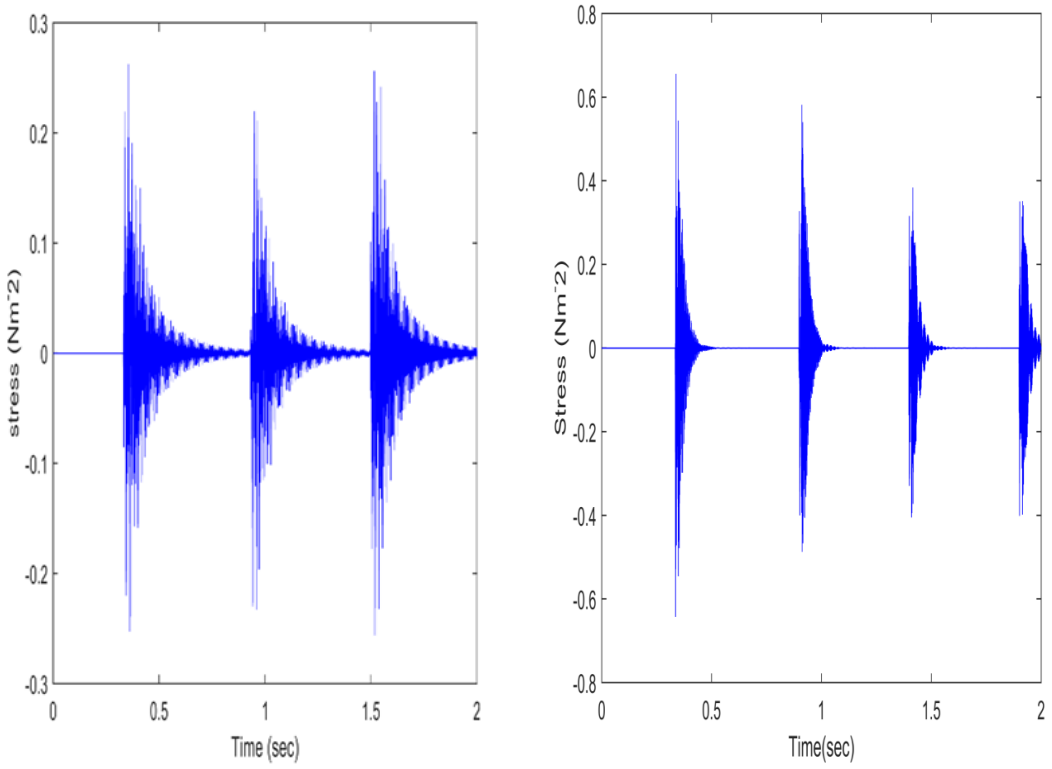

a. b.

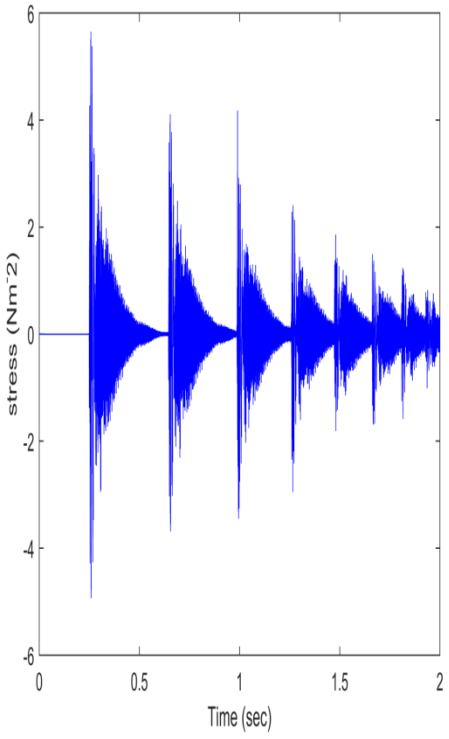

c.

Figure 7-18: *Time series of Cauchy stress for virtual sensors at 0.5m from the simulated source on a pipe for balls dropped from 20cm height a) 0.3g b) 3g c) 17g*

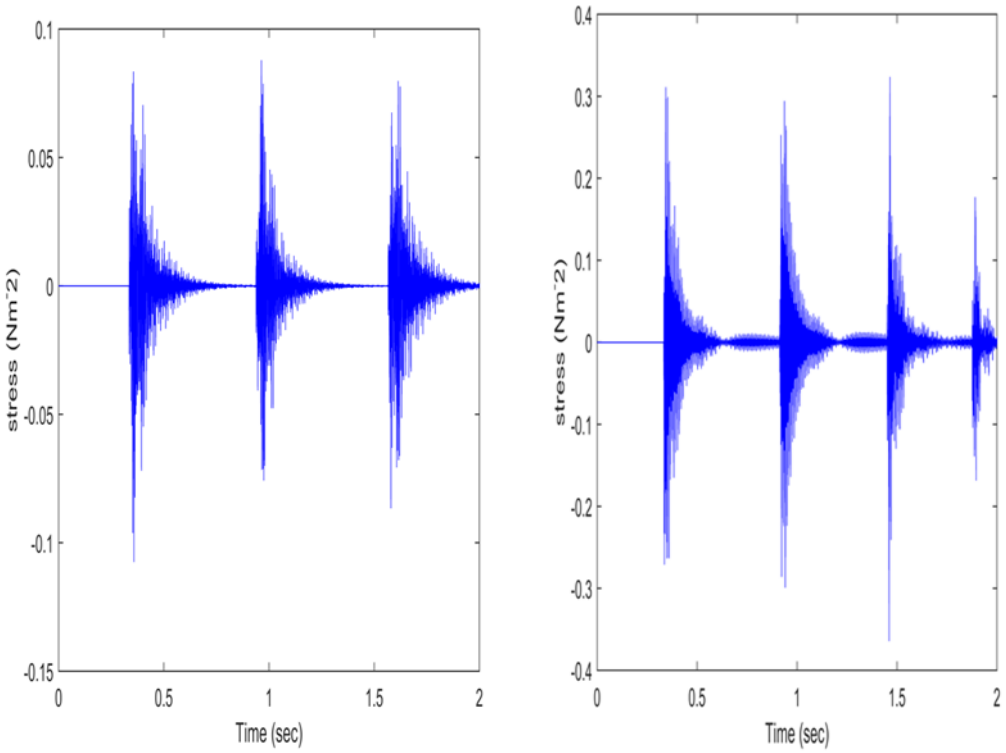

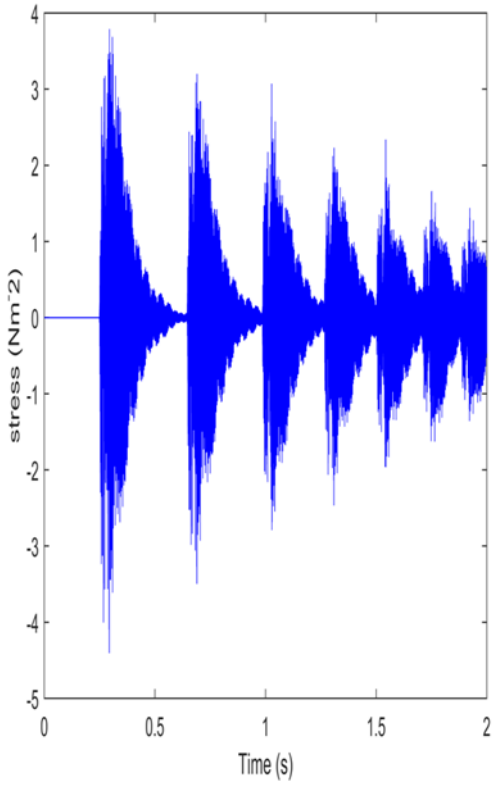

Figure 7-19: *Time series of Cauchy stress for virtual sensors at 0.5m from the simulated source on a pipe for balls dropped from 30cm height a) 0.3g b) 3g c) 17 g*

Figures 7-20, 7-21 and 7-22 show the stress time signals for the first bounce for the plots shown in Figures 7-17 to 7-19. Whereas the general amplitude increases with ball mass, as might be expected, it decreases with drop height for a given ball size. There are also some rather unexpected types if behaviour, such as the large numbers of zeroes seen in Figure 7.20c and some peculiarities in the short timescale responses, which indicate that the simulations are not working entirely as intended, probably due to the limited temporal resolution imposed by the computational time limitations and time step size. Given these limitations, it was decided only to analyse the data at the long- and medium-timescales.

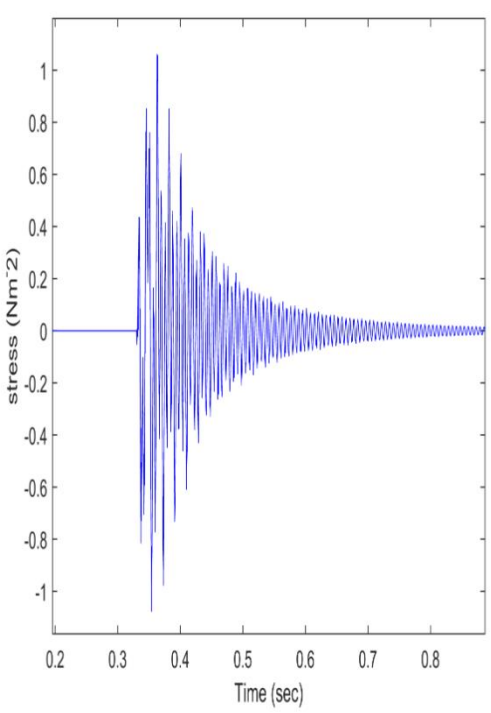

a.

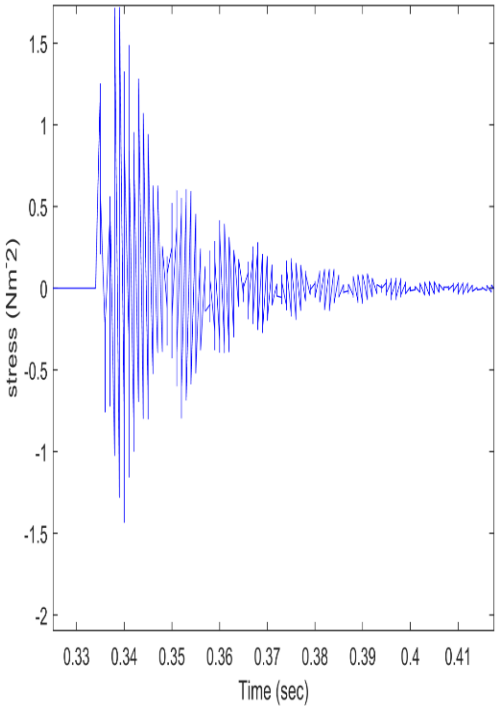

b.

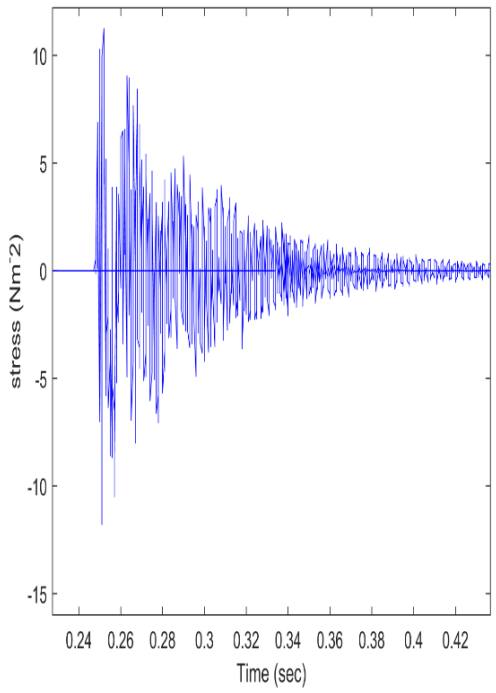

c.

Figure 7-20: *Raw medium time series of Cauchy stress for virtual sensors at 0.5m from the simulated source on a pipe for balls dropped from 10cm height a) 0.3g b) 3g c) 17g*

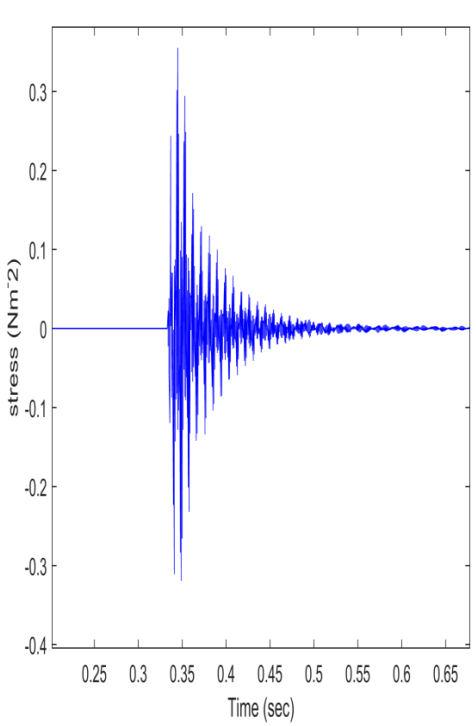

a)

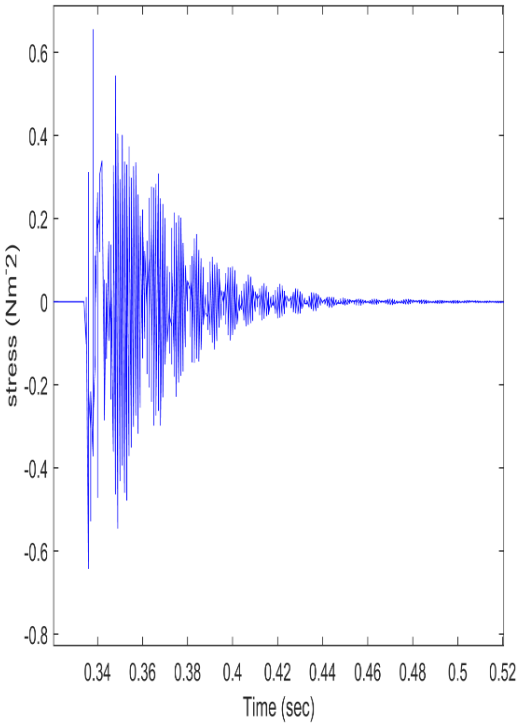

b)

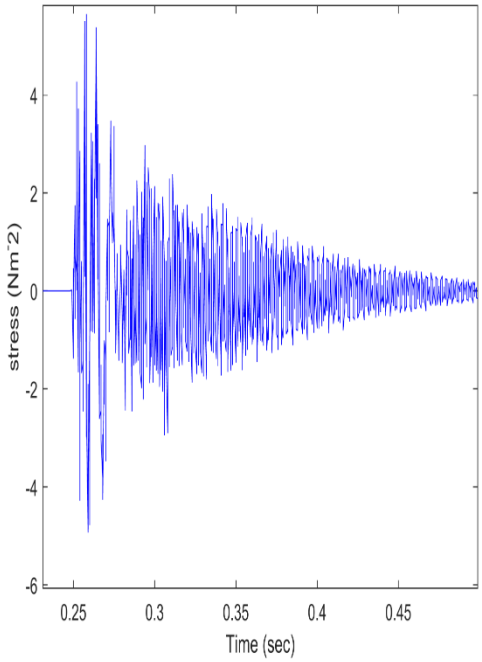

c)

Figure 7-21: *Raw medium time series of Cauchy stress for virtual sensors at 0.5m from the simulated source on a pipe for balls dropped from 20cm height a) 0.3g b) 3g c) 17g*

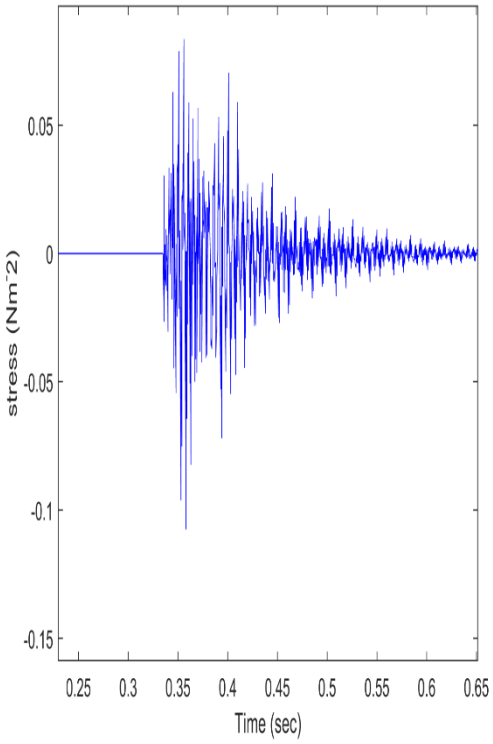

a.

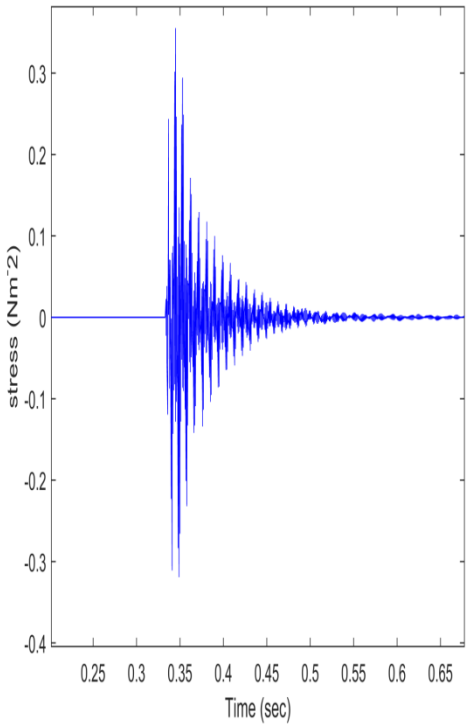

b.

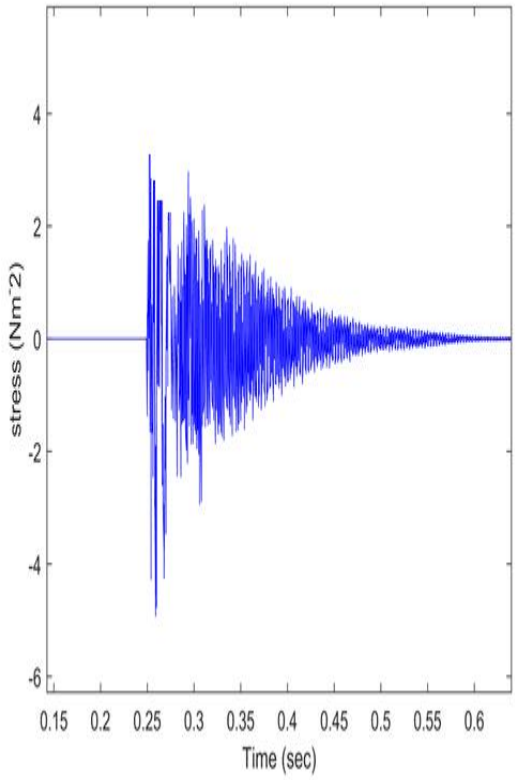

c.

Figure 7-22: *Raw medium time series of Cauchy stress for virtual sensors at 0.5m from the simulated source on a pipe for balls dropped from 30cm height a) 0.3g b) 3g c) 17g*

7.2.3 *Comparison of simulations with experiments*

Just as with the measurements, the first four bounces in the simulations were analysed and both the measured and incident energy were obtained as explained in section 5.3 for all nine combinations. Figures 7.23 to 7.25 show the relationship between the measured energy and incident energy for all three masses for each of the drop heights. In contrast with the measurements, there is very little difference in calculated incident energy between bounces, which is not surprising, since the coefficient of restitution for the simulations is unity. Similarly, the simulated energy for subsequent bounces is generally only about 10-20% different between the four bounces, which is within the error band of the experiments for any one bounce of the dropped ball bearing and it can be seen that as with the experiments, the measured energy increases with dropped object mass.

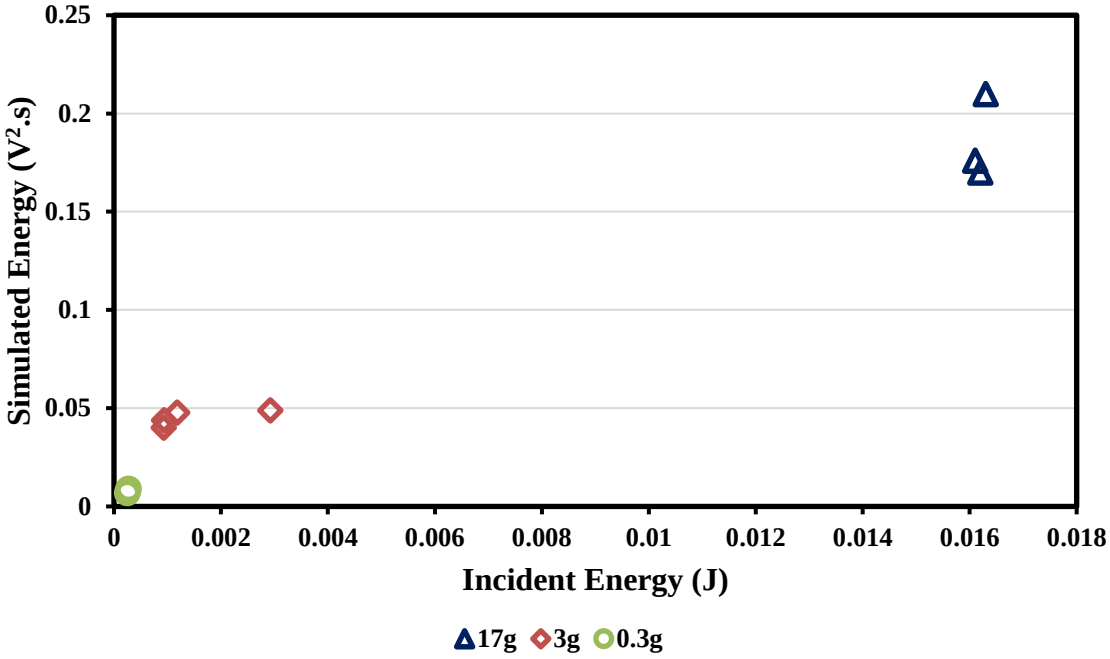

Figure 7-23: *Plot of simulated energy vs incident energy in the first four bounces dropped from 10cm height for the three ball sizes*

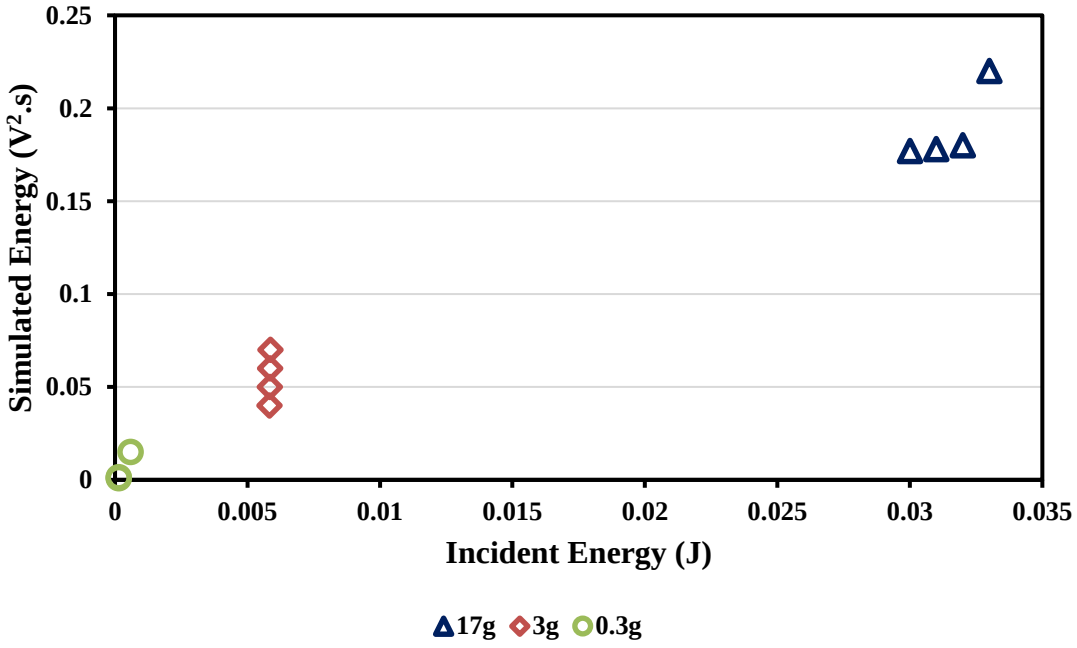

Figure 7-24: *Plot of simulated energy vs incident energy in the first four bounces dropped from 20cm height for the three ball sizes*

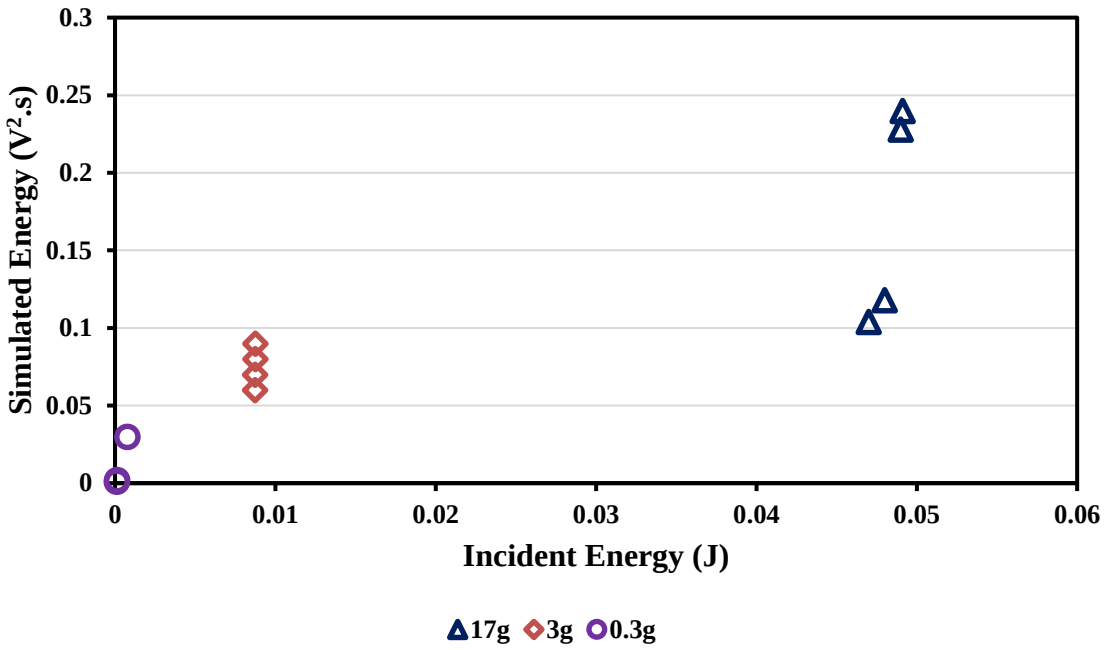

Figure 7-25: *Plot of simulated energy vs incident energy in the first four bounces dropped from 30cm height for the three ball sizes*

Figure 7.26 shows the relationship between the measured energy and incident energy for all three masses for all of the drop heights. Again, in contrast with the measurements, the increase in measured energy with incident energy is continuous across the entire range studied. Notwithstanding the limitations of the simulations, this would suggest that the measurements are a true reflection of the actual practical interaction between ball, plate and pipe including the effects of restitution and plasticity.

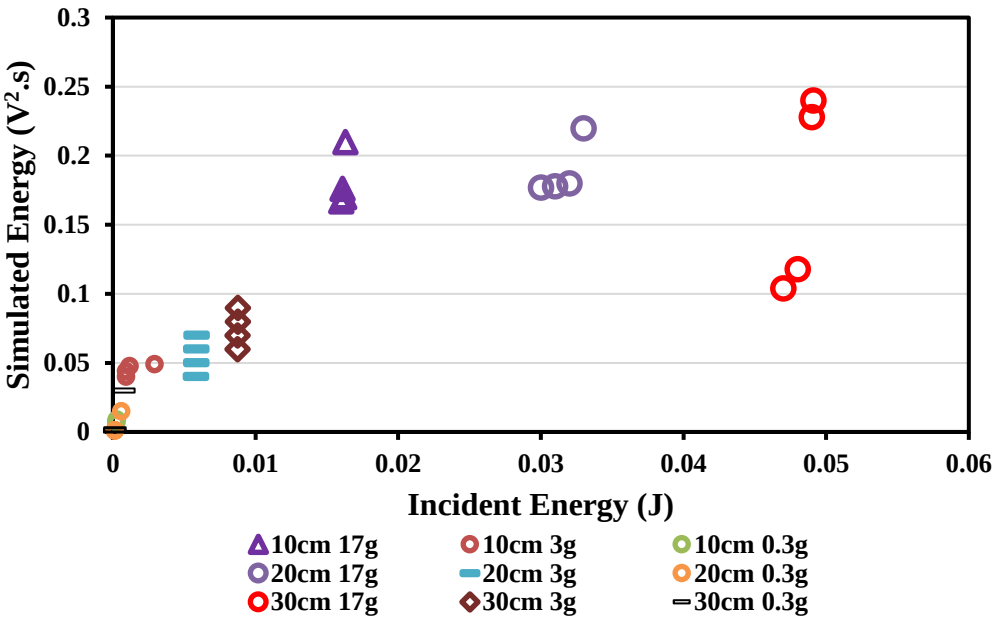

Figure 7-26: *Plot of simulated vs incident energy for the first four bounces for all the drop heights and all three-ball sizes*

7.3 Summary of findings

The main aim of the analysis in this chapter was to compare the experimental and simulated AE waves propagating along a steel pipe subjected to different ball bearing drop sizes and heights. The ball drops were chosen as a reproducible model for a source extended in time. As such, cross-reference has to be made to both Chapters 5 and 6, for dropped objects onto the relatively simple reference object and for impulsive sources on the pipe, respectively. The main findings are:

7.3.1 The experiments and simulations each had limitations, which would have made their comparison difficult without the foregoing analyses in Chapters 5 and 6. For practical reasons, the objects were dropped onto the pipe through a flat plate coupled to the surface, so a comparison with the relatively "clean" dropped object experiments analysed in Chapter 5 was necessary. Also, the dropped object simulations threw up some challenges with computational noise, which necessitated comparison with the simulations in Chapter 6 for the simpler impulsive sources.

7.3.2 The experiments and simulations exhibited the expected long-timescale behaviour with a burst of AE signalling the first landing and several subsequent bursts corresponding to the ball bouncing upwards and returning to the surface. In comparison with the

equivalent experiments on the flat cylindrical surface, the ball drops on the pipe exhibited a longer burst with each bounce and somewhat more erratic behaviour with subsequent bounces, much as might be expected from a see-sawing effect if the ball does not impact exactly on the contact line between ball and plate. This effect was certainly more evident for the larger ball masses and drop heights.

7.3.3 The experimental results were processed in the same way as for the drops onto the cylinder, yielding measured energy values at long-timescale of around 1sec (several bounces), medium-timescale of around 0.1sec (one bounce) and short-timescale of around 100μsec (section of propagating waveform uncontaminated by reflections). Over the range where both were measured, the relationship between the estimated incident energy (from mass and drop- or rebound-height) and the measured energy was similar to that for the reference object, although a little more erratic.

7.3.4 The experimental results for the entire range of drop heights and ball masses exhibited a monotonically increasing relationship between incident energy and measured energy at all three timescales, but with a decreasing gradient with increasing incident energy. The increase in measured energy could be associated with the increasing momentum change as drop height and/or mass increase, whereas the decrease in gradient could be attributed to changes in coefficient of restitution associated with plastic deformation.

7.3.5 The experimental and simulation results could only be compared at the long- and medium-timescales. At both timescales, the relationship between measured or simulated energy and estimated incident energy increased monotonically, and the differences could be attributed to the practical aspects of the experiments, including the see-sawing effect described above and changes in coefficient of restitution associated with plastic deformation.

Chapter 8- Conclusions and Future Work

This chapter brings together the findings of Chapters 5, 6 and 7 to address the original technological aim. Broadly, the aim was to assess the extent to which an AE time record from one or more sensors placed on the external surface of a pipeline could be used to discern the details of an external mechanical disturbance at some distance from the sensor.

The conclusions can be divided into three inter-related strands; the experiments on dropped objects as an exemplar source extended in time, the simulations of impulsive sources on and, finally, simulations of dropped objects. These are dealt with in turn below, followed by an overall assessment of contribution towards the overall aim. Finally, recommendations are made for future work which might answer the outstanding questions.

8.1 Dropped Objects

The ball drops onto the solid cylinder produced signals in which the first arrival and several rebounds could be discerned over a period of around 1 second. Each impact produced a burst of duration around 0.1 second, sufficient time for multiple reflections from the bottom face and edge of the cylinder. Despite this, there were clear relationships between the incident energy of the dropped object and the measured AE energy, confirming that these would be suitable sources to give a model for practical mechanical disturbances on the pipe.

For practical reasons, the objects were dropped onto the pipe through a flat plate coupled to the surface and again gave measured energy values at the long-timescale of around 1sec (several bounces), medium-timescale of around 0.1sec (one bounce) and short-timescale of around 100μsec (section of propagating waveform uncontaminated by reflections). As for the solid cylinder, here was a monotonically increasing relationship between incident energy and measured energy at all three timescales, but with a decreasing gradient with increasing incident energy. The increase in measured energy could be associated with the increasing momentum change as drop height and/or mass increase, whereas the decrease in gradient could be attributed to changes in coefficient of restitution associated with plastic deformation.

8.2 Simulation of Impulsive Sources

The available analytical solutions for AE propagation in cylinders were helpful in giving general guidance on the interpretation of simulated or measured AE responses, but only for the very simple case of a step-unload. In the reference object, with sensors equidistant, and on the same face as the source, the first wave to arrive was a lower amplitude, lower frequency Rayleigh wave, followed by pulses of higher frequency corresponding to subsequent reflections of a P-wave from the lower surface of the cylinder. In both experiments and simulations, the measured AE in the block quickly became contaminated with reflection for the edges of the block and its bottom surface.

The simulated and measured signals on the reference object exhibited similar behaviour in the first 25-30 μs. Thereafter, the measured signals were much cleaner, and this is most likely associated with the energy losses associated with reflections, for which there is no provision in the simulations. This finding indicates that the simulations, as they stand, are helpful in interpreting the structure of the source only in the early stages of event arrival for such small objects.

Although the frequency domain of the simulations was truncated due to the time-step chosen, a necessary compromise between simulation precision and computation time, it was still possible to determine and appropriate range of unload rate to use in the simulations on the pipe.

The PLB experiments and matching FE simulations on the pipe provided an assessment of the distortion of a simple impulsive source as it travels along a pipe. Comparison of the main set of simulations with experimental results indicated that the unloading rate corresponding to a PLB is at the high end of those investigated. Although the frequency content of the resulting wave is not highly sensitive to unloading rate, the amplitude of the simulated signal was. A comparison of the uncontaminated (first few tens of microseconds) of the simulated and experimental waveforms confirmed that the first arrival is consistent with a wave speed of around $5000 ms^{-1}$. However, the structure thereafter was complex for the experimental results, suggesting that the real wave generated by a pencil-lead break is probably not due to a simple compressive direct stress unload.

8.3 Simulation of Time-extended Sources

The experimental and simulation results could only be compared at the long- and medium-timescales. At both timescales, the relationship between measured or simulated energy and estimated incident energy increased monotonically, and the differences could be attributed to the practical aspects of the experiments, including changes in coefficient of restitution associated with plastic deformation.

Simulation of the ball-drop experiments at the short timescale met with little success, partly due to the intense requirements on temporal resolution for both the wave generation and the dynamic surface interaction. Nevertheless, the ability to simulate the medium- and long-timescale signals meets most of the thesis objectives and solving the details of interaction-generated AE would require a more intensive study, involving a greater range of damage inducing events.

8.4 General Implications for Monitoring Pipes

The work has been carried out at a relatively small scale, but a number of conclusions can be drawn for practical use in pipeline monitoring.

First of all, AE is propagated in pipes as waves of complex structure, but which can be divided into “fast” and “slow” components, each with a specific frequency structure. As the source-sensor distance increases, the faster components form a larger part of the record. This is important for impulsive, or near-impulsive sources, where it may be necessary to establish the frequency content of the AE (for example in leak detections), but is less likely to be important in heavy, or longer-timescale sources, where the energy content is more important.

Secondly, attenuation is likely to be important in any practical application, as, to be cost effective, sensors would have to be spaced kilometres or tens of kilometre apart for monitoring purposes. It is known from the literature that this is still feasible, although the effects of selective attenuation of some frequencies and separation of different wave speeds would need to be understood.

Thirdly, in the relatively small object studied here, reflections from ends and edges were detectable. In longer structures, these issues would be different, as would the effect of the inner and outer environments of the pipe, especially if either contained liquid.

Finally, although there was some suggestion that the heavier ball impacts might have involved plastic deformation, such events would be of little interest to a pipeline operator. Mechanical interactions which are of industrial interest are likely to involve such sources as excavators, drills or fishing gear and there would need to be a way of determining the severity of the event in terms of damage to the pipe.

8.5 Recommendations for Future Work

This work has developed methodologies to address the practical problem, although there remain a number of key issues to be addressed:

8.5.1 Experiments on near full-scale pipes on longer lengths (tens of metres) would help to understand attenuation at practical scales. Such experiments could also include variations of the internal and external environment of the pipe.

8.5.2 Currently, the simulations contain no attenuation mechanism apart from geometrical attenuation, which is small in pipes. Comparison of simulations with experiments of the type suggested in 8.5.1 would allow a realistic attenuation model to be developed.

8.5.3 The dropped objects, whilst providing a model of a source which is extended in time, were not of a severity that would cause concern for the structure of the pipe. A series of larger-scale tests with damaging mechanical impacts would allow a severity characteristic to be developed for extensive plastic deformation and fracture.

8.5.4 The simulations were not able to cope with the dynamics of the ball impacts and did not contain any failure criteria such as plastic deformation or fracture. Enhancing the simulations in conjunction with the experiments suggested in 8.5.3 would allow a damage severity assessment to be made.

References

1. Haastrup, P. and L.H. Brockhoff, *Reliability of accident case histories concerning hazardous chemicals: an analysis of uncertainty and quality aspects.* Journal of hazardous materials, 1991. **27**(3): p. 339-350.

2. DeWolf, G.B., *Process safety management in the pipeline industry: parallels and differences between the pipeline integrity management (IMP) rule of the Office of Pipeline Safety and the PSM/RMP approach for process facilities.* Journal of hazardous materials, 2003. **104**(1-3): p. 169-192.

3. Shehadeh, M., J. Steel, and R. Reuben, *Acoustic emission source location for steel pipe and pipeline applications: the role of arrival time estimation.* Proceedings of the Institution of Mechanical Engineers, Part E: Journal of Process Mechanical Engineering, 2006. **220**(2): p. 121-133.

4. Vidya Sagar, R., B. Raghu Prasad, and R. Sharma, *Evaluation of damage in reinforced concrete bridge beams using acoustic emission technique.* Nondestructive Testing and Evaluation, 2012. **27**(2): p. 95-108.

5. Nivesrangsan, P.,*Multi-source, multi-sensor approaches to diesel engine monitoring using acoustic emission*. 2004, Heriot-Watt University.

6. Webster, J., et al., *Acoustic emission for process control and monitoring of surface integrity during grinding.* CIRP Annals-Manufacturing Technology, 1994. **43**(1): p. 299-304.

7. Woo, S.-C., et al., *Correlation of fracture processes and damage mechanisms of armor structural materials under high strain rates with acoustic emission characteristics.* International journal of impact engineering, 2014. **63**: p. 29-42.

8. Hase, A., et al., *The relationship between acoustic emission signals and cutting phenomena in turning process.* The International Journal of Advanced Manufacturing Technology, 2014. **70**(5-8): p. 947-955.

9. Roberts, T. and M. Talebzadeh, *Acoustic emission monitoring of fatigue crack propagation.* Journal of Constructional Steel Research, 2003. **59**(6): p. 695-712.

10. Berkovits, A. and D. Fang, *Study of fatigue crack characteristics by acoustic emission.* Engineering Fracture Mechanics, 1995. **51**(3): p. 401-416.

11. Shehadeh, M.F., *Monitoring of long steel pipes using acoustic emission*. 2006, Heriot-Watt University.

12. Miller, R., et al., *A reference standard for the development of acoustic emission pipeline leak detection techniques.* NDT & E International, 1999. **32**(1): p. 1-8.

13. Crivelli, D., *Structural health monitoring with acoustic emission and neural networks*. 2014, Italy.

14. Crisfield, M.A., J.J. Remmers, and C.V. Verhoosel, *Nonlinear finite element analysis of solids and structures*. 2012: John Wiley & Sons.

15. Richmond, B.G., et al., *Finite element analysis in functional morphology.* The Anatomical Record, 2005. **283**(2): p. 259-274.

16. Wevers, M., *Listening to the sound of materials: acoustic emission for the analysis of material behaviour.* NDT & E International, 1997. **30**(2): p. 99-106.

17. Morton, T., R. Harrington, and J. Bjeletich, *Acoustic emissions of fatigue crack growth.* Engineering fracture mechanics, 1973. **5**(3): p. 691-697.

18. Prosser, W.H., M.R. Gorman, and D.H. Humes, *Acoustic emission signals in thin plates produced by impact damage.* 1999.

19. *EWGAE codes for acoustic emission examination: Code II — leak detection Code III — examination of small parts, in NDT international. 1984. p. 215*, 1984.

20. Thakkar, N., J. Steel, and R. Reuben, *Rail–wheel interaction monitoring using Acoustic Emission: A laboratory study of normal rolling signals with natural rail defects.* Mechanical Systems and Signal Processing, 2010. **24**(1): p. 256-266.

21. Nair, A. and C. Cai, *Acoustic emission monitoring of bridges: Review and case studies.* Engineering structures, 2010. **32**(6): p. 1704-1714.

22. Ukpai, J.I., et al., *Exploring the erosive wear of X65 carbon steel by acoustic emission method.* Wear, 2013. **301**(1-2): p. 370-382.

23. Fregonese, M., et al., *Initiation and propagation steps in pitting corrosion of austenitic stainless steels: monitoring by acoustic emission.* Corrosion science, 2001. **43**(4): p. 627-641.

24. Ding, Y., R. Reuben, and J. Steel, *A new method for waveform analysis for estimating AE wave arrival times using wavelet decomposition.* NDT & E International, 2004. **37**(4): p. 279-290.

25. El-Ghamry, M., R. Reuben, and J. Steel, *The development of automated pattern recognition and statistical feature isolation techniques for the diagnosis of reciprocating machinery faults using acoustic emission.* Mechanical Systems and Signal Processing, 2003. **17**(4): p. 805-823.

26. Singh, S.K., K. Srinivasan, and D. Chakraborty, *Acoustic emission studies on metallic specimen under tensile loading.* Materials & design, 2003. **24**(6): p. 471-481.

27. Gautschi, D.-I.E.G., *Acoustic Emission Sensors*, in *Piezoelectric Sensorics*. 2002, Springer. p. 199-207.

28. Brown, E., et al., *Acoustic emission source discrimination using a piezopolymer based sensor.* Materials evaluation, 1999. **57**(5): p. 515-520.

29. Theobald, P., et al., *Acoustic emission transducers—development of a facility for traceable out-of-plane displacement calibration.* ultrasonics, 2005. **43**(5): p. 343-350.

30. Vallen, H., *AE testing fundamentals, equipment, applications.* Journal of Nondestructive Testing(Germany), 2002. **7**(9): p. 1-30.

31. ASTM, A. *standard guide for determining the reproducability of acoustic emission sensor responce, 1994*. in *American society for testing and materials*.

32. Mostafapour, A. and S. Davoudi, *Analysis of leakage in high pressure pipe using acoustic emission method.* Applied Acoustics, 2013. **74**(3): p. 335-342.

33. Droubi, M., R. Reuben, and G. White, *Acoustic emission monitoring of abrasive particle impacts on carbon steel.* Proceedings of the Institution of Mechanical Engineers, Part E: Journal of Process Mechanical Engineering, 2012. **226**(3): p. 187-204.

34. Burstein, G. and K. Sasaki, *Effect of impact angle on the slurry erosion–corrosion of 304L stainless steel.* Wear, 2000. **240**(1): p. 80-94.

35. Morton, T., R. Harrington, and J. Bjeletich, *Acoustic emissions of fatigue crack growth.* Engineering fracture mechanics, 1973. **5**(3): p. 691IN17693-692IN18697.

36. Dornfeld, D.A. and E. Kannatey-Asibu Jr, *Quantitative relationships for acoustic emission from orthogonal metal cutting.* Transactions of the ASME, Journal of Engineering for Industry, 1981. **103**: p. 330-340.

37. Grandt Jr, A.F., *Fundamentals of structural integrity: damage tolerant design and nondestructive evaluation*. 2003: John Wiley & Sons.

38. Chang, F.-K., *Structural health monitoring 2000*. 1999: CRC Press.

39. Hamstad, M.A., *A review: acoustic emission, a tool for composite-materials studies.* Experimental Mechanics, 1986. **26**(1): p. 7-13.

40. Ward, C., *On-Line determination of component quality using acoustic emission*. 2011, Heriot-Watt University.

41. Liptai, R., H. Dunegan, and C. Tatro, *Acoustic emissions generated during phase transformations in metals and alloys*. 1968, California Univ., Livermore. Lawrence Radiation Lab.

42. Bechara, W., et al., *Stochastic approach to noise modeling for free turbulent flows.* AIAA journal, 1994. **32**(3): p. 455-463.

43. Sih, G.C., *Strain-energy-density factor applied to mixed mode crack problems.* International Journal of fracture, 1974. **10**(3): p. 305-321.

44. Irwin, G.R., *Analysis of stresses and strains near the end of a crack traversing a plate.* Journal of applied mechanics, 1957. **24**(3): p. 361-364.

45. Momber, A., R. Mohan, and R. Kovacevic, *On-line analysis of hydro-abrasive erosion of pre-cracked materials by acoustic emission.* Theoretical and Applied Fracture Mechanics, 1999. **31**(1): p. 1-17.

46. Miller, R., et al., *A reference standard for the development of acoustic emission pipeline leak detection techniques.* NDT & E International, 1999. **32**(1): p. 1-8.

47. Wang, X., et al., *Wavelet packet analysis for the propagation of acoustic emission signals across turbine runners.* NDT & E International, 2009. **42**(1): p. 42-46.

48. Sun, L., *Mathematical modeling of the flow in a pipeline with a leak.* Mathematics and computers in simulation, 2012. **82**(11): p. 2253-2267.

49. Feng, J. and H. Zhang, *Algorithm of pipeline leak detection based on discrete incremental clustering method.* Computational Intelligence, 2006: p. 602-607.

50. Emara-Shabaik, H., Y. Khulief, and I. Hussaini, *A non-linear multiple-model state estimation scheme for pipeline leak detection and isolation.* Proceedings of the Institution of Mechanical Engineers, Part I: Journal of Systems and Control Engineering, 2002. **216**(6): p. 497-512.

51. Ben-Mansour, R., et al., *Computational fluid dynamic simulation of small leaks in water pipelines for direct leak pressure transduction.* Computers & Fluids, 2012. **57**: p. 110-123.

52. Kolsky, H., *Stress waves in solids.* Journal of sound and Vibration, 1964. **1**(1): p. 88-110.

53. Meyers, M.A., *Dynamic Behavior of Materials*.1994: John Wiley & Sons, Inc.

54. Holroyd, T.J., *The acoustic emission & ultrasonic monitoring handbook*. 2000: Coxmoor Publishing Company.

55. Pollock, A.A., *Classical wave theory in practical AE testing.* Progress in Acoustic Emission III-JAP Society of Non-Destructive Testing, 1986: p. 708-721.

56. Nabil, M., *Predicting AE attenuation in Solids using Ray - Tracing within a 3D Solid Model*, in *Mechanical Engineering*. 2012, Heriot-Watt University: Edinburgh. p. 230.

57. Lee, B.C. and W.J. Staszewski, *Modelling of Lamb waves for damage detection in metallic structures: Part II. Wave interactions with damage.* Smart Materials and Structures, 2003. **12**(5): p. 815.

58. Jeong, H.D., H.-J. Shin, and J.L. Rose, *Detection of defects in a thin steel plate using ultrasonic guided wave.* Journal of the Korean Society for Nondestructive Testing, 1998. **18**(6): p. 445-454.

59. Wevers, M., *One sensor linear location of acoustic emission events using plate wave theories.* Materials Science and Engineering: A, 1999. **265**(1): p. 254-261.

60. Holford, K.M. and D. Carter. *Acoustic emission source location*. in *Key Engineering Materials*. 1999. Trans Tech Publ.

61. Ukpai, J., R. Barker, and A. Neville. *A combined electrochemical and acoustic emission technique for mechanistic and quantitative evaluation of erosion-corrosion and its components*. in *NACE-International Corrosion Conference Series*. 2014. NACE International.

62. Michaels, J., T. Michaels, and W. Sachse, *Applications of deconvolution to acoustic emission signal analysis.* Materials Evaluation, 1981. **39**(11): p. 1032-1036.

63. Shehadeh, M., et al., *Aspects of acoustic emission attenuation in steel pipes subject to different internal and external environments.* Proceedings of the Institution of Mechanical Engineers, Part E: Journal of Process Mechanical Engineering, 2008. **222**(1): p. 41-54.

64. Bolz, R.E., *CRC handbook of tables for applied engineering science*. 1973: CRC press.

65. Miller, R.K. and P. McIntire, *Nondestructive Testing Handbook. Vol. 5: Acoustic Emission Testing.* American Society for Nondestructive Testing, 4153 Arlingate Plaza, 28518, Columbus, Ohio 43228, USA, 1987. 603, 1987.

66. Ceranoglu, A. and Y.-H. Pao, *Propagation of Elastic Pulses and Acoustic Emission in a Plate—Part 1: Theory.* Journal of Applied Mechanics, 1981. **48**(1): p. 125-132.

67. Hudson, D.E., *Internal friction in metals*. 1942, California Institute of Technology.

68. James, D.R. and S.H. Carpenter, *Relationship between acoustic emission and dislocation kinetics in crystalline solids.* Journal of Applied Physics, 1971. **42**(12): p. 4685-4697.

69. Mainardi, F., *Fractional calculus and waves in linear viscoelasticity: an introduction to mathematical models*. 2010: World Scientific.

70. Newton, R.G., *Scattering theory of waves and particles*. 2013: Springer Science & Business Media.

71. Aggelis, D. and T. Matikas, *Effect of plate wave dispersion on the acoustic emission parameters in metals.* Computers & Structures, 2012. **98**: p. 17-22.

72. Nivesrangsan, P., J. Steel, and R. Reuben, *AE mapping of engines for spatially located time series.* Mechanical Systems and Signal Processing, 2005. **19**(5): p. 1034-1054.

73. Asamene, K., L. Hudson, and M. Sundaresan, *Influence of attenuation on acoustic emission signals in carbon fiber reinforced polymer panels.* Ultrasonics, 2015. **59**: p. 86-93.

74. Hsu, N.N. and S.C. Hardy, *Experiments in acoustic emission waveform analysis for characterization of AE sources, sensors and structures.* Elastic waves and non-destructive testing of materials, 1978: p. 85-106.

75. Pollock, A.A. and R.W. Stephens, *Waveform and frequency spectra of acoustic emissions.* The Journal of the Acoustical Society of America, 1971. **49**(1A): p. 110-110.

76. El-Shaib, M., R. Reuben, and T. Lim, *Predicting acoustic emission attenuation in small steel blocks using a ray tracing technique.* Insight-Non-Destructive Testing and Condition Monitoring, 2012. **54**(12): p. 673-680.

77. Mao, Y.L., G. Kinsman, and W. Duley, *Real- Time Fast Fourier Transform Analysis of Acoustic Emission during CO2 Laser Welding of Materials.* Journal of laser applications, 1993. **5**(2): p. 17-22.

78. Harčarik, T., J. Bocko, and K. Masláková, *Frequency analysis of acoustic signal using the Fast Fourier Transformation in MATLAB.* Procedia Engineering, 2012. **48**: p. 199-204.

79. Kuljanic, E., M. Sortino, and G. Totis, *Multisensor approaches for chatter detection in milling.* Journal of Sound and Vibration, 2008. **312**(4): p. 672-693.

80. Cohen, L., *Time-frequency distributions-a review.* Proceedings of the IEEE, 1989. **77**(7): p. 941-981.

81. Suzuki, H., et al., *Wavelet transform of acoustic emission signals.* Journal of Acoustic Emission, 1996. **14**: p. 69-84.

82. Hamstad, M., A. O'Gallagher, and J. Gary, *A wavelet transform applied to acoustic emission.* J. Acoust. Emiss, 2002. **20**: p. 39-61.

83. Jiao, J., et al., *Application of wavelet transform on modal acoustic emission source location in thin plates with one sensor.* International Journal of Pressure Vessels and Piping, 2004. **81**(5): p. 427-431.

84. Gu, D.S. and B.K. Choi, *Machinery Faults Detection Using Acoustic Emission Signal*, in *Acoustic Waves-From Microdevices to Helioseismology*. 2011, InTech.

85. Baxter, M.G., et al., *Delta T source location for acoustic emission.* Mechanical systems and signal processing, 2007. **21**(3): p. 1512-1520.

86. Ziola, S.M. and M.R. Gorman, *Source location in thin plates using cross-correlation.* The Journal of the Acoustical Society of America, 1991. **90**(5): p. 2551-2556.

87. Gorman, M.R. *Acoustic Emission for the 1990s*. in *Ultrasonics Symposium, 1991. Proceedings., IEEE 1991*. 1991. IEEE.

88. Mba, D., *Acoustic emissions and monitoring bearing health.* Tribology transactions, 2003. **46**(3): p. 447-451.

89. Gagar, D., et al., *New methods for onset detection of acoustic emission signals.* 2016.

90. Hamstad, M., A. O'Gallagher, and J. Gary, *A wavelet transform applied to acoustic emission.* J Acoust Emiss, 2002. **20**: p. 39-61.

91. Dahmene, F., et al., *On the modal acoustic emission testing of composite structure.* Composite Structures, 2016. **140**: p. 446-452.

92. Ni, Q.-Q. and M. Iwamoto, *Wavelet transform of acoustic emission signals in failure of model composites.* Engineering Fracture Mechanics, 2002. **69**(6): p. 717-728.

93. Promboon, Y., *Acoustic Emission Source Location*, in *Mechanical Engineering*. 2000, The University of Texas at Austin: Texas. p. 370.

94. Reuben, R.L., J.A. Steel, and M. Shehadeh, *Acoustic Emission Source Location for Steel Pipe and Pipeline Applications: The Role of Arrival Time Estimation.* Proceedings of the Institution of Mechanical Engineers, Part E: Journal of Process Mechanical Engineering, 2006. **220**(2): p. 121-133.

95. Gorman, M.R., *Plate Wave Acoustic Emission.* Journal of the Acoustical Society of America, 1991. **90**(1): p. 358-364.

96. Miller, R.K.a.M., P, *Nondestructive Testing Handbook*. Acoustic Emission Testing. Vol. 5. 1987, York.

97. Braginskii, A., B. Medvedev, and A. Platkov, *Amplitude-Frequency Location Procedure for Acoustic Emission.* Soviet Journal of Nondestructive Testing, 1989. **24**(9): p. 620-626.

98. Barat, P., P. Kalyanasundaram, and B. Raj, *Acoustic emission source location on a cylindrical surface.* NDT & E International, 1993. **26**(6): p. 295-297.

99. Carlin, B., *ultrasonics, 2nd edu*. 1960, McGraw Hill, New York.

100. Opydo, W., *Study of elastic waves of acoustic frequencies generated by surface partial discharges of solid insulators in vacuum.* Vacuum, 2004. **74**(1): p. 85-92.

101. Jeong, H. and Y.-S. Jang, *Fracture source location in thin plates using the wavelet transform of dispersive waves.* IEEE transactions on ultrasonics, ferroelectrics, and frequency control, 2000. **47**(3): p. 612-619.

102. Holford, K.M., et al., *A new methodology for automating acoustic emission detection of metallic fatigue fractures in highly demanding aerospace environments: An overview.* Progress in Aerospace Sciences, 2017. **90**: p. 1-11.

103. Bai, F., et al., *Comparison of alternatives to amplitude thresholding for onset detection of acoustic emission signals.* Mechanical Systems and Signal Processing, 2017. **84**: p. 717-730.

104. Ke, W., M. Castaings, and C. Bacon, *3D finite element simulations of an air-coupled ultrasonic NDT system.* NDT & E International, 2009. **42**(6): p. 524-533.

105. Gan, T., et al., *The use of broadband acoustic transducers and pulse-compression techniques for air-coupled ultrasonic imaging.* Ultrasonics, 2001. **39**(3): p. 181-194.

106. Ludwig, R.L., W. , *A finite-element study of ultrasonic wave propagation and scattering in an aluminum block* Materials Evaluation, 1998. **46**(1).

107. El-Shaib, M., et al., *Predicting Acoustic Emission Attenuation within solids by using Ray tracing technique in 3D modelling.*

108. Ceranoglu, A. and Y.-H. Pao, *Propagation of elastic pulses and acoustic emission in a plate—Part 2: Epicentral responses.* Journal of Applied Mechanics, 1981. **48**(1): p. 133-138.

109. Wilcox, P.D., et al. *Progress towards a forward model of the complete acoustic emission process*. in *Advanced Materials Research*. 2006. Trans Tech Publ.

110. Horn, M., *Acoustic emission source location by reverse ray tracing*. 1996, Google Patents.

111. Lim, T., et al. *Predicting AE attenuation in structures by geometric analysis*. in *Shape Modeling and Applications, 2005 International Conference*. 2005. IEEE.

112. El-Shaib, M.N., *Predicting acoustic emission attenuation in solids using ray-tracing within a 3D solid model*. 2013, Heriot-Watt University UK.

113. Delrue, S., et al., *Simulation study of the localization of a near-surface crack using an air-coupled ultrasonic sensor array.* Sensors, 2017. **17**(4): p. 930.

114. Rao, S.S., *The Finite Element Method in Engineering: Pergamon International Library of Science, Technology, Engineering and Social Studies*. 2013: Elsevier.

115. Koenig, H.A. and N. Davids, *Dynamical finite element analysis for elastic waves in beams and plates.* International Journal of Solids and Structures, 1968. **4**(6): p. 643-660.

116. Gorwade, C., et al., *Experimental and numerical analysis of stress wave propagation in polymers and the role of interfaces in armour systems.* Open Engineering, 2012. **2**(4): p. 578-584.

117. Sause, M.G. and S. Richler, *Finite element modelling of cracks as acoustic emission sources.* Journal of nondestructive evaluation, 2015. **34**(1): p. 4.

118. WH, P., H. MA, and J. Gary, *Finite Element and Plate Theory Modeling of Acoustic Emission Waveforms.* 1999.

119. Hamstad, M.A., *Small diameter waveguide for wideband acoustic emission.* J. Acoust. Emiss, 2006. **24**: p. 234-247.

120. Zelenyak, A.-M., M.A. Hamstad, and M.G. Sause, *Modeling of acoustic emission signal propagation in waveguides.* Sensors, 2015. **15**(5): p. 11805-11822.

121. Sause, M.G., *Investigation of pencil-lead breaks as acoustic emission sources.* Journal of acoustic emission, 2011. **29**.

122. Sause, M.G., M.A. Hamstad, and S. Horn, *Finite element modeling of conical acoustic emission sensors and corresponding experiments.* Sensors and Actuators A: Physical, 2012. **184**: p. 64-71.

123. Prosser, W., et al., *Reflections of AE waves in finite plates: finite element modeling and experimental measurements.* 1999.

124. Morscher, G.N. and A.L. Gyekenyesi, *The velocity and attenuation of acoustic emission waves in SiC/SiC composites loaded in tension.* Composites science and technology, 2002. **62**(9): p. 1171-1180.

125. Perduta, A. and R. Putanowicz, *Comparison of elastomer modelling in various FEM packages.* Procedia Engineering, 2015. **108**: p. 510-517.

126. Kolsky, H., *An investigation of the mechanical properties of materials at very high rates of loading.* Proceedings of the Physical Society. Section B, 1949. **62**(11): p. 676.

127. Tekriwal, P. and J. Mazumder, *Finite element analysis of three-dimensional transient heat transfer in GMA welding.* Welding Journal, 1988. **67**(7): p. 150s-156s.

128. Arias, A., J.A. Rodríguez-Martínez, and A. Rusinek, *Numerical simulations of impact behaviour of thin steel plates subjected to cylindrical, conical and hemispherical non-deformable projectiles.* Engineering Fracture Mechanics, 2008. **75**(6): p. 1635-1656.

129. Sadighi, M., et al., *Experimental and numerical investigation of metal type and thickness effects on the impact resistance of fiber metal laminates.* Applied Composite Materials, 2012. **19**(3-4): p. 545-559.

130. Kleiber, M., et al., *Parameter sensitivity in nonlinear mechanics: Theory and finite element computations*. 1997: Wiley.

131. Ascher, U.M., S.J. Ruuth, and B.T. Wetton, *Implicit-explicit methods for time-dependent partial differential equations.* SIAM Journal on Numerical Analysis, 1995. **32**(3): p. 797-823.

132. Bursi, O. and J.-P. Jaspart, *Calibration of a finite element model for isolated bolted end-plate steel connections.* Journal of Constructional Steel Research, 1997. **44**(3): p. 225-262.

133. Repetto, E., R. Radovitzky, and M. Ortiz, *Finite element simulation of dynamic fracture and fragmentation of glass rods.* Computer Methods in Applied Mechanics and Engineering, 2000. **183**(1-2): p. 3-14.

134. Sigmund, O. and J. Petersson, *Numerical instabilities in topology optimization: a survey on procedures dealing with checkerboards, mesh-dependencies and local minima.* Structural optimization, 1998. **16**(1): p. 68-75.

135. Ho-Le, K., *Finite element mesh generation methods: a review and classification.* Computer-aided design, 1988. **20**(1): p. 27-38.

136. Dutt, A., *Effect of mesh size on finite element analysis of beam.* Int J Mech Eng, 2015. **2**(12): p. 8-10.

137. Marfurt, K.J., *Accuracy of finite-difference and finite-element modeling of the scalar and elastic wave equations.* Geophysics, 1984. **49**(5): p. 533-549.

138. Macek, R.W. and S.A. Silling, *Peridynamics via finite element analysis.* Finite Elements in Analysis and Design, 2007. **43**(15): p. 1169-1178.

139. Hibbitt, H., *Abaqus/epgen–A general purpose finite element code with emphasis on nonlinear applications*, in *Structural Integrity Research of the Electric Power Research Institute*. 1984, Elsevier. p. 271-297.

140. Miller, R.K. and P. McIntire, *Acoustic emission testing*. 1987: American Society for Nondestructive Testing.

141. McFadden, P. and J. Smith, *Vibration monitoring of rolling element bearings by the high-frequency resonance technique—a review.* Tribology international, 1984. **17**(1): p. 3-10.

142. Nashed, M.S., *Acoustic emission monitoring of propulsion systems: a laboratory study on a small gas turbine*. 2010, Heriot-Watt University.

143. Maillet, E., et al., *Analysis of Acoustic Emission energy release during static fatigue tests at intermediate temperatures on Ceramic Matrix Composites: Towards rupture time prediction.* Composites Science and Technology, 2012. **72**(9): p. 1001-1007.

144. Droubi, M.G., *Monitoring particle impact energy using acoustic emission technique*. 2013, Heriot-Watt University.

145. Verruijt, A., *A complex variable solution for a deforming circular tunnel in an elastic half- plane.* International Journal for Numerical and Analytical Methods in Geomechanics, 1997. **21**(2): p. 77-89.

146. Niri, E.D. and S. Salamone, *A probabilistic framework for acoustic emission source localization in plate-like structures.* Smart Materials and Structures, 2012. **21**(3): p. 035009.

147. Alleyne, D.N. and P. Cawley, *Optimization of Lamb wave inspection techniques.* NDT & E International, 1992. **25**(1): p. 11-22.

148. Sun, J., K. Lee, and H. Lee, *Comparison of implicit and explicit finite element methods for dynamic problems.* Journal of Materials Processing Technology, 2000. **105**(1-2): p. 110-118.

149. Van Keulen, F., B. Liu, and R. Haftka. *Noise and discontinuity issues in response surfaces based on functions and derivatives*. in *41st Structures, Structural Dynamics, and Materials Conference and Exhibit*. 2000.

150. Madsen, J.I., W. Shyy, and R.T. Haftka, *Response surface techniques for diffuser shape optimization.* AIAA journal, 2000. **38**(9): p. 1512-1518.

151. McLaskey, G.C. and Glaser, S.D, *Hertzian impact: Experimental study of the force pulse and resulting stress waves*. Journal of the Acoustical Society of America, 2010. **128**(3): pp.1087-1096.

Appendix A: AE Sensor Calibration Certificates

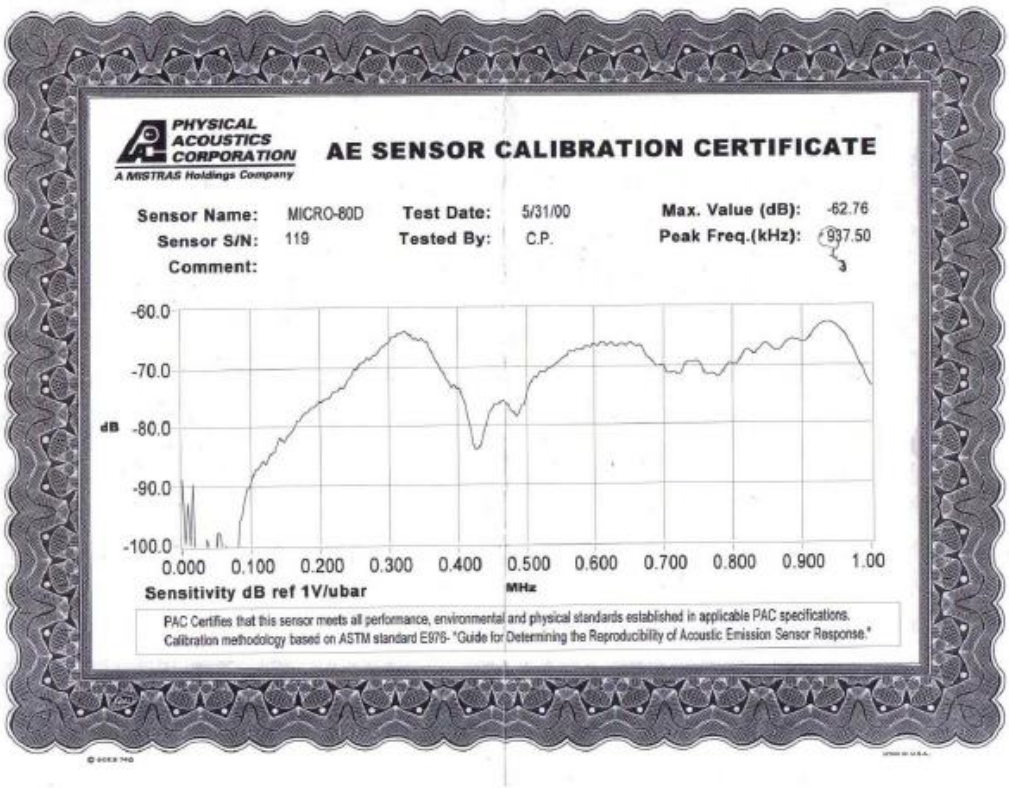
PHYSICAL ACOUSTICS CORPORATION
A MISTRAS Holdings Company

AE SENSOR CALIBRATION CERTIFICATE

Sensor Name: MICRO-80D Test Date: 5/31/00 Max. Value (dB): -62.76
Sensor S/N: 119 Tested By: C.P. Peak Freq.(kHz): 937.50
Comment:

-60.0
-70.0
dB -80.0
-90.0
-100.0
0.000 0.100 0.200 0.300 0.400 0.500 0.600 0.700 0.800 0.900 1.00
Sensitivity dB ref 1V/ubar
MHz

PAC Certifies that this sensor meets all performance, environmental and physical standards established in applicable PAC specifications.
Calibration methodology based on ASTM standard E976- "Guide for Determining the Reproducibility of Acoustic Emission Sensor Response."

A - 1 : *AE sensor certificate for sensor 119*

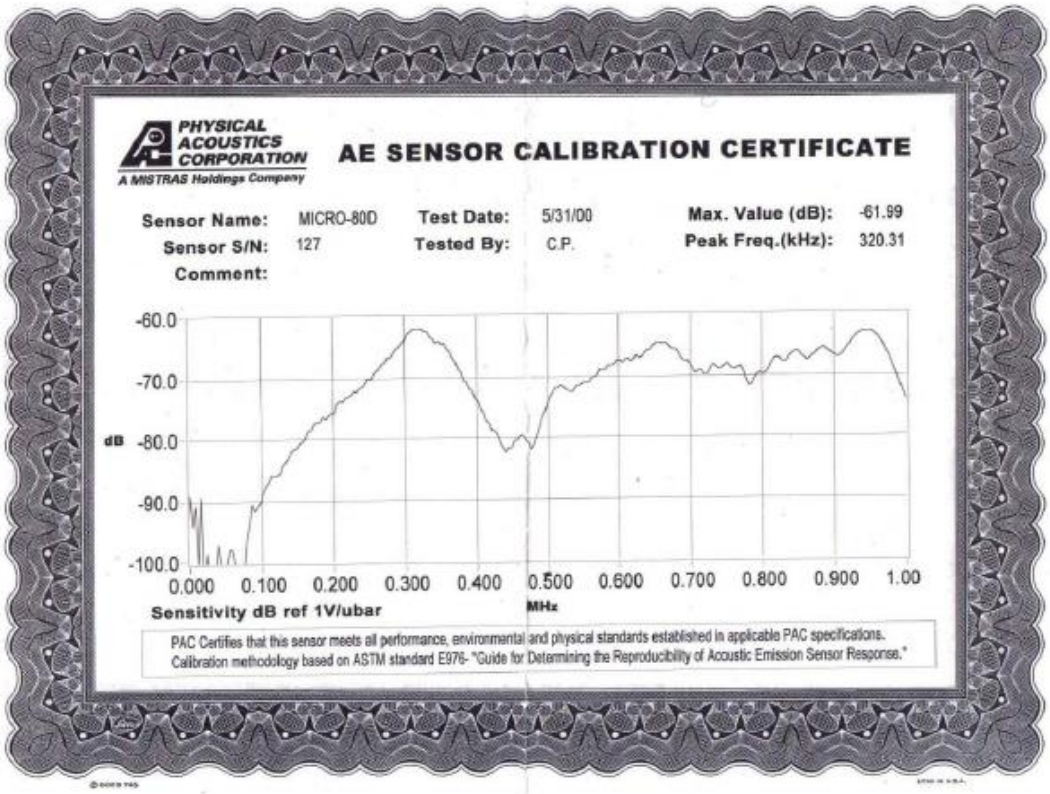
PHYSICAL ACOUSTICS CORPORATION
A MISTRAS Holdings Company

AE SENSOR CALIBRATION CERTIFICATE

Sensor Name: MICRO-80D Test Date: 5/31/00 Max. Value (dB): -61.99
Sensor S/N: 127 Tested By: C.P. Peak Freq.(kHz): 320.31
Comment:

-60.0
-70.0
dB -80.0
-90.0
-100.0
0.000 0.100 0.200 0.300 0.400 0.500 0.600 0.700 0.800 0.900 1.00
Sensitivity dB ref 1V/ubar
MHz

PAC Certifies that this sensor meets all performance, environmental and physical standards established in applicable PAC specifications.
Calibration methodology based on ASTM standard E976- "Guide for Determining the Reproducibility of Acoustic Emission Sensor Response."

A - 2: *AE sensor certificate for sensor 127*